

**EFFICIENT SENSITIVITY ANALYSIS AND DESIGN
OPTIMIZATION OF PHOTONIC DEVICES**

By

Mohamed A. Swillam, M.Sc., B.Sc.

A Thesis

Submitted to the School of Graduate Studies

in Partial Fulfillment of the Requirements

for the Degree

Doctor of Philosophy

McMaster University

Oct. 2008

DOCTOR OF PHILOSOPHY (2008)
(Electrical Engineering)

McMaster University
Hamilton, Ontario

TITLE: **Efficient Sensitivity Analysis and Design Optimization
of Photonic Devices**

AUTHORS: Mohamed A. Swillam
M.Sc.
(Faculty of Engineering, Ain Shams University, Egypt)
B.Sc.
(Faculty of Engineering, Ain Shams University, Egypt)

SUPERVISORS: M. H. Bakr
Associate Professor, Department of Electrical and
Computer Engineering
B.Sc., M.Sc. (Cairo University, Egypt)
Ph.D. (McMaster University, Canada)
P.Eng. (Province of Ontario)

X. LI
Professor, Department of Electrical and Computer
Engineering
B.Sc. (Shandong University, China)
M. Sc. (Wuhan research institute, China)
Ph. D. (Beijing Jiaotong University, China)
P.Eng (Province of Ontario)

Number of Pages: xvi, 221

ABSTRACT

In this thesis, we propose efficient approaches for design optimization of passive and active photonic devices. These approaches are based on utilizing gradient based optimization algorithms for efficient optimization of photonic devices. Some of the proposed approaches obtain the required gradient (sensitivity) information efficiently using adjoint variable method (AVM) applied directly to the exploited numerical techniques. Other approaches are based on formulating the design problem as an optimization problem using convex programming. These approaches utilize the gradient-based interior point method (IPM) for solving the design.

The AVM aims at efficiently obtaining the sensitivity information using the numerical technique. This technique requires a solution of an additional simulation of the adjoint system. The information obtained from the original and the adjoint simulation is sufficient to obtain the response and the sensitivity of the response with respect to all the design parameters. The AVM technique differs for different numerical method.

The obtained sensitivity using the AVM approach is not only useful for exploiting gradient based optimization for design optimization, but also for yield and tolerance analyses of the newly proposed designs.

We proposed a second order accurate approach to obtain the sensitivity information using finite difference time domain (FDTD) technique. This approach utilizes the AVM to efficiently obtain the sensitivity information. This approach is exploited for efficiently obtaining the sensitivity of the power reflectivity and coupling coefficient of

various devices. This approach has been also utilized for obtaining the sensitivity of the dispersion characteristics of different guided wave structures.

We also introduce a novel approach for sensitivity analysis of photonic devices using the beam propagation method (BPM). This approach is simple and easy to implement. It exploits the existing factorization of the system matrices for efficient calculation of the sensitivity of the required objective function. This approach is also utilized for sensitivity analysis of the vectorial modal properties of different guided wave structures. This approach is also exploited for sensitivity analysis of various surface plasmon devices.

This AVM approach is also exploited to propose a novel design of an optical switch with wide working wavelength band and compact size. The switch is based on the self imaging theory in multimode waveguide with a refractive index has approximate parabolic profile. The design problem is formulated as two stage optimization procedure. The optimization algorithm exploits the efficiently obtained sensitivity information from a BPM simulation. The final design has interesting characteristics.

An efficient approach is also proposed to obtain the sensitivity of the energy levels and wavefunctions of different quantum structures obtained using time dependent and time independent Schrödinger equation. This approach is exploited for design optimization of different quantum well lasers.

We also propose a convex formulation for the design problem of multilayer optical coatings. This formulation allows for efficient design of structures with large number of layers in fractions of a second without an initial design.

ACKNOWLEDGMENTS

I would like to express my sincere appreciation for my supervisor Dr. Mohamed Bakr, computational electromagnetics laboratory, McMaster University, for his guidance, constant support, encouragement and patience during the course of this work. His insightful ideas inspired most the resulted work of this thesis. Beside all that and most importantly, he really care about all the aspects of my life same as an elder brother. He helped me to enjoy my stay at Hamilton during the course of my Ph. D. I am indebt to him more that he knows.

I would like to express my sincere gratitude to my co-supervisor Dr. Xun Li, photonics research laboratory, McMaster University, for his advice, and crucial scientific contribution that made him the backbone of this thesis. I also would like to thank Dr. Natalia Nikolova and Dr. Wei-Ping Huang, members of my supervisory committee, for their useful discussion and interesting ideas.

I also wish to thank to my former colleagues at McMaster University, Dr. Ramy Gohary, Dr. Abounaser Hasanien and Dr. Ahmed Mohamed for their company that made most of me tough time bearable.

I would like to grant this thesis to Prof. Abd Elazim Swillam, my father, who taught me how to love my research work and enjoy spending my time and effort in it. He also did his best to support me and make my life easy and comfortable. All the love and thanks to my mother Dr. Karima and my sisters Esraa and Marwa for their encouragement, care and support.

Finally, I would like to express my deep gratitude to the person who worked harder than me to get this work done, my wife Rania. I am deeply thankful for her encouragement, patience, support and also for her effort in raising my sons Seif and Aly.

CONTENTS

| | | |
|-------|--|----|
| 1 | INTRODUCTION | 1 |
| 1.1 | Motivation..... | 1 |
| 1.2 | Contributions..... | 4 |
| 1.3 | Thesis Outline | 5 |
| 1.4 | References..... | 6 |
| 2 | NUMERICAL TECHNIQUES FOR MODELING PHOTONICS DEVICES | 11 |
| 2.1 | Introduction..... | 11 |
| 2.2 | Finite Difference Time Domain (FDTD)..... | 12 |
| 2.3 | Beam Propagation Method (BPM) | 17 |
| 2.3.1 | Iterative Methods | 21 |
| 2.3.2 | Non iterative Method (ADI method) | 21 |
| 2.4 | Conclusion | 23 |
| 2.5 | References..... | 24 |
| 3 | EFFICIENT SENSITIVITY ANALYSIS USING ADJOINT VARIABLE METHOD | 27 |
| 3.1 | Introduction..... | 27 |
| 3.2 | AVM Based on Electric Field Calculations for Time Domain Technique..... | 29 |
| 3.2.1 | AVM Approach for Dielectric Discontinuities..... | 32 |
| 3.3 | AVM Approach For Frequency Domain Techniques..... | 35 |
| 3.4 | Conclusion | 37 |
| 3.5 | References..... | 38 |
| 4 | ACCURATE AND EFFICIENT SENSITIVITY ANALYSIS FOR FDTD USING AVM..... | 41 |
| 4.1 | Introduction..... | 41 |
| 4.2 | Central AVM | 42 |
| 4.2.1 | SA-CAVM Approach For the Reflection Coefficient | 46 |
| 4.2.2 | Examples..... | 49 |
| 4.3 | Full Wave Calculations and Sensitivity Analysis of Dispersion Characteristics .. | 60 |
| 4.3.1 | Calculation of the Propagation Constants..... | 61 |
| 4.3.2 | Sensitivity Analysis of the Propagation Constants | 63 |
| 4.3.3 | Numerical Examples | 65 |
| 4.4 | Conclusion | 67 |
| 4.5 | References..... | 68 |
| 5 | BPM BASED EFFICIENT SENSITIVITY ANALYSIS EXPLOITING THE AVM..... | 71 |
| 5.1 | Introduction..... | 71 |
| 5.2 | Adjoint Sensitivity Analysis Using 2D Scalar BPM | 72 |
| 5.2.1 | Our CAVM Approach..... | 73 |
| 5.2.2 | Practical Implementation | 76 |
| 5.2.3 | Examples..... | 80 |

| | | |
|-------|--|-----|
| 5.2.4 | Computational Overhead..... | 94 |
| 5.3 | Sensitivity Analysis Using 3D Full Vectorial BPM..... | 96 |
| 5.3.1 | Sensitivity Analysis for Iterative Methods..... | 96 |
| 5.3.2 | Sensitivity Analysis for ADI-FVBPM..... | 97 |
| 5.3.3 | Sensitivity of the Modal Properties..... | 98 |
| 5.3.4 | Numerical Examples..... | 103 |
| 5.3.5 | Computational Efficiency..... | 112 |
| 5.4 | Sensitivity Analysis Using Analytical Derivative of the System Matrices..... | 114 |
| 5.4.1 | Sensitivity Analysis of Surface Plasmon Waveguide Structures..... | 115 |
| 5.5 | Conclusion..... | 126 |
| 5.6 | References..... | 127 |
| 6 | DESIGN OPTIMIZATION OF COMPACT WIDEBAND OPTICAL SWITCH EXPLOITING STAIR CASE INDEX MMI..... | 133 |
| 6.1 | Introduction..... | 133 |
| 6.2 | Parabolic Refractive Index MMI..... | 135 |
| 6.3 | Stair Case Refractive Index MMI (SCMMI) as an Optical Switch..... | 138 |
| 6.4 | Design Optimization of the SCMMI..... | 139 |
| 6.5 | Design Examples..... | 143 |
| 6.5.1 | Compact Design..... | 144 |
| 6.5.2 | A Weak Guiding Design..... | 147 |
| 6.5.3 | 3D Design using Strip Loaded Waveguide with Variable Heights..... | 149 |
| 6.6 | Discussion..... | 153 |
| 6.6.1 | Variable Applied Electric Field..... | 153 |
| 6.6.2 | Variable Doped Semiconductors..... | 154 |
| 6.7 | Conclusion..... | 154 |
| 6.8 | References..... | 155 |
| 7 | SENSITIVITY ANALYSIS OF QUANTUM STRUCTURES USING SCHRÖDINGER EQUATION..... | 161 |
| 7.1 | Introduction..... | 161 |
| 7.2 | Sensitivity Analysis of Time Independent Schrödinger Equation..... | 163 |
| 7.2.1 | Non Hermitian Hamiltonian..... | 164 |
| 7.2.2 | Hermitian Hamiltonian..... | 167 |
| 7.2.3 | Numerical Examples..... | 168 |
| 7.3 | Sensitivity Analysis of Time Dependent Schrödinger Equation..... | 175 |
| 7.3.1 | Numerical Examples..... | 178 |
| 7.4 | Conclusion..... | 179 |
| 7.5 | References..... | 180 |
| 8 | DESIGN OPTIMIZATION OF MULTILAYER OPTICAL COATING USING CONVEX OPTIMIZATION..... | 183 |
| 8.1 | Introduction..... | 183 |
| 8.2 | Theory of Multilayer Structures..... | 185 |
| 8.2.1 | 2-layers..... | 187 |
| 8.2.2 | 3-layers..... | 188 |
| 8.2.3 | 4-layer..... | 188 |

| | | |
|-------|---------------------------------------|-----|
| 8.3 | Problem Formulation | 189 |
| 8.3.1 | Linear Phase Formulation | 191 |
| 8.3.2 | Autocorrelation Formulation | 192 |
| 8.4 | Examples..... | 194 |
| 8.4.1 | 10-layer Antireflection Coatings..... | 194 |
| 8.4.2 | 6-layer Antireflection Coatings..... | 196 |
| 8.4.3 | 4-layer Antireflection Coatings..... | 196 |
| 8.4.4 | 10-layer Selective Filter | 198 |
| 8.5 | Discussion..... | 202 |
| 8.5.1 | Computational Time | 203 |
| 8.5.2 | Optimal Value..... | 204 |
| 8.6 | Conclusion | 205 |
| 8.7 | References..... | 205 |
| 9 | CONCLUSIONS..... | 209 |
| | BIBLIOGRAPHY..... | 213 |

LIST OF FIGURES

| | |
|---|----|
| Fig. 2.1. Yee's cell. | 15 |
| Fig. 3.1. Illustration of the stored points used to calculate the sensitivities with respect to the width of dielectric slab inside a waveguide with metallic boundaries using CAVM approach. | 34 |
| Fig. 4.1. Schematic diagram of an MMI 3 dB power splitter. | 49 |
| Fig. 4.2. The sensitivity of the energy function with respect to the length of the MMI 3dB power splitter for $W = 1.65 \mu\text{m}$ at wavelength $1.55 \mu\text{m}$ | 51 |
| Fig. 4.3. The sensitivity of the energy function with respect to the width of the MMI 3dB power splitter for $L_m = 3.2 \mu\text{m}$ at wavelength $1.55 \mu\text{m}$ | 52 |
| Fig. 4.4. Schematic diagram of the deeply etched waveguide terminator [8]. | 53 |
| Fig. 4.5. The sensitivity of the reflection coefficient with respect to the width of the trench L_l of the deeply etched waveguide terminator for $L_h = 280 \text{ nm}$ at $\lambda = 1.55 \mu\text{m}$ | 54 |
| Fig. 4.6. The sensitivity of the reflection coefficient with respect to the width of the residue L_h of the deeply etched waveguide terminator for $L_l = 120 \text{ nm}$ at $\lambda = 1.55 \mu\text{m}$ | 55 |
| Fig. 4.7. The sensitivity of the reflection coefficient with respect to the width of the trench L_l over a wavelength band of the deeply etched waveguide terminator at $[L_l, L_h] = [120.0, 280.0] \text{ nm}$ | 57 |
| Fig. 4.8. Schematic diagram of a waveguide terminated by double layer antireflection coatings. | 58 |
| Fig. 4.9. The reflectivity calculated using the FDTD simulation and measured data [10] of the double layer antireflection coatings. | 59 |
| Fig. 4.10. The sensitivity of the reflection coefficient with respect to L_2 of the double layer antireflection coatings for $L_1 = 181.6 \text{ nm}$ at wavelength of 1540 nm | 60 |
| Fig. 4.11. The propagation constants of the waveguide. | 66 |
| Fig. 4.12. Sensitivity of the propagation constants with respect to the core refractive index of the waveguide. | 67 |
| Fig. 5.1. Geometrical representation of the change of the grid cells due to forward change of the design parameters for on grid perturbation. The unperturbed structure is shown in (a), while the lateral perturbation is shown in (b), in (c) the propagation direction perturbation is shown, and the change in the refractive index is shown in (d). | 78 |
| Fig. 5.2. Schematic diagram of the directional coupler. | 81 |
| Fig. 5.3. The normalized sensitivity of the normalized power of the directional coupler example with respect to the separation distance d for a sweep of this parameter. | 82 |
| Fig. 5.4. Schematic diagram of MMI 3 dB power splitter. | 83 |
| Fig. 5.5. The normalized sensitivity of the real part of the coupling coefficient with respect to the length of the multimode section of the 3dB MMI power splitter for a width of $10.0 \mu\text{m}$ at wavelength of $1.55 \mu\text{m}$ | 84 |

Fig. 5.6. The normalized sensitivity of the imaginary part of the coupling coefficient with respect to the length of the multimode section of the 3dB MMI power for a width of 10.0 μm at wavelength of 1.55 μm 85

Fig. 5.7. The normalized sensitivity of the real part of the coupling coefficient with respect to the width of the multimode section of the 3dB MMI power for a length of 62.0 μm at wavelength of 1.55 μm 86

Fig. 5.8. The normalized sensitivity of the imaginary part of the coupling coefficient with respect to the width of the multimode section of the 3dB MMI power for a length of 62.0 μm at wavelength of 1.55 μm 87

Fig. 5.9. Schematic diagram of the Mach-Zehnder interferometer..... 87

Fig. 5.10. The normalized sensitivity of the real part of the coupling coefficient with respect to the refractive index of the modulation region of the Mach-Zehnder interferometer for $L_s = 8.0$ and $\lambda=1.55 \mu\text{m}$ 88

Fig. 5.11. The normalized sensitivity of the imaginary part of the coupling coefficient with respect to the refractive index of the modulation region of the Mach-Zehnder interferometer for $L_s = 8.0$ and $\lambda=1.55 \mu\text{m}$ 90

Fig. 5.12. The normalized sensitivity of the real part of the coupling coefficient with respect to the separation between the two waveguide L_s of the Mach-Zehnder interferometer for $n_m = 2.58$ and $\lambda=1.55 \mu\text{m}$ 91

Fig. 5.13. The normalized sensitivity of the imaginary part of the coupling coefficient with respect to the separation between the two waveguide L_s of the Mach-Zehnder interferometer. 92

Fig. 5.14. Schematic diagram of MMI 1x4 power splitter. 92

Fig. 5.15. The normalized sensitivity of the power coupling coefficient with respect to the shift of the axis of symmetry of the input waveguide s 93

Fig. 5.16. Schematic diagram of the polarization converter using periodically loaded rib waveguide. 103

Fig. 5.17. The normalized sensitivity of the coupling length of the polarization converter with respect to the refractive index of the loaded section n_l 104

Fig. 5.18. The normalized sensitivity of the beating length of the polarization converter with respect to the refractive index of the substrate n_s 105

Fig. 5.19. Schematic diagram of the rib waveguide..... 105

Fig. 5.20. The normalized sensitivity of the effective index of the quasi-TE mode of the rib waveguide with respect to the dimension D 107

Fig. 5.21. The normalized sensitivity of the effective index of the quasi-TE mode of the rib waveguide with respect to the dimension H 108

Fig. 5.22. The normalized sensitivity of the effective index of the quasi-TE mode of the rib waveguide with respect to the dimension W 108

Fig. 5.23. Schematic diagram of the polished fiber coupler. 109

Fig. 5.24. The normalized sensitivity of the power coupling coefficient of the polished fiber coupler with respect to refractive index of the index-matching liquid n_L 109

Fig. 5.25. The calculated power coupling coefficient at the output waveguide of the fiber coupler at each optimization iteration. 110

Fig. 5.26. Schematic diagram of the metal loaded waveguide 119

Fig. 5.27. Effective index of the fundamental mode of the metal loaded waveguide at wavelength $\lambda=1.55\mu\text{m}$ and $t=0.2\ \mu\text{m}$ 120

Fig. 5.28. Schematic diagram of the metal loaded channel waveguide. 120

Fig. 5.29. Normalized Sensitivity of the propagation length of the fundamental mode in a metal loaded on channel waveguide structure at wavelength $\lambda=1.55\mu\text{m}$, $W_m=W_s=0.5\ \mu\text{m}$, and $t_m=0.1\ \mu\text{m}$ 121

Fig. 5.30. Normalized Sensitivity of the propagation length of the fundamental mode in a metal loaded on channel waveguide structure at wavelength $\lambda=1.55\mu\text{m}$, $W_s=0.5\ \mu\text{m}$, $t_m=0.1\ \mu\text{m}$ and $t_s=0.5\ \mu\text{m}$ 122

Fig. 5.31. Normalized Sensitivity of the propagation length of the fundamental mode in a metal loaded on channel waveguide structure at wavelength $\lambda=1.55\mu\text{m}$, $W_m=0.5\ \mu\text{m}$, $t_m=0.1\ \mu\text{m}$ and $t_s=0.5\ \mu\text{m}$ 124

Fig. 5.32. Schematic diagram of 1x 3 power splitter SPPs structure. 125

Fig. 5.33. Normalized Sensitivity of the power coupling coefficient of 1x3 power splitter at wavelength $\lambda=1.55\mu\text{m}$, $L_m=78.2\ \mu\text{m}$, and $t_m=t_s=0.2\ \mu\text{m}$ 125

Fig. 5.34. Normalized Sensitivity of the power coupling coefficient of 1x3 power splitter at wavelength $\lambda=1.55\mu\text{m}$, $L_m=78.2\ \mu\text{m}$, and $t_s=0.2\ \mu\text{m}$ 126

Fig. 6.1. Schematic diagram of the MMI as an optical modulator. 137

Fig. 6.2. Schematic diagram of the stair case index profile for cross output case. 137

Fig. 6.3. Schematic diagram of the stair case index profile for bar output case. 141

Fig. 6.4. The refractive index of the SCI-MMI and PMMI. 141

Fig. 6.5. The field intensity of the a) PMMI and b) SCI-MMI. 142

Fig. 6.6. The power coupling versus the wavelength for the cross state for the compact design example. 146

Fig. 6.7. The power coupling versus the wavelength for the cross state for the weak guiding example. 147

Fig. 6.8. The schematic diagram of the OXC using SCMMI; a) the indexes of regions 1 and 2 match and b) the index of Region 2 is less than that of Region 1. 148

Fig. 6.9. Schematic diagram of the optical switch with variable height of strip loads. . 150

Fig. 6.10. The cross section of the proposed 3D optical switch with variable height strip load waveguide. 150

Fig. 6.11. The power coupling versus the wavelength at the output waveguide for the 3D design example using 2D BPM and the effective index method. 151

Fig 6.12. The power coupling at the cross arm versus the wavelength at the output waveguide for the 3D design example using 3D full vectorial simulation. 151

Fig. 7.1. Schematic diagram of the quantum well in the conduction band of single quantum well double hetrostructure laser. 168

Fig. 7.2 Normalized sensitivity of the wavefunction of the ground state with respect to V_2 170

Fig. 7.3. Schematic diagram of asymmetric quantum well laser. 172

Fig. 7.4. Normalized sensitivity of the energy level of the ground state of the first QW with respect to x_1 for $L_1=10\ \text{nm}$, $L_2=8\ \text{nm}$, $L_3=6\ \text{nm}$, $x_2=x_3=x_4=0.3$ 172

Fig. 7.5. Schematic diagram of the trapezoidal quantum well in the conduction band of a single quantum well double hetrostructure laser..... 173

Fig. 7.6. Normalized sensitivity of the energy level of the ground state of the trapezoidal QW with respect to η for $V_1=0.2501$ eV, $V_2=0.15$ eV, $V_3=0.101$ eV, $W=10$ nm, and $x=0.3$ 173

Fig. 7.7. Normalized sensitivity of α_1 of the ground state of the trapezoidal QW with respect to η for $V_1=0.2501$ eV, $V_2=0.15$ eV, $V_3=0.101$ eV, $W=10$ nm, and $x=0.3$. 174

Fig. 7.8 Normalized sensitivity of E_o of the ground state of the quantum wire with respect to W_y for $W_x=0.3$ nm, and barrier height of 0.1 eV. 179

Fig. 8.1. Schematic diagram of a multilayer dielectric structure with M layer..... 187

Fig. 8.2. Schematic diagram of the entire frequency band. 190

Fig. 8.3. The optimal normalized reflectivity response using the linear phase formulation of the 10-layer AR structure. 195

Fig. 8.4. The optimal normalized reflectivity response using the autocorrelation formulation of the 10-layer AR structure..... 195

Fig. 8.5. The optimal normalized reflectivity response of the 6-layer AR structure. 197

Fig. 8.6. The optimal reflectivity of 4-layer AR structure with 170 nm bandwidth. 198

Fig. 8.7. The optimal reflectivity of 4-layer AR structure with 100 nm bandwidth. 200

Fig. 8.8. The optimal normalized reflectivity of 10-layer selective filter structure using the autocorrelation formulation..... 200

Fig. 8.9. The optimal normalized reflectivity of 10-layer selective filter structure using the linear phase formulation. 201

Fig. 8.10. The computational time of solving the benchmark problem for different number of layers..... 201

Fig. 8.11. The relative deviation of the minimum reflectivity obtained by solving the benchmark problem for different number of layers. 202

LIST OF TABLES

| | |
|----------------|-----|
| Table 3.1..... | 35 |
| Table 4.1..... | 45 |
| Table 5.1..... | 95 |
| Table 5.2..... | 95 |
| Table 5.3..... | 114 |
| Table 5.4..... | 114 |
| Table 6.1..... | 154 |
| Table 7.1..... | 169 |
| Table 8.1..... | 196 |
| Table 8.2..... | 196 |
| Table 8.3..... | 196 |

1 INTRODUCTION

1.1 MOTIVATION

Photonic devices represent the backbone of the optical networks used for telecommunications and data transmission. In the last few decades, these devices have been used in a wide range of applications due to the enormous increase in the bandwidth requirements. These requirements motivated the design of novel components that meet the demanding applications. In addition to their application in data transmission, photonic devices have been also key elements in the advancement of biomedical technology. However, each of these applications may put fundamentally different constraints on the design of these devices. Therefore, it is of prime importance to study the behavioural model of these devices and to efficiently optimize their design parameters.

Motivated by the ever increasing applications of photonic devices, we propose in this thesis two different approaches for efficient design optimization of photonic devices. The first approach is based on efficient extraction of the sensitivities of the desired response to variations in the considered design parameters. In addition to their utility in studying design robustness, those sensitivities represent the gradient of the desired response. Hence, they can be utilized in conjunction with gradient-based optimization techniques to determine the optimal design parameters. The second approach is to transform the design problem into a convex optimization problem. Such a problem can be

usually solved efficiently and its convexity ensures the global optimality of the obtained solution.

Sensitivity Extraction Approach: Although the classical technique for extracting the sensitivities of the desired response is based on finite difference (FD) approximations, this technique is computationally inefficient. A considerably more efficient technique is the so-called adjoint variable method (AVM). This method is based on constructing a system that is dual to the original system of equations. This dual system is known as the adjoint system and its derivation and analysis depend on the particular numerical technique used in modeling the photonic device. The solution of the original and adjoint problems is sufficient to obtain the response and its sensitivity with respect to all the design parameters. If the objective function is one of the S -parameters of the structure, the information required from the adjoint problem can be deduced from the original problem without solving the adjoint problem. On the other hand, the central FD approaches requires at least $2N$ extra simulation to obtain the sensitivity with respect to N design parameters. Due to its efficiency, the AVM can be instrumental in extracting the sensitivity information of the numerical techniques that are widely used for modeling both passive and active devices.

In the last few years, this approach has been efficiently applied to sensitivity analysis of complex microwave structures for different numerical methods [1]-[5]. These methods include time domain techniques such as the transmission line method (TLM) [3] and the finite difference time domain (FDTD)[4]. The AVM has also been applied to frequency domain techniques including the finite element method (FEM) [5], the method

of moments (MoM)[1], and the frequency domain transmission line method (FD-TLM) [2].

Recently, the AVM is applied to photonic devices using the finite difference frequency domain (FDFD) method[6]. For this approach, the algorithm proposed in [7] has been directly applied to the FDFD method with nonuniform grid to extract the sensitivities of photonic crystals. In[6], the sensitivity of the transmission response of a photonic-crystal-based bandpass optical filter is extracted using the AVM technique.

Thus the application of the AVM for photonic devices is limited to the FDFD approach which is rarely utilized in modeling photonic devices. An efficient AVM approach for the widely used techniques such as FDTD and beam propagation method (BPM) is obviously desirable. This will result in providing an efficient and smart full vectorial photonic simulation package that is capable of obtaining the response and its sensitivity with minimum additional cost. This sensitivity information is then provided to gradient-based optimization algorithm for topology and tolerance optimization.

Convex Optimization Approach: The theory of convex optimization offers an efficient methodology for designing multilayer structures. This methodology is based on extracting the “hidden” convexity that the design problem may possess, and allows the designer to incorporate any (finite) number of convex constraints. The convexity of the design formulation typically implies that the global optimal design can be obtained using highly efficient gradient-based numerical optimization tools such as the Interior Point Method (IPM). This approach has been widely utilized in communication theory and signal processing research areas for design of different types of digital filters [8]-[10]. To

the best of our knowledge this approach has been never utilized for electromagnetic design problems. Utilizing this efficient approach for designing photonic devices should have a significant effect on reducing the computational resources.

1.2 CONTRIBUTIONS

The author has a considerable contribution in proposing original techniques for sensitivity analysis and design optimization of passive and active photonic devices.

The AVM technique has been successfully applied to efficiently analyze the sensitivities of passive photonic devices using the finite difference time domain (FDTD) method [11]-[14]. This technique is applied to optimize different passive structures and the antireflection coatings of semiconductor amplifiers. We also proposed an efficient approach to extract the dispersion characteristics of any guided structures and their sensitivities with respect to all the design parameters for all the modes over the desired frequency bandwidth using one FDTD simulation only [15]. This approach is useful for optimizing the dispersion characteristics for any novel structure.

We also proposed a new AVM approach for the scalar [16],[17] and the full vectorial 3-D versions of the beam propagation method (BPM) [18]-[20]. Those sensitivities have been utilized in efficient sensitivity and optimization of different structures such as directional couplers, multimode interference (MMI) sections, fiber couplers, rib waveguides, polarization converters, and Mach-Zehnder modulators. The AVM approach sensitivities have been also utilized to design and optimize a novel wideband ultra compact optical switch using stair case MMI [21],[22]. We also developed an efficient approach for sensitivity analysis and design optimization for surface plasmon

polariton guided wave structures [23].

For active photonic devices, we have employed the AVM technique in analyzing the sensitivity of the energy states and the wavefunctions of multiple quantum-well (QW) lasers for broadband and tunable applications using the FD approximation of the time-independent Schrödinger equation [24].

We have provided a convex formulation for the problem of designing multilayer optical structures. This approach is capable of obtaining the optimal design of multilayer structures of 40 layers in fractions of a second. This approach has been applied for different filter application such as band pass filters, antireflection coatings, and high reflection coatings [25]-[27].

1.3 THESIS OUTLINE

The objective of this thesis is to introduce novel techniques for efficient optimization of the different photonic devices.

In Chapter 2, a brief review of the numerical techniques widely used in modeling and simulating photonic devices is given. In this chapter, the governing equations of the FDTD and the BPM which are capable of modeling most of the conventional photonic devices are discussed. These governing equations are later utilized to calculate the sensitivity using AVM approach.

The basics of the existing AVM techniques for time domain and frequency domain numerical methods are briefly discussed in Chapter 3. In Chapter 4, a second order accurate AVM approach has been proposed for efficient sensitivity analysis using FDTD. The AVM approach for the BPM is presented in Chapter 5. In Chapter 6, an

application of the proposed AVM approach using BPM is discussed. In this chapter the sensitivity information has been utilized to obtain a novel optimized optical switch with wide working wavelength band and compact size.

In Chapter 7, novel approaches for sensitivity analysis of the eigen parameters of semiconductor quantum structures have been proposed. These approaches are applied for both time dependent and time independent Schrödinger equation.

The convex formulations of the multilayer optical structures are presented in Chapter 8. These formulations allow for efficient design of any filter type of the multilayer structures. Finally, the conclusion is given in Chapter 9.

1.4 REFERENCES

- [1] N. K. Nikolova, R. Safian, E. A. Soliman, M. H. Bakr, and J. W. Bandler, "Accelerated gradient based optimization using adjoint sensitivities," *IEEE Trans. Antennas Propagat.*, vol. 52, pp. 2147–2157, Aug. 2004.
- [2] M. H. Bakr and N. K. Georgieva, "An adjoint variable method for frequency domain TLM problems with conducting boundaries," *IEEE Microwave Wireless Comp. Lett.*, vol. 13, pp. 408–410, Nov. 2003.
- [3] M. H. Bakr and N. K. Nikolova, "An adjoint variable method for time domain TLM with wideband Johns matrix boundaries," *IEEE Trans. Microwave Theory Tech.*, vol. 52, pp. 678–685, Feb. 2004.
- [4] N. K. Nikolova, H. W. Tam, and M. H. Bakr, "Sensitivity analysis with the FDTD method on structured grids," *IEEE Trans. Microwave Theory Tech.*, vol. 52, pp. 1207–1216, Apr. 2004.

- [5] H. Akel and J. P. Webb, "Design sensitivities for scattering-matrix calculation with tetrahedral edge elements," *IEEE Trans. Magn*, vol. 36, pp. 1043–1046, July 2000.
- [6] G. Veronis, R. W. Dutton, and S. Fan, "Method for sensitivity analysis of photonic crystal devices," *Optics Letters*, vol. 29, pp. 2288–2290, Oct. 2004.
- [7] N. K. Georgieva, S. Glavic, M.H. Bakr, and J.W. Bandler, "Feasible adjoint sensitivity technique for EM design optimization," *IEEE Trans. Microwave Theory Tech.*, vol. 50, pp. 2751–2758, Dec. 2002.
- [8] S.-P. Wu, S. Boyd, and L. Vandenberghe, "FIR filter design via semidefinite programming and spectral factorization," *Proc. IEEE Conf. on Decision and Control*, 1996, pp. 271–276.
- [9] B. Alkire and L. Vandenberghe, "Convex optimization problems involving finite autocorrelation sequences," *Mathematical Programming*, vol. 93, pp. 331–359, July 2002.
- [10] S.-P. Wu, S. Boyd, and L. Vandenberghe, "FIR filter design via spectral factorization and convex optimization," In B. Datta, editor, *Applied and Computational Control, Signals, and Circuits*, vol. 1, pp.215–245. Birkhauser, 1998.
- [11] M. A. Swillam, M. H. Bakr, N. K. Nikolova, and X. Li, "Adjoint sensitivity analysis of dielectric discontinuities using FDTD," *J. Electromagnetics*, vol. 27 , pp. 123 – 140, Feb. 2007.
- [12] M. A. Swillam, M. H. Bakr, and X. Li, "Accurate sensitivity analysis of photonic devices exploiting the finite- difference time-domain central adjoint variable method," *Appl. Opt.*, vol. 46 , pp. 1492 – 1499, Mar. 2007.

- [13] M. A. Swillam, M. H. Bakr, and X. Li, “Accurate and efficient sensitivity extraction of complex structures using FDTD,” *Photonics North, proceedings of SPIE* 6796: 67963A-1– 67963A-8.I, Ottawa 2007. Best student paper award.
- [14] M. A. Swillam, M. H. Bakr, N. K. Nikolova, and X. Li, “Second order accurate sensitivities of dielectric discontinuities using FDTD,” *The 24th International Review of Progress in Applied Computational Electromagnetics (ACES)*: 1034–1039, Niagara falls 2008.
- [15] M. A. Swillam, M. H. Bakr, and X. Li, “Full wave sensitivity analysis of guided wave structures using FDTD,” *J. Electromag. Waves Applicat. (JEMWA)*. vol. 22, no. 16, pp 2135-2145, 2008.
- [16] M. A. Swillam, M. H. Bakr, and X. Li, “Efficient Adjoint sensitivity analysis exploiting the FD-BPM,” *IEEE/OSA J. Lightwave Technol.*, vol. 25, no. 7, pp. 1861 – 1869, Jul. 2007.
- [17] M. A. Swillam, M. H. Bakr, and X. Li, “BPM based efficient sensitivity analysis exploiting the adjoint variable method,” *Integrated Photonics and Nanophotonics Research and Applications (IPNRA)*, OSA Technical Digest (CD): IWB4. 1–3, Salt Lake City (2007).
- [18] M. A. Swillam, M. H. Bakr, and X. Li, “Full vectorial 3D sensitivity analysis and design optimization using BPM,” *IEEE/OSA J. Lightwave Technol.*, vol. 26, pp 528 – 536, Mar.. 2008.

- [19] M. A. Swillam, M. H. Bakr, and X. Li, “Accurate and efficient sensitivity analysis using the beam propagation method,” *Photonics North, proceedings of SPIE 7099: 70991C-1–70991C-8*. Montreal 2008.
- [20] M. A. Swillam, M. H. Bakr, and X. Li, “Efficient approach for 3D full vectorial sensitivity analysis using ADI-BPM,” *Integrated Photonics and Nanophotonics Research and Applications (IPNRA), OSA Technical Digest (CD): IWF8*. 1–3, Boston 2008.
- [21] M. A. Swillam, M. H. Bakr, and X. Li, “Design optimization of compact wideband optical switch exploiting stair case index MMI,” *IEEE/OSA J. Lightwave Technol.*, vol. 27. pp 80 – 87, Jan. 15th 2009 .
- [22] M. A. Swillam, M. H. Bakr, and X. Li, “Wide band optical switch using stair case MMI,” *LEOS Annual Meeting*, Newport Beach 2008.
- [23] M. A. Swillam, M. H. Bakr, and X. Li, “Efficient 3D sensitivity analysis of surface plasmon waveguide structures,” *Opt. Express*, vol. 16, pp. 16371-16381 Oct. 2008.
- [24] M. A. Swillam, M. H. Bakr, X. Li and J. Deen, “Efficient sensitivity analysis of time independent Schrödinger equation with application to quantum lasers,” *Opt. Comm.*, vol. 281, pp 4169-4554, Sep. 2008.
- [25] M. A. Swillam, M. H. Bakr, and X. Li, “The design of multilayer optical coatings using convex optimization,” *IEEE/OSA J. Lightwave Technol.*, vol. 25 , pp. 1078 – 1085, Apr. 2007.

- [26] M. A. Swillam, M. H. Bakr, and X. Li, “Design of multilayer optical filters using linear programming based on autocorrelation sequences,” *Integrated Photonics and Nanophotonics Research and Applications (IPNRA)*. OSA Technical Digest (CD): ITuA6.1–3, Salt Lake City 2007.
- [27] M. A. Swillam, M. H. Bakr, and X. Li, “A novel design approach for multilayer dielectric filters exploiting linear programming,” *IEEE Antenna and propagation international symposium (APs)*: 3940 – 3943, Honolulu 2007.

2 NUMERICAL TECHNIQUES FOR MODELING PHOTONICS DEVICES

2.1 INTRODUCTION

The fast growth in the computational power has an effective impact on the modeling techniques of photonic devices. As a result of this growth, these techniques moved from analytical and semi-analytical approaches that can handle only simple structures to rigorous numerical techniques that can handle very complex structures.

The analytical or semi-analytical based techniques include coupled mode theory, matrix method, and mode matching. However, the application of these techniques is limited to specific devices such as coupled devices, layered devices, and periodic devices, respectively. In order to model a wider class of devices, numerical techniques for solving Maxwell's equations or the wave equation should be utilized. Several numerical approaches are currently available. Some of these numerical approaches are utilized for solving the modal characteristics of the structures by obtaining the mode profile and the propagation constants of the device. However, the majority of these techniques are utilized for simulating the optical field behaviour inside the photonic devices. Depending on the application, some of these techniques are preferred to others. In general, the finite difference time domain (FDTD) is considered as a universal approach that can handle very wide range of devices. The main drawback of this approach is the huge consumption

of computer resources especially for photonic device with electrically long sections. In order to overcome this problem, other techniques can be utilized for modeling such long devices. The most widely used technique of those is the beam propagation method (BPM). By using different versions of this technique, it can handle wide range of devices. FDTD and BPM are considered the most widely used techniques for modeling guided wave photonic devices. Due to its universality, they are also utilized in many commercial packages.

There are many other approaches that attract the attention in the last decade such as method of lines and finite difference frequency domain. However, we believe that the amount of application of these techniques are still limited and they are not currently utilized in any commercial packages.

In this chapter, we briefly review the fundamentals of both the FDTD and the BPM. This review is limited to the basics and governing equations of these approaches.

2.2 FINITE DIFFERENCE TIME DOMAIN (FDTD)

FDTD is a direct solution of the time-dependent differential form of Maxwell's equations. The FDTD is mainly a discretization of the Maxwell's equations in time domain using central differences technique. This method was first introduced by Yee [1] in 1966 for microwave applications. It was later utilized for modeling optical structures [1]. Here, the Cartesian discretization of the electric field and magnetic field based on Yee's Algorithm is presented [2].

The electric field update equations are given by

$$\begin{aligned}
 E_x|_{i,j,k}^{n+1} &= C_a(i, j, k). E_x|_{i,j,k}^n \\
 &+ C_b(i, j, k). \left[\frac{H_z|_{i,j,k}^{n+0.5} - H_z|_{i,j-1,k}^{n+0.5}}{\Delta y} - \frac{H_y|_{i,j,k}^{n+0.5} - H_y|_{i,j,k-1}^{n+0.5}}{\Delta z} - J_{ex}|_{i,j,k}^{n+0.5} \right]
 \end{aligned} \quad (2.1)$$

$$\begin{aligned}
 E_y|_{i,j,k}^{n+1} &= C_a(i, j, k). E_y|_{i,j,k}^n \\
 &+ C_b(i, j, k). \left[\frac{H_x|_{i,j,k}^{n+0.5} - H_x|_{i,j,k-1}^{n+0.5}}{\Delta z} - \frac{H_z|_{i,j,k}^{n+0.5} - H_z|_{i-1,j,k}^{n+0.5}}{\Delta x} - J_{ey}|_{i,j,k}^{n+0.5} \right]
 \end{aligned} \quad (2.2)$$

$$\begin{aligned}
 E_z|_{i,j,k}^{n+1} &= C_a(i, j, k). E_z|_{i,j,k}^n \\
 &+ C_b(i, j, k). \left[\frac{H_y|_{i,j,k}^{n+0.5} - H_y|_{i-1,j,k-1}^{n+0.5}}{\Delta x} - \frac{H_x|_{i,j,k}^{n+0.5} - H_x|_{i,j-1,k}^{n+0.5}}{\Delta y} - J_{ez}|_{i,j,k}^{n+0.5} \right]
 \end{aligned} \quad (2.3)$$

where

$$C_a(i, j, k) = \frac{1 - \frac{\sigma(i, j, k)\Delta t}{2\varepsilon(i, j, k)}}{1 + \frac{\sigma(i, j, k)\Delta t}{2\varepsilon(i, j, k)}}, \text{ and } C_b(i, j, k) = \frac{\frac{\Delta t}{\varepsilon(i, j, k)}}{1 + \frac{\sigma(i, j, k)\Delta t}{2\varepsilon(i, j, k)}} \quad (2.4)$$

where the indices n , i , j , and k represent the discretization in time, x direction, y direction, and z direction, reactively. In (2.1) -(2.3), E , H and J are the electric field, the magnetic field and the electric current, respectively. σ and ε in (2.4) are the electric conductivity and the permittivity, respectively.

The update equations of the magnetic field are given by

$$H_x|_{i,j,k}^{n+0.5} = D_a(i, j, k). H_x|_{i,j,k}^{n-0.5} + D_b(i, j, k). \left[\frac{E_z|_{i,j,k}^n - E_z|_{i,j+1,k}^n}{\Delta y} - \frac{E_y|_{i,j,k}^n - E_y|_{i,j,k+1}^n}{\Delta z} \right] \quad (2.5)$$

$$H_y|_{i,j,k}^{n+0.5} = D_a(i, j, k).H_x|_{i,j,k}^{n-0.5} + D_b(i, j, k). \left[\frac{E_x|_{i,j,k}^n - E_x|_{i,j,k+1}^n}{\Delta z} - \frac{E_z|_{i,j,k}^n - E_z|_{i+1,j,k}^n}{\Delta x} \right] \quad (2.6)$$

$$H_z|_{i,j,k}^{n+0.5} = D_a(i, j, k).H_x|_{i,j,k}^{n-0.5} + D_b(i, j, k). \left[\frac{E_y|_{i,j,k}^n - E_x|_{i,j+1,k}^n}{\Delta x} - \frac{E_x|_{i,j+1,k}^n - E_x|_{i,j,k}^n}{\Delta y} \right] \quad (2.7)$$

where

$$D_a(i, j, k) = \frac{1 - \frac{\sigma_m(i, j, k)\Delta t}{2\mu(i, j, k)}}{1 + \frac{\sigma_m(i, j, k)\Delta t}{2\mu(i, j, k)}}, \text{ and } \frac{\Delta t}{1 + \frac{\sigma_m(i, j, k)\Delta t}{2\mu(i, j, k)}} \quad (2.8)$$

where σ_m and μ in (2.8) are the magnetic conductivity and the permeability respectively.

As shown from the update equations, the electric field and the magnetic field components are located at alternative half space steps as shown in Fig..2.1. They are also updated at alternative half time step. This approach is called the leap-frog approach.

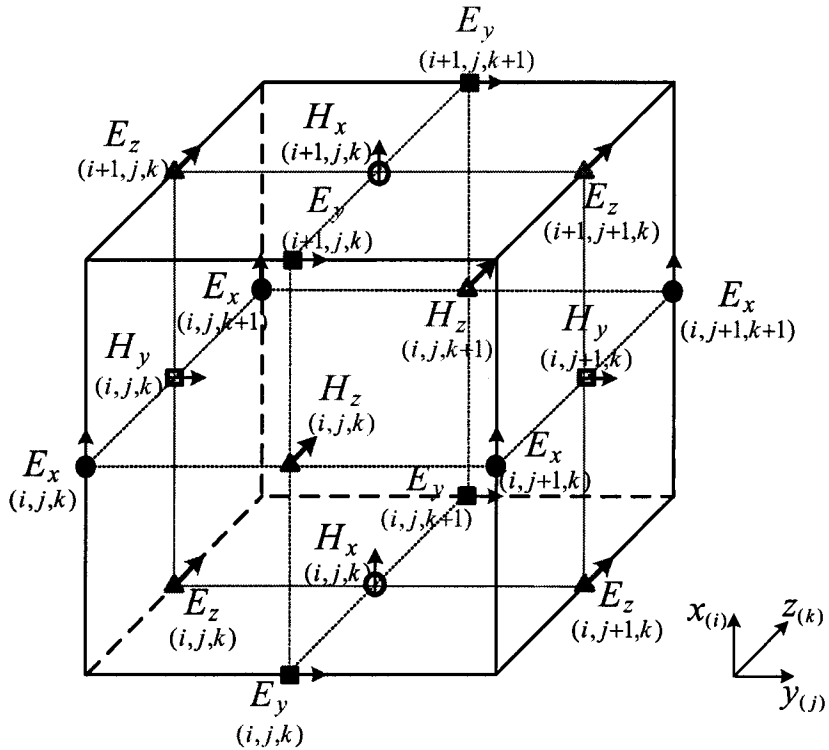


Fig..2.1. Yee's cell.

FDTD is very rigorous technique and can solve huge number of optical structures. However, this technique is slow for photonic structures. This is mainly due to the fact that most of the photonic structures are electrically large. FDTD also consumes huge computational resources. Thus, most of the applications that can be handled on a personal computer are limited to the 2D version of this approach. Complex 3D structures are usually simulated using parallel computational techniques to provide the necessary processing power and memory requirements of this technique.

The stability of the Yee' cell-based FDTD is mainly governed by the Courant relationship [2]. This relationship imposes a constraint on the time step of the stable algorithm to satisfy the following relationship

$$\Delta t \leq \frac{1}{C \sqrt{\frac{1}{(\Delta x)^2} + \frac{1}{(\Delta y)^2} + \frac{1}{(\Delta z)^2}}} \quad (2.9)$$

where C is the velocity of the light in the modeled medium.

As shown from the above stability condition, the time step of the FDTD algorithm reduces with the reduction of the spatial grid size. As a result, for structures with fine details this algorithm takes longer time to converge to a stable solution. This is one of the major drawbacks of the FDTD technique.

In general, photonic devices are considered open structures. An effective absorbing boundary condition (ABC) is thus needed in the implemented algorithm to avoid any reflection of the field from the edges of the finite numerical window. In general, the absorbing boundary should be few cells only outside the computational domain. In the ideal case, the absorbing medium should be reflectionless to all impinging waves over their full frequency spectrum, highly absorbing, and effective in the near field of a source. In 1994, Berenger introduced a highly effective absorbing material called the perfectly matched layer (PML) [3]. It is based on matching the incident wave with arbitrary frequency and polarization at the boundary. Many versions and modifications were later introduced to Berenger's PML such as stretched coordinate PML [4] and uniaxial PML [5]. These modifications have an effective impact on reducing the implementation efforts. They also make the update of the field components inside the absorbing medium similar to those inside the regular computational region.

2.3 BEAM PROPAGATION METHOD (BPM)

The huge computational resources consumed by the FDTD technique motivate the research for more suitable approach for photonic devices. The beam propagation method (BPM) provides an efficient solution for modeling and simulation of photonic devices. It is capable of modeling different structures using different versions of this technique. BPM was first introduced for modeling optical fiber using fast Fourier transform approach (FFT) [6]. However, the FFT-BPM is limited for low contrast structures and can not easily handle the polarization. An implicit finite difference approach is later exploited for the BPM (FD-BPM) [7]. This approach is superior and is utilized for most of the applications using BPM [8],[9]. This approach was developed for the scalar case and latter extended to the vectorial case [10]- [12].

A brief review of the BPM approach is given in this section. We start by reviewing the governing equations of this method [11]. For this propose, the vectorial wave equation for an isotropic medium can be written as:

$$\nabla \times \nabla \times \mathbf{E} - n^2 k^2 \mathbf{E} = 0 \quad (2.10)$$

where n is the refractive index of the medium. By using the vector identity

$$\nabla \times \nabla \times \mathbf{E} = \nabla(\nabla \cdot \mathbf{E}) - \nabla^2 \mathbf{E}, \quad (2.11)$$

the wave equation can be rewritten as

$$\nabla \times \nabla \times \mathbf{E} = \nabla(\nabla \cdot \mathbf{E}) - \nabla^2 \mathbf{E} = n^2 k^2 \mathbf{E}. \quad (2.12)$$

By using Gauss law

$$\nabla \cdot (\epsilon \mathbf{E}) = \epsilon \nabla \cdot \mathbf{E} + \nabla \epsilon \cdot \mathbf{E} = 0, \quad (2.13)$$

we have

$$\nabla \cdot \mathbf{E} = -\frac{\nabla \varepsilon}{\varepsilon} \cdot \mathbf{E} \quad (2.14)$$

Substituting (2.14) into (2.12) we get

$$\nabla \times \nabla \times \mathbf{E} = \nabla \left(-\frac{\nabla \varepsilon}{\varepsilon} \cdot \mathbf{E} \right) - \nabla^2 \mathbf{E} \quad (2.15)$$

Thus the vectorial equation can be written as

$$\nabla^2 \mathbf{E} + n^2 k^2 \mathbf{E} = -\nabla \left(\frac{\nabla \varepsilon}{\varepsilon} \cdot \mathbf{E} \right) \quad (2.16)$$

For the transverse component of the electric field we get

$$\nabla^2 \mathbf{E}_t + n^2 k^2 \mathbf{E}_t = -\nabla \left(\frac{\nabla \varepsilon}{\varepsilon} \cdot \mathbf{E}_t \right) \quad (2.17)$$

By using $\frac{\partial n^2}{\partial z} \cdot \mathbf{E}_z \approx 0$,

The equation (2.17) can be expressed in terms of the transverse field components as follows:

$$\nabla^2 E_x + n^2 k^2 E_x = -\frac{\partial}{\partial x} \left(\frac{\partial \ln n^2}{\partial x} \cdot E_x \right) - \frac{\partial}{\partial x} \left(\frac{\partial \ln n^2}{\partial y} \cdot E_y \right) \quad (2.18)$$

$$\nabla^2 E_y + n^2 k^2 E_y = -\frac{\partial}{\partial y} \left(\frac{\partial \ln n^2}{\partial y} \cdot E_y \right) - \frac{\partial}{\partial y} \left(\frac{\partial \ln n^2}{\partial x} \cdot E_x \right) \quad (2.19)$$

In the BPM method, the field is assumed to have a slowly varying envelope and a fast oscillating phase term. The field can thus be written as

$$\mathbf{E}_t = \boldsymbol{\psi}_t e^{-jn_0 k z} \quad (2.20)$$

where n_o is the reference refractive index. Substituting (2.20) into (2.18) and (2.19), and making use of the slowly varying approximation:

$$\left| \frac{\partial^2 \psi_t}{\partial z^2} \right| \ll 2n_o k \left| \frac{\partial \psi_t}{\partial z} \right|, \quad (2.21)$$

we get the following system of equations

$$\frac{\partial}{\partial z} \psi_t = \frac{\partial}{\partial z} \begin{bmatrix} \psi_x \\ \psi_y \end{bmatrix} = \mathbf{P} \psi_t = \begin{pmatrix} \mathbf{P}_{xx} & \mathbf{P}_{xy} \\ \mathbf{P}_{yx} & \mathbf{P}_{yy} \end{pmatrix} \begin{bmatrix} \psi_x \\ \psi_y \end{bmatrix}. \quad (2.22)$$

The different operators in (2.22) are given by

$$\mathbf{P}_{xx} \psi_x = \frac{-j}{2n_o k} \left(\frac{\partial}{\partial x} \left(\frac{1}{n^2} \frac{\partial}{\partial x} (n^2 \psi_x) \right) + \frac{\partial^2 \psi_x}{\partial y^2} + (n^2 - n_o^2) k^2 \psi_x \right) \quad (2.23)$$

$$\mathbf{P}_{xy} \psi_y = \frac{-j}{2n_o k} \left(\frac{\partial}{\partial x} \left(\frac{1}{n^2} \frac{\partial}{\partial y} (n^2 \psi_y) \right) - \frac{\partial^2 \psi_y}{\partial x \partial y} \right) \quad (2.24)$$

$$\mathbf{P}_{yy} \psi_y = \frac{-j}{2n_o k} \left(\frac{\partial}{\partial y} \left(\frac{1}{n^2} \frac{\partial}{\partial y} (n^2 \psi_y) \right) + \frac{\partial^2 \psi_y}{\partial x^2} + (n^2 - n_o^2) k^2 \psi_y \right) \quad (2.25)$$

$$\mathbf{P}_{yx} \psi_x = \frac{-j}{2n_o k} \left(\frac{\partial}{\partial y} \left(\frac{1}{n^2} \frac{\partial}{\partial x} (n^2 \psi_x) \right) - \frac{\partial^2 \psi_x}{\partial y \partial x} \right) \quad (2.26)$$

where \mathbf{P}_{xy} and \mathbf{P}_{yx} represent the cross coupling terms. \mathbf{P}_{xx} and \mathbf{P}_{yy} represent the polarization terms.

The vector properties cause the polarization dependant propagation of the optical waves due to $\mathbf{P}_{xx} \neq \mathbf{P}_{yy}$ and the coupling between the two polarizations through \mathbf{P}_{xy} , and $\mathbf{P}_{yx} \neq \mathbf{0}$. For the two dimensional case, the polarization coupling terms associated with \mathbf{P}_{xy} , and \mathbf{P}_{yx} vanish. In this case, the vector waves may be decomposed

into the TE and TM waves and can be treated separately. If the refractive index contrast between the core and cladding regions is small (weakly guiding structure), the polarization dependence can be ignored. Thus the vector wave equation in (2.22) can be replaced with the scalar equation

$$\frac{\partial}{\partial z} \psi = \frac{-j}{2n_o k} \left(\frac{\partial^2}{\partial x^2} + \frac{\partial^2}{\partial y^2} + (n^2 - n_o^2)k^2 \right) \psi \quad (2.27)$$

For three dimensional structures, the polarization dependence and the coupling usually exist especially for high contrast index difference. Thus the propagating waves are usually hybrid. However, the couplings between the two polarizations are usually weak and can be ignored. Therefore, the coupling terms P_{xy} , and $P_{yx} \neq 0$. Thus the two polarizations can be treated independently using a decoupled set of equations given as

$$\frac{\partial}{\partial z} \psi_x = P_{xx} \psi_x \quad (2.28)$$

and

$$\frac{\partial}{\partial z} \psi_y = P_{yy} \psi_y \quad (2.29)$$

The two systems of equations given in (2.28) and (2.29) are called the semivectorial formulation of the BPM.

There are different methods to solve the system of equations given in (2.22),. These methods can be classified into iterative and non iterative methods. Hereafter, we give a brief review of both methods.

2.3.1 Iterative Methods

In these methods, successive over relaxation techniques are usually used to solve the system of equations at each propagation step. By using a weighted finite difference discretization in the z direction, the field state ψ_i^{l+1} at the propagation step $z_{l+1}=(l+1)\Delta z$ is obtained as follows:

$$(\mathbf{I} + j\Delta z\alpha\mathbf{P})\psi_i^{l+1} = (\mathbf{I} - j\Delta z(1-\alpha)\mathbf{P})\psi_i^l, \quad (2.30)$$

where \mathbf{I} is the identity matrix and α is a weighting factor that controls the finite difference scheme. For instance, $\alpha = 0$, $\alpha = 1$, and $\alpha = 0.5$ correspond to the explicit finite difference scheme, the implicit scheme, and the Crank-Nicholson scheme, respectively. Stability studies show that the algorithm is stable if $\alpha \geq 0.5$ [11]-[13].

The system of equations given in (2.30) can be discretized using finite differences (FD-FVBPM) [11]-[13]. For FD-FVBPM, the system of equations is solved using iterative methods [11]-[13]. For this method, the matrix \mathbf{P} is a banded non symmetric matrix with nine nonzero elements in each row [12].

The convergence and the efficiency of the iterative methods is an issue [14]. Non iterative procedures for solving multidimensional problems were later developed. These procedures mainly utilize the alternating direction implicit method (ADI) [14],[15].

2.3.2 Non iterative Method (ADI method)

The main advantage of the ADI-FVBPM is to avoid the operator inversion of the cross coupling terms. This ADI approach was first applied for scalar 3D BPM [16] and then extended to the semivectorial version [17]. The full vectorial algorithm was first

introduced in [15] using an explicit formulation for the cross coupling terms. However, this approach may cause stability problems. Later, unconditionally stable algorithm using the Crank-Nicholson approach is proposed for 3D-FVBPM [14]. This approach exploits the finite difference method to approximate the operators. The system of equations using this approach at each propagation step is given as [14]

$$\boldsymbol{\psi}'_{t+1} = \mathbf{K}' \boldsymbol{\psi}'_t = \left[(\boldsymbol{\Gamma}'_4)^{-1} \boldsymbol{\Gamma}'_3 (\boldsymbol{\Gamma}'_2)^{-1} \boldsymbol{\Gamma}'_1 \right] \boldsymbol{\psi}'_t \quad (2.31)$$

where

$$\begin{aligned} \boldsymbol{\Gamma}'_1 &= \mathbf{I} + \frac{\Delta z}{2} \begin{bmatrix} \mathbf{A}_x & \mathbf{P}_{xy} \\ \mathbf{0} & \mathbf{B}_x \end{bmatrix}, \quad \boldsymbol{\Gamma}'_2 = \mathbf{I} - \frac{\Delta z}{2} \begin{bmatrix} \mathbf{A}_y & \mathbf{0} \\ \mathbf{P}_{yx} & \mathbf{B}_y \end{bmatrix}, \\ \boldsymbol{\Gamma}'_3 &= \mathbf{I} + \frac{\Delta z}{2} \begin{bmatrix} \mathbf{A}_y & \mathbf{0} \\ \mathbf{P}_{yx} & \mathbf{B}_y \end{bmatrix}, \quad \boldsymbol{\Gamma}'_4 = \mathbf{I} - \frac{\Delta z}{2} \begin{bmatrix} \mathbf{A}_x & \mathbf{P}_{xy} \\ \mathbf{0} & \mathbf{B}_x \end{bmatrix} \end{aligned} \quad (2.32)$$

In (2.32), \mathbf{A}_x and \mathbf{A}_y represent the x -dependent and y -dependent components of the term \mathbf{P}_{xx} , respectively, and are given by

$$\mathbf{A}_x \boldsymbol{\psi}_x = \frac{-j}{2n_o k} \left(\frac{\partial}{\partial x} \left(\frac{1}{n^2} \frac{\partial}{\partial x} (n^2 \boldsymbol{\psi}_x) \right) + \frac{1}{2} (n^2 - n_o^2) k^2 \boldsymbol{\psi}_x \right) \quad (2.33)$$

and

$$\mathbf{A}_y \boldsymbol{\psi}_x = \frac{-j}{2n_o k} \left(\frac{\partial^2 \boldsymbol{\psi}_x}{\partial y^2} + \frac{1}{2} (n^2 - n_o^2) k^2 \boldsymbol{\psi}_x \right). \quad (2.34)$$

Similarly, \mathbf{B}_x and \mathbf{B}_y represent the x -dependent and y -dependent components of the term \mathbf{P}_{yy} given in (2.25), respectively.

The solution of the system of equations given in (2.31) is performed in a way to avoid the inversion of the cross coupling terms as shown in [14]. At each propagation

step, we need to solve a tridiagonal system of equations twice.

Transparent boundary condition (TBC) is one of the most efficient boundary conditions utilized to avoid the reflections from the boundary of the calculation window [18] with the BPM method. PML approaches were later developed and utilized for the BPM as an effective ABC [19].

The BPM is mainly based on the slowly varying approximation as given in (2.21). This approximation is considered as the main reason for simplifying the implementation. However, this approach is not accurate for modeling structures that have sharp bends or contain modes with propagation angles more than few degrees from the propagation axis. In order to increase the accuracy of the BPM for modeling these structures, wide-angle BPM approaches (WA-BPM) are developed. The most popular approach is based on utilizing Padé approximant operator for solving the governing equations given in (2.18) and (2.19) [20].

It is also clear from the assumption in (2.20) that the wave propagation is assumed to be in one direction. Thus the reflection from any interface is ignored in this approach. Many techniques were developed to take into account the effect of the reflection from any interfaces [21],[22].

2.4 CONCLUSION

A brief review of the modeling approaches for photonic device is given in this chapter. More emphasis is given to the widely used FDTD and BPM approaches. The governing equations and the basics of these techniques are given in this chapter. The advantages and disadvantages of these techniques are also discussed.

2.5 REFERENCES

- [1] K. S. Yee, “Numerical solution of initial boundary value problems involving Maxwell's equations in isotropic media,” *IEEE Trans. Antenna Propagat.*, vol 14, pp 302-307, May 1966.
- [2] A. Taflov, *Computational Electrodynamics: The Finite Difference Time Domain Method*. Norwood, MA: Artech House, 1995
- [3] J. P. Berenger, “A Perfectly matched layer for the absorption of electromagnetic-waves,” *J. of Comp. Phys.*, vol. 114, no. 2, pp. 185-200, Oct. 1994.
- [4] W.C Chew, and W.H Weedon, “A 3-D perfectly matched medium from modified Maxwell’s equations with stretched coordinates,” *Microw. Opt. Technol. Lett.* , vol. 7, pp.599–603, Sept. 1994
- [5] Z. S. Sacks, D. M. Kingsland, R. Lee, and J. F. Lee, “A perfectly matched anisotropic absorber for use as an absorbing boundary condition,” *IEEE Trans. Antennas Propagat.* vol. 43, pp. 1460-1463, Dec. 1995.
- [6] M. D. Feit and J. A. Fleck Jr. “Light propagation in graded-index optical fibers,” *Appl. Opt.*, vol. 17, pp. 3990-3998, Dec. 1978.
- [7] Y. Chung and N. Dagli, “An assessment of finite difference beam propagation method,” *IEEE J. Quantum Electron.*, vol. 26, pp.1335-1339, Aug. 1990.
- [8] D. Yevick and B. Hermansson, “New formulations of the matrix beam propagation method: Application to rib waveguides,” *IEEE J. Quantum Electron.*, vol. 25, pp. 221-229, 1989.

- [9] R. Scarmozzino, A. Gopinath, R. Pregla, and S. Helfert, "Numerical techniques for modeling guided-wave photonic devices," *IEEE J. Select. Topics Quantum Electron.*, vol. 6, pp. 150–162, Jan./Feb. 2000.
- [10] W. P. Huang, C. L. Xu, S. T. Chu, and S. K. Chaudhuri, "A vector beam propagation method for guided-wave optics," *IEEE Photon. Tech. Lett.*, vol. 3, pp. 910-913, Oct. 1991.
- [11] W. P. Huang and C. L. Xu, "Simulation of three-dimensional optical waveguides by a full-vector beam propagation method," *IEEE J. Quantum Electron.*, vol. 29, pp. 2639–2649, Oct. 1993.
- [12] C. L. Xu, W. P. Huang, S. K. Chaudhuri, and J. Chrostowski, "An unconditionally stable vectorial beam propagation method for 3-D structures," *IEEE Photon. Technol. Lett.*, vol. 6, pp. 549 – 551, Apr. 1994.
- [13] E. E. Kriezis and A. G. Papagiannakis, "A three-dimensional full vectorial beam propagation method for z-dependent structures," *IEEE J. Quantum Electron.*, vol. 33, pp. 883–890, May 1997.
- [14] Y. Hsueh, M. Yang, and H. Chang, "Three-dimensional noniterative full-vectorial beam propagation method based on the alternating direction implicit method," *IEEE/OSA J. Lightwave Technol.*, vol. 19, pp. 2389–2397, Nov. 1999.
- [15] I. Mansour, A. D. Capobianco, and C. Rosa, "Noniterative vectorial beam propagation method with a smoothing digital filter," *IEEE/OSA J. Lightwave Technol.*, vol. 14, pp. 908–913, May 1996.

- [16] J. Yamauchi, T. Ando, and H. Nakano, "Beam-propagation analysis of optical fibers by alternating direction implicit method," *Electron. Lett.*, vol. 27, pp. 1663–1665, Aug. 1991.
- [17] P. L. Liu and B. J. Li, "Semivectorial beam-propagation method for analyzing polarized modes of rib waveguides," *IEEE J. Quantum Electron.*, vol. 28, pp. 778–782, Apr. 1992.
- [18] G. R. Hadley, "Transparent boundary condition for the beam propagation method," *IEEE J. Quantum Electron.*, vol. 28, pp. 363-370, Jan. 1992.
- [19] W. P. Huang, C. Xu, W. W. Lui, and K. Yokoyama, "The perfectly matched layer (PML) boundary condition for the beam propagation method," *IEEE Photon. Technol. Lett.*, vol. 8, pp. 649–651, May 1996.
- [20] G. R. Hadley, "Wide-angle beam propagation using Padé approximant operators," *Opt. Lett.*, vol. 17, pp. 1426-1428, Oct. 1992.
- [21] I. Ilic, R. Scarmozzino, and R. M. Osgood Jr., "Investigation of the Pade approximant-based wide-angle beam propagation method for accurate modeling of waveguiding circuits," *IEEE/OSA J. Lightwave Technol.*, vol. 14, pp. 2813–2822, 1996.
- [22] H. El-Refaei, D. Yevick, and Ian Betty, "Stable and noniterative bidirectional beam propagation method," *IEEE Photon. Technol. Lett.*, vol. 12, No. 4, pp. 389-391, April 2000.

3 EFFICIENT SENSITIVITY ANALYSIS

USING ADJOINT VARIABLE METHOD

3.1 INTRODUCTION

Calculating the sensitivities of a given objective function with respect to the design parameters of electromagnetic (EM) structures is a desirable feature in any EM solver. These sensitivities are required by both the designer and the manufacturer for design optimization, yield and tolerance analyses. The adjoint variable method (AVM) is one of the most powerful methods for sensitivity analysis. It offers an efficient approach for design sensitivity analysis. The AVM is a well established general technique for sensitivity analysis in both the time and frequency domains. The efficient application of this general approach to different numerical techniques is still the subject of ongoing research in both the microwaves and photonic communities. The AVM implementation differs with different numerical methods as the governing equations are different.

An exact AVM approach was first applied to network theory where the exact derivatives of the system matrices are available [1]-[4]. This approach was later extended to the frequency domain finite element method (FEM) [5]-[7], and the finite element time domain (FETD) method [8] for microwave applications. Both FEM and FETD have analytical system matrices that can be differentiated with respect to the design parameters.

In the last few years, this approach has been efficiently applied to sensitivity analysis of complex microwave structures for different numerical methods using approximate approaches [9]-[12]. These methods include time domain techniques such as the transmission line method (TLM) [11] and the finite difference time domain (FDTD) [12]. The AVM has also been applied to frequency domain techniques such as the method of moments (MoM) [9], and the frequency domain transmission line method (FD-TLM) [10].

Recently, the AVM is applied to photonic devices using the finite difference frequency domain (FDFD) method [13]. In this work, the FDFD with nonuniform grid is used to extract the sensitivities of photonic crystals.

In general, the application of the AVM varies with the variation of the numerical techniques as mentioned earlier. More specifically, the time domain and the frequency domain approaches have conceptually different approaches to apply the AVM approach. Even for the techniques that belong to the same domain, the application of the AVM may be different. This is mainly due to the fact that it depends on the system of equations which vary from technique to the other.

In this chapter, we briefly review the basic theory of the adjoint variable method (AVM) for efficient estimation of the sensitivity analysis. The review includes both the time domain and frequency domain approaches.

3.2 AVM BASED ON ELECTRIC FIELD CALCULATIONS FOR TIME DOMAIN TECHNIQUE

This approach was first developed for the application with FDTD [12]. However, it can be applied to any time domain technique based on electric field solutions. Here, we briefly review the application of this approach with the FDTD method.

The AVM approach aims at estimating the sensitivities of a general objective function of the form [14]

$$F = \int_0^{T_{\max}} \int_{\Omega} f(\mathbf{E}, \mathbf{p}) d\Omega dt \quad (3.1)$$

where T_{\max} is the total simulation time, \mathbf{E} is the vector of the electric field temporal values in the computational domain, \mathbf{p} is the vector of the design parameters, and Ω is the observation domain where the objective function is evaluated. The sensitivity of the objective function with respect to the n th design parameter p_n is given by

$$\frac{\partial F}{\partial p_n} = \frac{\partial^e F}{\partial p_n} + \int_0^{T_{\max}} \int_{\Omega} \frac{\partial f}{\partial \mathbf{E}} \cdot \frac{\partial \mathbf{E}}{\partial p_n} d\Omega dt, \quad n = 1, \dots, N \quad (3.2)$$

where $\partial^e / \partial p_n$ represents the explicit dependence of F on the design parameter p_n . The sensitivities (3.2) are usually estimated using finite differences at the response level. This requires N extra FDTD simulations if forward differences are used. Additional $2N$ simulations are required if the more accurate central differences are utilized. This computational cost motivates research for a more efficient sensitivity estimation approaches.

The algorithm presented in [12] aims at efficiently estimating the objective function gradient with the FDTD method. This approach utilizes the second order vectorial wave equation for a lossy isotropic medium [12]:

$$\nabla \times \nabla \times \mathbf{E} + \mu \varepsilon \frac{\partial^2 \mathbf{E}}{\partial t^2} + \sigma \mu \frac{\partial \mathbf{E}}{\partial t} = -\mu \frac{\partial \mathbf{J}}{\partial t} \quad (3.3)$$

where \mathbf{J} , ε , σ , and μ are the electric current density, permittivity, conductivity and, permeability, respectively. This equation is then discretized into the matrix equation [12]

$$\mathbf{M}\ddot{\mathbf{E}} + \mathbf{N}\dot{\mathbf{E}} + \mathbf{K}\mathbf{E} = \mathbf{Q} \quad (3.4)$$

where $\dot{\mathbf{E}}$ and $\ddot{\mathbf{E}}$ are the first and second time derivatives of the electric field components, respectively. \mathbf{M} , \mathbf{N} , \mathbf{K} are the symmetric system matrices and \mathbf{Q} is the excitation vector.

If the n th design parameter is perturbed from p_n to $p_n + \Delta p_n$, the corresponding perturbed system is given by [12]

$$\tilde{\mathbf{M}}_{p_n} \Delta p_n \ddot{\mathbf{E}} + \tilde{\mathbf{N}}_{p_n} \Delta p_n \dot{\mathbf{E}} + \tilde{\mathbf{K}}_{p_n} \Delta p_n \mathbf{E} + \Delta p_n \mathbf{R} = \mathbf{0} \quad (3.5)$$

where

$$\begin{aligned} \tilde{\mathbf{A}}_{p_n} &= \mathbf{A} + \Delta p_n \mathbf{A}, & \mathbf{A} &= \mathbf{M}, \mathbf{N}, \mathbf{K}, \text{ and } \mathbf{Q} \\ \Delta p_n \mathbf{R} &= \Delta p_n \mathbf{M} \cdot \ddot{\mathbf{E}} + \Delta p_n \mathbf{N} \cdot \dot{\mathbf{E}} + \Delta p_n \mathbf{K} \cdot \mathbf{E} - \Delta p_n \mathbf{Q} \end{aligned} \quad (3.6)$$

The corresponding adjoint simulation is derived as follows; Multiplying (3.5) by an arbitrary variable λ_{p_n} , integrating twice, and imposing the terminal conditions

$\lambda_{p_n}(T_{\max}) = \mathbf{0}$ and $\dot{\lambda}_{p_n}(T_{\max}) = \mathbf{0}$, we get

$$\int_0^{T_{\max}} (\ddot{\lambda}_{p_n}^T \tilde{\mathbf{M}}_{p_n} - \dot{\lambda}_{p_n}^T \tilde{\mathbf{N}}_{p_n} + \lambda_{p_n}^T \tilde{\mathbf{K}}_{p_n}) \cdot \Delta p_n \mathbf{E} dt = - \int_0^{T_{\max}} \lambda_{p_n}^T \cdot \Delta p_n \mathbf{R} dt \quad (3.7)$$

By comparing (3.7) and (3.2), the expression for the AVM sensitivity is obtained as [12]:

$$\frac{\partial F}{\partial p_n} \approx \frac{\partial^e F}{\partial p_n} - \int_0^{T_{\max}} \int_{\Omega} \lambda_{p_n}^T \cdot \frac{\Delta_{p_n} R}{\Delta p_n} d\Omega dt, \quad n = 1, \dots, N \quad (3.8)$$

where the adjoint vector λ_{p_n} is obtained by solving

$$\tilde{M}_{p_n} \ddot{\lambda}_{p_n} - \tilde{N}_{p_n} \dot{\lambda}_{p_n} + \tilde{K}_{p_n} \lambda_{p_n} = \frac{\partial f}{\partial E}^T \quad (3.9)$$

The system (3.9) supplies the values of the adjoint variable λ_{p_n} at all time steps. The expression (3.8) is then utilized to estimate the required sensitivities. To avoid carrying out N such adjoint simulations, a one-to-one mapping is applied [10]. We carry out only one adjoint simulation of the unperturbed system

$$M \ddot{\lambda} - N \dot{\lambda} + K \lambda = \frac{\partial f}{\partial E}^T \quad (3.10)$$

The second order system of equations (3.10) is shown to be equivalent to the Maxwell's curl equations [12]

$$\nabla \times \lambda^H = \frac{\partial \varepsilon \lambda}{\partial t} - \sigma \lambda + J^\lambda \quad (3.11)$$

$$\nabla \times \lambda = -\frac{\partial \mu \lambda^H}{\partial t} \quad (3.12)$$

with the terminal conditions $\lambda(T_{\max}) = \mathbf{0}$, $\lambda^H(T_{\max}) = \mathbf{0}$, where the adjoint excitation

J^λ is given by:

$$\frac{\partial J^\lambda}{\partial t} = \frac{1}{\mu} \frac{\partial f}{\partial E}^T \quad (3.13)$$

In (3.11) and (3.12), λ and λ^H are the electric and magnetic fields of the adjoint problem, respectively. The update equations of the FDTD algorithm for the adjoint problem are the same as those of the original simulation if we solve for $(-\lambda, \lambda^H)$. Therefore, the same absorbing boundary conditions are used in both simulations, which simplify the implementation and allows for using the commercial tools.

3.2.1 AVM Approach for Dielectric Discontinuities

The technique described in Section 3.2 was applied only to perfectly conducting discontinuities. Since most of the photonic devices are dielectric based structures, in this section we show how the same approach can be adapted to dielectric discontinuities. We illustrate the approach for the 2-D case where the TM_x mode is analyzed. In this case, the respective matrices have the form

$$\mathbf{M} = -\mu_r \mathbf{B}_{\varepsilon_r} \left(\frac{\Delta h}{c\Delta t} \right)^2 \quad (3.14)$$

$$\mathbf{N} = -\frac{\mathbf{B}_{\sigma} \mu_o \mu_r}{\Delta t} \Delta h^2 \quad (3.15)$$

$$\mathbf{Q} = \frac{\mu_o \mu_r \Delta h^2}{\Delta t} D_t \mathbf{J}_x \quad (3.16)$$

$$D_t \mathbf{J}_x = \mathbf{J}_x \left(t + \frac{\Delta t}{2} \right) - \mathbf{J}_x \left(t - \frac{\Delta t}{2} \right) \quad (3.17)$$

Here, $\mathbf{B}_{\varepsilon_r}$ and $\mathbf{B}_{\sigma} \in \mathfrak{R}^{j_{max} \times k_{max}}$ where j_{max} and k_{max} are the number of cells in y and z directions, respectively. These diagonal matrices contain the values of ε_r and σ at each grid point. The double curl operator \mathbf{K} has three vector components and can be written as

$$(\mathbf{KE})_x = h_y^2 D_{yy} E_x + h_z^2 D_{zz} E_x - h_z h_x D_{zx} E_z - h_y h_x D_{yx} E_y, \quad (3.18)$$

$$(\mathbf{KE})_y = h_x^2 D_{xx} E_y + h_z^2 D_{zz} E_y - h_x h_y D_{xy} E_x - h_z h_y D_{zy} E_z, \quad (3.19)$$

$$(\mathbf{KE})_z = h_x^2 D_{xx} E_z + h_y^2 D_{yy} E_z - h_x h_z D_{xz} E_x - h_y h_z D_{yz} E_y \quad (3.20)$$

where

$$h_x = \frac{\Delta h}{\Delta x}, h_y = \frac{\Delta h}{\Delta y}, h_z = \frac{\Delta h}{\Delta z}, \text{ and } \Delta h = \min(\Delta x, \Delta y, \Delta z).$$

The second order difference with respect to variables κ , and v ($\kappa, v = x, y, z, t$) are calculated using central difference approach as

$$D_{\kappa\kappa} \mathbf{E} = \mathbf{E}(\kappa - \Delta\kappa) + 2\mathbf{E}(\kappa) + \mathbf{E}(\kappa + \Delta\kappa), \quad (3.21)$$

and

$$\begin{aligned} D_{\kappa v} \mathbf{E} = & \mathbf{E}\left(\kappa + \frac{\Delta\kappa}{2}, v + \frac{\Delta v}{2}\right) + \mathbf{E}\left(\kappa - \frac{\Delta\kappa}{2}, v - \frac{\Delta v}{2}\right) \\ & - \mathbf{E}\left(\kappa + \frac{\Delta\kappa}{2}, v - \frac{\Delta v}{2}\right) - \mathbf{E}\left(\kappa - \frac{\Delta\kappa}{2}, v + \frac{\Delta v}{2}\right) \end{aligned} \quad (3.22)$$

The expression (3.6) can thus be evaluated as

$$\Delta_{p_n} \mathbf{R} = (\Delta_{p_n} \mathbf{M}) D_{tt} \mathbf{E}_x + (\Delta_{p_n} \mathbf{N}) D_{tt} \mathbf{E}_x + (\Delta_{p_n} \mathbf{K}) \mathbf{E}_x - \Delta_{p_n} \mathbf{Q} \quad (3.23)$$

Evaluating the sensitivity expression (3.8) requires storing the field information for the nodes corresponding to nonzero components of the vector $\Delta_{p_n} \mathbf{R}$ [12]. Here, a virtual

perturbation of the respective parameter is assumed in the forward direction only. The corresponding vector perturbation is denoted by $\Delta_{p_n}^+ \mathbf{R}$.

To illustrate this approach, consider the dielectric slab of width L , permittivity ϵ_{r2} , and conductivity σ_2 inserted between two perfect electric walls (see Fig. 3.1). This waveguide structure is filled with a material that has permittivity ϵ_{r1} and conductivity σ_1 . Perturbing the parameter L , in the forward direction in a symmetric way, changes the dielectric properties of the cells outside the dielectric, marked with squares. Their field values are thus stored for both the original and adjoint simulations. We demonstrate the calculation of the system matrices $\Delta_{p_n}^+ \mathbf{R}$ in this case for a point (j, k) in Table 3. 1

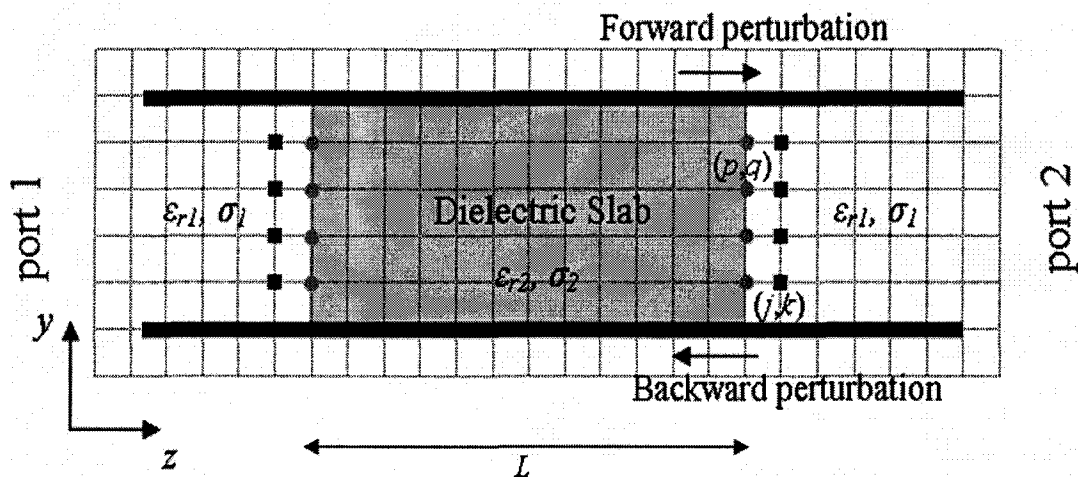


Fig. 3.1. Illustration of the stored points used to calculate the sensitivities with respect to the width of dielectric slab inside a waveguide with metallic boundaries using CAVM approach.

Our experience shows that the sensitivities obtained using this approach is very similar to those obtained using forward finite difference approximation applied at the

response level. A better accuracy can be obtained, especially for a highly nonlinear objective functions, if a central approach is adopted. A possible central AVM (CAVM) approach is presented in the following chapter.

Table 3.1.
The variations in the system matrices due to forward perturbation

| | (j,k) | $(j+1,k)$ | $(j-1,k)$ | $(j,k+1)$ | $(j,k-1)$ |
|---------------------|--|------------|------------|------------|------------|
| $K(p_n=L)$ | $-2(h_y^2 + h_z^2)$ | h_y^2 | h_y^2 | h_z^2 | h_z^2 |
| $K(p_n=L+\Delta L)$ | $-2(h_y^2 + h_z^2)$ | h_y^2 | h_y^2 | h_z^2 | h_z^2 |
| ΔK | 0 | 0 | 0 | 0 | 0 |
| E | $E \neq 0$ | $E \neq 0$ | $E \neq 0$ | $E \neq 0$ | $E \neq 0$ |
| $M(p_n=L)$ | $-\mu_r \varepsilon_{r1} (\Delta h/c\Delta t)^2$ | 0 | 0 | 0 | 0 |
| $M(p_n=L+\Delta L)$ | $-\mu_r \varepsilon_{r2} (\Delta h/c\Delta t)^2$ | 0 | 0 | 0 | 0 |
| ΔM | $-\mu_r \Delta \varepsilon_r (\Delta h/c\Delta t)^2$ | 0 | 0 | 0 | 0 |
| $D_{ii} E$ | $\neq 0$ | $\neq 0$ | $\neq 0$ | $\neq 0$ | $\neq 0$ |
| $N(p_n=L)$ | $-\mu_r \mu_o \sigma_1 \Delta h^2/\Delta t$ | 0 | 0 | 0 | 0 |
| $N(p_n=L+\Delta L)$ | $-\mu_r \mu_o \sigma_2 \Delta h^2/\Delta t$ | 0 | 0 | 0 | 0 |
| ΔN | $-\mu_r \mu_o \Delta \sigma (\Delta h^2/\Delta t)$ | 0 | 0 | 0 | 0 |
| $D_t E$ | $\neq 0$ | $\neq 0$ | $\neq 0$ | $\neq 0$ | $\neq 0$ |

$$\Delta_{p_n}^+ R_{j,k} = \Delta_{p_n} R_{j,k} = -\mu_r \Delta \varepsilon_r (\Delta h/c\Delta t)^2 D_{ii} E(j,k) - \mu_r \mu_o \Delta \sigma (\Delta h^2/\Delta t) D_t E(j,k),$$

$$\Delta \varepsilon_r = \varepsilon_{r2} - \varepsilon_{r1} \text{ and } \Delta \sigma = \sigma_2 - \sigma_1$$

3.3 AVM APPROACH FOR FREQUENCY DOMAIN TECHNIQUES

In this section, the general fundamentals of the AVM approach for frequency domain techniques are illustrated. We start by assuming that the electromagnetic (EM) problem can be casted in the following system of equations [15]

$$A(p)x = b \tag{3.24}$$

where A and b are the system matrix and the excitation vector, respectively. In (3.24), x is the state variable which can be the voltages, the currents or the electric field. By differentiating (3.24) with respect to the n th design parameter p_n and rearranging, we get

$$\frac{\partial x}{\partial p_n} = A^{-1} \left[\frac{\partial b}{\partial p_n} - \frac{\partial A}{\partial p_n} x \right] \quad (3.25)$$

The sensitivity of the objective function f can be calculated using the chain rule as follow

$$\frac{\partial f}{\partial p_n} = \frac{\partial^e f}{\partial p_n} + \frac{\partial f}{\partial x} \cdot \frac{\partial x}{\partial p_n} \quad (3.26)$$

where $\partial^e f / \partial p_n$ represents the explicit dependence of f on the design parameter p_n . By substituting (3.25) into (3.26), the sensitivity of the objective function can be obtained as follows [15]

$$\frac{\partial f}{\partial p_n} = \frac{\partial^e f}{\partial p_n} + \frac{\partial f}{\partial x} A^{-1} \left[\frac{\partial b}{\partial p_n} - \frac{\partial A}{\partial p_n} x \right] \quad (3.27)$$

Now, we define the adjoint variable \hat{x} as

$$\hat{x}^T = \frac{\partial f}{\partial x} A^{-1} \quad (3.28)$$

This adjoint variable can be obtained by solving the system of equation:

$$A^T \hat{x} = \left(\frac{\partial f}{\partial x} \right)^T \quad (3.29)$$

The system of equation given in (3.29) is called the adjoint system. Now by substituting (3.28) into (3.27), the sensitivity of the objective function is given by:

$$\frac{\partial f}{\partial p_n} = \frac{\partial^e f}{\partial p_n} + \hat{x}^T \left[\frac{\partial b}{\partial p_n} - \frac{\partial A}{\partial p_n} x \right] \quad (3.30)$$

Since the LU factorization of the matrix A is readily available from solving the original system given in (3.24), the adjoint variable \hat{x} can be obtained efficiently using (3.29) by forward–backward substitution [15].

In (3.30), the sensitivity of the excitation $\partial b/\partial p_n$ is zero in most cases. This is mainly due to the fact that the excitation is usually the output of an optical fiber or a laser source or any other device in the optical system.

In order to evaluate the sensitivity of the objective function using the expression (3.30), the derivative of the system matrix with respect to the design parameter $\partial A/\partial p_n$ needs to be evaluated efficiently for all parameters. There are different approaches to calculating this term according to the nature of this system matrix and also according to the type of the design parameter [15]. The derivative of the system matrices can be obtained by assuming virtual perturbation in the system matrices due to the change of the design parameters. It can be also calculated analytically if the system matrices have analytical dependence on the design parameters. More details regarding the calculation of the system matrices of different numerical approaches will be discussed in the following two chapters.

3.4 CONCLUSION

In this chapter, we briefly review the adjoint variable method (AVM) for efficient extraction of the sensitivity information. This approach has two different versions for time domain and frequency domain electromagnetic numerical techniques. The details of the two versions are discussed and given in this chapter.

3.5 REFERENCES

- [1] S. W. Director and R. A. Rohrer, “The generalized adjoint network and network sensitivities,” *IEEE Trans. Circuit Theory*, vol. CT-16, pp. 318–323, Aug. 1969.
- [2] J. W. Bandler and R. E. Seviora, “Wave sensitivities of networks,” *IEEE Trans. Microwave Theory Tech.*, vol. MTT-20, pp. 138–147, Feb. 1972.
- [3] K. C. Gupta, R. Garg, and R. Chadha, *Computer-Aided Design of Microwave Circuits*. Dedham, MA: Artech House, 1981.
- [4] F. Alessandri, M. Mongiardo, and R. Sorrentino, “New efficient full wave optimization of microwave circuits by the adjoint network method,” *IEEE Microwave Guided Wave Lett.*, vol. 3, pp. 414–416, Nov. 1993.
- [5] I. H. Park, I. G. Kwak, H. B. Lee, S. Y. Hahn, and K. S. Lee.,” Design sensitivity analysis for transient eddy current problems using finite element discretization and adjoint variable method.” *IEEE Trans. Magn.* vol. 32, pp 1242-1245, May. 1996
- [6] H. Lee and T. Itoh, “A systematic optimum design of waveguide-to-microstrip transition,” *IEEE Trans. Microwave Theory Tech.*, vol. 45, pp. 803-809, May 1997.
- [7] H. Akel and J. P. Webb, “Design sensitivities for scattering matrix calculation with tetrahedral edge elements,” *IEEE Trans. Magn.*, vol. 36, pp. 1043-1046, July 2000.
- [8] Y. Chung, J. Ryu, C. Cheon, I. Park, and S. Hahn, “Optimal design method for microwave device using time domain method and design sensitivity analysis—Part I : FETD case,” *IEEE Trans. Magn.*, vol. 37, pp. 3289-3293, Sept. 2001.

- [9] N. K. Nikolova, R. Safian, E. A. Soliman, M. H. Bakr, and J. W. Bandler, “Accelerated gradient based optimization using adjoint sensitivities,” *IEEE Trans. Antennas Propagat.*, vol. 52, pp. 2147–2157, Aug. 2004.
- [10] M. H. Bakr and N. K. Georgieva, “An adjoint variable method for frequency domain TLM problems with conducting boundaries,” *IEEE Microwave Wireless Comp. Lett.*, vol. 13, pp. 408–410, Nov. 2003.
- [11] M. H. Bakr and N. K. Nikolova, “An adjoint variable method for time domain TLM with wideband Johns matrix boundaries,” *IEEE Trans. Microwave Theory Tech.*, vol. 52, pp. 678–685, Feb. 2004.
- [12] N. K. Nikolova, H. W. Tam, and M. H. Bakr, “Sensitivity analysis with the FDTD method on structured grids,” *IEEE Trans. Microwave Theory Tech.*, vol. 52, pp. 1207–1216, Apr. 2004.
- [13] G. Veronis, R. W. Dutton, and S. Fan, “Method for sensitivity analysis of photonic crystal devices,” *Opt. Lett.*, vol. 29, pp. 2288–2290, Oct. 2004.
- [14] E. J. Haug, K. K. Choi, and V. Komkov, *Design Sensitivity Analysis of Structural Systems*, Orlando, FL: Academic. 1986.
- [15] N. K. Nikolova, J. W. Bandler, and M. H. Bakr, “Adjoint techniques for sensitivity analysis in high-frequency structure CAD,” *IEEE Trans. Microwave Theory Tech. (Special Issue)*, vol. 52, pp. 403–419, Jan. 2004.

4 ACCURATE AND EFFICIENT SENSITIVITY ANALYSIS FOR FDTD USING AVM

4.1 INTRODUCTION

In this chapter, we propose an accurate technique for estimating the sensitivities of the objective function relative to the variations of the geometry and the permittivity of dielectric discontinuities using the FDTD method on structured grids. A central AVM (CAVM) approach that utilizes both virtual positive and negative perturbations of each parameter obtains an improved accuracy of the estimated sensitivities. This central adjoint variable method using FDTD is applied, for the first time, to sensitivity analysis of photonic devices. We show that using only one extra adjoint FDTD simulation, the sensitivities of the desired response are obtained with respect to all design parameters regardless of their number. The effectiveness of our approach is illustrated by using different response functions and different structures.

In addition, we apply a self-adjoint CAVM (SA-CAVM) to sensitivity analysis of power reflectivity. Here, the original FDTD simulation used to calculate the power reflectivity of multilayer structures supplies its gradient as well. Our SA-CAVM approach is then applied to minimize the power reflectivity of deeply etched waveguide

terminators, and double layer antireflection coatings on laser diode (LD) facets which can be used as an optical amplifier. The accuracy of the SA-CAVM is illustrated by comparing the results with the second order accurate CFD.

Finally, we propose an efficient approach for calculating and analyzing the dispersion characteristics of guided wave structures. The design parameters such as the refractive index contrast and the index profile of these structures have a significant effect on its characteristics. The dispersion characteristics are also essential for calculating the coupling length optical of directional couplers. Here, we propose a comprehensive approach for extracting the propagation constants β of all the guided modes at all the required frequencies using a single FDTD simulation. It also provides the sensitivities of the propagation constants with respect to all the design parameters without any additional simulation. Our approach utilizes the adjoint variable method (AVM) to extract the sensitivity of the propagation constants β with respect to the design parameters. These design parameters may include the dimensions and the constitutive parameters of the structures.

4.2 CENTRAL AVM

The CAVM approach utilizes the vectorial second-order wave equation of the electric field in a lossy, nondispersive, and isotropic medium

$$\nabla \times \nabla \times \mathbf{E} + \mu\epsilon \frac{\partial^2 \mathbf{E}}{\partial t^2} + \sigma\mu \frac{\partial \mathbf{E}}{\partial t} = -\mu \frac{\partial \mathbf{J}}{\partial t} \quad (4.1)$$

where ε , σ , and μ are the permittivity, conductivity, and permeability, respectively. This equation is then discretized into the matrix equation as shown in Chapter 3

$$M\ddot{\mathbf{E}} + N\dot{\mathbf{E}} + \mathbf{K}\mathbf{E} = \mathbf{Q} \quad (4.2)$$

where $\dot{\mathbf{E}}$ and $\ddot{\mathbf{E}}$ are the first and second time derivatives of the electric field components, respectively. M , N , K are the system matrices and Q is the excitation vector.

To formulate the central AVM (CAVM) approach, we start by assuming a virtual perturbation of the n th design parameter p_n , $n=1, 2, \dots, N$ in both the forward and backward directions. The perturbed parameter values are $p_n \pm \Delta p_n$. Using (4.2), these perturbations result in the perturbed system:

$$\begin{aligned} (M + \Delta_{p_n}^{\pm} M)(\ddot{\mathbf{E}} + \Delta_{p_n}^{\pm} \ddot{\mathbf{E}}) + (N + \Delta_{p_n}^{\pm} N)(\dot{\mathbf{E}} + \Delta_{p_n}^{\pm} \dot{\mathbf{E}}) \\ + (K + \Delta_{p_n}^{\pm} K)(\mathbf{E} + \Delta_{p_n}^{\pm} \mathbf{E}) = \mathbf{Q} + \Delta_{p_n}^{\pm} \mathbf{Q} \end{aligned} \quad (4.3)$$

where $\Delta_{p_n}^+ A$ and $\Delta_{p_n}^- A$ represent the variation in the matrix A due to the perturbations $\pm \Delta p_n$, respectively. This system of equations can be reduced using (4.2) and then split into two equations depending on the direction of the perturbation. Applying a similar procedure to that given in [1], we obtain the corresponding equations [2]:

$$\begin{aligned} \int_0^{T_{\max}} (\dot{\lambda}_{p_n}^{+T} M_{p_n}^+ - \dot{\lambda}_{p_n}^{+T} N_{p_n}^+ + \lambda_{p_n}^{+T} K_{p_n}^+) \Delta_{p_n}^+ \mathbf{E} dt \\ = - \int_0^{T_{\max}} \lambda_{p_n}^{+T} \Delta_{p_n}^+ \mathbf{R} dt, \quad n = 1, \dots, N \end{aligned} \quad (4.4)$$

$$\int_0^{T_{\max}} (\ddot{\lambda}_{p_n}^{-T} M_{p_n}^- - \dot{\lambda}_{p_n}^{-T} N_{p_n}^- + \lambda_{p_n}^{-T} K_{p_n}^-) \Delta_{p_n}^- E dt$$

$$= - \int_0^{T_{\max}} \lambda_{p_n}^{-T} \Delta_{p_n}^- R dt, \quad n=1, \dots, N \quad (4.5)$$

where

$$\Delta_{p_n}^+ R = \Delta_{p_n}^+ M \ddot{E} + \Delta_{p_n}^+ N \dot{E} + \Delta_{p_n}^+ K E - \Delta_{p_n}^+ Q \quad (4.6)$$

$$\Delta_{p_n}^- R = \Delta_{p_n}^- M \ddot{E} + \Delta_{p_n}^- N \dot{E} + \Delta_{p_n}^- K E - \Delta_{p_n}^- Q \quad (4.7)$$

To derive the CAVM expression, we compare the objective function sensitivity

$$\frac{\partial F}{\partial p_n} \approx \frac{\partial^e F}{\partial p_n} + \frac{1}{2} \int_0^{T_{\max}} \int_{\Omega} \frac{\partial f}{\partial E} \frac{(\Delta_{p_n}^+ E + \Delta_{p_n}^- E)}{\Delta p_n} d\Omega dt, \quad n=1, \dots, N \quad (4.8)$$

with (4.4) and (4.5) to obtain

$$\frac{\partial F}{\partial p_n} \approx \frac{\partial^e F}{\partial p_n} - \frac{1}{2} \int_0^{T_{\max}} \int_{\Omega} \frac{(\lambda_{p_n}^{+T} \Delta_{p_n}^+ R + \lambda_{p_n}^{-T} \Delta_{p_n}^- R)}{\Delta p_n} d\Omega dt, \quad n=1, \dots, N \quad (4.9)$$

where the adjoint vectors $\lambda_{p_n}^+$ and $\lambda_{p_n}^-$ are the solutions of the adjoint system of differential equations:

$$M_{p_n}^+ \ddot{\lambda}_{p_n}^+ - N_{p_n}^+ \dot{\lambda}_{p_n}^+ + K_{p_n}^+ \lambda_{p_n}^+ = \frac{\partial f}{\partial E} \quad (4.10)$$

$$M_{p_n}^- \ddot{\lambda}_{p_n}^- - N_{p_n}^- \dot{\lambda}_{p_n}^- + K_{p_n}^- \lambda_{p_n}^- = \frac{\partial f}{\partial E} \quad (4.11)$$

Solving for $\lambda_{p_n}^+$ and $\lambda_{p_n}^-$ requires two FDTD simulations for each design parameter. It follows that $2N$ adjoint simulations are required. To avoid carrying out these simulations, we utilize a one-to-one mapping similar to [3]. Only one adjoint

simulation of the unperturbed FDTD problem is carried out. The adjoint field information required from (4.10) and (4.11) can be approximated using this adjoint simulation.

Our CAVM approach is illustrated using the dielectric structure shown in Fig. 3.1. The system of equations for the points that have permittivity ϵ_{r1} and located on the boundaries of the dielectric sheet is changed due to the forward perturbation $\Delta_{p_n}^+ \mathbf{R}$ (as described before in TABLE 3.1). On the other hand, the variation of the system matrices due to backward perturbation $\Delta_{p_n}^- \mathbf{R}$ occurs for the points indicated by circles in Fig. 3.1. Table 4.1 illustrates the non zero variation in the system matrices due to a backward perturbation at point (p, q) . The adjoint field solution due to forward perturbation $\lambda_{p_n}^+$ and backward perturbation $\lambda_{p_n}^-$ are stored at each time step for points indicated by squares and circles, respectively. The points that are not marked in Fig. 3.1 have zero values for both $\Delta_{p_n}^+ \mathbf{R}$ and $\Delta_{p_n}^- \mathbf{R}$ terms as the system matrices at these points are insensitive to the perturbation. Therefore, the adjoint field is not stored for all these points. In the previous derivation, we assume that the excitation vector \mathbf{Q} is insensitive to perturbations in the designable parameters.

Table 4.1
The variations in the system matrices due to backward perturbation

| $M(p_n=L)$ | $M(p_n=L-\Delta L)$ | ΔM | $N(p_n=L)$ | $N(p_n=L-\Delta L)$ | ΔN |
|---|---|---|---|---|--|
| $-\mu_r \epsilon_{r2} (\Delta h/c\Delta t)^2$ | $-\mu_r \epsilon_{r1} (\Delta h/c\Delta t)^2$ | $-\mu_r \Delta \epsilon_r (\Delta h/c\Delta t)^2$ | $-\mu_r \mu_0 \sigma_2 \Delta h^2/\Delta t$ | $-\mu_r \mu_0 \sigma_1 \Delta h^2/\Delta t$ | $-\mu_r \mu_0 \Delta \sigma \Delta h^2/\Delta t$ |
| $\Delta_{p_n}^- R_{p,q} = -\mu_r \Delta \epsilon_r (\Delta h/c\Delta t)^2 D_{tt} E(p,q) - \mu_r \mu_0 \Delta \sigma (\Delta h^2/\Delta t) D_t E(p,q)$ | | | | | |

4.2.1 SA-CAVM Approach for the Reflection Coefficient

The excitation of the adjoint simulation is dependent on the objective function as shown in Chapter 3 and is given by:

$$\frac{\partial J^\lambda}{\partial t} = \frac{1}{\mu} \frac{\partial f^T}{\partial E} \quad (4.12)$$

For some special objective functions such as the scattering parameters, the adjoint field values can be deduced from the original simulation [3],[4]. It follows that the adjoint simulation can be eliminated. Here, we apply this self-adjoint approach to the estimation of the reflection coefficient sensitivities.

Consider $\Gamma(\lambda_o)$, the reflection coefficient at wavelength λ_o . It can be written as:

$$\Gamma(\lambda_o) = \frac{\int_{\Omega} \tilde{E}_r(\lambda_o) \cdot E_{inc} d\Omega}{\int_{\Omega} E_{inc} \cdot E_{inc} d\Omega} \quad (4.13)$$

where E_{inc} is the modal field distribution of the fundamental mode. The vector $\tilde{E}_r(\lambda_o)$ is the reflected electric field at the wavelength λ_o . The reflection coefficient can also be written as:

$$\Gamma(\omega_o) = \frac{\int_0^{T_{max}} \int_{\Omega} E_r(t) \cdot E_{inc} d\Omega e^{-j\omega_o t} dt}{\int_{\Omega} E_{inc} \cdot E_{inc} d\Omega} \quad (4.14)$$

where $\omega_o = 2\pi c / \lambda_o$, is the angular frequency, and c is the velocity of light in free space.

The expression given in (4.14) can be written in a form similar to (4.12)

$$\Gamma(\omega_o) = \frac{1}{S} F(\omega_o) = \frac{1}{S} \int_0^{T_{\max}} \int_{\Omega} f(\Omega, t) d\Omega dt \quad (4.15)$$

where

$$f(\Omega, t) = \mathbf{E}_r(t) \cdot \mathbf{E}_{inc} e^{-j\omega_o t} \quad (4.16)$$

and

$$S = \int_{\Omega} \mathbf{E}_{inc} \cdot \mathbf{E}_{inc} d\Omega \quad (4.17)$$

The reflection coefficient is thus a complex function and its sensitivities with respect to the n th parameter, $n = 1, 2, \dots, N$, are given by

$$\frac{\partial \Gamma}{\partial p_n} = \frac{1}{S} \frac{\partial F(\omega_o)}{\partial p_n} = \frac{1}{S} \left(\text{Re} \left\{ \frac{\partial F(\omega_o)}{\partial p_n} \right\} + j \text{Im} \left\{ \frac{\partial F(\omega_o)}{\partial p_n} \right\} \right) \quad (4.18)$$

Accordingly, the adjoint excitation in (4.12) can be written as

$$\mathbf{J}^\lambda = \frac{1}{\gamma} \int_0^{T_{\max}} \frac{\partial f^T}{\partial \mathbf{E}} dt \quad (4.19)$$

where

$$\gamma = \mu_o \mu_r \Delta h^2 \quad (4.20)$$

Following a similar procedure to that in [5], the adjoint field is deduced through the expression[6]:

$$\left(\lambda_{p_n}^{\pm T} \right)_{i,j,k} = \frac{\left| \left(E_{p_n}^{\pm T}(\omega_o) \right)_{i,j,k} \right|}{\gamma J_o \omega_o |H(\omega_o)|} \cdot \begin{pmatrix} \cos(\omega_o t + \varphi_o - (\phi_{E^\pm})_{i,j,k} - \beta d - \pi/2) \\ + j \cos(\omega_o t + \varphi_o - (\phi_{E^\pm})_{i,j,k} - \beta d) \end{pmatrix} \quad (4.21)$$

where $\left| \left(E_{p_n}^{\pm T}(\omega_o) \right)_{i,j,k} \right|$ and $(\phi_{E^\pm})_{i,j,k}$ are the magnitude and the phase of the original field of the point (i, j, k) at frequency ω_o , respectively. $|H(\omega_o)|$ and φ_o in (4.21) are the magnitude and the phase of the spectral component of the wideband excitation function $h(t)$ at ω_o , respectively. J_o is a scaling factor which accounts for the normalization of the incident field. In (4.21), β is the propagation constant of the fundamental mode, d is the distance between the excitation plane and the reference plane.

In order to evaluate the sensitivity using CAVM approach, the following discretization for (4.9) is used

$$\frac{\partial F}{\partial p_n} = -\frac{\Delta s \Delta t}{2} \sum_{m=1}^{m_{\max}} \sum_{\Omega} \frac{(\lambda_{p_n}^{+T} \cdot \Delta_{p_n}^+ \mathbf{R} + \lambda_{p_n}^{-T} \cdot \Delta_{p_n}^- \mathbf{R})}{\Delta p_n}, \quad n = 1, \dots, N \quad (4.22)$$

where Δs is the unit cell area. The adjoint field values are given in (4.21) with $t = m\Delta t$, and $T_{\max} = m_{\max} \Delta t$.

4.2.2 Examples

In this section, we illustrate our CAVM approach through three examples. Different response functions are used to illustrate the universality of our CAVM algorithm. We also apply the self-adjoint approach discussed in Section 4.2.1 to estimate the sensitivities of the reflection coefficient without performing any FDTD adjoint simulations. Hence, the computational overhead is practically removed. In these examples, the perfect matched layer (PML) [7] is used as an absorbing boundary condition for the computational domain.

4.2.2.1 Multimode Interference (MMI) 3dB Power Splitter

In this example, a compact multimode interference (MMI) device (1×2) is used as a 3 dB power splitter as shown in Fig. 4.1. Strong guided structure is used with core index of 3.0. The width of the multimode section is taken to be $1.65 \mu\text{m}$ which supports six guided modes at $\lambda_0 = 1.55 \mu\text{m}$. The lengths of the access waveguides at the input and the output are $3.75 \mu\text{m}$.

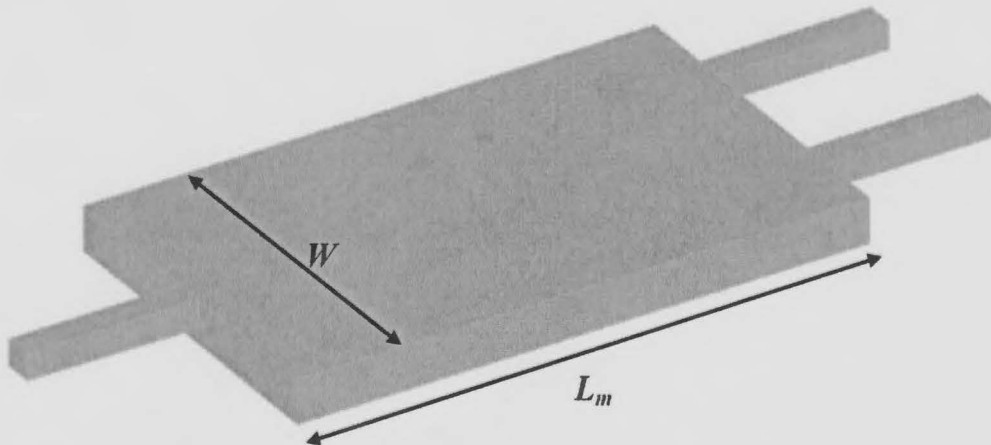


Fig. 4.1. Schematic diagram of an MMI 3 dB power splitter.

In this example, the sensitivities of an output energy function with respect to the dimensions of the structure are studied using our CAVM technique. Here, the TE case is assumed where the electric field has only one component, E_y .

The energy function is given in the form

$$F = \int_{\Omega} \int_0^{T_{\max}} \frac{E_y^2}{2} dt d\Omega. \quad (4.23)$$

For evaluating the objective function in (4.23), the following discretization is used

$$F = \sum_{m=1}^{m_{\max}} \sum_{j=1}^{j_{\max}} \frac{E_y^2}{2} \Delta x \Delta t. \quad (4.24)$$

where Δx and Δt are the special step size and time step size, respectively. According to (4.19), the adjoint current of excitation is given by

$$J^\lambda = \frac{\Delta t}{\gamma} \sum_{m=1}^{m_{\max}} \frac{\partial f}{\partial E_y} \quad (4.25)$$

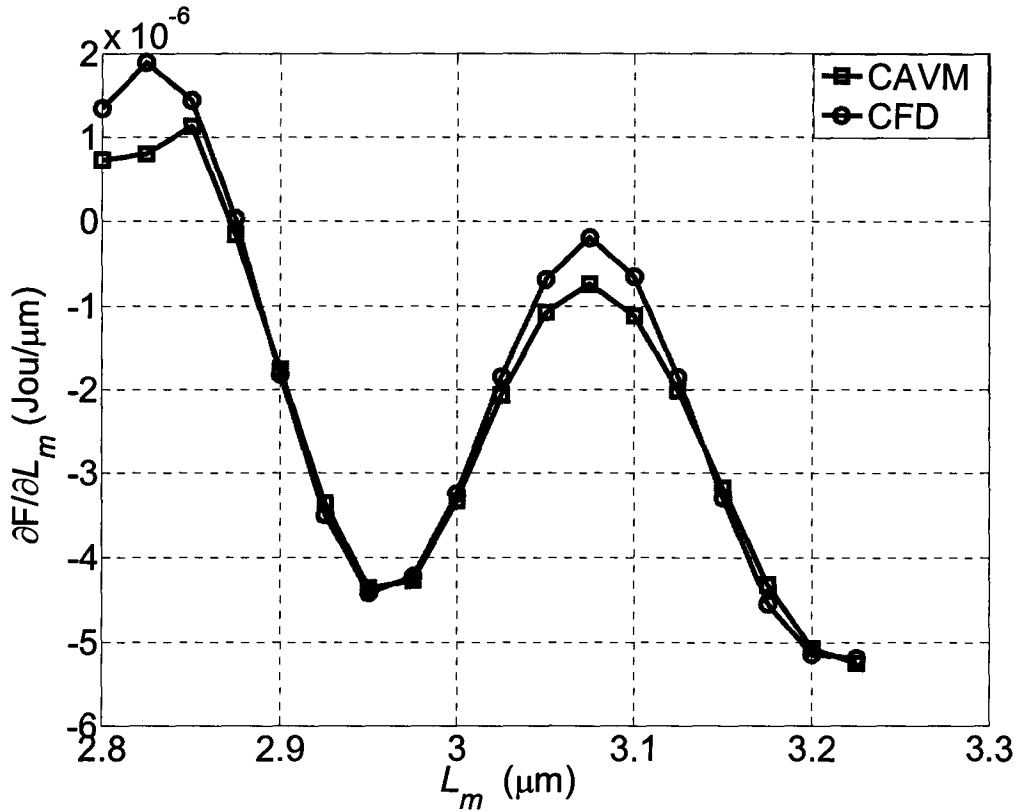


Fig. 4.2. The sensitivity of the energy function with respect to the length of the MMI 3dB power splitter for $W = 1.65 \mu\text{m}$ at wavelength $1.55 \mu\text{m}$.

where $f = \frac{E_y^2}{2}$.

The discretized form given in (4.22) is used to calculate the sensitivities of the energy function with respect to the parameters $\mathbf{p} = [W \ L_m]^T$ using the CAVM approach. The cell size is $\Delta x = \Delta z = 25.0 \text{ nm}$. The sensitivities of the energy function with respect to the length and the width of the multimode section are calculated using the CAVM

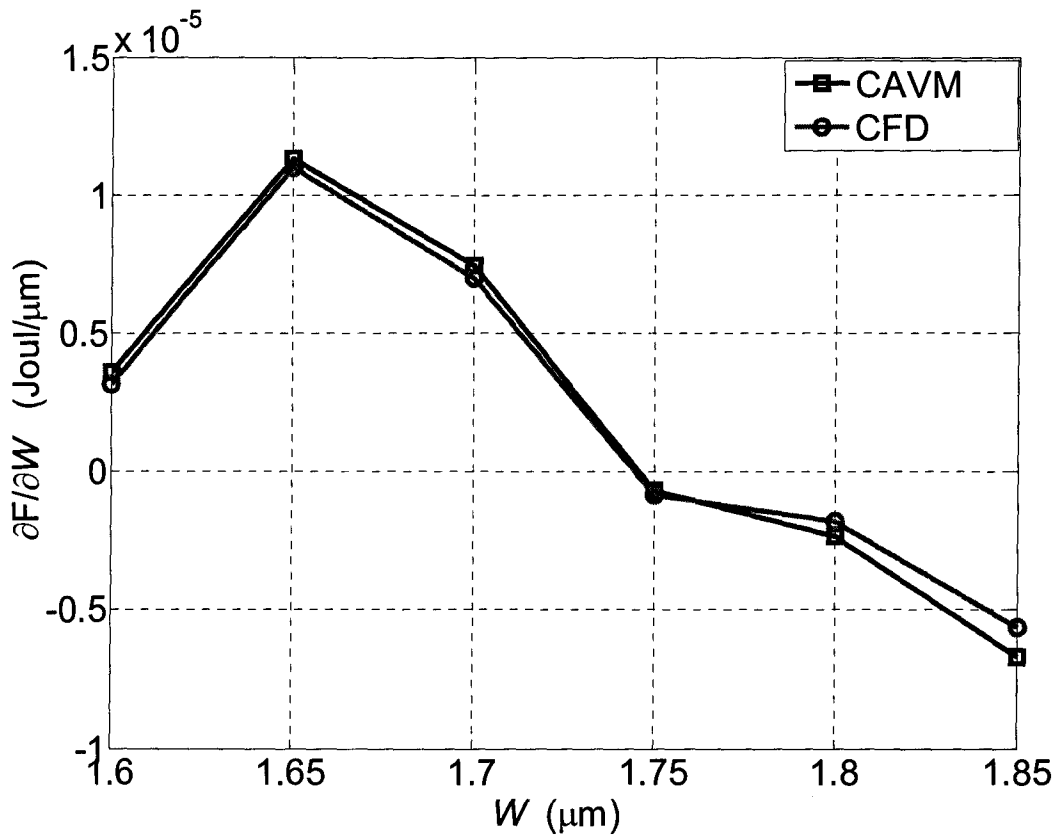


Fig. 4.3. The sensitivity of the energy function with respect to the width of the MMI 3dB power splitter for $L_m = 3.2 \mu\text{m}$ at wavelength $1.55 \mu\text{m}$.

approach and central finite-differences (CFD). The results are shown in Figs. 4.2 and 4.3. Good agreement is obtained between our CAVM approach and the expensive central finite difference approximation (CFD). The CAVM approach requires one extra simulation only while the CFD requires four additional FDTD simulations.

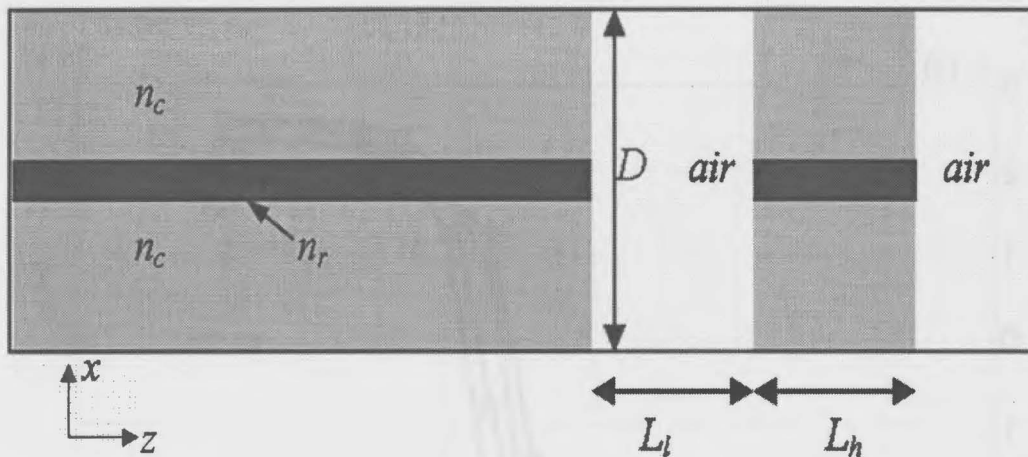


Fig. 4.4. Schematic diagram of the deeply etched waveguide terminator [8].

4.2.2.2 Deeply Etched Waveguide Terminator

A deeply etched waveguide was proposed to minimize the reflected power from waveguide terminators [8],[9]. In this design, a single deep trench is etched at the end of the waveguide as shown in Fig. 4.4. The design parameters are the width of the trench area and the width of the residue ($\mathbf{p} = [L_l \ L_h]^T$). Here, we apply the CAVM approach to get the optimal design parameters that minimize the power reflectivity. The SA-CAVM approach discussed in Section 4.2.1 is applied to get the gradient of the objective function with no adjoint simulations. The power reflectivity can be written as [10]:

$$R(\lambda_o) = |\Gamma(\lambda_o)|^2 \quad (4.26)$$

Using the reflectivity expression in (4.26) as our objective function needs an adjoint simulation. However, the same optimal design parameters can be obtained if the magnitude of the reflection coefficient is taken as our objective function, *i.e.*,

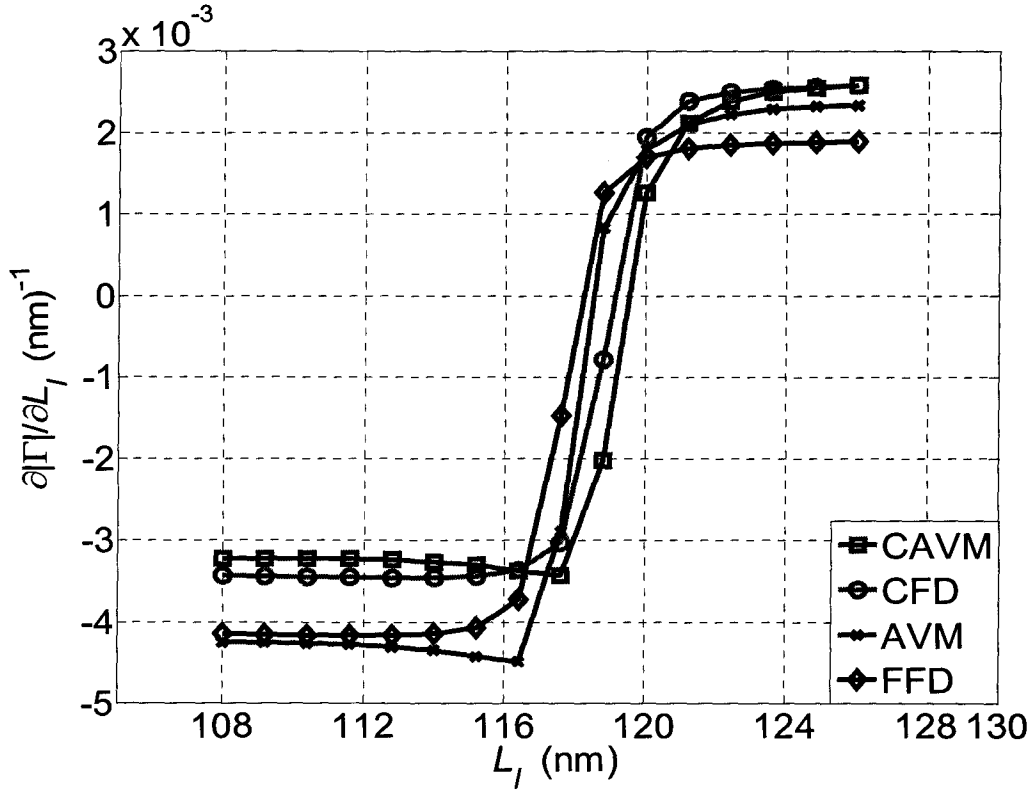


Fig. 4. 5. The sensitivity of the reflection coefficient with respect to the width of the trench L_l of the deeply etched waveguide terminator for $L_h = 280$ nm at $\lambda = 1.55\mu\text{m}$.

$$\min_{L_l, L_h} |\Gamma(\lambda_o)|^2 \equiv \min_{L_l, L_h} |\Gamma(\lambda_o)| \quad (4.27)$$

The expression in (4.27) is valid as long as $\Gamma(\lambda_o)$ is a scalar.

The problem given in the right hand side of (4.27) has a self-adjoint form as discussed in Section 4.2.1. The sensitivity of the objective function ($|\Gamma(\lambda_o)|$) is given by

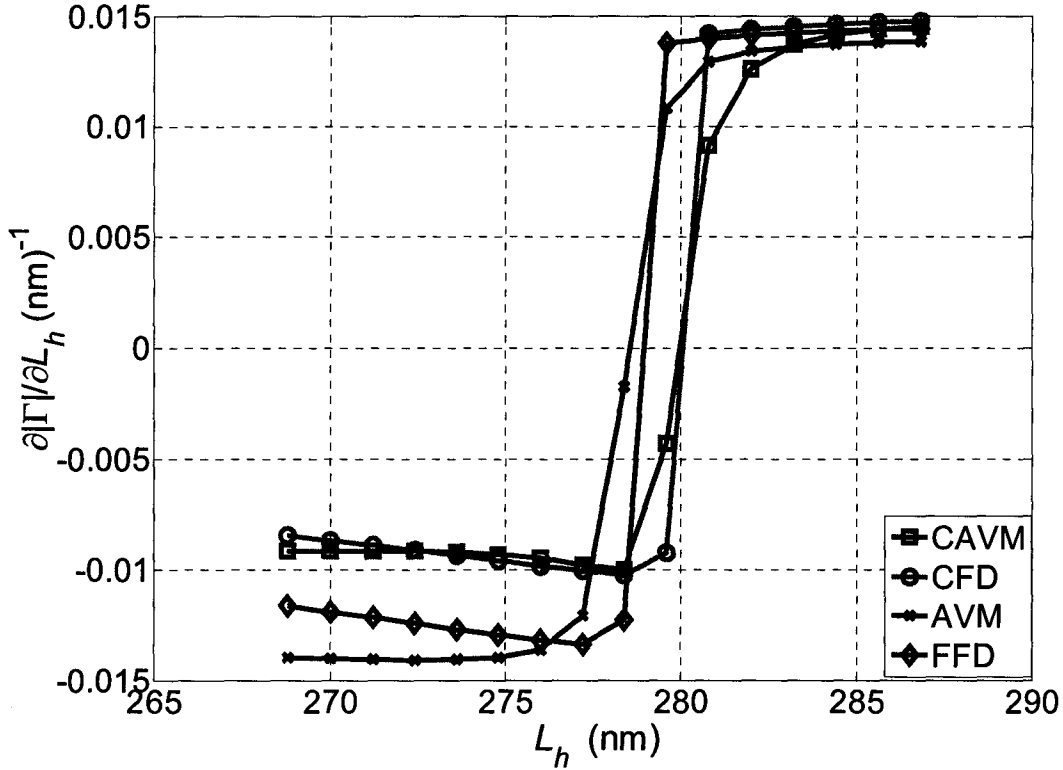


Fig. 4.6. The sensitivity of the reflection coefficient with respect to the width of the residue L_h of the deeply etched waveguide terminator for $L_l=120$ nm at $\lambda = 1.55$ μm .

$$\frac{\partial|\Gamma(\lambda_o)|}{\partial p_n} = \frac{1}{|S|} \frac{\partial|F(\lambda_o)|}{\partial p_n} = \frac{1}{|S|} \cdot \frac{1}{|F|} \left(F_r \cdot \text{Re} \left\{ \frac{\partial F(\lambda_o)}{\partial p_n} \right\} + F_m \cdot \text{Im} \left\{ \frac{\partial F(\lambda_o)}{\partial p_n} \right\} \right) \quad (4.28)$$

where F_r and F_m are the real and the imaginary parts of the function F given in (4.15).

For FDTD simulations, the cell sizes are 1.2 nm and 5.5 nm in the z and x directions, respectively. The width of the high index region (core) of the waveguide is 0.11 μm and the depth of the trench is $D = 3.0$ μm [8]. The material model of GaAsP-InP has refractive indices of $n_r = 3.524$ and $n_c = 3.17$. The parameters of the perfectly matched layer (PML) are the same as those used in [8]. The gradient of the reflection coefficient

with respect to the design parameters is evaluated using (4.28). The calculated sensitivities for the TE case are shown in Figs. 4.5 and 4.6. It is clear from the shown results that the optimal parameter values, at which minimum reflection occurs, are approximately $\mathbf{p} = [119.55 \ 280.0]^T$ nm. These results are very close to those obtained in [8],[9]. The sensitivities obtained using CFD are also shown for comparison. Good agreement is achieved between our SA-CAVM and the CFD. We also compare our SA-CAVM with the self-adjoint approach (AVM) suggested in [4]. The results are also shown in Figs. 4.5 and 4.6. It is clear that SA-CAVM produces more accurate sensitivities that are comparable to the CFD values. In this example, the sensitivities of the response with respect to all the design parameters are obtained without any additional simulation.

In all previous examples, we addressed narrow band sensitivity estimation. For many devices, such as semiconductor optical amplifier (SOA) or superluminescent light emitting diode (SLED), it is desirable to obtain the wideband response and its sensitivities. The FDTD-CAVM approach can supply such wideband sensitivities. They are obtained by applying a wideband adjoint excitation and performing discrete Fourier transform (DFT). Here, the additional cost is mainly that of the DFT which is negligible compared to the FDTD simulation cost. We demonstrate this approach by estimating the sensitivity of the reflection coefficient with respect to the width of the trench L_l over a bandwidth of 100 nm centered around 1.55 μm as shown in Fig. 4.7. Good match is obtained between our CAVM wideband sensitivity estimates and those obtained using CFD.

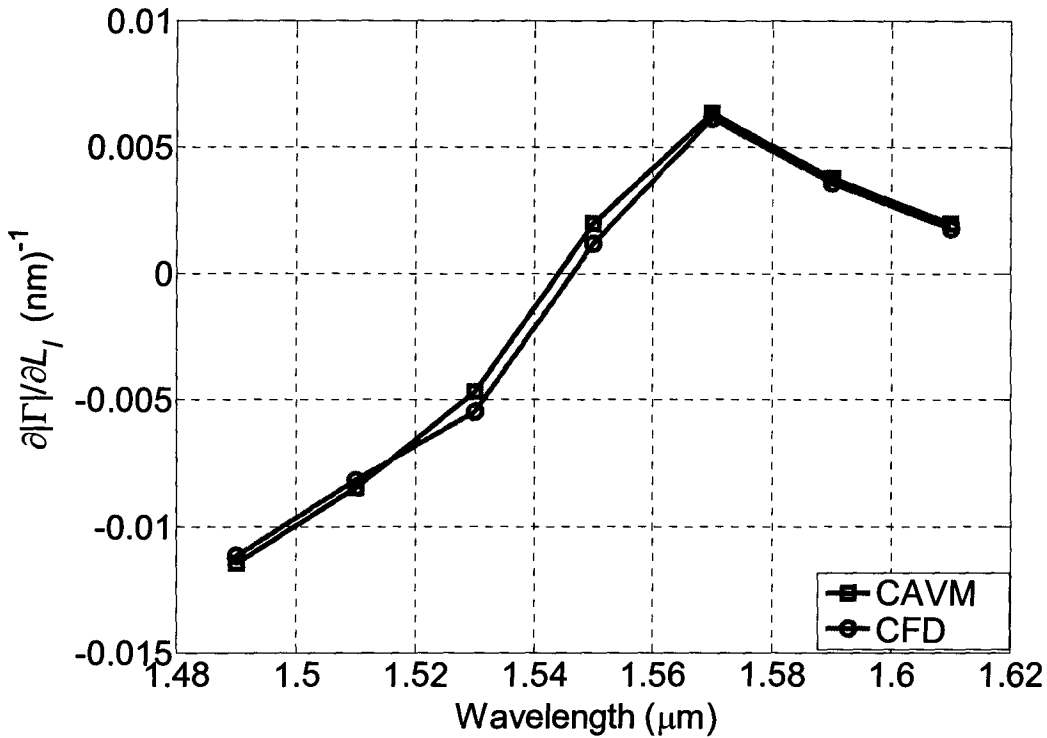


Fig. 4.7. The sensitivity of the reflection coefficient with respect to the width of the trench L_l over a wavelength band of the deeply etched waveguide terminator at $[L_l L_h]=[120.0 \ 280.0]$ nm.

4.2.2.3 Double Layer Antireflection Coatings

Minimizing the reflection from the laser diode (LD) facets is one of the major applications of the antireflection coatings for designing SOAs or SLEDs. In this example, we show how to extract the sensitivities of the reflection from the LD facets with respect to the widths of the antireflection (AR) coating areas. The design used to illustrate our approach is the same as in [10].

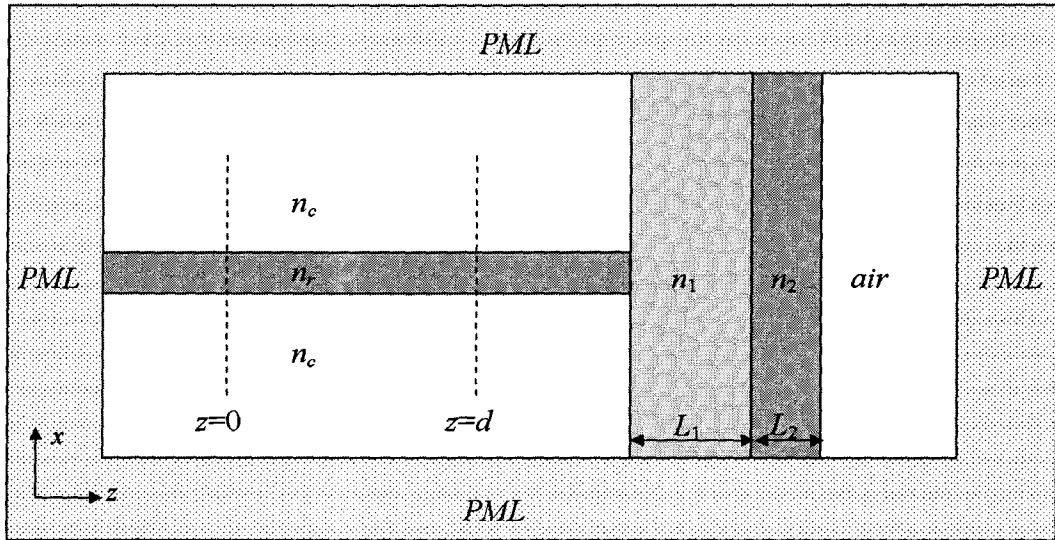


Fig. 4.8. Schematic diagram of a waveguide terminated by double layer antireflection coatings.

The optical field inside the LD is modeled based on three layer waveguide model [10] as shown in Fig. 4.8. The values of the refractive indices of the core n_r and the cladding n_c are 3.524 and 3.17, respectively. The refractive indices of the AR coatings are $n_1=1.82$ and $n_2=1.65$. The width of the first AR film is $L_1=181.6$ nm. In [10], the power reflectivity for the TE case is measured for different widths of the second film L_2 of AR coatings at wavelength of 1540 nm. Here, the structure shown in Fig. 4.8 is simulated using our FDTD in-house simulator and the simulation results are compared with measurements [10]. Both results are shown in Fig. 4.9. The reflectivity calculated using FDTD has a good match with the reported measurements. In the FDTD simulation, the cell size in the x and z directions are 5.5 nm and 1.0 nm, respectively. The separation between the excitation plan at $z = 0$ and the reference plan at $z = d$ is $100 \Delta z$ as shown in

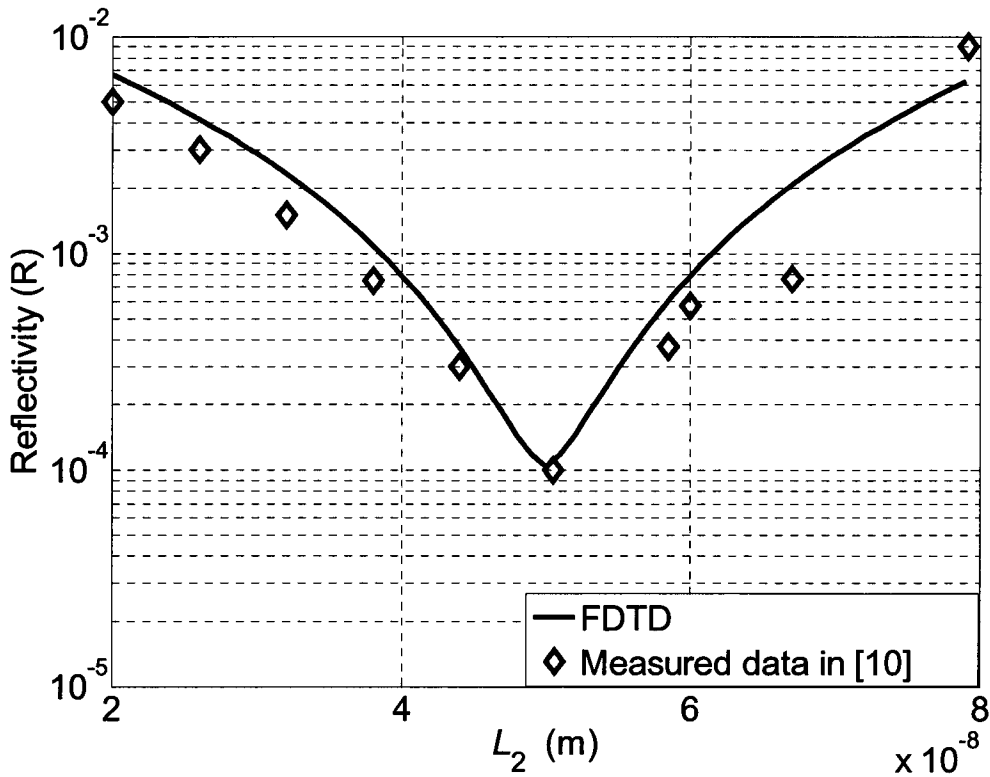


Fig. 4.9. The reflectivity calculated using the FDTD simulation and measured data [10] of the double layer antireflection coatings.

Fig. 4.8. The thickness of the PML layer is 20 cells in both directions. The sensitivity of the reflection coefficient with respect to L_2 is calculated using both the SA-CAVM and the CFD approaches as shown in Fig. 4.10. It is clear that our SA-CAVM approach matches well the expensive CFD approach. Using Fig. 10, the optimum width for L_2 calculated using our approach is 50.02 nm which agrees with the measured results. A minimum reflectivity of -40 dB is obtained at the optimal width at a wavelength of 1.54 μm . In this example, the sensitivity of the reflection coefficient with respect to the parameter L_2 is calculated without any additional simulation.

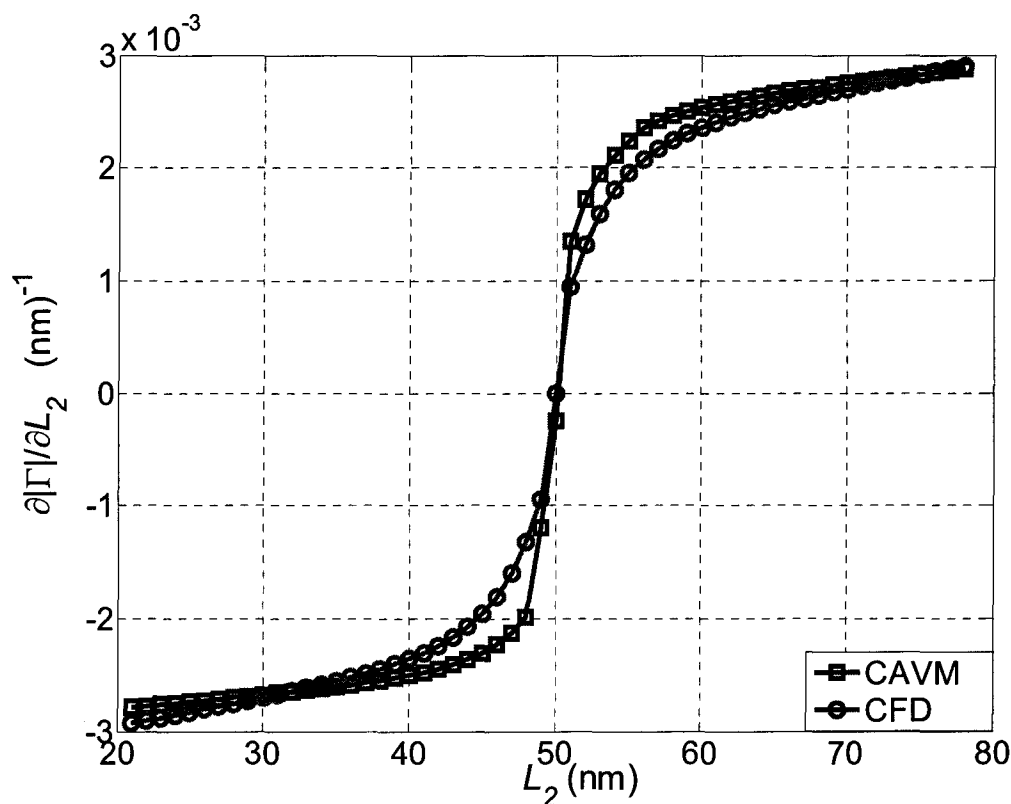


Fig. 4.10. The sensitivity of the reflection coefficient with respect to L_2 of the double layer antireflection coatings for $L_1=181.6$ nm at wavelength of 1540 nm.

4.3 FULL WAVE CALCULATIONS AND SENSITIVITY ANALYSIS OF DISPERSION CHARACTERISTICS

In this Section, we propose a simple and efficient approach to extract the dispersion characteristics with the FDTD method using only one simulation. In addition, the AVM approach proposed in previous sections is utilized to extract the sensitivity of the dispersion characteristics with respect to all the design parameters without the need of any extra simulation.

4.3.1 Calculation of the Propagation Constants

In general, the recorded field at any point in the transverse plan can be utilized to extract the propagation constants. However, this approach cannot guarantee the extraction of all the excited modes due to the spatial dependency of these modes. This approach may become inefficient due to extensive memory resources if the field is recorded at many points to assure the extraction of all the excited modes. Alternatively, we propose the utilization of an objective function that is capable of extracting all the excited modes. The special formulation of this objective function allows for the extraction of the sensitivities of propagation constants without any extra simulation.

The excitation field of the FDTD simulation in the frequency domain can be decomposed into the modes of the structures as follows:

$$\psi_{inp} = \psi(x, y, 0) = \sum_{m=0}^{\infty} a_m^i \Phi_m^i(x, y) \quad (4.29)$$

where $\Phi_m^i(x, y)$ is the modal field of the m th mode of the guided structure at frequency f_i , and a_m^i is the coefficient of the m th mode. The summation in (4.29) includes all modes in the guided structures. However, in this section we limit the application to structures with guided and leaky modes. Direct application to other structures is straightforward.

For a structure with M modes, the total field $\tilde{\psi}_i^i(x, y, z)$ at any propagation distance z for a specific frequency f_i can be calculated as follow

$$\tilde{\psi}_i^i(x, y, z) = \sum_M a_m^i \Phi_m^i(x, y) e^{-j\beta_m^i z} \quad (4.30)$$

where β_m^i is the propagation constant of the m th mode at frequency f_i . For photonic structures, z should be far enough from the source to avoid the contribution of any radiation mode. Our experience shows that 2-3 multiples of the longest wavelength is enough to satisfy this condition.

We define the following objective function in the frequency domain [11]:

$$\tilde{P}^i(z) = \iint \psi_{inp}^H \tilde{\psi}_t^i(x, y, z) dx dy = \sum_m c_m^i e^{-j\beta_m^i z} \quad (4.31)$$

where,

$$c_m^i = |a_m^i|^2 \iint \Phi_m^{iH} \Phi_m^i dx dy \quad (4.32)$$

Here, Φ_m^{iH} is the Hermitian transpose of the m th modal field.

Using the objective function in (4.31), the propagation constants can be obtained by utilizing curve fitting methods in the z - domain [12]. Fourier transform (FT) from the z - domain to β -domain can be also exploited to extract the propagation constants. Hence, if the modal expansion is limited to the guided modes only in the structure, the objective function in the β -domain is given by:

$$\tilde{P}^i(\beta) = \sum_m c_m^i \delta(\beta + \beta_m^i) \quad (4.33)$$

where δ is Dirac delta function. Thus, the propagation constants of all the modes can be obtained at an arbitrary frequency f_i . In addition, the amount of power coupled to each mode can also be obtained through the coefficient c_m^i . The objective function in (4.31) can be rewritten as follows:

$$\tilde{P}^i(z) = \int \left(\iint \psi_{inp}^H \psi_t^i(x, y, z, t) dx dy \right) e^{-j\omega_i t} dt \quad (4.34)$$

This objective function can be obtained by performing discrete Fourier transform (DFT) on the fly during the time domain simulation. Once the propagation constants are obtained, the modal field can be extracted by performing an inverse FT for (4.30) using the following relationship

$$\Phi_m^i(x, y) = \Delta z \sum_k \tilde{\psi}_t^i(x, y, k\Delta z) e^{j\beta_m^i k\Delta z} \quad (4.35)$$

4.3.2 Sensitivity Analysis of the Propagation Constants

Here, we propose an efficient method to extract the sensitivity of the propagation constants [13] obtained using the approach given in Section 4.3.1.

By differentiating (4.31) with respect to the n th design parameter p_n at propagation distance z_1 we get

$$\frac{\partial \tilde{P}^i(z_1)}{\partial p_n} = \sum_{m=1}^M \frac{\partial c_m^i}{\partial p_n} e^{-j\beta_m^i z_1} - jz_1 c_m^i e^{-j\beta_m^i z_1} \cdot \frac{\partial \beta_m^i}{\partial p_n} \quad (4.36)$$

A similar expression can be obtained at different propagation distances. Thus, by evaluating the sensitivities of the objective function at different propagation steps ($[z_1, \dots, z_K]$), the following system of equations can be constructed:

$$\mathbf{Ax} = \mathbf{b} \quad (4.37)$$

where

$$\mathbf{A} = \begin{bmatrix} e^{-j\beta_1^i z_1} & \dots & e^{-j\beta_M^i z_1} & -jz_1 c_1^i e^{-j\beta_1^i z_1} & \dots & -jz_1 c_M^i e^{-j\beta_M^i z_1} \\ \dots & \dots & \dots & \dots & \dots & \dots \\ e^{-j\beta_1^i z_K} & \dots & e^{-j\beta_M^i z_K} & -jz_K c_1^i e^{-j\beta_1^i z_K} & \dots & -jz_K c_M^i e^{-j\beta_M^i z_K} \end{bmatrix}$$

$$\mathbf{x} = \left[\frac{\partial c_1^i}{\partial p_n} \quad \dots \quad \frac{\partial c_M^i}{\partial p_n} \quad \frac{\partial \beta_1^i}{\partial p_n} \quad \dots \quad \frac{\partial \beta_M^i}{\partial p_n} \right]^T,$$

$$\text{and} \quad \mathbf{b} = \left[\frac{\partial \tilde{P}^i(z_1)}{\partial p_n} \quad \dots \quad \frac{\partial \tilde{P}^i(z_K)}{\partial p_n} \right]^T \quad (4.38)$$

In order to calculate the sensitivity of the propagation constants and coefficients given in \mathbf{x} , this system of equations should be first estimated. The values of β_m^i and c_m^i are readily available as described in Section 4.3.1. Once the sensitivity of the objective function in \mathbf{b} is obtained, the system of equations (4.37) can be solved efficiently. The number of the steps K at which the sensitivity of the objective function is evaluated should be at least $2M$ in order to solve a determined system of equation. It is also possible to take the number of steps K larger than $2M$. In this case, a least square approach can be utilized to obtain the pseudo inverse of the matrix A . This approach should increase the accuracy of the obtained results. However, it requires more post processing and larger memory requirements.

In order to calculate the sensitivity of the objective function in \mathbf{b} efficiently, the adjoint variable method (AVM) [4] is utilized. In general, this technique utilizes one extra simulation (adjoint simulation) to obtain the sensitivity of the objective function with respect to all the design parameters. However, the special formulation of the objective function in (4.34) allows us to utilize the self adjoint approach [4]. Using this approach, no extra simulation is needed and the information of the adjoint simulation can be deduced from the original one. Thus, the sensitivity of the objective function (4.31) at a propagation distance z_k is given by [4]

$$\frac{\partial \tilde{P}^i(z_k)}{\partial p_n} = - \int_0^{T_{\max}} \int \frac{\lambda_n \cdot \Delta_n R}{\Delta p_n} dx dy dz dt, \quad n = 1, \dots, N \quad (4.39)$$

where $\Delta_n R$ is the perturbation of the FDTD system matrices due to the perturbation of the design parameter p_n as given in [4]. λ_n in (4.39), is the adjoint field which can be calculated in terms of the original field obtained from the FDTD simulation using the following expression [4]

$$\left(\lambda_{p_n}^T\right)_q = \frac{\left| \left(E_{p_n}^T(\omega_i)\right)_q \right|}{\mu \Delta h^2 J_o \omega_i |H(\omega_i)|} \cdot \begin{pmatrix} \cos(\omega_i t + \varphi_i - (\phi_E)_q - \beta_e^i z_k - \frac{\pi}{2}) \\ + j \cos(\omega_i t + \varphi_i - (\phi_E)_q - \beta_e^i z_k) \end{pmatrix} \quad (4.40)$$

where $\left| \left(E_{p_n}^T(\omega_i)\right)_q \right|$ and $(\phi_E)_q$ are the magnitude and the phase of the original field of the point q at frequency ω_i , respectively. $|H(\omega_i)|$ and φ_i are the magnitude and the phase of the spectral component of the wideband excitation function at ω_i , respectively. J_o is a scaling factor which accounts for the normalization of the incident field and $\Delta h = \min(\Delta x, \Delta y, \Delta z)$. In (4.40), z_k is the distance between the excitation plane and the reference plane, μ is the permeability of the media, and β_e^i is the effective propagation constant of and given by

$$\beta_e^i = \sum_M c_m^i \beta_m^i / \sum_M c_m^i \quad (4.41)$$

It follows that using this approach the sensitivity of the propagation constants with respect to all the design parameters are calculated efficiently.

4.3.3 Numerical Example

In order to illustrate our approach the propagation constants of a multimode waveguide are calculated over wide band of wavelengths. The width of the core region is

0.75 μm with a refractive index of 3.0. The cladding index is taken to be 1.0. The calculated propagation constants are obtained using single FDTD simulation and shown in Fig. 4.11. The obtained results are also compared with those obtained using the solution of the eigenvalue wave equation based on finite difference scheme [13]. A good agreement is obtained between our approach and the FD-method. A uniaxial perfectly matched layer is utilized to terminate the computational domain [5]. The sensitivities of the propagation constants with respect to the refractive index of the core region are calculated as an example and shown in Fig. 4.12.

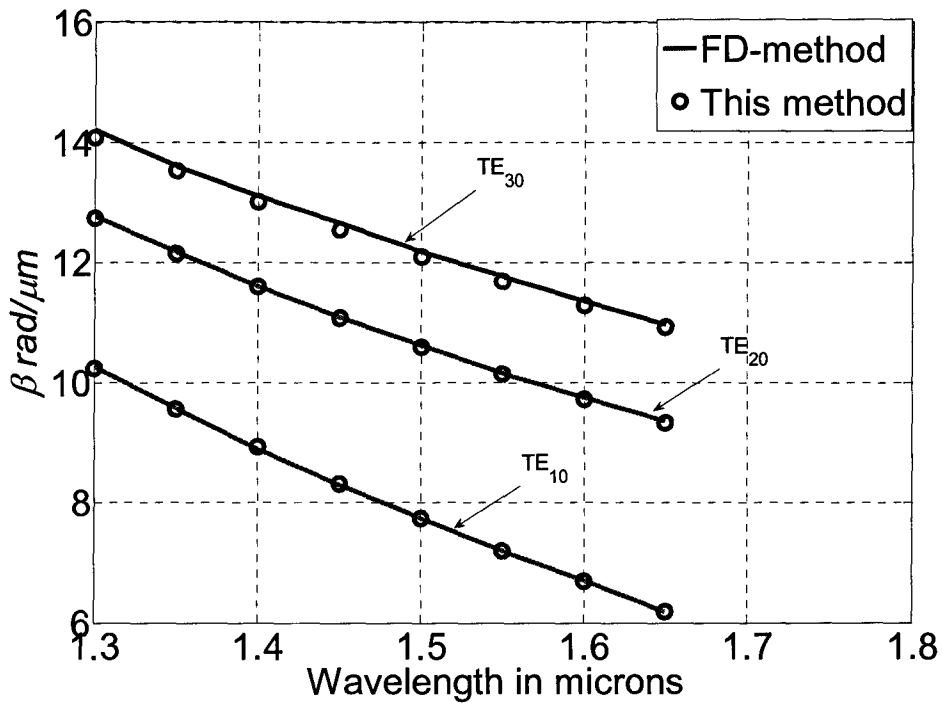


Fig. 4.11. The propagation constants of the waveguide.

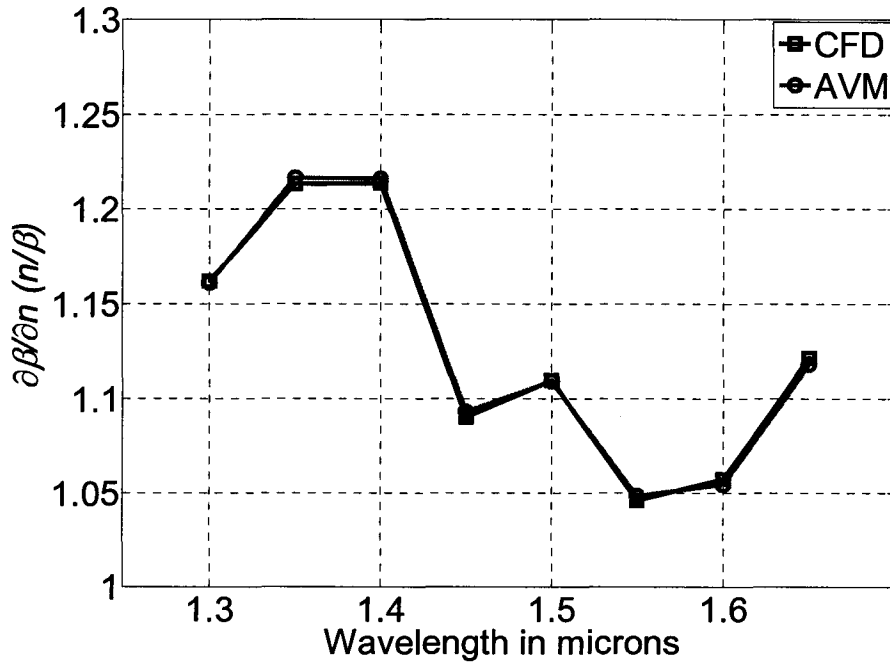


Fig. 4.12. Sensitivity of the propagation constants with respect to the core refractive index of the waveguide.

The results are also compared with the central finite difference sensitivity CFD obtained directly at the response level. The CFD sensitivities are calculated as

$$\frac{\partial \beta_m}{\partial n} \approx \frac{\beta_m(n + \Delta n) - \beta_m(n - \Delta n)}{2\Delta n} \quad (4.42)$$

As shown in Fig. 4.12, a good match is obtained between the sensitivities obtained using out AVM approach and those obtained using CFD.

4.4 CONCLUSION

In this chapter, an efficient approach is proposed for obtaining a second order accurate sensitivities using adjoint variable method applied on FDTD. This technique is

utilized to obtain different responses. It has been also applied to calculate the sensitivity of the power reflectivity using no additional simulations using a self adjoint version of this approach. In addition, an efficient technique is proposed to obtain the propagation constants of the optical structures and their sensitivities with respect to all the design parameters using only single FDTD simulation.

4.5 REFERENCES

- [1] N. K. Nikolova, H. W. Tam, and M. H. Bakr, “Sensitivity analysis with the FDTD method on structured grids,” *IEEE Trans. Microwave Theory Tech.*, vol. 52, pp. 1207–1216, Apr. 2004.
- [2] M. A. Swillam, M. H. Bakr, N. K. Nikolova, and X. Li, “Adjoint sensitivity analysis of dielectric discontinuities using FDTD,” *Electromagnetics*, vol. 27, pp. 123 – 140, Feb. 2007.
- [3] M. H. Bakr and N. K. Nikolova, “An adjoint variable method for time domain TLM with wideband Johns matrix boundaries,” *IEEE Trans. Microwave Theory Tech.*, vol. 52, pp. 678–685, Feb. 2004.
- [4] N. K. Nikolova, Ying Li, Yan Li, and M. H. Bakr, “Sensitivity analysis of scattering parameters with electromagnetic time-domain simulators,” *IEEE Trans. Microwave Theory Tech.* vol. 54, pp.1598-1610 Apr. 2006.
- [5] M. H. Bakr, N.K. Nikolova, and P.A.W. Basl, “Self-adjoint *S*-parameter sensitivities for lossless homogeneous TLM problems,” *Int. J. of Numerical Modelling: Electronic Networks, Devices and Fields.* vol. 18, pp. 441-455 Nov. 2005.

- [6] M. A. Swillam, M. H. Bakr, and X. Li, “Accurate sensitivity analysis of photonic devices exploiting the finite- difference time-domain central adjoint variable method,” *Appl. Opt.*, vol. 46 , pp. 1492 – 1499, Mar. 2007
- [7] J. P. Berenger, “A perfectly matched layer for the absorption of electromagnetic waves,” *J. Comput. Phys.* vol. 114, pp.185–200 Oct. 1994.
- [8] G. -R. Zhou, X. Li, and N.-N. Feng, “Design of deeply-etched antireflective waveguide terminators,” *IEEE J. Quantum Electron.* vol. 39, pp. 384–391, Feb. 2003.
- [9] G. -R. Zhou, X. Li and N. -N.Feng, “Optimization of deeply-etched antireflective waveguide terminators by space mapping technique” *Integrated Photonics Research (IPR)*, IThH2, San Francisco, 2004 .
- [10] T. Sitoh, T. Mukai, and O. Mikami, “Theoretical analysis and fabrication of antireflection coatings on laser-diode facets,” *IEEE/OSA J. Lightwave Technol.* vol. 3, pp. 288-293. Apr. 1985
- [11] M. D. Feit and J. A. Fleck Jr., “Computation of mode properties in optical fiber waveguides by a propagation beam method,” *Appl. Opt.*, vol. 19, pp. 1154–1164, Apr. 1980.
- [12] T. K. Sarkar and O. Pereira, “Using the matrix pencil method to estimate the parameters of a sum of complex exponentials,” *IEEE Antennas Propagat. Mag.*, vol. 37, pp. 48–55, Feb. 1995.

- [13] M. A. Swillam, M. H. Bakr, and X. Li, Full wave sensitivity analysis of guided wave structures using FDTD,” *J. Electromag. Waves Applicat. (JEMWA)*. vol. 22, no. 16, pp 2135-2145, 2008.
- [14] K. Kawano and T. Kitoh, *Introduction of Optical Waveguide Analysis*, John Willy Canada 2001.
- [15] Z. S. Sacks, D. M. Kingsland, R. Lee, and J. F. Lee, “A perfectly matched anisotropic absorber for use as an absorbing boundary condition,” *IEEE Trans. Antennas Propagat.* vol. 43, pp. 1460-1463, Dec. 1995.

5 BPM BASED EFFICIENT SENSITIVITY ANALYSIS EXPLOITING THE AVM

5.1 INTRODUCTION

In this chapter, we propose a novel central adjoint variable method (CAVM) for sensitivity analysis using the finite difference beam propagation method (FD-BPM). The beam propagation method (BPM) is one of the most efficient techniques for simulating photonic devices. It has been applied to the design and modeling of many optical components over the past three decades, see for example [1]-[8]. In our approach, the response sensitivities with respect to all the design parameters are obtained with very little computational overhead. On-grid parameter central perturbation is assumed and exploited to approximate the derivatives of the system matrices using virtual perturbations. This technique is also extended to the 3D full vectorial BPM (FVBPM). We demonstrate the application of our approach for both iterative and non iterative FVBPM based on the alternating direction implicit approach (ADI-FVBPM). Our technique is applied to the imaginary distance FVBPM to extract the sensitivity of the modal properties. It is also applied to extract the sensitivity of all the guided modes of

any guided structure without any additional simulation and with minimum computational overhead. To demonstrate the powerfulness of our approach, the obtained sensitivities are utilized within a gradient-based optimization algorithm to obtain the optimal response in few iterations.

5.2 ADJOINT SENSITIVITY ANALYSIS USING 2D SCALAR BPM

The 2D scalar BPM, which is based on the paraxial wave equation discussed in Chapter 3 is given by [9]

$$j2kn_o \frac{\partial \Phi}{\partial z} = \frac{\partial^2 \Phi}{\partial x^2} + k^2(n^2 - n_o^2)\Phi \quad (5.1)$$

Here, $\partial^2 \Phi / \partial z^2$ has been neglected by assuming that $|\partial^2 \Phi / \partial z^2| \ll 2kn_o |\partial \Phi / \partial z|$. This approximation is called the paraxial approximation or Fresnel approximation.

The differential equation (5.1) can be approximated using the Crank Nicolson finite difference method as [10],[11]

$$\frac{\partial^2 \Phi(m\Delta x, (i+1/2)\Delta z)}{\partial x^2} = \frac{1}{2} \left(\frac{\phi_{i+1}^{m+1} - 2\phi_{i+1}^m + \phi_{i+1}^{m-1}}{(\Delta x)^2} + \frac{\phi_i^{m+1} - 2\phi_i^m + \phi_i^{m-1}}{(\Delta x)^2} \right) \quad (5.2)$$

$$\frac{\partial \Phi(m\Delta x, (i+1/2)\Delta z)}{\partial z} = \frac{\phi_{i+1}^m - \phi_i^m}{\Delta z} \quad (5.3)$$

$$k^2(n^2 - n_o^2)\Phi(m\Delta x, (i+1/2)\Delta z) = k^2 \left[(n_{i+1/2}^m)^2 - n_o^2 \right] \frac{\phi_{i+1}^m + \phi_i^m}{2} \quad (5.4)$$

where Δx and Δz denote the calculation steps in the x and z directions, respectively. The subscripts m and i are the indices of the sampling points along the x and z directions,

respectively. The number of grid points along the x and z axes directions are M ($m = 1, 2, \dots, M$) and N ($i = 1, 2, \dots, N$), respectively. The term ϕ_i^m denotes the discrete values of the field at $x_m = m \Delta x$ and $z_i = i \Delta z$

Substituting (5.2)-(5.4) into (5.1), we obtain the following system of equations [11]

$$-\phi_{i+1}^{m+1} + a_i^m \phi_{i+1}^m - \phi_{i+1}^{m-1} = \phi_i^{m+1} + b_i^m \phi_i^m + \phi_i^{m-1}, \quad i = 1, \dots, N \quad (5.5)$$

where

$$a_i^m = 2 - k^2 (\Delta x)^2 \left[(n_{i+1/2}^m)^2 - n_o^2 \right] + j \frac{4kn_o (\Delta x)^2}{\Delta z} \quad (5.6)$$

$$b_i^m = -2 + k^2 (\Delta x)^2 \left[(n_{i+1/2}^m)^2 - n_o^2 \right] + j \frac{4kn_o (\Delta x)^2}{\Delta z} \quad (5.7)$$

Once the initial electric field distribution ϕ_o^m ($m = 1, 2, \dots, M$) at the input position is given, the electric field profile ϕ_i^m ($i = 1, 2, \dots, N$) can be calculated at any distance z_i by solving the tridiagonal system of linear equations given by (5.5).

5.2.1 Our CAVM Approach

From equation (5.5), it is obvious that the BPM solves the following system of equations at each propagation step

$$A_i \phi_{i+1} = B_i \phi_i \quad (5.8)$$

where A_i , and B_i are the system matrices at the i th step given by

$$A_i = \begin{bmatrix} a_i^1 & -1 & 0 & 0 \\ -1 & a_i^2 & -1 & 0 \\ 0 & \dots & \dots & -1 \\ 0 & 0 & -1 & a_i^M \end{bmatrix}, \text{ and } B_i = \begin{bmatrix} b_i^1 & 1 & 0 & 0 \\ 1 & b_i^2 & 1 & 0 \\ 0 & \dots & \dots & 1 \\ 0 & 0 & 1 & b_i^M \end{bmatrix}, \quad (5.9)$$

The coefficients a_i^1 and a_i^M may be modified if the transparent boundary condition (TBC) is applied [12]. Φ_i and Φ_{i+1} are the field distributions at the propagation distances z_i and z_{i+1} :

$$\Phi_i = \begin{bmatrix} \phi_i^1 \\ \phi_i^2 \\ \vdots \\ \phi_i^M \end{bmatrix}, \quad \text{and} \quad \Phi_{i+1} = \begin{bmatrix} \phi_{i+1}^1 \\ \phi_{i+1}^2 \\ \vdots \\ \phi_{i+1}^M \end{bmatrix} \quad (5.10)$$

By differentiating the system in (5.8) with respect to the j th design parameter p_j and rearranging, we get

$$\frac{\partial \Phi_{i+1}}{\partial p_j} = A_i^{-1} \left[\frac{\partial B_i}{\partial p_j} \Phi_i + B_i \frac{\partial \Phi_i}{\partial p_j} - \frac{\partial A_i}{\partial p_j} \Phi_{i+1} \right] \text{ for } i=1, \dots, N \quad (5.11)$$

where $j = 1, 2, \dots, J$ is the index of the design parameters p_j . These design parameters can be dimensions of discontinuities or material properties. The relation (5.11) can be applied to obtain the derivatives of the first state by setting $i = 0$:

$$\frac{\partial \Phi_1}{\partial p_j} = A_0^{-1} \left[\frac{\partial B_0}{\partial p_j} \Phi_0 - \frac{\partial A_0}{\partial p_j} \Phi_1 \right], \text{ and } \frac{\partial \Phi_0}{\partial p_j} = 0 \quad (5.12)$$

where Φ_0 is the excitation field which is assumed independent of the design parameters.

We first assume that the objective function of interest depends on the field states

at a number of distances. This objective function is denoted by $f(\boldsymbol{\phi}_1, \boldsymbol{\phi}_2, \dots, \boldsymbol{\phi}_m), i_\kappa \in I \quad \forall \kappa$, where I is the index set of the associated field states.

By using the chain rule, we get

$$\frac{\partial f}{\partial p_j} = \sum_{\kappa \in I} \left(\frac{\partial f}{\partial \boldsymbol{\phi}_\kappa} \right)^T \frac{\partial \boldsymbol{\phi}_\kappa}{\partial p_j} \quad (5.13)$$

In (5.13) we assume that the objective function has only an implicit dependence on the design parameters through the field states. Also, in some cases the objective function is dependent on the field distribution at only one distance z_ν ($f_\nu = f(\boldsymbol{\phi}_\nu)$). For this case, the derivative (5.13) can be reduced to

$$\frac{\partial f}{\partial p_j} = \frac{\partial f_\nu}{\partial p_j} = \left(\frac{\partial f_\nu}{\partial \boldsymbol{\phi}_\nu} \right)^T \frac{\partial \boldsymbol{\phi}_\nu}{\partial p_j} \quad (5.14)$$

The CAVM method is derived for this case as follows: Multiplying (5.11) by $(\partial f_\nu / \partial \boldsymbol{\phi}_\nu)^T$, and using (5.14), the sensitivity expression has a non-zero value only if $i = \nu - 1$. Thus the sensitivity expression is given by

$$\frac{\partial f_\nu}{\partial p_j} = \left(\frac{\partial f_\nu}{\partial \boldsymbol{\phi}_\nu} \right)^T \frac{\partial \boldsymbol{\phi}_\nu}{\partial p_j} = \boldsymbol{\lambda}_\nu^T \left[\frac{\partial \mathbf{B}_{\nu-1}}{\partial p_j} \boldsymbol{\phi}_{\nu-1} + \mathbf{B}_{\nu-1} \frac{\partial \boldsymbol{\phi}_{\nu-1}}{\partial p_j} - \frac{\partial \mathbf{A}_{\nu-1}}{\partial p_j} \boldsymbol{\phi}_\nu \right] = \boldsymbol{\lambda}_\nu^T \boldsymbol{\eta}_{\nu,j} \quad (5.15)$$

where

$$\mathbf{A}_{\nu-1}^T \boldsymbol{\lambda}_\nu = \frac{\partial f_\nu}{\partial \boldsymbol{\phi}_\nu} \quad (5.16)$$

The system given in (5.16) is called the adjoint system and $\boldsymbol{\lambda}_\nu$ is called the adjoint variable. The adjoint variable $\boldsymbol{\lambda}_\nu$ can thus be obtained by solving a system of equations which is equivalent to one propagation step of the BPM simulation. It should be clear that

the adjoint variable λ_v is parameter independent. It is calculated only once regardless of the number of the design parameters.

In the general case where the objective function is defined as a function of the field distributions at many propagation distances, the sensitivity expression can be written using (5.13) and (5.15) as

$$\frac{\partial f}{\partial p_j} = \sum_{\kappa \in I} \lambda_{\kappa}^T \cdot \eta_{\kappa,j} \quad (5.17)$$

where

$$\eta_{\kappa,j} = \frac{\partial \mathbf{B}_{\kappa-1}}{\partial p_j} \boldsymbol{\Phi}_{\kappa-1} + \mathbf{B}_{\kappa-1} \frac{\partial \boldsymbol{\Phi}_{\kappa-1}}{\partial p_j} - \frac{\partial \mathbf{A}_{\kappa-1}}{\partial p_j} \boldsymbol{\Phi}_{\kappa}, \quad (5.18)$$

and

$$\mathbf{A}_{\kappa-1}^T \lambda_{\kappa} = \frac{\partial f}{\partial \boldsymbol{\Phi}_{\kappa}}, \quad \forall \kappa \in I \quad (5.19)$$

It should be clear from (5.19) that the number of the parameter-independent adjoint variables is the same as the number of field responses in I . Each adjoint variable is obtained using a linear system of equations which is equivalent to one propagation step of the BPM simulation.

5.2.2 Practical Implementation

Here, we discuss the efficient implementation of our sensitivity analysis algorithm with minimum memory and computational requirements. The first step to implement our sensitivity expression is to calculate the derivatives of the system matrices given in(5.15).

The perturbation theory is utilized to calculate the system derivatives by assuming on-grid virtual perturbation of the system matrices due to the change in the design parameters. The matrices' derivatives are calculated at each propagation step. These matrices are, however, sparse and very few of their components are affected by the change in the refractive index due to a parameter perturbation. This results in very few non-zero elements of these derivative matrices. It follows that the derivatives of the system matrices are calculated in an efficient way.

The central differences are utilized to calculate an approximate derivative of the system matrices. The approximate system matrix derivative is given by:

$$\frac{\partial A_i}{\partial p_j} \approx \frac{(\Delta^+ A_i + \Delta^- A_i)}{2\Delta p_j} \quad (5.20)$$

where Δp_j is the perturbation in the design parameter p_j .

In (5.20), $\Delta^+ A_i$, $\Delta^- A_i$ are the perturbed matrices due to forward and backward perturbation of the design parameter p_j . These perturbed matrices are given by

$$\Delta^+ A_i = A_i(p_j + \Delta p_j) - A_i(p_j) = \begin{bmatrix} \Delta^+ a_i^1 & 0 & 0 & 0 \\ 0 & \Delta^+ a_i^2 & 0 & 0 \\ 0 & \dots & \dots & 0 \\ 0 & 0 & 0 & \Delta^+ a_i^M \end{bmatrix} \quad (5.21)$$

and

$$\Delta^- A_i = A_i(p_j) - A_i(p_j - \Delta p_j) = \begin{bmatrix} \Delta^- a_i^1 & 0 & 0 & 0 \\ 0 & \Delta^- a_i^2 & 0 & 0 \\ 0 & \dots & \dots & 0 \\ 0 & 0 & 0 & \Delta^- a_i^M \end{bmatrix} \quad (5.22)$$

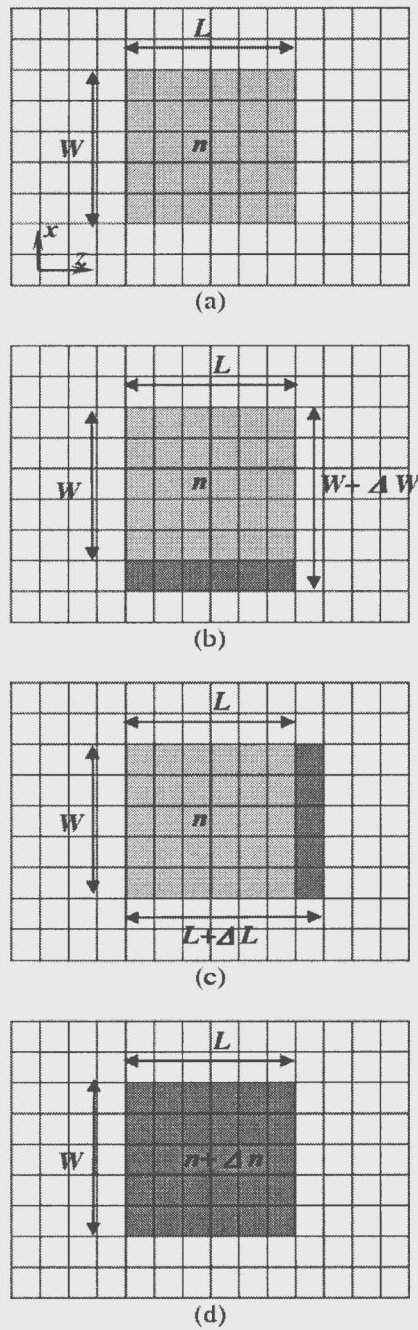


Fig. 5.1. Geometrical representation of the change of the grid cells due to forward change of the design parameters for on grid perturbation. The unperturbed structure is shown in (a), while the lateral perturbation is shown in (b), in (c) the propagation direction perturbation is shown, and the change in the refractive index is shown in (d).

From (5.6) and (5.7), one can show that

$$\Delta^+ \mathbf{B}_i = -\Delta^+ \mathbf{A}_i, \text{ and } \Delta^- \mathbf{B}_i = -\Delta^- \mathbf{A}_i \quad (5.23)$$

As shown in (5.21)-(5.23), the derivative matrices are diagonal matrices which can be calculated efficiently. Once the system derivatives are calculated and the adjoint systems in (5.19) are solved, the sensitivity expression given in (5.17) can be calculated for all design parameters.

In general, for any photonic structure, there are two types of parameters; dimensions of discontinuities and material properties. Perturbations of these parameters cause perturbation in the system matrices. Some of the possible parameter perturbations are shown in Fig. 5.1. In this figure, the perturbation due to a parameter change is classified as either lateral direction change (Fig. 5.1.b), propagation direction change (Fig. 5.1.c), or local refractive index change (Fig. 5.1.d). Here, we assume one grid perturbation for each design parameter. The grid cells whose refractive index value is changed due to the perturbation correspond to the non-zero elements in the derivative of the system matrices. Thus for the lateral perturbation, the derivative matrices contain one or two diagonal elements only according to the symmetry of the structure. However, if the perturbation occurs in the propagation direction, the change in the system matrices occurs only once for the distance at which the structure is perturbed. Meanwhile, if the refractive index at any region inside the structure is perturbed, this will result in a change in the system matrices in the whole affected region. The diagonal system derivatives given in (5.21)-(5.23) are obtained at each propagation step at which the perturbation occurs.

5.2.3 Examples

Here, we illustrate our approach through the estimation of the sensitivities of different objective functions with respect to the dimensions and material properties of different structures. Our results are compared with the accurate and time-intensive central finite difference (CFD) approximation. This approximation is given by:

$$\frac{\partial f}{\partial p_j} \approx \frac{f(p_j + \Delta p_j) - f(p_j - \Delta p_j)}{2\Delta p_j} \quad (5.24)$$

Our AVM approach does not require any extra BPM simulation. The computational overhead involves only the evaluation of (5.11) at each propagation step for each design parameter p_j and the evaluation of (5.17) -(5.19) after the end of the simulation.

5.2.3.1 Directional Coupler

In this example, the directional coupler shown in Fig. 5.2 is designed such that the power injected in Waveguide 1 is totally transferred to Waveguide 2. The effective index of the core region of the waveguides n_r is 1.7 and the cladding index n_c is 1.5. The width of the waveguide w is taken to be $0.8 \mu\text{m}$ for single mode operation at wavelength $1.55 \mu\text{m}$. The separation between the two waveguides d is $1.2 \mu\text{m}$. The length of the coupler is determined using simulation results of the BPM to be $147.5 \mu\text{m}$. This length is chosen such that the launched power in Waveguide 1 is totally transferred to the second waveguide for the TE case [13].

In order to verify the accuracy of the BPM simulation results, the coupling length is also calculated using coupled mode theory (CMT) [11], [13]. The length calculated

using CMT is $148.18 \mu\text{m}$ with a relative error of 4.65×10^{-3} which confirms the accuracy of our BPM results.

For the BPM simulation, the cell sizes are $\Delta x = 0.05 \mu\text{m}$ and $\Delta z = 0.5 \mu\text{m}$. The normalized fundamental mode of the Waveguide 1 is used as an excitation source.

The objective function is taken as the normalized power at the output port of Waveguide 2:

$$f = \int_w |\Phi_y|^2 dx = \Delta x \sum_{d_1}^{d_2} |\Phi_y|^2 \quad (5.25)$$

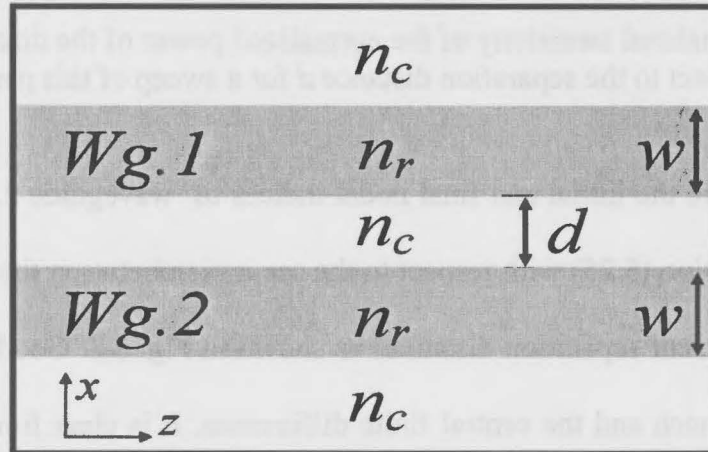


Fig. 5.2. Schematic diagram of the directional coupler.

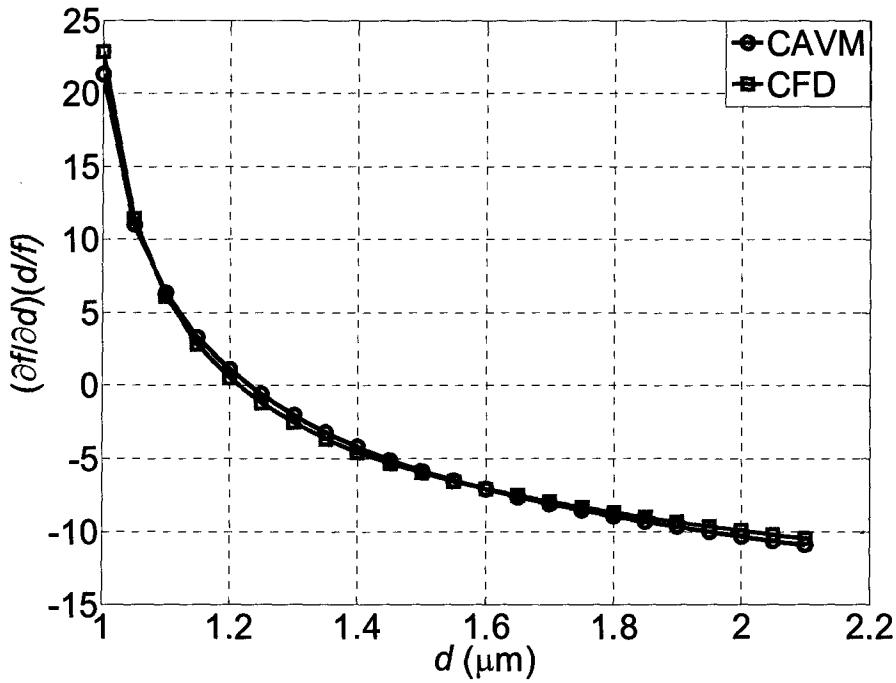


Fig. 5.3. The normalized sensitivity of the normalized power of the directional coupler example with respect to the separation distance d for a sweep of this parameter.

where d_1 and d_2 are the initial and final nodal indices of waveguide 2. The sensitivity of the objective function (5.25) with respect to the separation between the two waveguides d is studied for different separation distances as shown in Fig. 5.3. Good match is obtained between our approach and the central finite differences. It is clear from Fig. 5.3 that the sensitivity has its zero crossing point near the value of $d = 1.2 \mu\text{m}$ at which the device is designed to have its maximum power transferred to Waveguide 2. This also illustrates the accuracy of the calculated sensitivities. The CFD requires two additional BPM simulations meanwhile the CAVM approach requires no extra simulation.

5.2.3.2 Multimode Interference 3 dB Power Splitter

A compact multimode interference (MMI) device (1×2) is used as a 3 dB power splitter as shown in Fig. 5.4. The refractive index of the core region is chosen to be 1.7. The width of the access waveguide is taken to be $0.8 \mu\text{m}$ for single mode of operation at $\lambda_0 = 1.55 \mu\text{m}$. The lengths of the access waveguides at the input and the output are $10.0 \mu\text{m}$. The sensitivity of the coupling coefficient of the 2-D MMI with respect to the dimensions of the structure $\mathbf{p} = [W \ L_m]^T$ is studied using our CAVM technique. In this example, the TE case is studied where the electric field has only one component Φ_y . The coupling coefficient is defined as

$$C = \int_{-\infty}^{\infty} \Phi_N \cdot \Psi \, dx \quad (5.26)$$

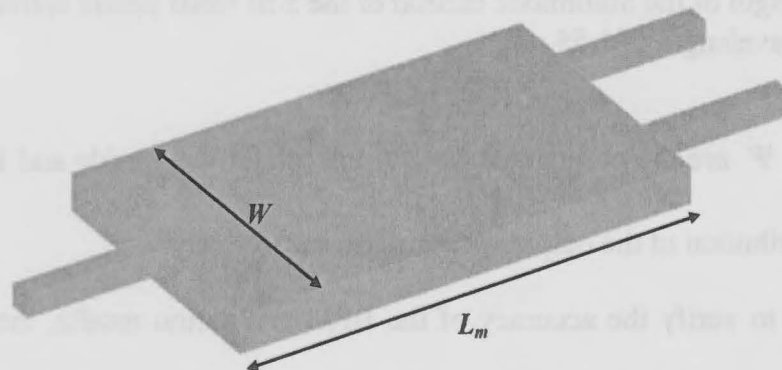


Fig. 5.4. Schematic diagram of MMI 3 dB power splitter.

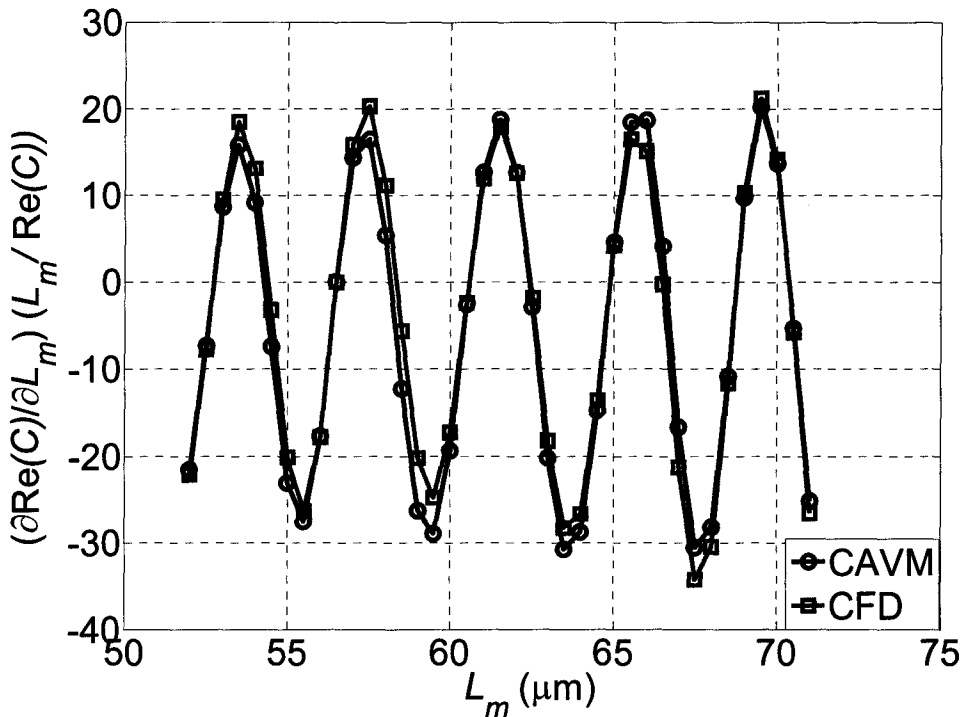


Fig. 5.5. The normalized sensitivity of the real part of the coupling coefficient with respect to the length of the multimode section of the 3dB MMI power splitter for a width of 10.0 μm at wavelength of 1.55 μm .

where Φ_N and Ψ are the normalized field at the output waveguide and the normalized modal field distribution of the output waveguides, respectively.

In order to verify the accuracy of the BPM simulation results, the length of the multimode (MM) section is calculated using the self imaging theory [14] to be 61.82 μm for a width of 10.0 μm . This length is also calculated using BPM by calculating the length for which the magnitude of the coupling coefficient (5.26) is maximum. The calculated coupling length using BPM is 62.0 μm for a width of 10.0 μm which confirms the accuracy of the BPM results.

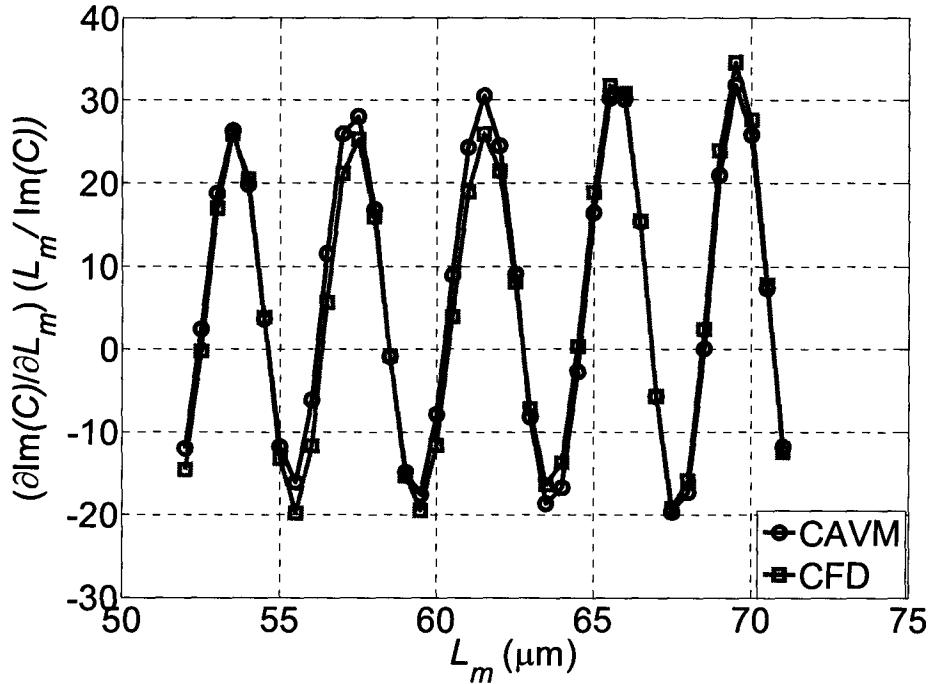


Fig. 5.6. The normalized sensitivity of the imaginary part of the coupling coefficient with respect to the length of the multimode section of the 3dB MMI power for a width of 10.0 μm at wavelength of 1.55 μm .

The sensitivities of the real part and the imaginary part of the coupling coefficient with respect to the length and the width of the multimode section are calculated using the CAVM approach and the central finite differences method (CFD). The results are shown in Figs. 5.5 - 5.8. Good agreement is obtained between our CAVM approach and the expensive CFD. The CAVM approach requires no extra simulation while the CFD requires four additional BPM simulations.

It should be noted that the sensitivity of the magnitude of the coupling coefficient (5.26) can be easily calculated from the real part and imaginary part sensitivities as follows

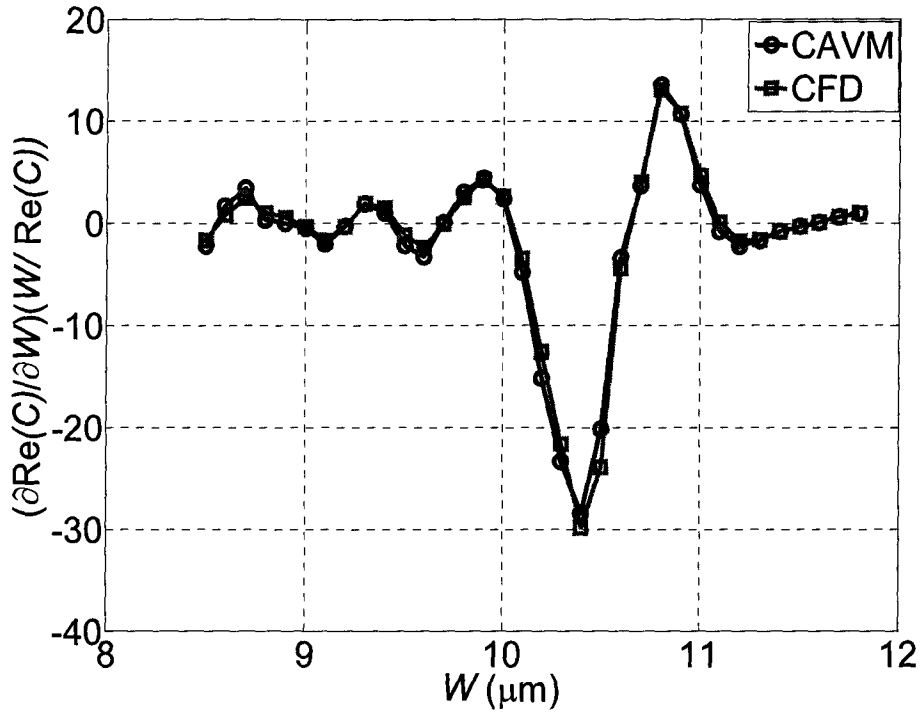


Fig. 5.7. The normalized sensitivity of the real part of the coupling coefficient with respect to the width of the multimode section of the 3dB MMI power for a length of 62.0 μm at wavelength of 1.55 μm.

$$\frac{\partial|C|}{\partial p_j} = \frac{1}{|C|} \left(C_r \operatorname{Re} \left\{ \frac{\partial C}{\partial p_j} \right\} + C_m \operatorname{Im} \left\{ \frac{\partial C}{\partial p_j} \right\} \right) \quad (5.27)$$

where C_r and C_m are the real part and the imaginary part of the coupling coefficient, respectively.

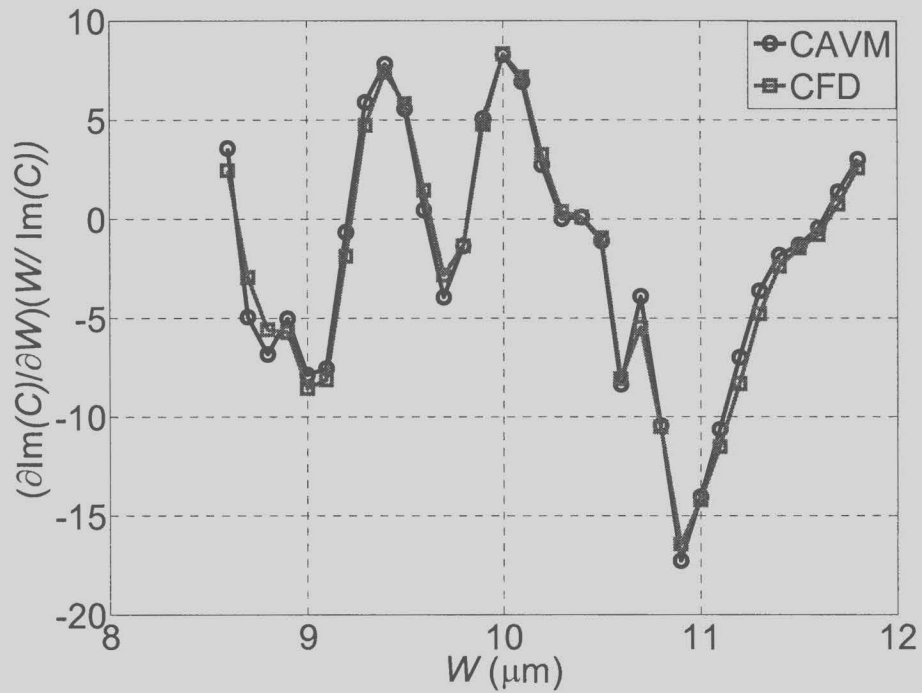


Fig. 5.8. The normalized sensitivity of the imaginary part of the coupling coefficient with respect to the width of the multimode section of the 3dB MMI power for a length of 62.0 μm at wavelength of 1.55 μm.

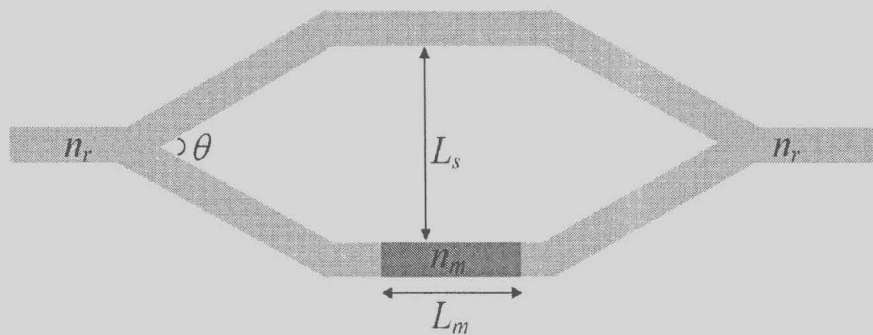


Fig. 5.9. Schematic diagram of the Mach-Zehnder interferometer.

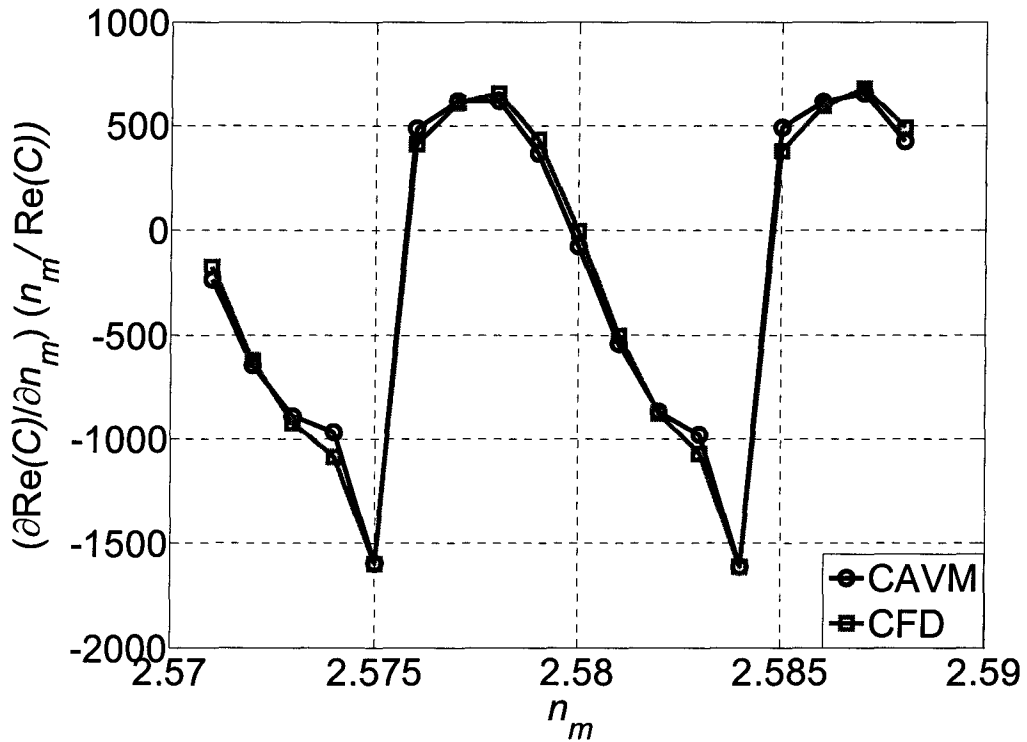


Fig. 5.10. The normalized sensitivity of the real part of the coupling coefficient with respect to the refractive index of the modulation region of the Mach-Zehnder interferometer for $L_s = 8.0$ and $\lambda = 1.55 \mu\text{m}$.

5.2.3.3 Mach-Zehnder Modulator

In this example a Mach-Zehnder interferometer is used as an optical modulator as shown in Fig. 5.9. The refractive index of the core region n_r is 2.58 and the cladding index is 2.5. The width of the access waveguide is $1.0 \mu\text{m}$ for a single mode operation at $\lambda_0 = 1.55 \mu\text{m}$. The lengths of the access waveguides at the input and the output are $100.0 \mu\text{m}$. The separation between the two waveguides L_s is $8.0 \mu\text{m}$ and the branching angle θ is 1.432° . The length of modulated region L_m is $200 \mu\text{m}$. The total length of the simulated structure is $1060 \mu\text{m}$.

To verify the accuracy of our BPM simulator, it is used to determine the refractive index value of the modulated region n_m for which the coupled power to the output waveguide is minimum. The change of the index which produces minimum power at the output arm is $\delta n = n_m - n_r = 4.0 \times 10^{-3}$. This change can be also calculated analytically [11] using the expression $\delta n = \lambda_0 / 2L_m$ to be 3.875×10^{-3} with a relative error of 0.032.

The sensitivity of the real part and the imaginary part of the coupling coefficient given in (5.26) are calculated with respect to the change in the refractive index of the modulated area n_m and the separation of the two waveguides ($\mathbf{p} = [n_m \ L_s]^T$) using the CAVM approach and the central finite differences method (CFD). In (5.26), Ψ is the modal field of the single mode output waveguide. The refractive index step size Δn is taken to be 10^{-3} . The results of the sensitivities are shown in Figs. 5.10 - 5.13. Good agreement is obtained between our CAVM approach and the expensive central finite difference approximation (CFD) which requires four additional simulations. Our technique, however, needs no additional simulations.

5.2.3.4 1×4 power splitter

In this example, a 1×4 MMI power splitter is designed as shown in Fig. 5.14. The refractive indices of the core and the cladding are 1.505 and 1.5, respectively. The width of the MM section W is 80.0 μm . The width of the access waveguide at the input and the output is taken to be 3.0 μm for single mode operation at a wavelength of 1.3 μm . The length of these access waveguide is taken to be 200.0 μm . This ensures that the higher order modes which are possibly excited by the light coupling at the input port will be

completely decayed. The objective function is defined as the power coupling coefficient which is given by:

$$\eta = |C|^2 \tag{5.28}$$

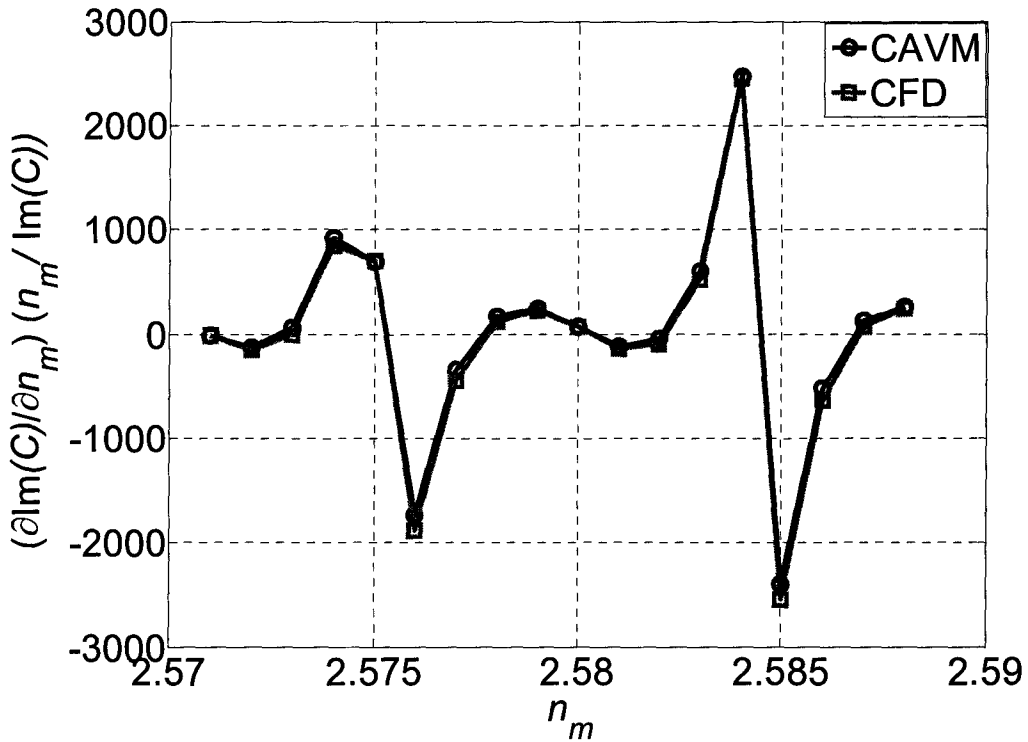


Fig. 5.11. The normalized sensitivity of the imaginary part of the coupling coefficient with respect to the refractive index of the modulation region of the Mach-Zehnder interferometer for $L_s = 8.0$ and $\lambda = 1.55 \mu\text{m}$.

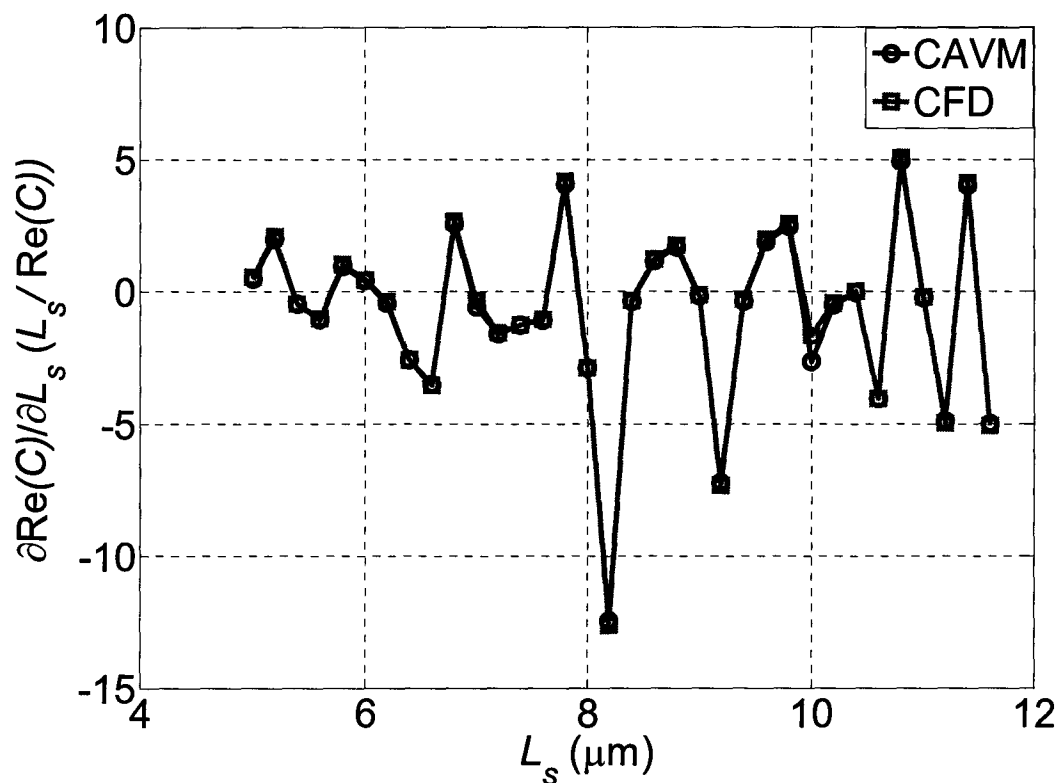


Fig. 5.12. The normalized sensitivity of the real part of the coupling coefficient with respect to the separation between the two waveguide L_s of the Mach-Zehnder interferometer for $n_m = 2.58$ and $\lambda = 1.55 \mu\text{m}$.

The BPM simulation is utilized to calculate the length of the MM section L at which the power coupling is maximum for the TE case at a wavelength of $1.3 \mu\text{m}$. This length is calculated using the BPM to be $2042.0 \mu\text{m}$. This length is calculated using the self imaging theory [14] to be 2012.0 with relative error of 0.02% which validates the accuracy of the BPM results. The total device length is $2442.0 \mu\text{m}$. The input waveguide is designed to be at the center of the MM section. However, due to fabrication tolerance this waveguide may be shifted from its designed position. The design parameter s in this example is defined as the shift of the axis of symmetry of the input waveguide from the

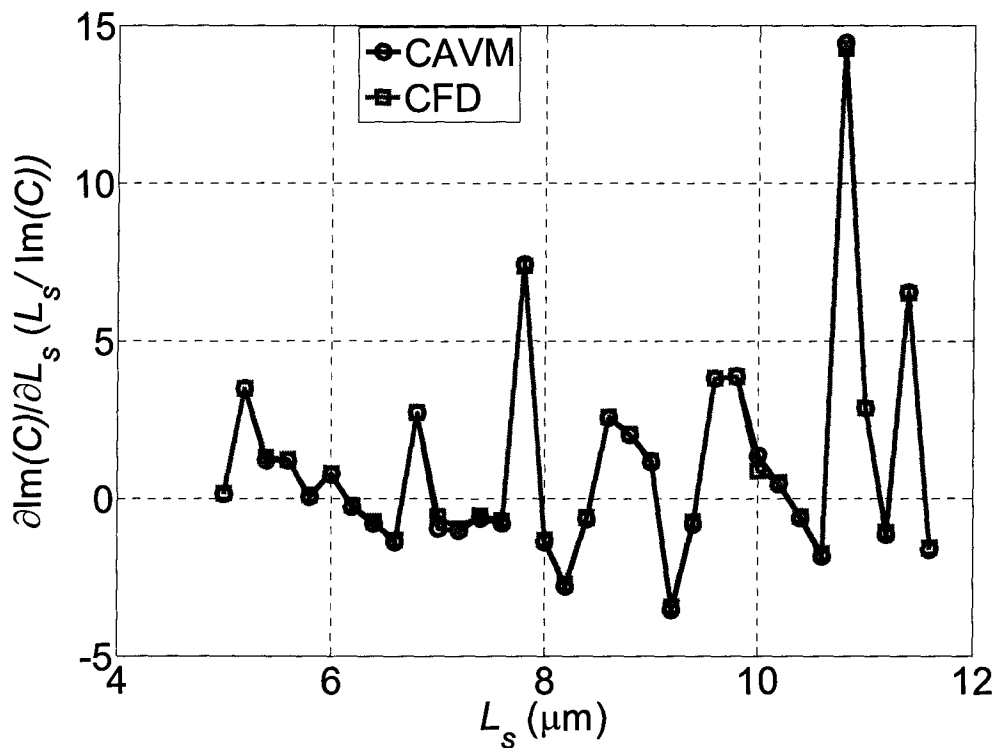


Fig. 5.13. The normalized sensitivity of the imaginary part of the coupling coefficient with respect to the separation between the two waveguide L_s of the Mach-Zehnder interferometer.

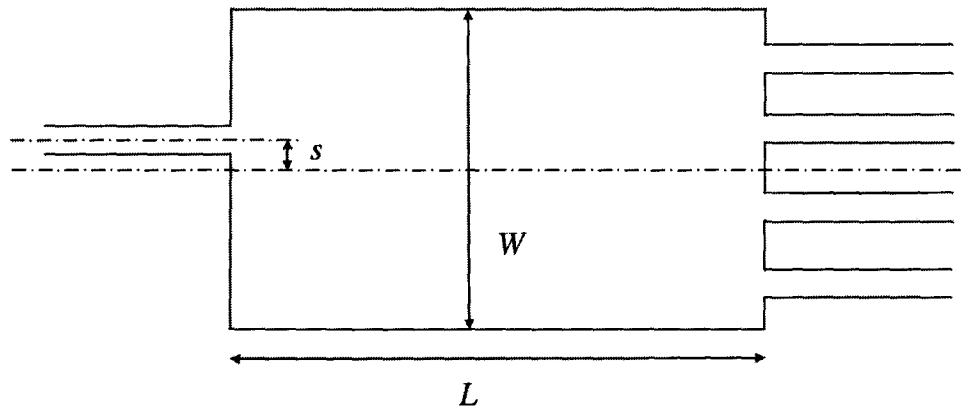


Fig. 5.14. Schematic diagram of MMI 1x4 power splitter.

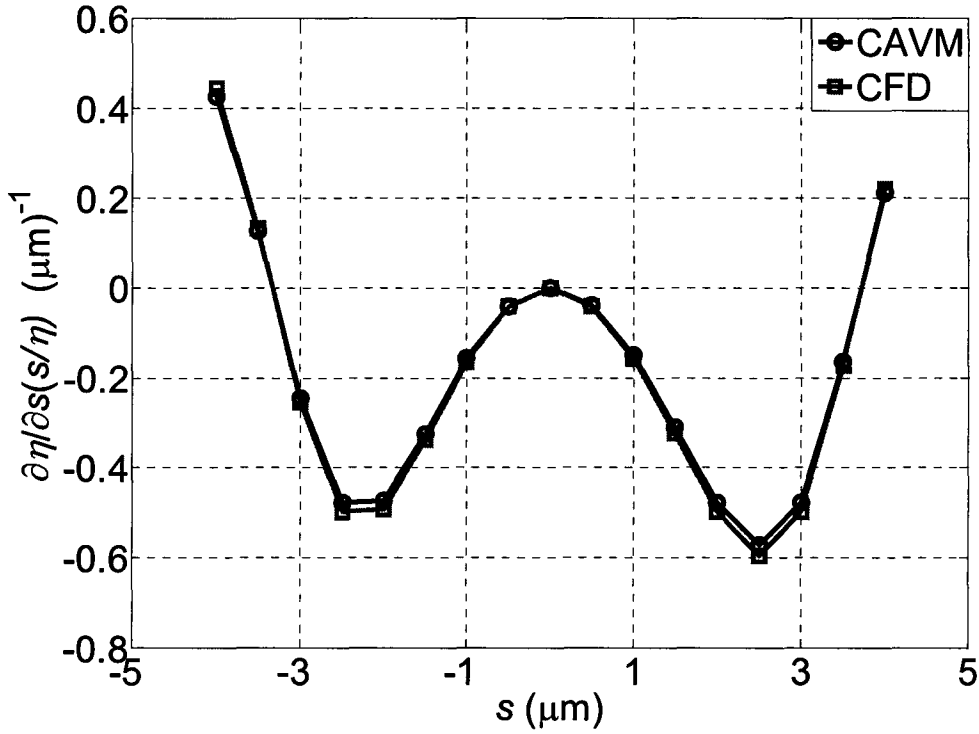


Fig. 5.15. The normalized sensitivity of the power coupling coefficient with respect to the shift of the axis of symmetry of the input waveguide s .

axis of symmetry of the MM section and the output waveguide section as shown in Fig. 5.14.

The sensitivity of the power coupling with respect to s is calculated using the CAVM technique as shown in Fig. 5.15. This sensitivity is compared with CFD which requires two additional simulations and has a good match.

It is clear from the last two examples that the structures are electrically very large. Simulating such structures using FDTD or FDFD would take very long time and huge memory requirements. However, simulating these structures using BPM takes few minutes which proves the efficiency of this technique. Moreover, extracting the

sensitivities using our CAVM approach utilizing the efficient BPM technique allows for efficient tolerance analysis and fast design optimization process.

5.2.4 Computational Overhead

In this section, the computational overhead of our approach is discussed and compared with the computational overhead of calculating the sensitivities using the CFD (5.24). For this purpose, the computational time of extracting the response and its sensitivities is calculated for both our CAVM and the CFD approach for the last two examples given in Section 5.2.3. The computational time of CAVM includes all preprocessing and post processing calculations. The results of this comparison are shown in Table 5.1 for the MMI example and Table 5.2 for the Mach-Zehnder example for different number of design parameters J . We define a time saving factor as the ratio $S_T = T_{CFD} / T_{CAVM}$, where T_{CFD} and T_{CAVM} are the computational time of the CFD approach and our CAVM approach, respectively. These results show that the computational time for our CAVM approach (T_{CAVM}) is always smaller than the computational time of the CFD approach (T_{CFD}). Moreover, the significant time saving increases, as expected, with the increase of the number of design parameters J . Our technique becomes therefore more efficient for problems with large number of design parameters. It should be clear that our technique utilizes the unperturbed system matrices A_i in generating the adjoint vectors given by (5.19). The factorizations of these matrices are readily available through the original BPM simulation. This makes the CAVM approach efficient compared with the CFD which utilizes the BPM method with perturbed system matrices.

The additional memory requirement needed for the CAVM is the storage of the

state derivative vector given by (5.11) at the previous step. This vector is later used in (5.18). There is no need to store the matrices A_i or the vectors λ_κ and $\eta_{\kappa,j}$ as they are both calculated and utilized in (5.17) directly after the original field solution is obtained at the current propagation step. It follows that the memory storage of our CAVM is negligible in comparison with the memory requirement of a single BPM simulation.

Table 5.1

The computational time of CAVM and CFD approaches for the MMI 3dB power splitter example.

| J | 1 | 2 |
|-------------------|--------|-------|
| T_{CAVM} (sec.) | 18.4 | 24.1 |
| T_{CFD} (sec.) | 48.625 | 81.1 |
| S_T | 2.643 | 3.365 |

Table 5.2.

The computational time of CAVM and CFD approaches for the Mach-Zehnder Modulator example.

| J | 1 | 2 |
|-------------------|-------|-------|
| T_{CAVM} (sec.) | 185.3 | 212.5 |
| T_{CFD} (sec.) | 474.9 | 791 |
| S_T | 2.56 | 3.722 |

5.3 SENSITIVITY ANALYSIS USING 3D FULL VECTORIAL BPM

5.3.1 Sensitivity Analysis for Iterative Methods

For iterative methods, the system of equations given in (2.30) can be rewritten as

$$\mathbf{C}^l \boldsymbol{\psi}_i^{l+1} = \mathbf{D}^l \boldsymbol{\psi}_i^l \quad (5.29)$$

where \mathbf{C}^l , and \mathbf{D}^l are the system matrices at the l th propagation step and they are given by

$$\mathbf{C}^l = \mathbf{I} + j\Delta z \alpha \mathbf{P}^l, \quad \mathbf{D}^l = \mathbf{I} - j\Delta z (1 - \alpha) \mathbf{P}^l \quad (5.30)$$

By differentiating the system in (5.29), with respect to the i th design parameter p_i and rearranging, we get

$$\frac{\partial \boldsymbol{\psi}_i^{l+1}}{\partial p_i} = (\mathbf{C}^l)^{-1} \left[\frac{\partial \mathbf{D}^l}{\partial p_i} \boldsymbol{\psi}_i^l + \mathbf{D}^l \frac{\partial \boldsymbol{\psi}_i^l}{\partial p_i} - \frac{\partial \mathbf{C}^l}{\partial p_i} \boldsymbol{\psi}_i^{l+1} \right] \quad \text{for } l=1, \dots, M \quad (5.31)$$

The relation (5.31) can be applied to obtain the derivatives of the first state by setting $l=0$:

$$\frac{\partial \boldsymbol{\psi}_i^1}{\partial p_i} = (\mathbf{C}^0)^{-1} \left[\frac{\partial \mathbf{D}^0}{\partial p_i} \boldsymbol{\psi}_i^0 - \frac{\partial \mathbf{C}^0}{\partial p_i} \boldsymbol{\psi}_i^1 \right], \quad \text{and} \quad \frac{\partial \boldsymbol{\psi}_i^0}{\partial p_i} = \mathbf{0} \quad (5.32)$$

where $\boldsymbol{\psi}_i^0$ is the excitation field which is assumed independent of the design parameters.

Following a similar approach to [15] as described in Section 5.2.1, the sensitivity expression in (5.13) can be rewritten as

$$\frac{\partial f}{\partial p_i} = \sum_{k \in I} \mathbf{X}_k^T \cdot \boldsymbol{\eta}_i^k \quad (5.33)$$

where

$$\eta_i^k = \frac{\partial \mathbf{D}^{k-1}}{\partial p_i} \psi_t^{k-1} + \mathbf{D}^{k-1} \frac{\partial \psi_t^{k-1}}{\partial p_i} - \frac{\partial \mathbf{C}^{k-1}}{\partial p_i} \psi_t^k, \quad (5.34)$$

and

$$(\mathbf{C}^k)^T \mathbf{X}_k = \frac{\partial f}{\partial \psi_t^k}, \quad \forall k \in I \quad (5.35)$$

In (5.33), \mathbf{X}_k is the adjoint variable of the k th state. It is solved once regardless of the number of design parameters. It should be clear that the number of the parameter-independent adjoint variables \mathbf{X}_k is the same as the number of field states in I .

The expression (5.34) requires the parameter-dependent derivatives of the system matrices. These derivatives are given by:

$$\frac{\partial \mathbf{C}^l}{\partial p_i} = j\Delta z \alpha \frac{\partial \mathbf{P}^l}{\partial p_i} = j\Delta z \alpha \begin{pmatrix} \frac{\partial \mathbf{P}_{xx}^l}{\partial p_i} & \frac{\partial \mathbf{P}_{xy}^l}{\partial p_i} \\ \frac{\partial \mathbf{P}_{yx}^l}{\partial p_i} & \frac{\partial \mathbf{P}_{yy}^l}{\partial p_i} \end{pmatrix} \quad (5.36)$$

$$\frac{\partial \mathbf{D}^l}{\partial p_i} = -j\Delta z(1-\alpha) \frac{\partial \mathbf{P}}{\partial p_i} = -j\Delta z(1-\alpha) \begin{pmatrix} \frac{\partial \mathbf{P}_{xx}^l}{\partial p_i} & \frac{\partial \mathbf{P}_{xy}^l}{\partial p_i} \\ \frac{\partial \mathbf{P}_{yx}^l}{\partial p_i} & \frac{\partial \mathbf{P}_{yy}^l}{\partial p_i} \end{pmatrix} \quad (5.37)$$

5.3.2 Sensitivity Analysis for ADI-FVBPM

The system of equation given in (2.31) is discretized using central difference scheme. At each propagation step, the system of equation given in (2.31) is solved.

By differentiating (2.31) with respect to the i th design parameter p_i , we get

$$\frac{\partial \boldsymbol{\psi}_t^{l+1}}{\partial p_i} = \left[\frac{\partial \mathbf{K}^l}{\partial p_i} \boldsymbol{\psi}_t^l + \mathbf{K}^l \frac{\partial \boldsymbol{\psi}_t^l}{\partial p_i} \right] \quad (5.38)$$

where

$$\begin{aligned} \frac{\partial \mathbf{K}^l}{\partial p_i} = & -(\Gamma_4^l)^{-1} \frac{\partial \Gamma_4^l}{\partial p_i} (\Gamma_4^l)^{-1} \Gamma_3^l (\Gamma_2^l)^{-1} \Gamma_1^l + (\Gamma_4^l)^{-1} \frac{\partial \Gamma_3^l}{\partial p_i} (\Gamma_2^l)^{-1} \Gamma_1^l \\ & - (\Gamma_4^l)^{-1} \Gamma_3^l (\Gamma_2^l)^{-1} \frac{\partial \Gamma_2^l}{\partial p_i} (\Gamma_2^l)^{-1} \Gamma_1^l + (\Gamma_4^l)^{-1} \Gamma_3^l (\Gamma_2^l)^{-1} \frac{\partial \Gamma_1^l}{\partial p_i} \end{aligned} \quad (5.39)$$

The derivatives of the system matrices in (5.39) are given by

$$\frac{\partial \Gamma_1^l}{\partial p_i} = \frac{\Delta z}{2} \begin{bmatrix} \frac{\partial A_x}{\partial p_i} & \frac{\partial P_{xy}}{\partial p_i} \\ \mathbf{0} & \frac{\partial B_x}{\partial p_i} \end{bmatrix} = -\frac{\partial \Gamma_4^l}{\partial p_i} \quad (5.40)$$

$$\frac{\partial \Gamma_3^l}{\partial p_i} = \frac{\Delta z}{2} \begin{bmatrix} \frac{\partial A_y}{\partial p_i} & \mathbf{0} \\ \frac{\partial P_{yx}}{\partial p_i} & \frac{\partial B_y}{\partial p_i} \end{bmatrix} = -\frac{\partial \Gamma_2^l}{\partial p_i} \quad (5.41)$$

The sensitivity of the desired objective function can thus be calculated using (5.33) with

$$\boldsymbol{\eta}_i^k = \frac{\partial \mathbf{K}^{k-1}}{\partial p_i} \boldsymbol{\psi}_t^{k-1} + \mathbf{K}^{k-1} \frac{\partial \boldsymbol{\psi}_t^{k-1}}{\partial p_i} \quad \text{and} \quad X_k = \frac{\partial f}{\partial \boldsymbol{\psi}_t^k} \quad (5.42)$$

The derivatives of the system matrices required in (5.34) and (5.42) are estimated using perturbation theory as described in Section 5.2.2.

5.3.3 Sensitivity of the Modal Properties

Sensitivity analysis for objective functions such as the coupling coefficient, and the power in the output waveguide is discussed above and in [15]. In this section, we

illustrate the strength of our approach by extracting the sensitivities of the modal properties of guided structures. We propose two approaches for both the imaginary distance FVBPM (ID-FVBPM) and the FVBPM.

5.3.3.1 Sensitivity of Vector Mode Properties Using ID-FVBPM

The technique of calculating the vector mode properties using ID-FVBPM is given in [16]. Using this technique, the propagation constant and the modal profile of the vector modes can be calculated iteratively. Here, we show how the CAVM approach can be also utilized to extract the sensitivities of the modal properties using the ID-FVBPM.

The ID-FVBPM is mainly dependent on changing the propagation to the imaginary axis i.e. $z = jz'$. The field at any distance z' is thus given by [16]

$$\psi(x, y, z') = \sum_{\infty} a_m e^{z' \lambda_m} \Phi_m(x, y) \quad (5.43)$$

where λ_m and $\Phi_m(x, y)$, $\forall m$, are the eigenvalues and the eigenvectors of the operator P given in (2.22), respectively. These eigenvectors represent the guided and the radiation modes.

An expression is derived in [16] to calculate the propagation constant of all desirable modes. This expression is given by:

$$\beta_m = k_0 n_0 + \frac{1}{\Delta z'} \ln \left(\frac{\iint \psi(x, y, z' + \Delta z') dx dy}{\iint \psi(x, y, z') dx dy} \right) \quad \forall m \quad (5.44)$$

Here, $\psi(x, y, z')$ is the field state at the m th iteration used to calculate the modal properties of the m th mode. The expression (5.44) may be utilized as an objective

function and its sensitivities can be obtained using (5.33). This objective function, however, is dependent on the field state at two consecutive propagation steps. The sensitivities can thus be obtained using (5.33) where I contains two consecutive field states. The memory requirement at each step is double that of an objective function that has dependence on the field state at one step only. To reduce this computational cost, we introduce another objective function to calculate the derivatives of the propagation constant that is dependent on the field state at only one step.

By multiplying (5.43) by the eigenvector Φ_m^H and integrating over the transverse plan, we get

$$\iint \Phi_m^H \psi(x, y, z) dx dy = \sum_M \iint a_m e^{z' \lambda_m} \Phi_m^H \Phi_m dx dy \quad (5.45)$$

where Φ_m^H is the Hermitian transpose of the m th modal field.

It can thus be shown that the m th modal coefficient is given by:

$$a_m = \frac{\iint \Phi_m^H \psi_{inp}(x, y, 0) dx dy}{\iint \Phi_m^H \Phi_m dx dy}, \quad (5.46)$$

Also, we exploit the fact that after appropriate propagation distance, we have $\psi(x, y, z') \rightarrow \Phi_m$. It follows that the eigenvalues can be calculated using the alternative expression

$$\lambda_m = \frac{1}{z'} \ln \left(\frac{\iint \psi(x, y, z')^H \psi(x, y, z') dx dy}{\iint \psi(x, y, z')^H \psi_{inp}(x, y, 0) dx dy} \right) \quad (5.47)$$

where

$$\beta_m = k_o n_o + \lambda_m \quad (5.48)$$

The expression given in (5.47) depends on the field state at one step only. The sensitivity of the eigenvalues can thus be calculated more efficiently.

The main drawback of utilizing the ID-FVBPM is the iterative technique used to extract the modal properties. This technique is thus efficient for structures with small number of guided modes or for single mode structures. In the following subsection, we propose an efficient approach to extract the sensitivity of all the guided modes without any additional simulation.

5.3.3.2 Sensitivity of Vector Mode Properties Using FVBPM

By utilizing the approach given in [16], [18] the eigenvalues can be calculated using the correlation function [16]

$$P(z) = \iint \psi_{inp}^H \psi_t(z) dx dy = \sum_m c_m e^{-j\lambda_m z} \quad (5.49)$$

where

$$c_m = |a_m|^2 \iint \Phi_m^H \Phi_m dx dy \quad (5.50)$$

Using this correlation function, the eigenvalues can be obtained using Fourier transform (FT), Prony's method [19] or the matrix pencil method [18],[20].

By differentiating with respect to the i th design parameter p_i we get

$$\frac{\partial P(z_l)}{\partial p_i} = \sum_{m=1}^M \frac{\partial c_m}{\partial p_i} e^{-j\lambda_m z_l} - j z_l c_m e^{-j\lambda_m z_l} \cdot \frac{\partial \lambda_m}{\partial p_i} \quad (5.51)$$

where M is the number of the excited guided modes, and z_l is the propagation distance $l\Delta z$.

The proposed approach in Sections 5.3.1 and 5.3.2 is first utilized to calculate the sensitivity of the correlation function. By evaluating the sensitivities of the correlation function at different propagation steps ($l \in [l_1, \dots, l_k]$), a system of equations can be constructed as given in (4.37). In order to solve this system of equations, the eigenvalues and the coefficients of the modes are calculated first. The number of the steps k at which the sensitivity of the correlation function is evaluated should be at least $2M$ in order to solve a determined system of equation of the form:

$$\begin{bmatrix} e^{-j\lambda_1 z_1} & \cdot & e^{-j\lambda_M z_1} & -jz_1 c_1 e^{-j\lambda_1 z_1} & \cdot & -jz_1 c_M e^{-j\lambda_M z_1} \\ \cdot & \cdot & \cdot & \cdot & \cdot & \cdot \\ \cdot & \cdot & \cdot & \cdot & \cdot & \cdot \\ e^{-j\lambda_1 z_k} & \cdot & e^{-j\lambda_M z_k} & -jz_k c_1 e^{-j\lambda_1 z_k} & \cdot & -jz_k c_M e^{-j\lambda_M z_k} \end{bmatrix} \begin{bmatrix} \frac{\partial c_1}{\partial p_i} \\ \frac{\partial c_M}{\partial p_i} \\ \frac{\partial \lambda_1}{\partial p_i} \\ \frac{\partial \lambda_M}{\partial p_i} \end{bmatrix} = \begin{bmatrix} \frac{\partial P(z_1)}{\partial p_i} \\ \frac{\partial P(z_2)}{\partial p_i} \\ \cdot \\ \frac{\partial P(z_k)}{\partial p_i} \end{bmatrix} \quad (5.52)$$

Using (4.37), the sensitivities of the eigenvalues (propagation constants) and the modal coefficients c_M are extracted.

The propagation constants and their sensitivities shown here are based on the paraxial full vectorial beam propagation equation given in (2.22). The propagation constants (and hence their sensitivities) of the Helmholtz equation (wide angle) are obtained for the full vectorial case by following a similar procedure to that used for the scalar equation [16]:

$$\beta_{wm} = -kn_o \left(1 - (1 + 2\beta_m / kn_o)^{0.5} \right) \quad (5.53)$$

where β_{wm} and β_m are the propagation constants of the guided modes for the Helmholtz equation given in (2.17) and the paraxial beam propagation equation given in (2.22), respectively.

5.3.4 Numerical Examples

In this section, we illustrate our approach using different structures with different objective functions. Our results are compared with the accurate and time-intensive central finite difference (CFD) approximation applied at the response level obtained using the full vectorial BPM simulation.

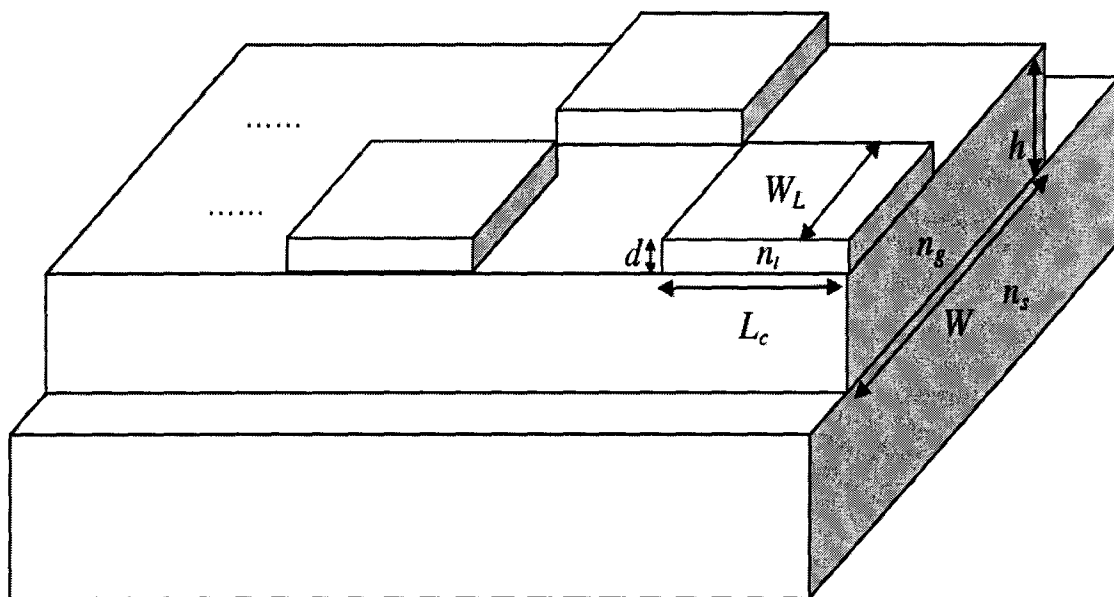


Fig. 5.16. Schematic diagram of the polarization converter using periodically loaded rib waveguide.

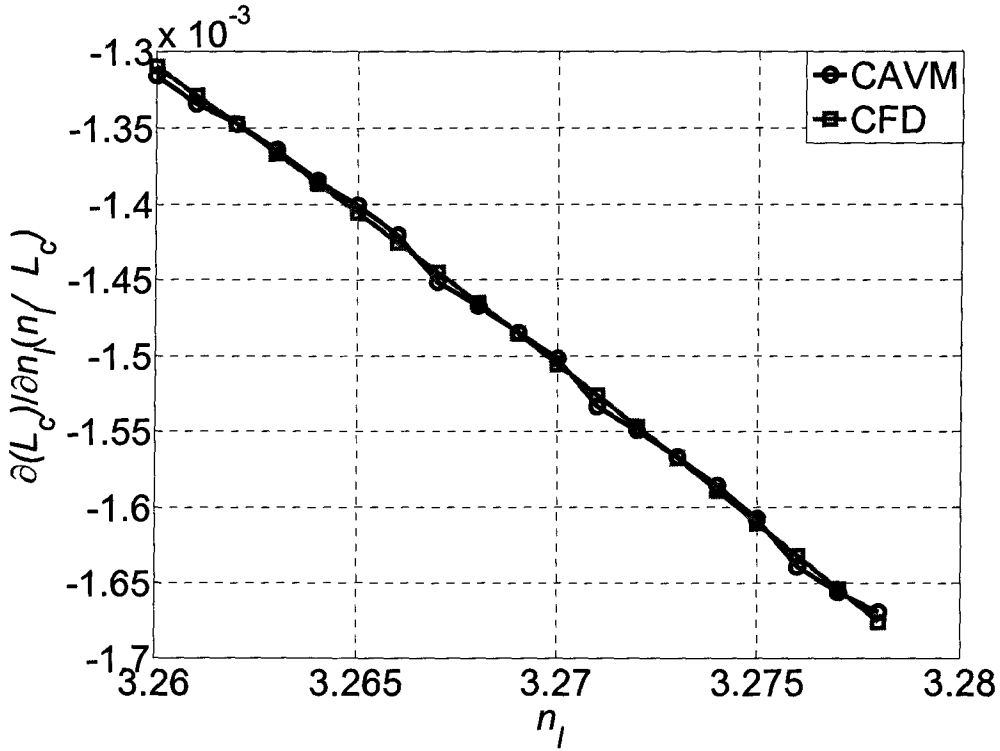


Fig. 5.17. The normalized sensitivity of the coupling length of the polarization converter with respect to the refractive index of the loaded section n_l .

5.3.4.1 A periodically loaded Rib waveguide polarization converter

In this example, a periodically loaded waveguide is utilized as a polarization converter [21]. A schematic diagram of this device is shown in Fig. 5.16. The refractive indexes are $n_s=3.27$, $n_g=3.4$, and $n_f=3.27$. The polarization conversion length is an integer multiple of the loading period L_c . The length of L_c is chosen the same as the beating length of the quasi-TE and quasi-TM modes [21]. This beating length is given by

$$L_c = \frac{\pi}{\beta_{TE} - \beta_{TM}} \tag{5.54}$$

The propagation constants for the quasi-TE β_{TE} and quasi-TM β_{TM} fundamental modes are calculated using the ID-FVBPM based on the iterative method. The width of the

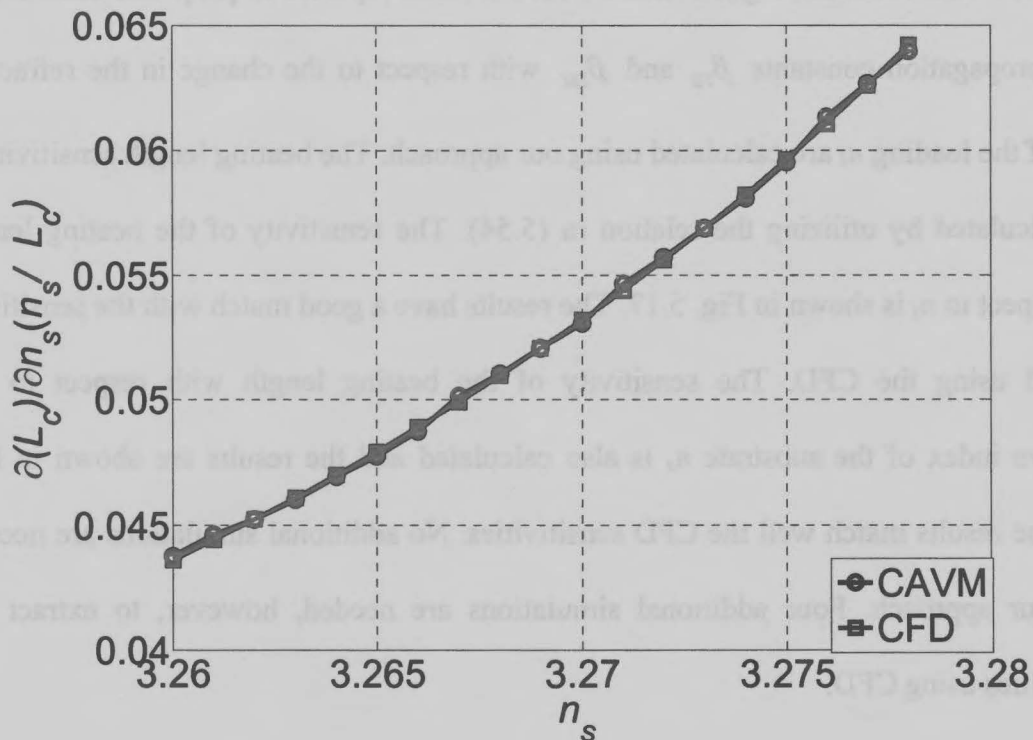


Fig. 5.18. The normalized sensitivity of the beating length of the polarization converter with respect to the refractive index of the substrate n_s .

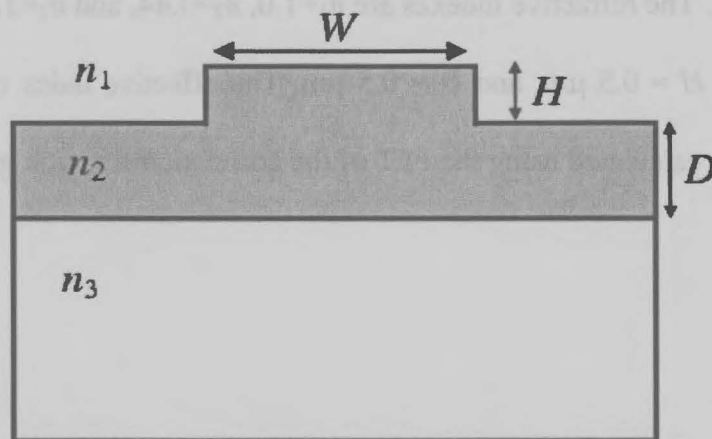


Fig. 5.19. Schematic diagram of the rib waveguide.

waveguide $W = 2W_L$ is $3.0 \mu\text{m}$. The height of the guide h is $0.5 \mu\text{m}$ and the thickness of the load d is $0.1 \mu\text{m}$. The beating length is then calculated to be $159.5 \mu\text{m}$ at a wavelength

of $1.3 \mu\text{m}$. This value has a good match with the result reported in [21]. The sensitivities of the propagation constants β_{TE} and β_{TM} with respect to the change in the refractive index of the loading n_l are calculated using our approach. The beating length sensitivity is then calculated by utilizing the relation in (5.54). The sensitivity of the beating length with respect to n_l is shown in Fig. 5.17. The results have a good match with the sensitivity obtained using the CFD. The sensitivity of the beating length with respect to the refractive index of the substrate n_s is also calculated and the results are shown in Fig. 5.18. The results match well the CFD sensitivities. No additional simulations are needed using our approach. Four additional simulations are needed, however, to extract the sensitivities using CFD.

5.3.4.2 Guided Modes in Rib Waveguide

The strongly guided rib waveguide shown in Fig. 5.19 is simulated using the iterative FVBPM. The refractive indexes are $n_1=1.0$, $n_2=3.44$, and $n_3=3.4$. The dimensions are $W = 3.0 \mu\text{m}$, $H = 0.5 \mu\text{m}$, and $D = 0.5 \mu\text{m}$. The effective index of the fundamental quasi-TE mode is calculated using the FFT of the correlation function given

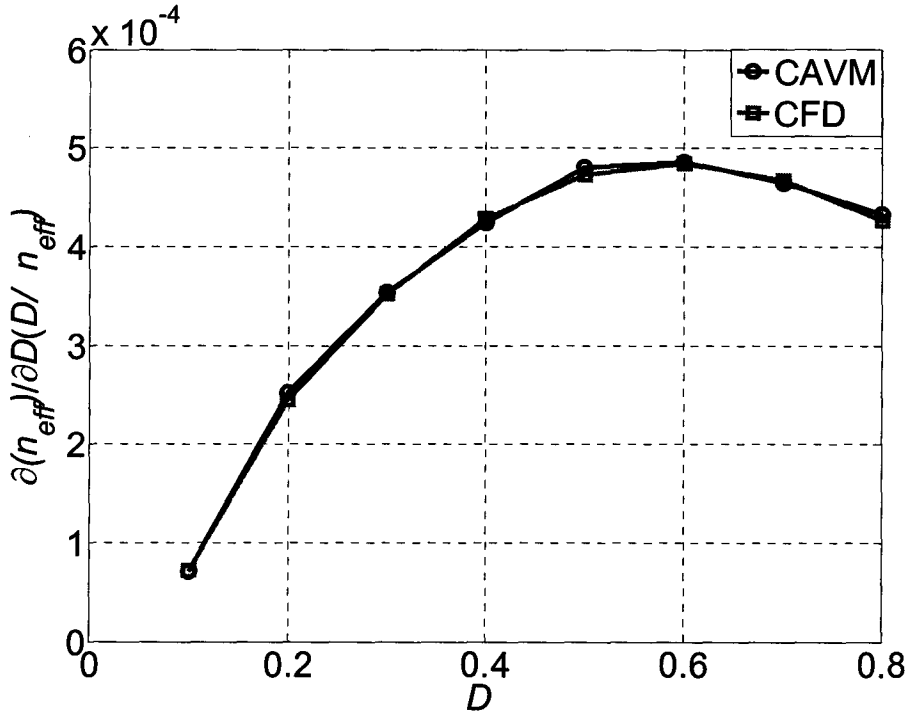


Fig. 5.20. The normalized sensitivity of the effective index of the quasi-TE mode of the rib waveguide with respect to the dimension D .

in (4.31). It is found to be 3.402544 at wavelength of $1.55 \mu\text{m}$ which matches well the result given in [22]. The mesh size is taken to be $0.01 \times 0.01 \mu\text{m}^2$ while the size of the calculation window is $10 \times 10 \mu\text{m}^2$. The transparent boundary condition (TBC) for full vectorial BPM is utilized [22].

The sensitivities of the effective index of the fundamental quasi-TE mode with respect to the dimensions of the waveguide $\mathbf{p} = [D H W]^T$ are calculated using the method proposed in Section 5.3.3.2. They are compared with the CFD as shown in Figs. 5.20 - 5.22. Our technique does not need any additional simulation. The CFD approach, however, requires six additional simulations.

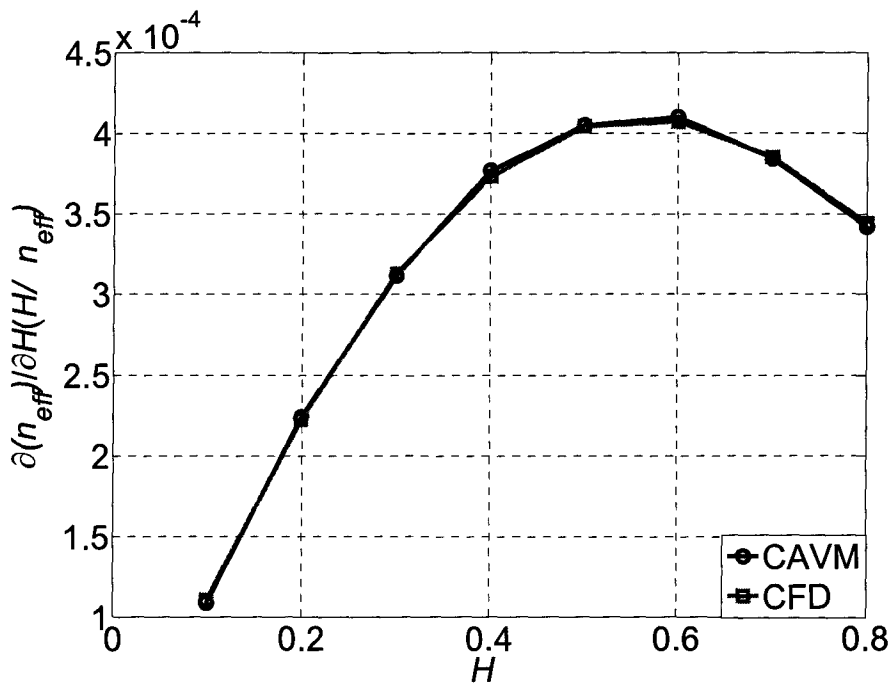


Fig. 5.21. The normalized sensitivity of the effective index of the quasi-TE mode of the rib waveguide with respect to the dimension H .

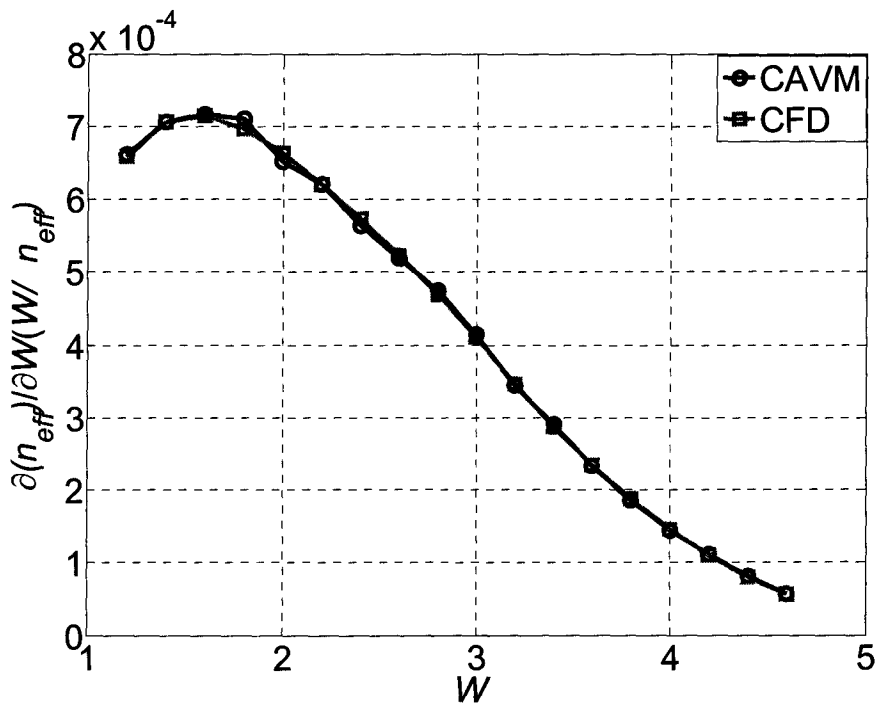


Fig. 5.22. The normalized sensitivity of the effective index of the quasi-TE mode of the rib waveguide with respect to the dimension W .

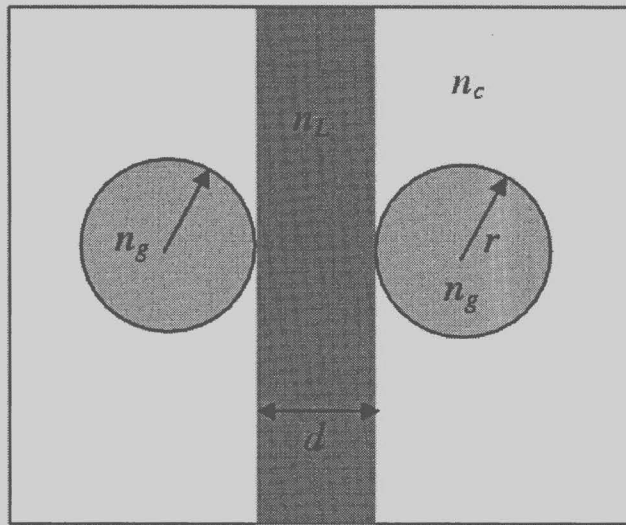


Fig. 5.23. Schematic diagram of the polished fiber coupler.

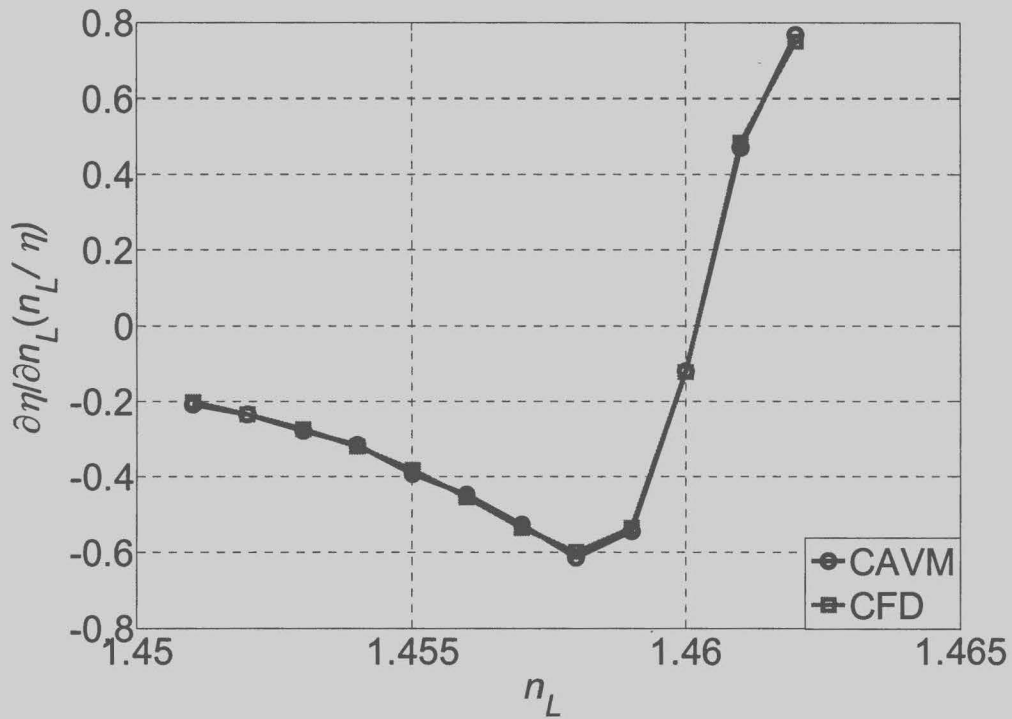


Fig. 5.24. The normalized sensitivity of the power coupling coefficient of the polished fiber coupler with respect to refractive index of the index-matching liquid n_L .

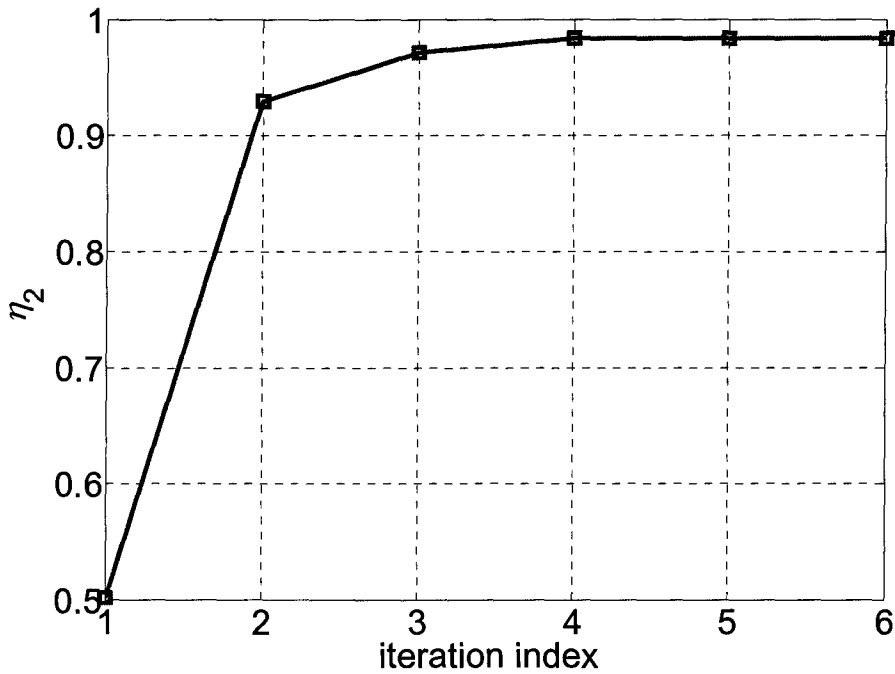


Fig. 5.25. The calculated power coupling coefficient at the output waveguide of the fiber coupler at each optimization iteration.

5.3.4.3 Polished Fiber Coupler

In this example, the polished fiber coupler shown in Fig. 5.23 is simulated using ADI-FVBPM. The refractive index of the core n_g is 1.469, the refractive index of the cladding n_c is 1.46 and the refractive index of the index-matching liquid n_L between the two cores is 1.46. The radius of the core is 2.0 μm . The separation between the two cores d is 1.0 μm . The coupling length after which a power transfer from one guide to the other is calculated to be 308.0 μm at a wavelength of 1.55 μm . The maximum power transfer at this length is calculated, by sweeping the coupling length, to be 0.979. The calculated coupling length has been also verified using the coupled mode theory [11].

The sensitivity of the power coupling coefficient of the fiber coupler with respect to the refractive index of the index matching liquid layer n_L is studied using the ADI-FVBPM. The power coupling coefficient of the input waveguide is given by

$$\eta = \left| \iint \psi_{inp}^H \psi_t dx dy \right|^2 \quad (5.55)$$

where ψ_t, ψ_{inp} are the normalized field at the end of the input waveguide and the normalized modal field distribution of the input waveguide, respectively. Our CAVM approach is utilized to extract the sensitivity of the power coupling coefficient for a sweep of n_L as shown in Fig. 5.24. The results show excellent match with the expensive CFD approach.

5.3.4.4 Optimization of the Polished Fiber Coupler

In this example, we utilize the calculated sensitivities in the previous example to optimize the performance of the polished fiber coupler. The desired response in this example is to maximize the power transfer from one waveguide to the other over a fixed length of the fiber coupler. The design parameters are the refractive index of the index-matching liquid n_L and the separation between the two cores d , ($\mathbf{p} = [n_L d]^T$). The optimization problem can be written as:

$$\begin{aligned} \max_{\mathbf{p}} \quad & \eta_2 \\ \text{subject to} \quad & 0.7 \leq d \leq 1.2 \\ & 1.4 \leq n_L \leq 1.47 \end{aligned} \quad (5.56)$$

where η_2 is the power coupling coefficient of the second waveguide where the power is injected at the input of the first waveguide. The coupler length is 308.0 μm at a

wavelength of 1.55 μm . The initial design parameters are chosen to be $[1.461 \ 1.0 \mu\text{m}]^T$. The power coupling at the initial parameters is 0.502. A maximum power coupling of 0.9839 is achieved after 6 iterations only. This value of the power coupling is higher than that obtained in Example 5.3.4.3. This is mainly because of the more degrees of freedom available by changing two designable parameters.

The obtained objective function at each iteration is shown in Fig. 5.25. The optimal design parameters are $[1.4569 \ 0.70 \mu\text{m}]^T$. It is clear that the sensitivity information accelerates the convergence of the optimization procedure. The large scale constrained optimization package of Matlab [23] is utilized to solve this problem. At each optimization iteration, the optimization algorithm utilizes both the response value and its CAVM sensitivities. This optimization algorithm exploits a subspace trust region method that is based on the interior-reflective Newton method described in [24]-[25]. At each iteration, the approximate solution of the large linear system is calculated using the method of preconditioned conjugate gradients (PCG)[23].

5.3.5 Computational Efficiency

In this section, we discuss the computational time and the memory requirements of our approach. For this purpose, the computational time of calculating the sensitivities of both the iterative and the ADI-based FVBPM is computed for the second and the third examples given in Section 5.3.4 using both our CAVM method and the CFD. The computational time of CAVM includes all preprocessing and post processing calculations. In addition to the solution of the original BPM system of equation, the computational time of our CAVM approach involves also the calculation of the

derivatives of the system matrices in (5.36), and (5.37) or (5.39)-(5.41). It also includes the calculation time of the field derivatives in (5.32) or (5.38) at each required propagation step and the evaluation of the sensitivity expression in (5.33) after the end of the BPM simulation. The computational times are shown in Table 5.3 and Table 5.4. This comparison is performed on a 1.73 GHz Core 2 Duo computer with 1.0 GB of RAM using Matlab[23]. Here, we define the time saving factor S_T as the ratio $S_T = T_{CFD} / T_{CAVM}$, where T_{CFD} and T_{CAVM} are the computational time of the CFD approach and our CAVM approach, respectively.

Table 5.3 shows the computational time of calculating the sensitivities of the effective index for the rib waveguide in Section 5.3.4.2 with respect to the three dimensions $\mathbf{p} = [D H W]^T$. In Table 5.4, the computational time of calculating the sensitivities of the coupling coefficient given in Section 5.3.4.3 with respect to n_L and d is shown ($\mathbf{p} = [n_L d]^T$).

Tables 5.3 and 5.4 show that the CAVM approach for both the ADI-FVBPM and iterative FVBPM techniques are more efficient than the CFD. The saving factor for the ADI method is higher because of the ability to utilize the factorization of the system matrices to calculate the field derivatives in (5.38). This is not the case for the iterative method. For the rib waveguide example, the saving factor S_T in the case of $N = 2$ ($\mathbf{p} = [D H]^T$) is calculated to be 2.34 for the ADI-FVBPM. It is thus clear that our approach becomes more efficient with the increase of the number of design parameters N .

The additional memory requirement needed for the CAVM approach is the storage of the state derivative vector given at each step. This derivative vector is given in

(5.32) for the iterative method and in (5.38) for the ADI method. The memory storage of the CAVM is thus negligible in comparison with the memory requirement of a single additional BPM simulation.

Table 5.3

The computational time of CAVM and CFD approaches for the rib waveguide example ($N=3$)

| | T_{CFD} (sec.) | T_{CAVM} (sec.) | S_T |
|-----------------|------------------|-------------------|-------|
| ADI-FVBPM | 317 | 108.2 | 2.935 |
| Iterative FVBPM | 871.5 | 446.1 | 1.953 |

Table 5.4

The computational time of CAVM and CFD approaches for the fiber coupler example ($N=2$).

| | T_{CFD} (sec.) | T_{CAVM} (sec.) | S_T |
|-----------------|------------------|-------------------|-------|
| ADI-FVBPM | 4094.32 | 1710 | 2.39 |
| Iterative FVBPM | 11545.0 | 6012.1 | 1.92 |

5.4 SENSITIVITY ANALYSIS USING ANALYTICAL DERIVATIVE OF THE SYSTEM MATRICES

The derivatives of the system matrices required in (5.38) and (5.41) are estimated using perturbation theory in [15],[26] as described in Section 5.2.2. However, this technique may be inefficient for a large number of design parameters and large structures. This is mainly due to the need to construct the system matrices of the perturbed system for each design parameter. By utilizing the explicit dependence of these system matrices on the refractive index, we provide an analytical derivative. This can be done by

assuming a change in the refractive index value of Q grid points due to the change in the design parameter p_i . Following a similar approach to that in [27], the derivatives of the system matrices can be rewritten using the following formula

$$\frac{\partial \mathbf{R}^k}{\partial p_i} = \sum_{q=1}^Q \frac{\partial \mathbf{R}^k}{\partial n_q} \frac{\partial n_q}{\partial p_i} \quad (5.57)$$

The derivative of the system matrix with respect to the refractive index value of the q th grid point $\partial \mathbf{R} / \partial n_q$ is analytically calculated. This derivative is sparse with non zero elements at the elements corresponding to the grid point q . It is calculated only once for all the design parameters. This approach reduces the computational cost of obtaining the derivative of the system matrices especially for structures with large number of design parameters. This approach is utilized for efficient sensitivity analysis of surface plasmon structures as described in the following section.

5.4.1 Sensitivity Analysis of Surface Plasmon Waveguide Structures

Surface plasmon polaritons (SPPs) based structures attracted much attention in the last decade [28]-[36]. This is mainly due to their ability to guide light in subwavelength dimensions [28]-[32]. These structures can thus combine the small physical dimensions of electronic circuits with the high operational speed of optical circuits. These features allow the SPPs circuits to be utilized in subwavelength optical interconnects and photonic circuits. SPPs guide the light at the interface between the dielectric and the metal with exponential decaying in both media. The guided optical field is very sensitive to the

properties of the media. Consequently, SPPs have been also successfully exploited in biosensing application [33]-[36].

Investigating the behavior and the sensitivity of the SPPs structures is essential to determine its potential in the different proposed applications. The sensitivity information of these structures with respect to its design parameters is also useful for yield and tolerance analyses. Various modeling techniques have been utilized for studying the behavior and the sensitivity of the optical field in different SPPs structures. They include the finite difference frequency domain (FDFD) method [28], method of lines [30], and the finite element (FEM) method [31]. Most of these techniques are utilized for solving the modes of the SPPs structures to investigate the behavior and the sensitivity of the propagation constants and the losses of the different modes. Very little research is carried out to study the behavior of the propagating optical field for these structures [36]. For both applications, all of the utilized techniques are based on performing many simulations to study the sensitivity of the SPPs structures with respect to the design parameters. This approach, however, is inefficient especially for a large number of design parameters. For example, for N design parameters N extra simulations are need to extract the sensitivity information if the forward finite difference approximation is used.

In order to efficiently model the SPPs waveguide structures, the beam propagation method (BPM) can be exploited. It is capable of both calculating the modal field and simulating the propagating optical field assuming that the utilized BPM technique suits the structure under investigation. This technique has been recently applied for both

applications for SPPs structures [36],[37]. Accordingly, efficient sensitivity extraction of SPPs structures using BPM is of prime importance.

In order to reduce the computational cost of obtaining sensitivity information, the adjoint variable method (AVM) is exploited. This technique is described for efficient sensitivity analysis using full vectorial BPM based on ADI technique in Section 5.3. This approach can be also applied for semi-vectorial 3D ADI BPM using analytical derivative of the system matrices.

For SPPs structures, the metal is represented by a complex refractive index. Hereafter, we propose an efficient approach to calculate the derivatives of the system matrix with respect to design parameters which are related to the change of the dimensions or the material parameters of the metal. This complex refractive index can be written as:

$$n = n_r - jn_{im} \quad (5.58)$$

where n_r represents the real refractive index of the material and n_{im} represents the losses of this material. Using the theory of complex analysis, the derivative of the system matrix with respect to the refractive index for the complex case is given by:

$$\frac{\partial R^k}{\partial n} = \frac{\partial R_r^k}{\partial n_r} + j \frac{\partial R_m^k}{\partial n_r} \quad (5.59)$$

where R_r^k and R_m^k are the real part and the imaginary part of the system matrix R^k . Here, the matrix R^k is assumed to be analytical. In addition, the derivatives of the system

matrices with respect to the imaginary part of the refractive index can be efficiently calculated using the Cauchy-Riemann formula as follow:

$$\frac{\partial \mathbf{R}^k}{\partial n_{im}} = -j \frac{\partial \mathbf{R}^k}{\partial n_r} \quad (5.60)$$

It follows that the sensitivity with respect to any design parameter can be obtained efficiently by utilizing only one analytical derivative of the system matrix.

In order to verify the accuracy of the implemented 3D ADI BPM, the obtained results are compared with those obtained in [37] using a similar method. This comparison is based on the imaginary distance version of the 3D ADI BPM for a structure containing a metal loaded on a dielectric substrate as shown in Fig. 5.26. The same parameters in [37] are utilized to extract the effective index and the attenuation coefficient. An excellent agreement is obtained between the implemented method and the results in [37]. As an example, the effective index of the given structure is calculated using our implemented 3D ADI BPM and compared with the one in [37] as shown in Fig. 5.27.

5.4.1.1 A Metal Loaded On a Dielectric Waveguide

In this example, a SPP waveguide design is proposed for subwavelength applications as shown in Fig. 5.28. In this design, the silicon on insulator (SOI) material is utilized due to its wide application in electronic circuits. It also allows for strong guiding and hence subwavelength light confinement. The utilized metal is gold (Au) with refractive index $n_m=0.18-j10.2$ at a wavelength of $1.55 \mu\text{m}$. The refractive indexes of silicon (Si) and the insulator (SiO_2) are $n_s=3.46$, and $n_i=1.46$, respectively. The thickness

of the metal layer and the silicon layer are $t_m=0.1 \mu\text{m}$, and $t_s=0.5 \mu\text{m}$, respectively. The width of the metal and silicon layers are taken as $W_m=W_s=0.5 \mu\text{m}$. The propagation length of this waveguide structure is given as $L_p=1/2\text{Im}(\beta)$, where β is the complex propagation constant of the fundamental TM mode of this structure. This length is calculated using the imaginary distance 3D ADI BPM to be $32.0 \mu\text{m}$. The vector of design parameters of this structure is $\mathbf{p} = [t_s \ t_m \ W_s \ W_m]^T$. The sensitivity of the propagation length and the effective index of the fundamental mode are calculated using the proposed AVM. The results are compared with the sensitivity information obtained using the CFD approach applied directly at the response level. A very good agreement is obtained between our approach and the CFD as shown in Figs. 5.29 - 5.31. The CFD requires 8 additional simulations. Our approach, however, requires no additional simulations.

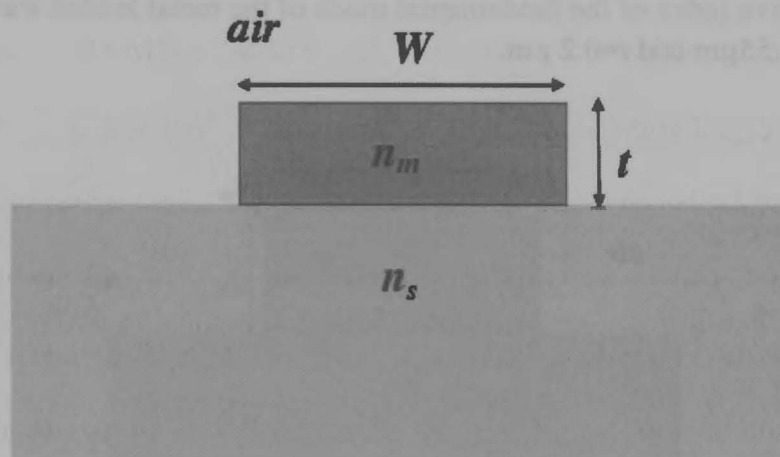


Fig. 5.26. Schematic diagram of the metal loaded waveguide

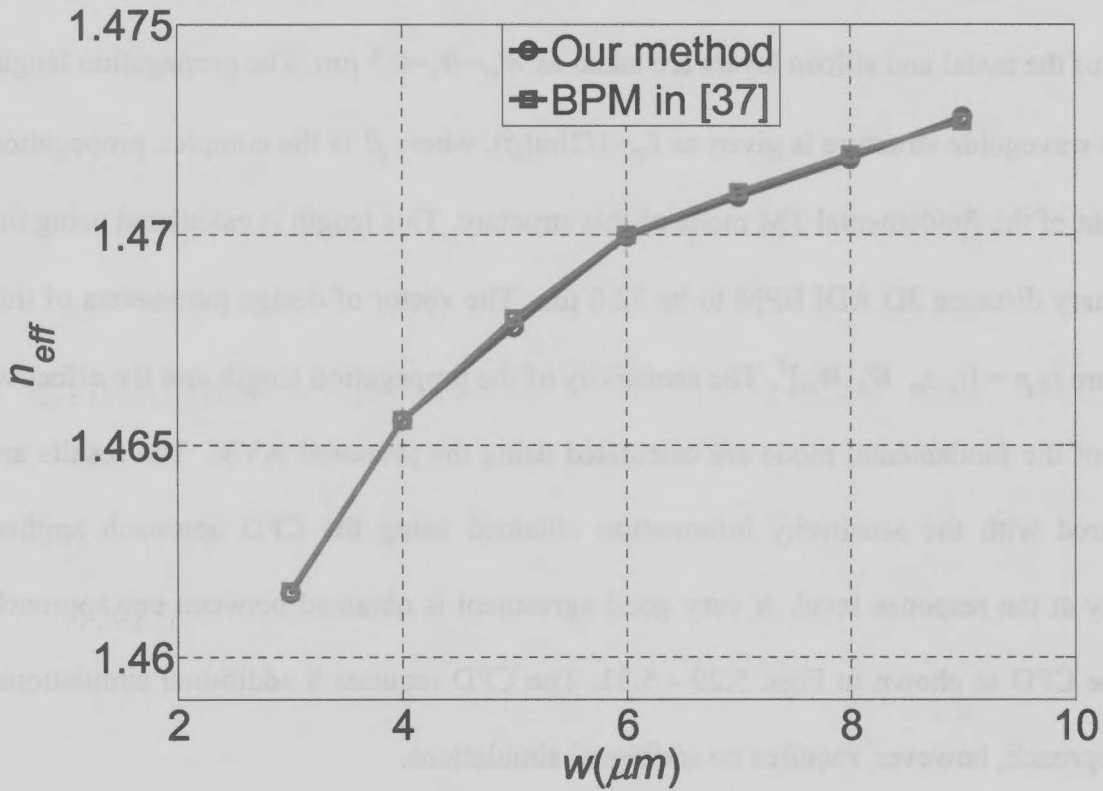


Fig. 5.27. Effective index of the fundamental mode of the metal loaded waveguide at wavelength $\lambda=1.55\mu\text{m}$ and $t=0.2\mu\text{m}$.

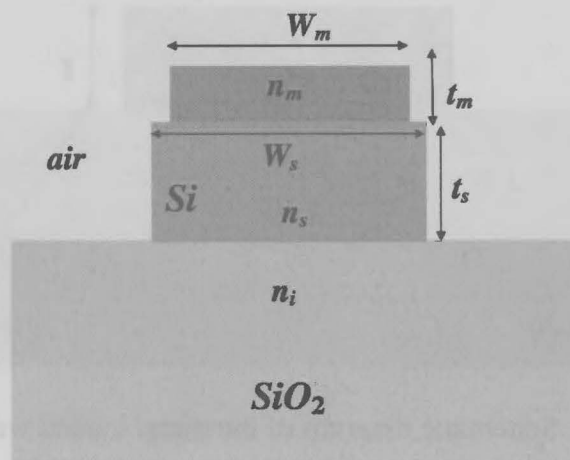


Fig. 5.28. Schematic diagram of the metal loaded channel waveguide.

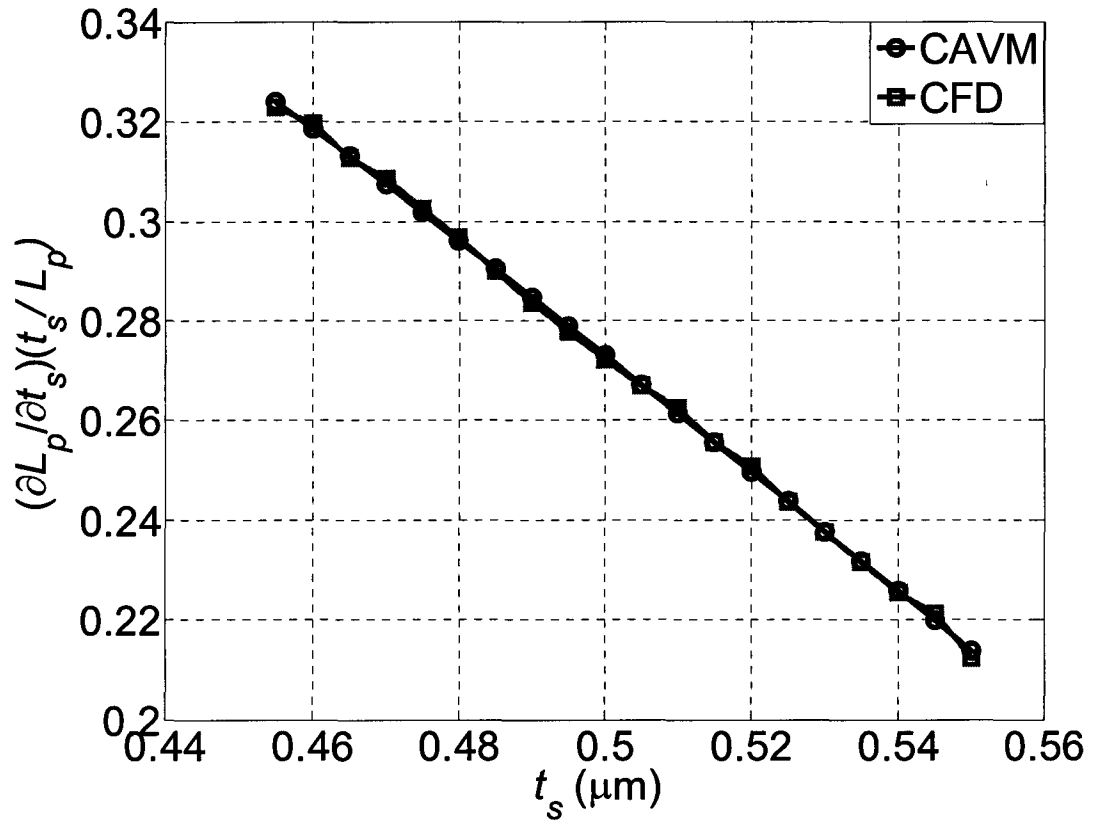


Fig. 5.29. Normalized Sensitivity of the propagation length of the fundamental mode in a metal loaded on channel waveguide structure at wavelength $\lambda=1.55\mu\text{m}$, $W_m=W_s=0.5\mu\text{m}$, and $t_m=0.1\mu\text{m}$.

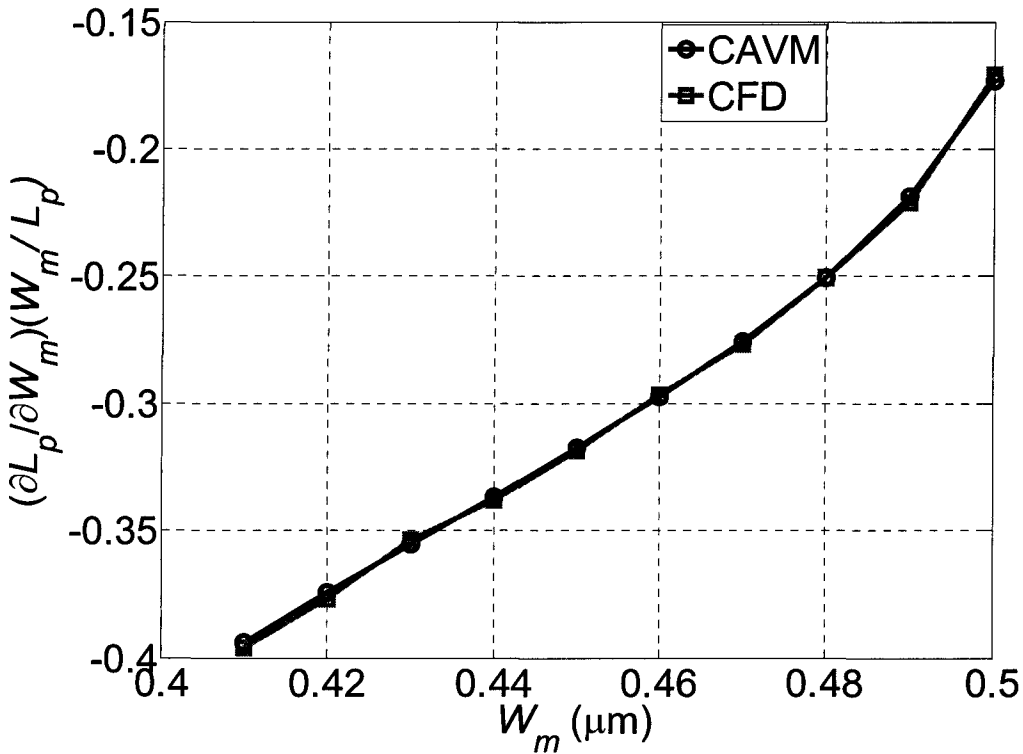


Fig. 5.30. Normalized Sensitivity of the propagation length of the fundamental mode in a metal loaded on channel waveguide structure at wavelength $\lambda=1.55\mu\text{m}$, $W_s=0.5\mu\text{m}$, $t_m=0.1\mu\text{m}$ and $t_s=0.5\mu\text{m}$.

5.4.1.2 A compact 1x3 power splitter

In this example, a compact 1x3 power splitter is designed using SPPs waveguide structure as shown in Fig. 5.32. This simple structure consists of a thin layer of metal (Au) with refractive index $n_m=0.18-j10.2$ deposited on an insulator (SiO_2) with refractive index $n_s=1.459$. The various widths of the metal sections define the region of single mode and multimode operation. The design of this structure is based on the multimode interference in the multimode waveguide by utilizing the self imaging principle [14]. The width of the metal in the multimode section W_m is taken to be $15.0\mu\text{m}$. The width of the metal in the single waveguides W_s is taken to be $3.0\mu\text{m}$ to ensure single mode operation

at 1.55 μm [37]. The thickness of the metal layer of the multimode region t_m is 0.2 μm . The thickness of the metal layer of the single mode region t_s is also 0.2 μm . The sensitivity of the coupling coefficient of the power splitter with respect to the design parameters of the structure $\mathbf{p} = [W_m \ t_m \ L_m \ t_s]^T$ is studied using our AVM technique. The coupling coefficient is defined as

$$C = \left| \int_{-\infty}^{\infty} \Phi_N \cdot \Psi \ dx \right|^2 \quad (5.61)$$

where Φ_N and Ψ are the normalized modal field of the output waveguides and the normalized field distribution at the output waveguides, respectively. The length of the multimode section L_m is calculated to be 78.2 μm . This length, which is calculated using the 3D ADI BPM, maximizes the power coupling coefficient at output waveguides. The total insertion loss at the optimal parameters is 1.5 dB. A good agreement is obtained between the sensitivity information obtained using our AVM approach and the sensitivity obtained using the time consuming CFD approach. In order to illustrate the accuracy of our approach, the normalized sensitivity of the power coupling with respect to width of the multimode region W_m is shown in Fig. 5.33. The normalized sensitivity of the power coupling sensitivity is also calculated with respect to the thickness of the metal in the multimode region t_m as shown in Fig. 5.34. As shown from this figure, the sensitivity of the coupling power approaches zero when the thickness reaches the value of 0.2 μm . Hence, the power coupling is maximum and the loss is minimized once the thickness exceeds this value. This result agrees with the result obtained in [37].

By utilizing the CFD approach, 8 additional simulations are needed to obtain the sensitivity of all the design parameters. On the other hand, our approach is utilized to obtain the sensitivity information with no additional simulation.

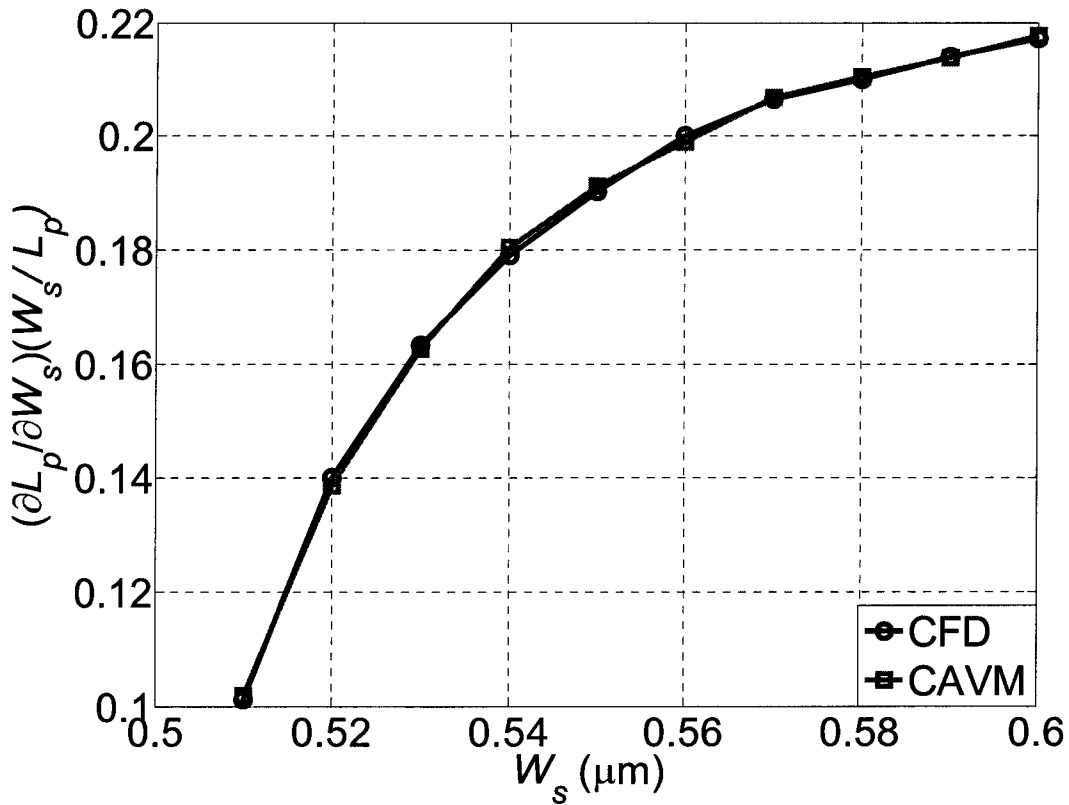


Fig. 5.31. Normalized Sensitivity of the propagation length of the fundamental mode in a metal loaded on channel waveguide structure at wavelength $\lambda=1.55\mu\text{m}$, $W_m=0.5\mu\text{m}$, $t_m=0.1\mu\text{m}$ and $t_s=0.5\mu\text{m}$.

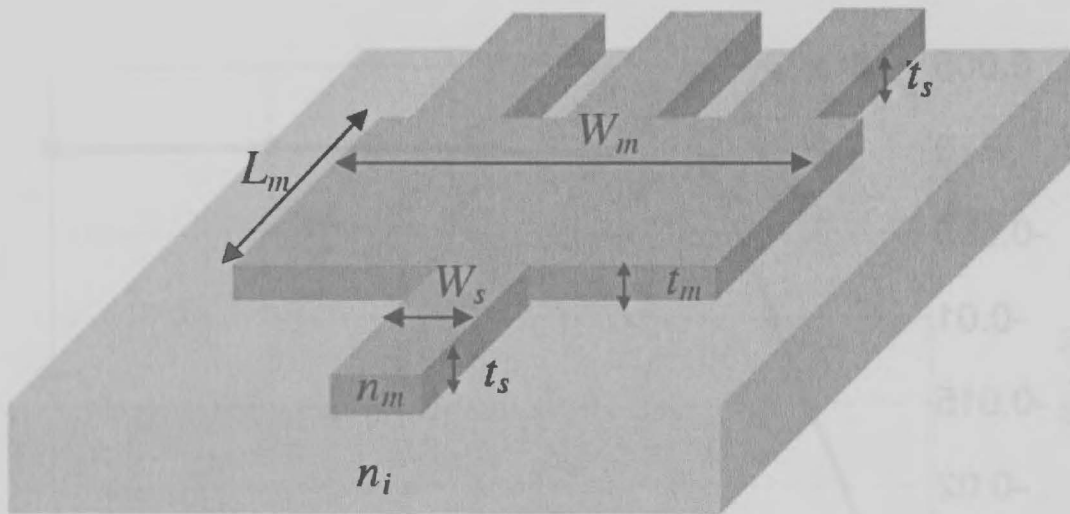


Fig. 5.32. Schematic diagram of 1x3 power splitter SPPs structure.

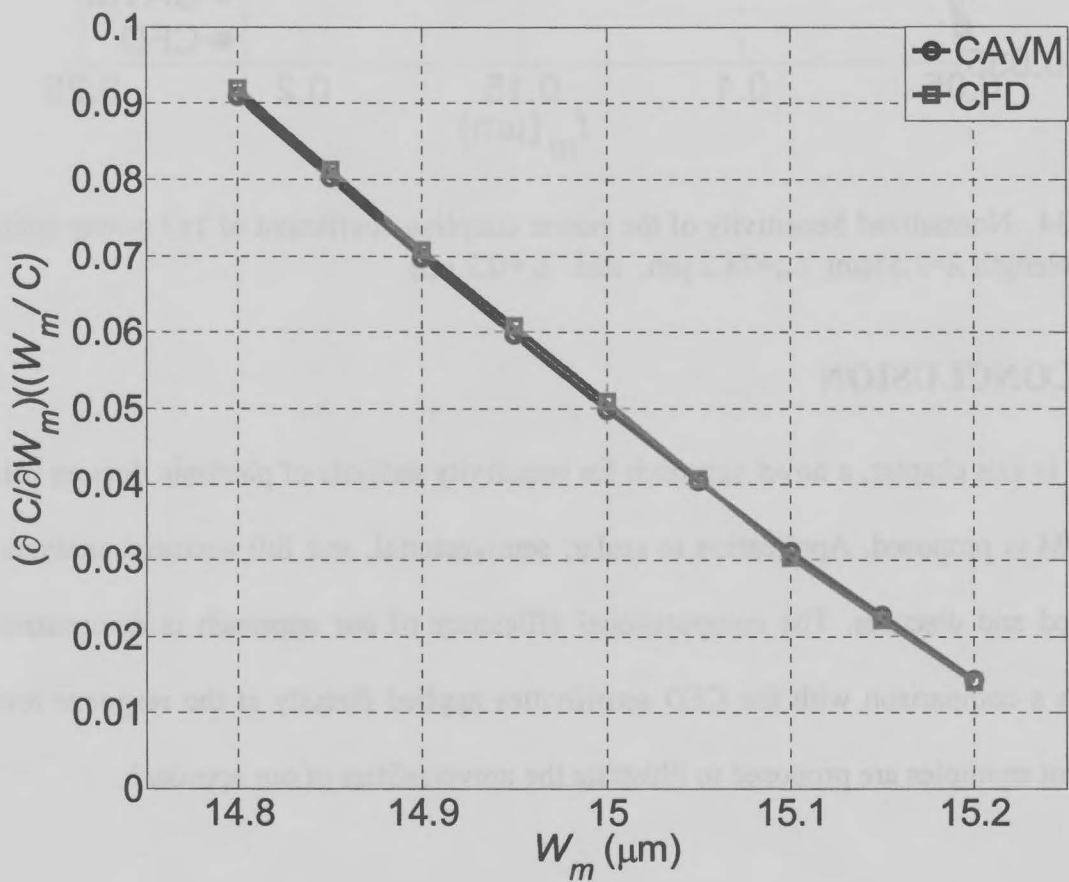


Fig. 5.33. Normalized Sensitivity of the power coupling coefficient of 1x3 power splitter at wavelength $\lambda=1.55\mu\text{m}$, $L_m=78.2\mu\text{m}$, and $t_m=t_s=0.2\mu\text{m}$

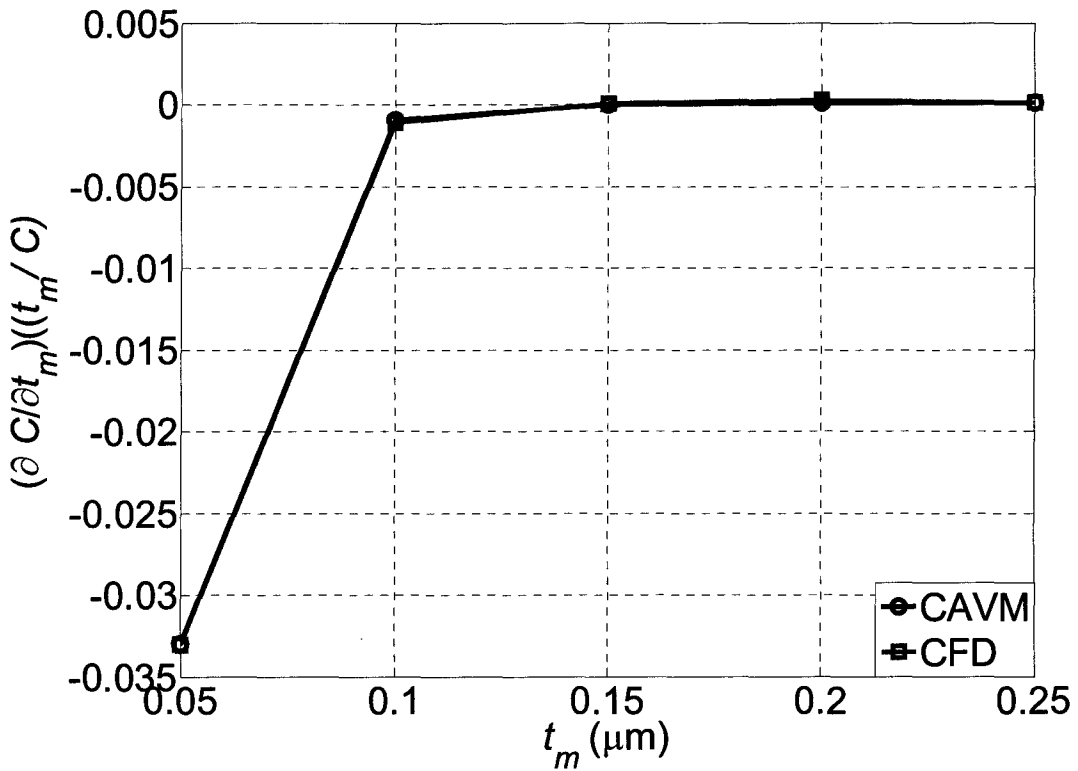


Fig. 5.34. Normalized Sensitivity of the power coupling coefficient of 1x3 power splitter at wavelength $\lambda=1.55\mu\text{m}$, $L_m=78.2\mu\text{m}$, and $t_s=0.2\mu\text{m}$

5.5 CONCLUSION

In this chapter, a novel approach for sensitivity analysis of photonic devices using the BPM is proposed. Application to scalar, semivectorial, and full vectorial analysis is proposed and discussed. The computational efficiency of our approach is demonstrated through a comparison with the CFD sensitivities applied directly at the response level. Different examples are proposed to illustrate the universalities of our approach.

5.6 REFERENCES

- [1] D. Yevick and B. Hermansson, “New formulation of the matrix beam propagation method: application to rib waveguide”, *IEEE J. Quantum Electron.*, vol 25, pp. 221–229, Feb. 1989.
- [2] W. -P. Huang, C. L. Xu, and S. K. Chaudhuri, “A finite-difference vector beam propagation method for three-dimensional structures,” *IEEE Photon. Technol. Lett.*, vol. 4, pp. 148–151, Feb. 1992.
- [3] E. Kriezis and A. G. Papagiannakis, “A three-dimensional full vectorial beam propagation method for z-dependent structures,” *IEEE J. Quantum Electron.*, vol. 33, pp. 883–890, May 1997.
- [4] P. L. Ho and Y. Y. Lu, “A bidirectional beam propagation method for periodic waveguides,” *IEEE Photon. Technol. Lett*, vol. 14, pp. 325–327, Mar. 2002.
- [5] B. Saadany, D. A. Khalil, “Modeling of MOEMS components using HDL-A,” *IEEE J. Select. Topics Quantum Electron.*, vol. 33, pp. 132–138, Jan./Feb. 2002.
- [6] K. Zinoviev, C. Dominguez, J. A Plaza, V. J. C Busto, and L. M Lechuga, “A novel optical waveguide microcantilever sensor for the detection of nanomechanical forces,” *IEEE/OSA J. Lightwave Technol.*, vol. 24 pp 2132 – 2138, May 2006.
- [7] L. D. S. Alcantara, F. L. Teixeira, A. C. Cesar, and B. V. Borges, “A new full-vectorial FD-BPM scheme: application to the analysis of magneto optic and nonlinear saturable media,” *IEEE/OSA J. Lightwave Technol.*, vol. 23, pp 2579–2585, Aug. 2005.

- [8] M. D. Feit and J. A. Fleck Jr., “Light propagation in graded-index optical fibers,” *Appl. Opt.*, vol. 17, pp. 3990–3998, Dec. 1978.
- [9] H. A. Haus, *Waves and Fields in Optoelectronics*, Englewood Cliffs, NJ: Prentice Hall, 1984.
- [10] Y. Chung and N. Dagli, “An assessment of finite difference beam propagation method,” *IEEE J. Quantum Electron.*, vol 26, pp.1335–1339, Aug. 1990.
- [11] K. Okamoto, *Fundamentals of Optical Waveguides*, Academic Press, 2000.
- [12] G. R. Hadley, “Transparent boundary condition for the beam propagation method,” *IEEE J. Quantum Electron.*, vol. 28, pp. 363–370, Jan. 1992.
- [13] D. Marcuse, *Light Transmission Optics*, Van Nostrand Reinhold Company, 1972.
- [14] L. B. Soldano, and E. C. Pennings, “Optical multi-mode interference devices based on self-imaging: principles and applications,” *IEEE/OSA J. Lightwave Technol.*, vol. 13, pp 615–627, Apr. 1995.
- [15] M. A. Swillam, M. H. Bakr, and X. Li, “Efficient adjoint sensitivity analysis exploiting the FD-BPM,” *IEEE/OSA J. Lightwave Technol.*, vol. 25 , pp. 1861 – 1869, Jul. 2007.
- [16] C. L. Xu, W. P. Huang, and S. K. Chaudhuri, “Efficient and accurate vector mode calculations by beam propagation method,” *IEEE/OSA J. Lightwave Technol.*, vol. 11, pp. 1209–1215, July 1993.
- [17] M. D. Feit and J. A. Fleck Jr., “Computation of mode properties in optical fiber waveguides by a propagation beam method,” *Appl. Opt.*, vol. 19, pp. 1154–1164, Apr. 1980.

- [18] N. N. Feng, G. R. Zhou, and W. P. Huang, “Mode calculation by beam propagation method combined with digital signal processing technique,” *IEEE J. Quantum Electron.*, vol. 39, pp. 1111–1117, Sept. 2003.
- [19] P. Chamorro-Posada, R. Gómez-Alcalá, F. J. Fraile-Peláez, “Modal analysis of optical waveguides using prony's method and BPM,” *Microwe. Opt. Tech. Letters*, vol. 7, pp. 529-532, Aug. 1994.
- [20] T. K. Sarkar and O. Pereira, “Using the matrix pencil method to estimate the parameters of a sum of complex exponentials,” *IEEE Antennas Propagat. Mag.*, vol. 37, pp. 48–55, Feb. 1995.
- [21] W. P. Huang and C. L. Xu, “Simulation of three-dimensional optical waveguides by a full-vector beam propagation method,” *IEEE J. Quantum Electron.*, vol. 29, pp. 2639–2649, Oct. 1993.
- [22] Y. Hsueh, M. Yang, and H. Chang, “Three-dimensional noniterative full-vectorial beam propagation method based on the alternating direction implicit method,” *IEEE/OSA J. Lightwave Technol.*, vol. 19, pp. 2389–2397, Nov. 1999.
- [23] *Matlab*[™], 2005. Version 7.04.
- [24] T. F. Coleman, and Y. Li, “An interior, trust region approach for nonlinear minimization subject to bounds,” *SIAM Journal on Optimization*, vol. 6, pp. 418-445, May 1996.
- [25] T. F. Coleman, and Y. Li, “On the convergence of interior-reflective Newton methods for large-scale nonlinear minimization subject to bounds,” *Math. Programm.*, vol. 67, pp. 189-224, Oct. 1994.

- [26] M. A. Swillam, M. H. Bakr, and X. Li, “Full vectorial 3D sensitivity analysis and design optimization using BPM,” *IEEE/OSA J. Lightwave Technol.* vol 26, pp 528-536, Mar. 2008.
- [27] P. A. W. Basl, M. H. Bakr and N. K. Nikolova, “Efficient estimation of sensitivities in TLM with dielectric discontinuities,” *Microwave and Wireless Compon. Lett.* vol. 15, pp 89-91 Feb. 2005.
- [28] G. Veronis, and S. Fan, “Modes of Subwavelength Plasmonic Slot Waveguides,” *IEEE/OSA J. Lightwave Technol.*, vol. 25, pp 2511-2521, Sep. 2007.
- [29] W. L. Barnes, A. Dereux and T. W. Ebbesen “Surface plasmon subwavelength optics,” *Nature.* vol. 424, pp. 824-830, Aug. 2003.
- [30] P. Berini, “Plasmon-polariton waves guided by thin lossy metal films of finite width: Bound modes of symmetric structures,” *Phys. Rev. B, Condens. Matter.* vol 61, pp 10484–10503, Apr. 2000.
- [31] I. Breukelaar, R. Charbonneau, and P. Berini, “Long-range surface plasmon-polariton mode cutoff and radiation in embedded strip waveguides,” *J. Appl. Phys.* vol 100, pp. 043104-1–043104-9, Aug. 2006.
- [32] N. N. Feng; M. L Brongersma, and L. D Negro, “Metal–Dielectric slot-waveguide structures for the propagation of surface plasmon polaritons at 1.55 μm ,” *IEEE J. Quantum Electron.* vol. 43, pp. 479 – 485, Jun. 2007.
- [33] J. Homola, S. S. Yee, G. Gauglitz, “Surface plasmon resonance sensors: review,” *Sensors and Actuators B*, vol. 54, pp. 3-15, Jan. 1999.

- [34] R. D. Harris, J.S. Wilkinson, “Waveguide surface plasmon resonance sensors,” *Sensors and Actuators B* vol. 29, pp.261-267, Oct. 1995.
- [35] J. Homola, “Present and future of surface plasmon resonance biosensors,” *Analytical and Bioanalytical Chemistry*, vol. 377, pp. 528-539, Oct. 2003.
- [36] J. Shibayama, S. Takagi, T. Yamazaki, J. Yamauchi, and H. Nakano, “Numerical analysis of waveguide-based surface Plasmon resonance sensor with adsorbed layer using two- and three-dimensional beam-propagation methods,” *IEICE TRANS. Electron.* vol. E90–C, pp. 95-100, Jan. 2007.
- [37] J. Shibayama, S. Takagi, T. Yamazaki, J. Yamauchi, and H. Nakano, “Eigenmode analysis of a light-guiding metal line loaded on a dielectric substrate using the imaginary-distance beam-propagation method,” *IEEE/OSA J. Lightwave Technol.* vol. 23, pp.1533- 1539, Mar. 2005.

6 DESIGN OPTIMIZATION OF COMPACT WIDEBAND OPTICAL SWITCH EXPLOITING STAIR CASE INDEX MMI

6.1 INTRODUCTION

Optical switching is considered one of the key functions in optical networking and communication applications. Various structures can be utilized for this purpose. However, most of these structures are suitable for working over narrow wavelength band. Designing an integrated optical switch that is capable of working over the different wavelengths of the optical communication systems without significant performance deterioration is of prime importance. The fabrication cost of optical systems can be reduced using such a switch.

Multimode interference based devices (MMI) are considered suitable candidates for this application. MMI devices are utilized in different optical processing applications. This is mainly due to their wide wavelength band, ease of fabrication and integration, and fabrication tolerance. MMI devices have been utilized as optical power splitters,

combiners, optical hybrid couplers, multiplexers and demultiplexers [1]-[10]. MMI devices have been also recently utilized as optical switches for network applications [11]-[14]. This switching application was first proposed in [11] based on the first cross image for weakly guiding MMI. The electro-optic effect is utilized to change the refractive index of the multimode (MM) region. The same application was later demonstrated and fabricated in [12]. The carrier induced charge is utilized to change the refractive index of the MM region. The same application is also reported using self guiding material [13]. However, in this technique an optical power amplifier is used to perform the switching function. Thermo-optic effect is also reportedly utilized to obtain a switching function using a heater to change the refractive index [14]. In all these devices [11]-[14], the step index waveguide is utilized to design the MMI device. The length of the device is wavelength sensitive because the position of the cross image is dependent on the wavelength as indicated by the self imaging theory [4].

Graded refractive index MMI is a possible solution to the wavelength dependency. Recently, the self imaging in a parabolic refractive index MMI (PMMI) is proposed [15]. For this device, the imaging length is wavelength insensitive. The quality of the image and hence the power coupling is also improved using this index profile. This profile can thus be used for designing an optical switch that can operate over wide wavelength band. The fabrication of a parabolic index profile, however, is not simple or compatible with the current technology of photonic devices fabrication.

In this chapter, we propose a novel optical switch design based on the PMMI. A stair case index approximation of this index profile is utilized. The fabrication of this

profile is feasible through the current technology using multiple etching. Alternatively, electro-optic effect can be applied using variable electric field. A new design methodology is proposed to ensure that the response of the stair case MMI (SCMMI) imitates the response of the PMMI. In this methodology, a two-stage optimization procedure is exploited to obtain the optimal design. Gradient-based optimizers are utilized in these two stages exploiting the wide angle BPM. The required response gradient is efficiently obtained using the adjoint variable method (AVM) [16]-[18].

6.2 PARABOLIC REFRACTIVE INDEX MMI

The self imaging phenomenon in multimode (MM) waveguides with parabolic index profile is studied in [15]. Here, we give a brief review of the theory of this phenomenon. We also explain how to make use of its advantages in designing compact optical switches. In this theory, the 2-D parabolic index case is considered. The refractive index profile is given as

$$n(x) = \begin{cases} n_{max} - \Delta n \left(\frac{x}{W/2} \right)^2 & -W/2 \leq x \leq W/2 \\ n_{cl} & otherwise \end{cases} \quad (6.1)$$

where n_{max} , and Δn are the peak value of the refractive index inside the core region and the refractive index difference between the peak value n_{max} and the cladding value n_c , respectively. In (6.1), W is the total width of the guided region. For $\Delta n \ll n_{max}$, the index profile can be rewritten after ignoring the cladding effect as follows:

$$n^2(x) = n_{max}^2 - \Delta n^2 \left(\frac{x}{x_o} \right)^2 \quad (6.2)$$

$$\text{with } x_o^2 = \frac{\Delta n W^2}{8n_{max}}$$

The index profile in (6.2) corresponds to the potential well of the harmonic oscillators [19]. The solutions of the wave equation are thus known and the propagation constant β_m of the m th mode can be approximated by [15],[19]- [20]

$$\beta_m = kn_{max} - \frac{(2m+1)\Delta n}{2n_{max}x_o} \quad (6.3)$$

where k is the wave number. Following a similar procedure to the one used for the step index MMI in [4], the imaging length can be calculated as [15]:

$$L = \frac{p\pi W}{2} \sqrt{\frac{n_{max}}{2\Delta n}} \quad (6.4)$$

which is an exact (bar) image for p even and a mirror (cross) image for p odd.

The imaging length in (6.4) shows some important characteristics of PMMI devices. First, this length is independent of the wavelength. Second, the imaging length is directly proportional to the waveguide width and not to its square as in SMMI case [4]. It follows that the device length can be much shorter than the SMMI. Third, the imaging length is the same for all the excitation's positions as β is linearly dependant on the mode order.

According to the above mentioned features of this device, we conclude that the position of the cross output is insensitive to the wavelength. This device can thus be used as an optical switch or as a modulator over a wideband of wavelengths. This device has also a compact size compared with the SMMI. The main difficulty is in the practical realization of such a profile. This profile does not lend itself to the available fabrication

technologies. To overcome this, we propose a stair case approximation of such a profile in order to achieve a comparable response with more feasible fabrication processes.

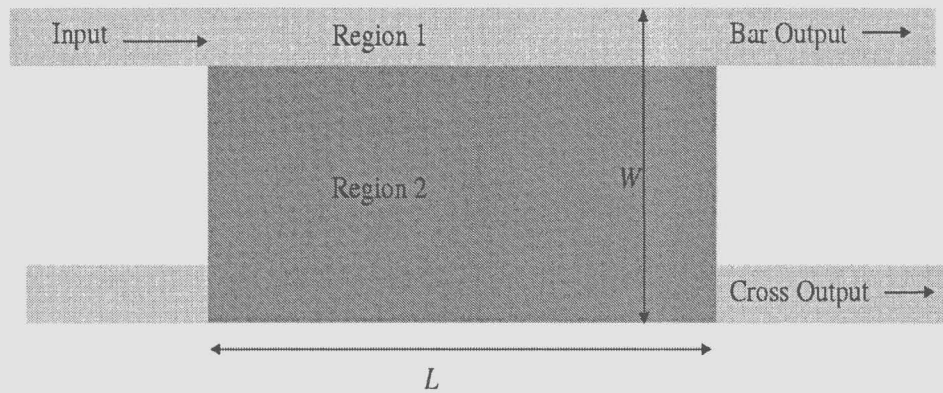


Fig. 6.1. Schematic diagram of the MMI as an optical modulator.

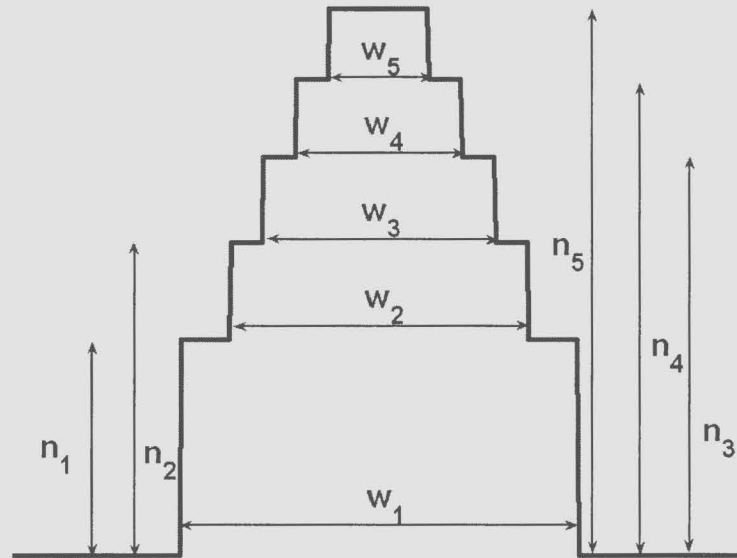


Fig. 6.2. Schematic diagram of the stair case index profile for cross output case.

6.3 STAIR CASE REFRACTIVE INDEX MMI (SCMMI) AS AN OPTICAL SWITCH

The switching function can be obtained using SMMI devices by controlling the value of the refractive index of Region 2 in Fig. 6.1. Thus the device is mainly designed to have a maximum power at the cross output waveguide if the indexes of Regions 1 and 2 match. On the other hand, if the refractive index of Region 2 is less than the refractive index of Region 1 the optical power will be maximum at the bar output waveguide.

The proposed SCMMI can be used as an optical switch using similar approach to the one used for SMMI. The main difference is the utilization of the parabolic index (or an approximation to it) in the multimode region for the cross state output as shown in Fig. 6.2. The device becomes less sensitive to the wavelength and more compact in size as explained in Section 6.2. The same switching mechanism used for the SMMI switches can be utilized as well for this device.

The stair case index (SCI) profile is used mainly to mimic the response of the parabolic index profile in the case of the cross state as shown in Fig. 6.2. For the bar state, the SCI profile gives the ability to easily define the single mode waveguide region which is compatible with single mode output waveguide as shown in Fig. 6.3. This region can be defined by having the refractive index n_s less than n_1 . To maximize the power coupling to the output waveguide in the case of bar state n_s should be as close as possible to n_{cl} . The stair case index is more superior to the parabolic index for its compatibility with the output waveguide. It can be easily integrated with other devices which usually have step index profile.

In order to mimic the response of the PMMI using stair case index profile, we formulate the design problem as an optimization problem. The design parameters of this problem are the refractive indices and the widths of the stairs as shown in Fig. 6.2. Thus the vector of design parameters \mathbf{p} is given as,

$$\mathbf{p} = [w_1 \ w_2 \ w_3 \ w_4 \ w_5 \ n_1 \ n_2 \ n_3 \ n_4 \ n_5]^T, \quad (6.5)$$

where the number of stairs is chosen to be 5. This is considered as a reasonable choice to minimize the number of design parameters but yet maintain a good approximation for the parabolic profile. The maximum index change Δn is determined by designer beforehand (See Fig. 6.2). In order to efficiently calculate the optimal design \mathbf{p}^* , gradient based optimization is utilized in conjunction with 2D BPM. The adjoint variable method (AVM) is utilized in estimating the response gradient. This method provides an efficient approach to extract the gradients without any additional simulations.

6.4 DESIGN OPTIMIZATION OF THE SCMMI

In this section, we propose a new methodology to obtain the optimal design of SCMMI which satisfies the required specifications of the switch. Our main goal in this design is to maintain the main features of the PMMI. This can be done by obtaining the optimal design parameters for which the response of the SCMMI is insensitive, or having a weak sensitivity, to the wavelength variation of the incident field. We need also to ensure that the optimal structure is compact in size and has a comparable length to the PMMI that is shorter than the SMMI.

In order to achieve these requirements, we propose to solve our design problem

using a two-stage optimization process. The first stage involves solving an optimization problem to maximize the power coupling to the output waveguide η for the cross state. The maximization of the coupling coefficient is mainly performed at the center wavelength of the desired bandwidth λ_c . The design equation (6.4) of the PMMI is utilized to obtain an initial design of the device. This can be done by choosing a starting width of the PMMI W_p and determining the maximum index change Δn . Now, these parameters can be utilized to calculate the length of the MM section L of the PMMI using (6.4). This length is utilized as the length of SCMMI device. At this length we aim at maximizing the power transfer to the cross output waveguide over the working band of wavelengths. The wavelength band of interest is then determined and the center wavelength λ_c of this band is utilized in the first optimization stage. Accordingly, the optimization problem of this stage is given by:

$$\begin{aligned}
 & \max_p \quad \eta(\lambda_c) \\
 & \text{subject to} \quad n_{cl} \leq n_1 \leq n_2 \leq n_3 \leq n_4 \leq n_5 \leq \Delta n \\
 & \quad \quad \quad 0 \leq w_5 \leq w_4 \leq w_3 \leq w_2 \leq w_1 \leq W_p
 \end{aligned} \tag{6.6}$$

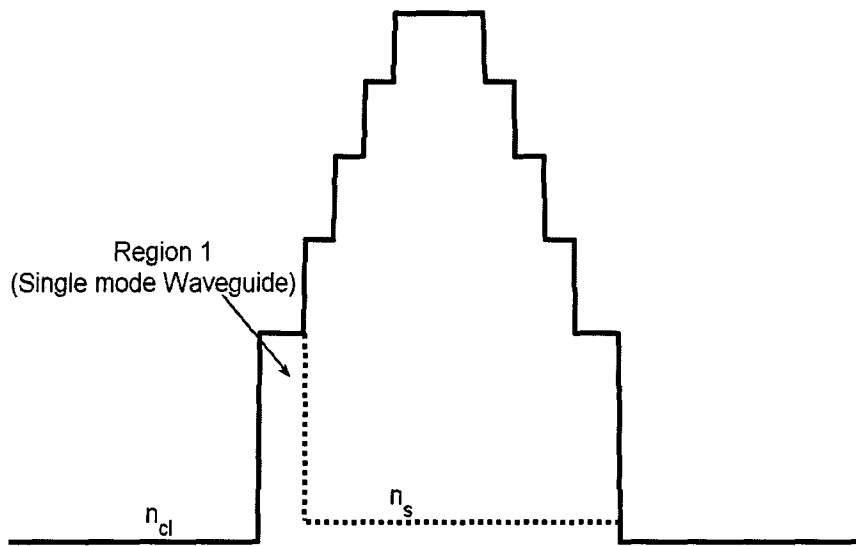


Fig. 6.3. Schematic diagram of the stair case index profile for bar output case.

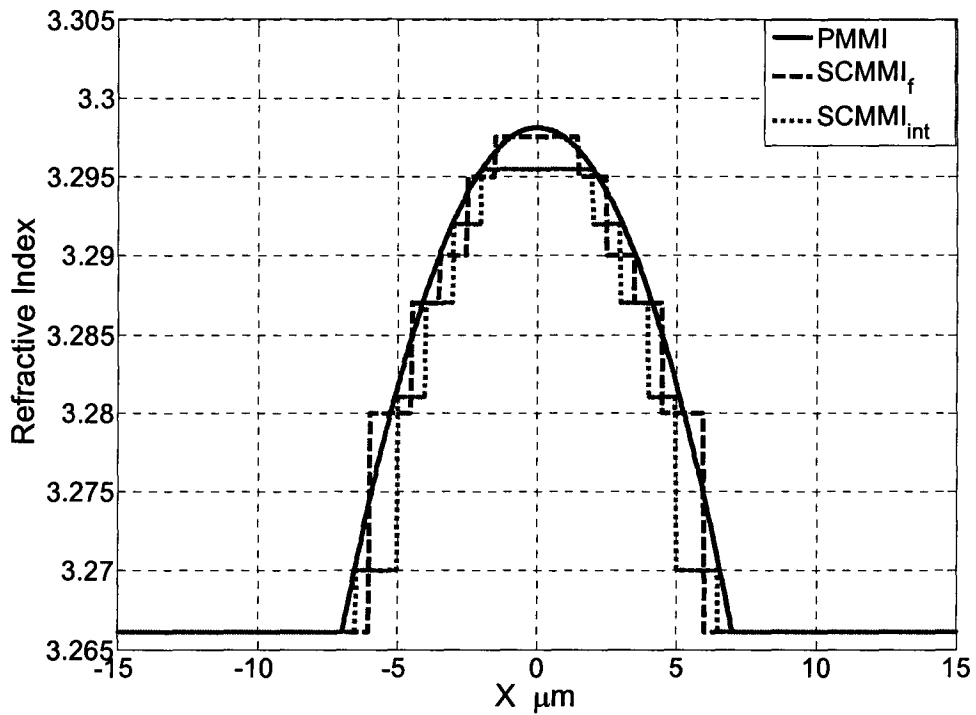
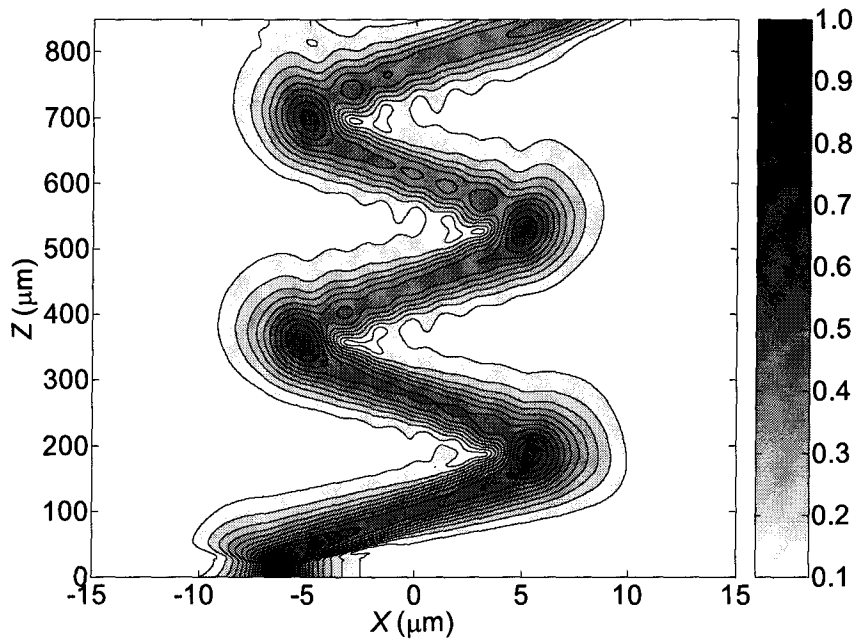
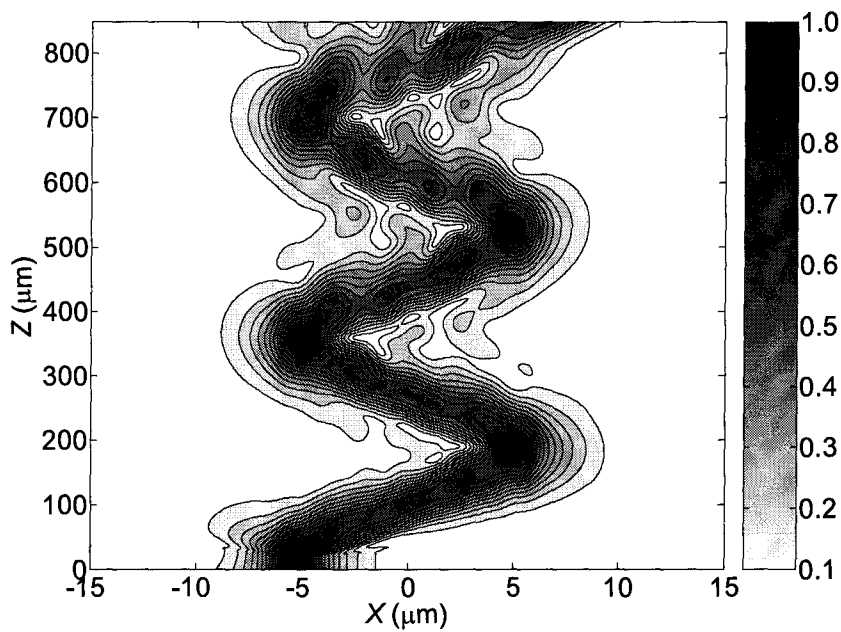


Fig. 6.4. The refractive index of the SCI-MMI and PMMI.



(a)



(b)

Fig. 6.5. The field intensity of the a) PMMI and b) SCI-MMI.

The optimal parameters obtained in (6.6) are utilized as the initial design of the second stage. The optimal value of the coupling coefficient $\eta_1(\lambda_c)$ obtained from (6.6) is also utilized in the second stage. The second stage ensures that the response obtained at the center wavelength λ_c in the first stage can be attained over the whole working wavelength band. This can be done by minimizing the deviations of the coupling coefficient at different wavelength from its value at the center wavelength. Thus the optimization problem can be written as follow

$$\begin{aligned} \min_p \quad & \max_{\lambda \in B} |\eta(\lambda) - \eta_1(\lambda_c)| \\ \text{subject to} \quad & n_{cl} \leq n_1 \leq n_2 \leq n_3 \leq n_4 \leq n_5 \leq \Delta n \\ & 0 \leq w_5 \leq w_4 \leq w_3 \leq w_2 \leq w_1 \leq W_p \end{aligned} \quad (6.7)$$

where B is the set of the wavelengths of interest.

6.5 DESIGN EXAMPLES

In this section, the design methodology given in previous sections is utilized for obtaining a complete design of an optical switch with wide operating bandwidth. Different designs are introduced as examples for our procedure. In these examples the TE case is mainly considered. However, the application for TM case is straight forward. For all the proposed examples, the modal field profile of the access input waveguide is calculated first at the specific wavelength. It is then utilized as the excitation of the MM waveguide section. In addition, the modal field profile at the output waveguide is calculated and utilized in calculating the coupling coefficient and the crosstalk.

6.5.1 Compact Design

To illustrate this procedure, a PMMI is first designed with width W_p taken to be $14.0 \mu\text{m}$, and a maximum refractive index of $n_{max} = 3.2981$, and $\Delta n = 0.032$. The index profile of the MM section of PMMI is shown in Fig. 6.4. The desired wavelength band is chosen to be $[1.2 \mu\text{m} : 1.8 \mu\text{m}]$. The center wavelength λ_c is thus equal to $1.5 \mu\text{m}$.

By using the design equation in (6.4), the imaging length is calculated to be $157.86 \mu\text{m}$ at the center wavelength. The width of the single mode waveguide at the input and output ports is taken to be $1.5 \mu\text{m}$ with a core refractive index of 3.28.

The length of the MM section is also calculated using wide angle BPM with (1,1) Padé approximate operator [21]. This length is calculated by sweeping of the power coupling coefficient between the propagated field and the modal field of the cross output waveguide over propagation distance. The length of the MM section is calculated using this simulation to be $161.0 \mu\text{m}$ with a relative deviation of 0.02 from the theoretical results. The maximum value of the coupling coefficient is calculated to be 0.89.

The first stage optimization problem is then utilized to maximize the power coupling coefficient at $\lambda_c = 1.5 \mu\text{m}$. The initial refractive indices are chosen to have the same refractive indices values as the parabolic profile at specific widths as shown in Fig. 4. The initial set of parameters is given by $p = [13.0 \mu\text{m} \ 10.0 \mu\text{m} \ 8.0 \mu\text{m} \ 6.0 \mu\text{m} \ 4.0 \mu\text{m} \ 3.27 \ 3.281 \ 3.287 \ 3.292 \ 3.2955]^T$.

The power coupling obtained at $L = 161.0 \mu\text{m}$ using the initial parameters is calculated to be 0.65. The optimization problem is then solved using the gradient information obtained using the AVM method applied to the wide angle (1,1) BPM. The

large scale constrained optimization package of Matlab [22] is utilized to solve this problem. At each optimization iteration, the optimization algorithm utilizes both the response value and its AVM sensitivities. This optimization algorithm exploits a subspace trust region method that is based on the interior-reflective Newton method described in [23],[24]. At each iteration, the approximate solution of the large linear system is calculated using the method of preconditioned conjugate gradients (PCG)[22]. The maximum power coupling obtained after this stage is 0.971 and the optimal parameters obtained are given by $p_1=[12.0 \mu\text{m } 9.0 \mu\text{m } 7.0 \mu\text{m } 5.0 \mu\text{m } 2.5 \mu\text{m } 3.28 \ 3.287 \ 3.29 \ 3.295 \ 3.298]^T$.

The optimal parameters obtained from this stage are then utilized as initial parameters for the second stage. The second stage is mainly used to ensure that the response of the SCMMI is similar to the response of the PMMI over the required bandwidth. Sequential quadratic programming (SQP) included in the minimax optimization toolbox in Matlab [22] is utilized to solve the optimization problem at the second stage. The AVM is also utilized to extract the sensitivity of the response using BPM simulation. The optimal parameters obtained are given by $p^*=[12.0 \mu\text{m } 9.0 \mu\text{m } 7.0 \mu\text{m } 5.0 \mu\text{m } 3.0 \mu\text{m } 3.28 \ 3.287 \ 3.29 \ 3.295 \ 3.2975]^T$.

The final stair case index profile which is used to imitate the performance of the PMMI is shown in Fig. 6.4. The maximum width of the SCMMI is $12.0 \mu\text{m}$ and the minimum is $3.0 \mu\text{m}$. In order to assure that the obtained SCMMI and PMMI have similar self imaging phenomenon, the field intensity distribution is calculated over a sweep of propagation distance. The calculated field intensity of SCMMI and PMMI has similar self

imaging behavior as shown in Fig. 6.5. The power coupling coefficient at the cross arm is shown in Fig. 6.6. It is clear from this figure that the SCMMI has a similar response of the cross state as those obtained using PMMI. Moreover, the SCMMI has a better power coupling at the output arm. The dependence of the coupling coefficient on the wavelength is studied for the SCMMI, PMMI, and the conventional SMMI with a width of $12.0\ \mu\text{m}$ and a length of $1807.0\ \mu\text{m}$ which is the optimal length at the central wavelength as shown in Fig. 6. It is clear from this figure that the power coupling is almost constant for both SCMMI and PMMI. However, for SMMI the bandwidth is limited. Moreover, the SCMMI is more than 11 times shorter than the conventional SMMI. The cross talk is also calculated to be -39.2dB at the center wavelength for the cross state. The cross talk for the bar state is calculated to be $-39.4\ \text{dB}$ at the center wavelength.

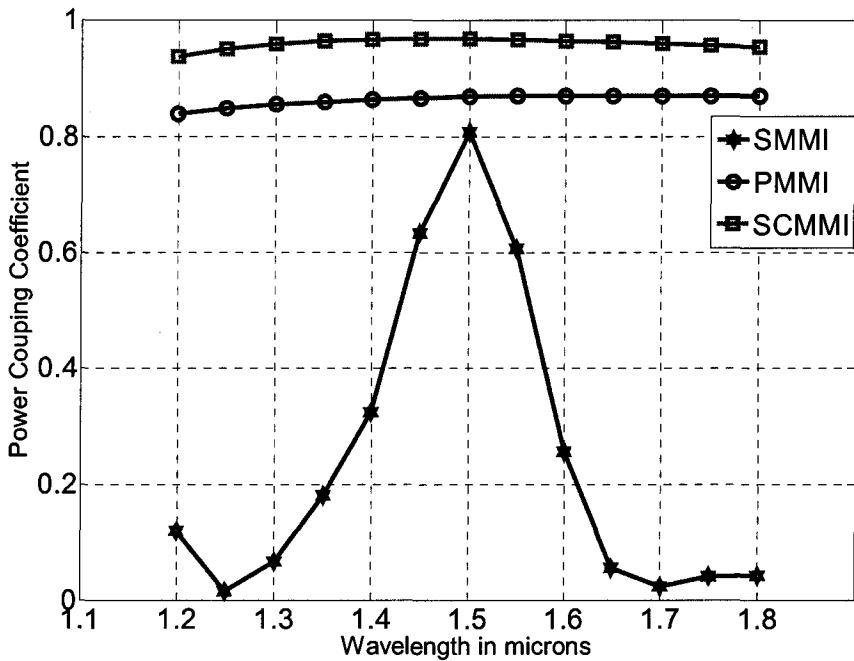


Fig. 6.6. The power coupling versus the wavelength for the cross state for the compact design example.

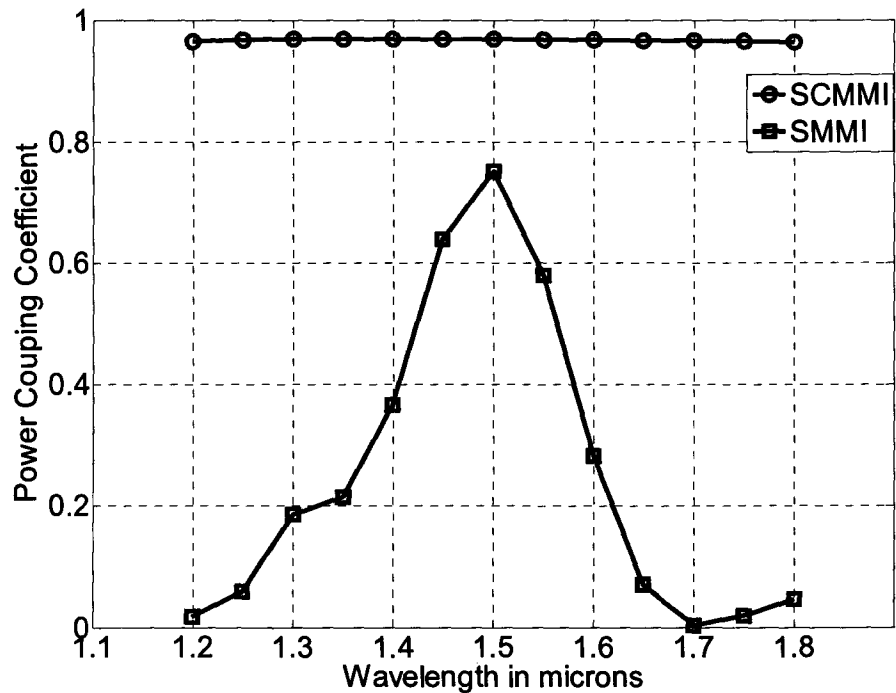


Fig. 6.7. The power coupling versus the wavelength for the cross state for the weak guiding example.

6.5.2 A Weak Guiding Design

Electro-optic effect that may be utilized to change the value of the refractive index produces small index change especially for semiconductor materials [11]. Thus to ensure that our design can be implemented, a weak guiding structure is utilized.

Following a similar procedure to the one described in the previous example, we design an SCMMI with $W_p = 24.0 \mu\text{m}$ and $\Delta n = 0.0052$. The cladding refractive index is taken to be 3.25. The operating bandwidth is taken to be $[1.2 \mu\text{m} : 1.8 \mu\text{m}]$. The length of the multimode section is calculated to be $685.0 \mu\text{m}$. The optimal design parameters are $p^* = [20.0 \mu\text{m} \ 15.0 \mu\text{m} \ 12.0 \mu\text{m} \ 8.0 \mu\text{m} \ 5.0 \mu\text{m} \ 3.2525 \ 3.2533 \ 3.254 \ 3.2545 \ 3.255]^T$.

The power coupling over the working bandwidth for the cross state is shown in

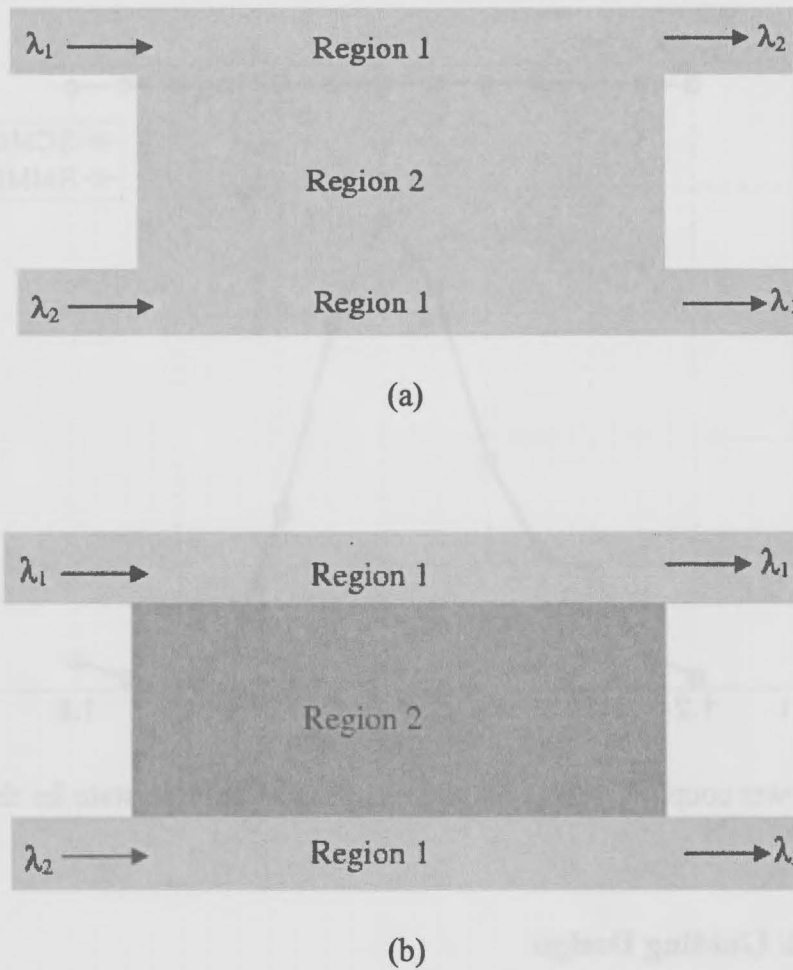


Fig. 6.8. The schematic diagram of the OXC using SCMMI; a) the indexes of regions 1 and 2 match and b) the index of Region 2 is less than that of Region 1.

Fig. 6.7. The power coupling of the SMMI with core index of 3.255 is also calculated and shown in Fig. 6.7. However, the length of the multimode section of the SMMI is calculated to be 4730.0 μm which is much longer than the optimized device. The cross talk of the optimized device is -23.2 dB at the center wavelength for the cross state. The cross talk for the bar state is calculated to be -23.14 dB at the center wavelength.

All the calculations and the design optimization process utilize a wide angle BPM with (1,1) Padé approximate operator. The increase in the power coupling is mainly due

to the enhancement of the quality of the image. This is mainly due to the grading effect which has been proved to enhance the image quality [25]-[27]. The BPM simulations show that the proposed structure has negligible polarization dependence which is considered an extra advantage for our design.

The proposed device can also be used as an optical cross connect (OXC) for routing any two different wavelengths within its band of operation as shown in Fig. 6.8. The two wavelengths are routed by changing the refractive index of Region 2.

6.5.3 3D Design Using Strip Loaded Waveguide with Variable Heights

In this example, a strip loaded waveguide configuration is utilized. The height of the strip can be utilized to change the effective index underneath the strip. By using a MM waveguide with multiple strips with different heights, a stair case index is achieved as shown in Fig. 6.9. Electro-optic effect can be utilized to perform the switching function. A three dimensional structure operating over wide range of frequencies can be constructed using this design. For this example, the range of frequencies is chosen to be $[1.3 \mu\text{m} : 1.6 \mu\text{m}]$ with center frequency $\lambda_c = 1.45 \mu\text{m}$. The electro-optic effect of the GaAs is exploited to perform the switching function. Using this effect, a maximum index change $\Delta n = -n_o^3 r_{41} E / 2$ is obtained, where r_{41} is the electro-optic coefficient of the GaAs tensor, n_o is refractive index before applying the electric field, and E is the electric field across the junction.

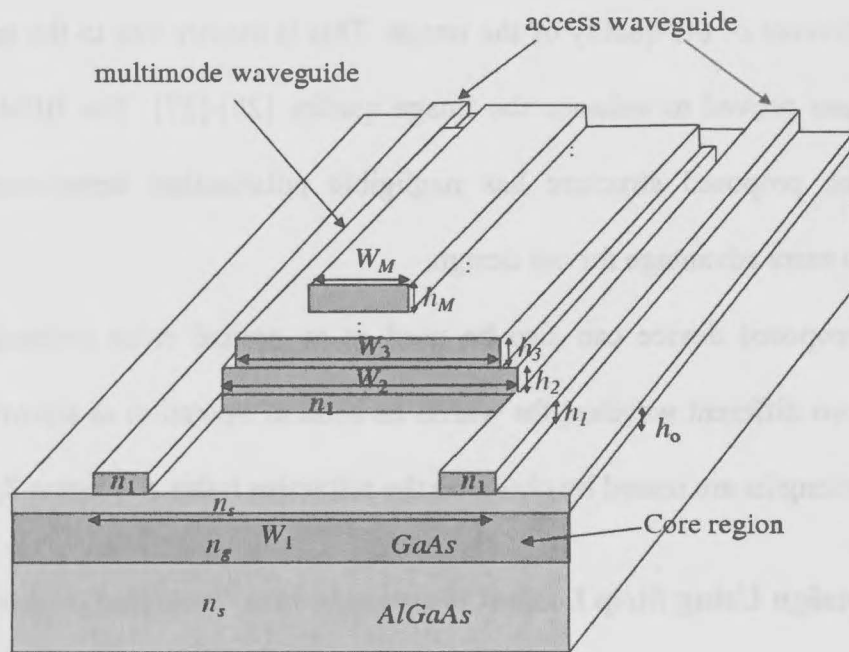


Fig. 6.9. Schematic diagram of the optical switch with variable height of strip loads.

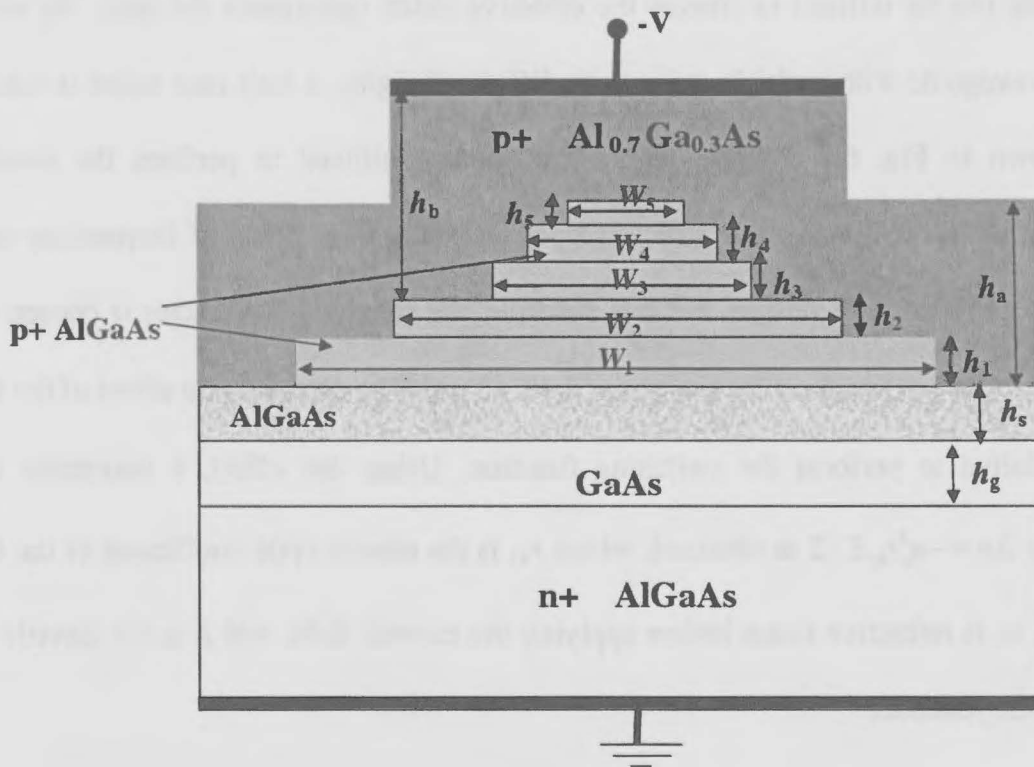


Fig. 6.10. The cross section of the proposed 3D optical switch with variable height strip load waveguide.

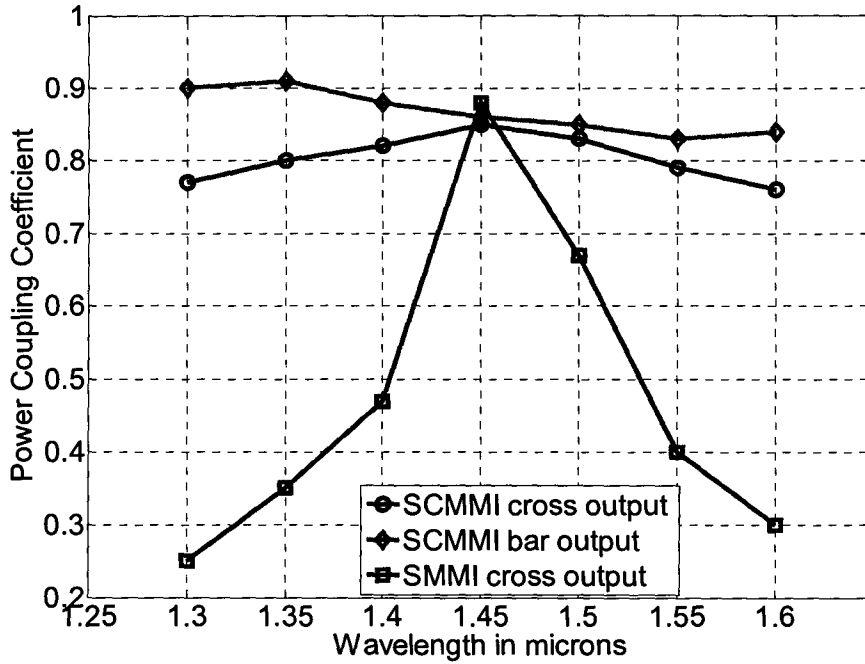


Fig. 6.11. The power coupling versus the wavelength at the output waveguide for the 3D design example using 2D BPM and the effective index method.

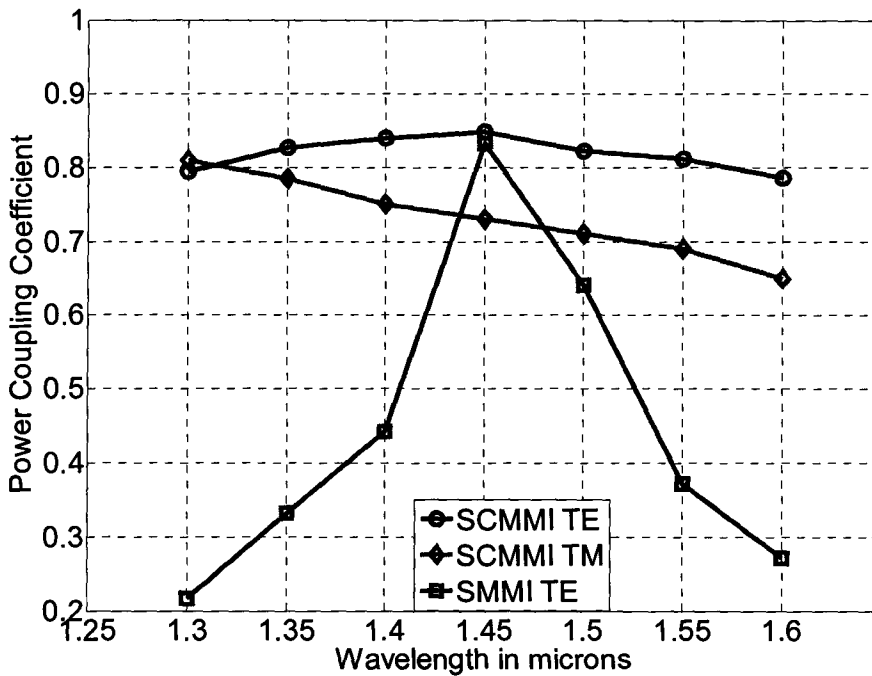


Fig 6.12. The power coupling at the cross arm versus the wavelength at the output waveguide for the 3D design example using 3D full vectorial simulation.

The maximum refractive index change Δn is calculated to be 10^{-4} at λ_c for an electric field of 3.5×10^5 V/cm which is less than the breakdown field of GaAs (4×10^5 V/cm).

The approach given in Section 6.4 is utilized to obtain the optimal effective indexes for SCMMI with $w_1=20.0 \mu\text{m}$. The effective index method is exploited to obtain the corresponding 3D structure as shown in Fig. 6.10. The heights of the strips are calculated to have the same optimal effective index values at λ_c using the effective index method. The optimal geometrical design parameters of this structure are given in Table 6.1. The obtained 3D SCMMI structure is then simulated using 2D BPM after reducing the problem to 2D using the effective index method. In this simulation, the power coupling at the cross arm waveguide is calculated over the desired bandwidth taking into account the material dispersion and the dependence of the refractive index on the wavelength [28]. The results are shown in Fig. 6.11. It is clear that there is a 5-10% decrease in the power coupling to the output waveguide at the cross state due to the material dispersion. The coupling coefficient at the cross state of the SMMI with the width of $20.0 \mu\text{m}$ and $\Delta n = 10^{-4}$ is also shown in Fig. 6.11. It is clear that our proposed structure has a wider bandwidth than the conventional SMMI. In addition, the length of the SMMI is calculated to be 3.1 times longer than the length of the SCMMI.

The reverse biased p-i-n structure shown in Fig. 6.10 is utilized to perform the electro- optic effect over the desired region. The voltage required to obtain the required index change is 21.5 V. The coupling power to the bar output waveguide is calculated over the desired bandwidth. It is shown in Fig. 6.10 in the case of the applied voltage.

In order to verify the obtained results, a 3D full vectorial BPM simulation of the structure is carried out [25]. The coupling power over the desired bandwidth is calculated for the cross state output for both the quasi TE and the quasi TM cases as shown in Fig 6.12. It is clear from this figure that the quasi TM case has a wide bandwidth with less coupling coefficient due to the weak polarization dependence of the proposed structure.

The main advantage of the proposed structure is its simplicity and ease of fabrication. It can be fabricated by growing the intrinsic GaAs core layer over the AlGaAs substrate and then the intrinsic AlGaAs layer can be grown above the core layer. Afterwards, the doped AlGaAs strip layers can be grown. Successive etching with different depths can be utilized to define the stair case profile of the strips. The $\text{Al}_{0.7}\text{Ga}_{0.3}\text{As}$ layer can be then grown and the metal electrodes are defined.

6.6 DISCUSSION

The stair case index profile can be obtained using the current technology through different approaches. In addition to the proposed design in Section 6.5.3 some other possible approaches are discussed in this section. The fabrication details and the experimental results of these approaches will be addressed elsewhere.

6.6.1 Variable Applied Electric Field

In this approach, the reconfigurable electro-optic waveguide method is utilized to achieve the SCI profile [29]. This profile can be obtained by using multiple electrodes with different applied electric field on each one. Using a reverse biased p-i-n $\text{InP}/\text{In}_{0.61}\text{Ga}_{0.39}\text{As}_{0.84}\text{P}_{0.16}/\text{InP}$ structure a stair case index profile is obtained with

maximum index change of 0.011 [29]. This device is mainly utilized for optical signal processing. However, the same structure can be used in our application. Modulating the electric field of Region 2 can be used for the switching function.

6.6.2 Variable Doped Semiconductors

In this approach, the doping concentration of the semiconductor material is used to produce a permanent refractive index change over wide range of wavelengths [30]. Varying the doping will produce a variation in the refractive index. Thus by fabricating an MM waveguide with different doping regions, an SCMMI can be created. An external effect is then utilized to obtain the switching function by altering the refractive index of Region 2.

Table 6.1.
The geometrical design parameter of Example 6.5.3.

| Parameter | Value | Parameter | Value |
|-----------|--------------------|-----------|--------------------|
| h_g | 0.6 μm | h_s | 0.01 μm |
| h_a | 1.0 μm | h_b | 1.9 μm |
| h_1 | 0.05 μm | h_2 | 0.05 μm |
| h_3 | 0.04 μm | h_4 | 0.04 μm |
| h_5 | 0.05 μm | w_1 | 20 μm |
| w_2 | 12.0 μm | w_3 | 8.0 μm |
| w_4 | 6.0 μm | w_5 | 4.0 μm |

6.7 CONCLUSION

In this chapter, we proposed a new methodology to design an optical switch using stair case MMI. This device has a good performance over a wide wavelength band and

can be used for optical network/communications. An AVM is utilized to extract the gradient of the response efficiently. This gradient is utilized in gradient-based optimizers to obtain the optimal design of this device. This device is compact and has a low cross talk. It can be fabricated using different technologies.

6.8 REFERENCES

- [1] K. C. Lin and W. Y. Lee, "Guided-wave 1.30/1.55 μm wavelength division multiplexer based on multimode interference," *Electron. Lett.* vol. 32, pp. 1259-1261, Jul. 1996.
- [2] B. Li, G. Li, E. Liu, Z. Jiang, J. Qin, and X. Wang, "Low-loss 1x2 multimode interference wavelength demultiplexer in silicon-germanium alloy," *IEEE Photon. Technol. Lett.* vol. 11, pp. 575-577, May. 1999.
- [3] S. L. Tsao, H. C. Guo, and C. W. Tsai, "A novel 1x2 single-mode 1300/1550nm wavelength division multiplexer with output facet-tilted MMI waveguide," *Opt. Comm.* vol. 232, 371-379 Mar. 2004.
- [4] L. B. Soldano and E. C. M. Pennings, "Optical multimode interference devices based on self-imaging: principles and applications," *IEEE/OSA J. Lightwave Technol.* vol. 3, pp. 615-627, Apr. 1995.
- [5] J. Xiao, X. Liu, and X. Sun, "Design of an ultracompact MMI wavelength demultiplexer in slot waveguide structures," *Opt. Express*, vol. 15, pp. 8300-8308, Jun. 2007.
- [6] M. H. Ibrahim, S. Lee, M. Chin, N. M. Kassim, and A. B. Mohammad, "Multimode interference wavelength multi /demultiplexer for 1310 and 1550 nm operation based

- on BCB 4024-40 photo definable polymer,” *Opt. Comm.*, vol. 273, pp. 383–388, May 2007.
- [7] A. Ferreras, F. Rodriguez, E. Gomez-Salas, J. L. de Miguel and F. Hernandez-Gil, “Useful formulas for multimode interference power splitter/combiner design,” *IEEE Photon. Technol. Lett.*, vol. 5, no. 10, pp. 1224-1227, Oct. 1993.
- [8] M. Bouda, J. W. M. van Uffelen, C. van Dam and B. H. Verbeek, “Compact 1x16 power splitter based on 1x2 MMI splitters,” *Electron. Lett.*, vol. 30, pp. 1756-1758, Oct.1994.
- [9] R. M. Jenkins, R. W. J. Devereux, and J.M. Heaton, “Waveguide beam splitters and combiners based on multimode propagation phenomen,” *Opt. Lett.*, vol. 17, pp. 991-993, Jul. 1992
- [10] S. El-sabban, I. Schanen, D. Khalil and P. Benech, “Fabrication and test of an integrated optical magic Ton a glass substrate,” *IEEE Photon. Technol. Lett.*, vol. 13, pp. 684-686, Jul. 2001.
- [11] H. El-Refaei and D. Khalil,“ Design of strip loaded weak guiding multimode interference structure for an optical route,” *IEEE J. of Quantum Electron.*, vol. 34, pp. 2286-2290, Dec. 1998.
- [12] S. Nagai, G. Morishima, H. Inayoshi, and K. Utaka, “Multimode Interference Photonic Switches (MIPS),” *IEEE/OSA J. Lightwave Technol.*, vol. 20, pp. 675-680, Apr. 2002.
- [13] J. S. Rodgers, S. E. Ralph, and R. P. Kenan, “Self-guiding multimode interference threshold switch,” *Opt. Lett.*, vol. 25, pp 1717-1719. Dec.2000,

- [14] F. Wang, J. Yang, L. Chen, X. Jiang, and M. Wang, “Optical switch based on multimode interference coupler,” *IEEE Photon Technol. Lett.*, vol. 18 , Jan. 2006, pp. 421-423.
- [15] M. A. Swillam, A. Yehia, A. H. Morshed, and D. Khalil, “Self-Imaging in graded index multimode interference devices,” *Mediterranean Microwave Symposium (MMS’2003)*, Cairo, pp. 61-64, May 2003.
- [16] M. A. Swillam, M. H. Bakr, and X. Li, “Efficient adjoint sensitivity analysis exploiting the FD-BPM,” *IEEE/OSA J. Lightwave Technol.*, vol. 25 , pp. 1861-1869, Jul. 2007.
- [17] M. A. Swillam, M. H. Bakr, and X. Li, “BPM based efficient sensitivity analysis exploiting the adjoint variable method,” *Integrated Photonics and Nanophotonics Research and Applications (IPNRA)*, Salt Lake City, Utah, paper IWB4, Jul. 2007.
- [18] M. A. Swillam, M. H. Bakr, and X. Li, “Full vectorial 3D sensitivity analysis and design optimization using BPM,” *IEEE/OSA J. Lightwave Technol.*, Mar. 2008.
- [19] R. L. White, *Basic Quantum Mechanics*, McGraw Hill, 1966, Ch.5.
- [20] D. L. Lee, *Electromagnetic Principles of Integrated Optics*, John Wiley, 1986, Ch.5.R
- [21] G. R. Hadley, “Wide-angle beam propagation using Padé approximate operators,” *Opt. Lett.*, vol. 17, no. 10, pp. 1743-1775, Oct. 1992.
- [22] Matlab™, 2005. Version 7.04.

- [23] T. F. Coleman, and Y. Li, “An interior, trust region approach for nonlinear minimization subject to bounds,” *SIAM J. Optimization*, vol. 6, pp. 418-445, May 1996.
- [24] T. F. Coleman, and Y. Li, “On the convergence of interior-reflective Newton methods for large-scale nonlinear minimization subject to bounds,” *Math. Programm.*, vol. 67, pp. 189-224, Oct. 1994.
- [25] Y. B. lin, J. Liu, and W. Wang, “Analysis of Multimode Interference Couplers With Lateral Graded-Index Profiles,” *CLEO/Pacific Rim*, vol. 2, pp. 244 –245, 2001.
- [26] M. A. Swillam, A. H. Morshed, and D. Khalil “Optimization of Optical Wide Band 3-dB MMI Splitter with Graded-Index Side Diffusions,” *IEEE International Conf. on Electrical, Electronic and Computer Engineering ICEEC’04*, no. 173, pp. 633 – 636, Sept. 2004.
- [27] R. Yin, X. Jiang, J. Yang, and M. Wang, “Structure with improved self-imaging in its graded-index multimode interference region,” *J. Opt. Soc. Am. B*, vol. 19, pp. 1301-1303 , Jun. 2002.
- [28] S. Gehrsitz, F. K. Reinhart, C. Gourgon, N. Herres, A. Vonlanthen and H. Sigg, “The refractive index of $\text{Al}_x\text{Ga}_{1-x}\text{As}$ below the band gap: Accurate determination and empirical modeling,” *J. of Appl. Phys.* vol. 87, pp. 7825-7837, Jun. 2000.
- [29] D. Dragoman and M. Dragoman, “Reconfigurable electro optical waveguide for optical processing,” *Appl. Opt.*, vol. 42, pp. 6439-6444, Nov. 2003.

- [30] B. Bennett, R. Soref, and J. Alamo, "Carrier-induced change in refractive index of InP, GaAs, and InGaAsP," *IEEE J. Quantum Electron.*, vol. QE-26, pp. 113–122, Jan. 1987.

7 SENSITIVITY ANALYSIS OF QUANTUM STRUCTURES USING SCHRÖDINGER EQUATION

7.1 INTRODUCTION

Semiconductor quantum structures have recently attracted great attention due to their unique physical properties and wide range of applications in micro- and optoelectronics [1]-[3]. These structures are utilized for many optical application such as quantum well and quantum dot lasers, semiconductor amplifier, and electro-absorption modulator. Accurate modeling and sensitivity analysis of these structures are thus of prime importance. Sensitivity information is very useful in yield and tolerance analyses. It is also essential in gradient-based optimization algorithms.

In general semiconductor quantum systems are described by the Schrödinger equation. This equation can be formulated in a time independent or time dependent form. The time independent Schrödinger equation (TISE) is used mainly for application with static solution. On the other hand, the time dependent Schrödinger equation (TDSE) is used for modeling the quantum structures in the dynamic case. To apply the Schrödinger equation for a specified problem, a differential equation needs to be solved to obtain characteristic parameters such as eigenvalues and eigenfunctions of that problem. These

parameters are essential in the design of quantum structures. They are utilized in calculating key parameters such as the gain of quantum dot lasers [1], and the absorption cross section of quantum photodiodes [2]. Thus obtaining the sensitivity of the eigen parameters is essential for obtaining the sensitivity of any of the key parameters of the structure.

The classical approach for estimating first-order sensitivities invokes finite difference (FD) approximations at the response level. FD-based sensitivity estimation requires at least N extra eigenvalue calculations if forward differences (FFD) are used, where N is the number of design parameters. Additional $2N$ calculations are required if the more accurate central finite differences (CFD) are utilized. This high cost of sensitivity analysis motivates research for more computationally efficient approaches.

In this chapter, we propose efficient approaches to calculate the sensitivities of the eigen parameters of quantum structures with respect to all the design parameters with minimum additional cost. These design parameters may include the dimensions of the quantum structure or the height of the energy barriers. We propose two different approaches for sensitivity analysis of both TISE and TDSE.

We utilize a finite difference approximation to represent the Hamiltonian matrix (system matrix). Our approaches also utilize an adjoint variable method (AVM) to extract the sensitivities with respect to all the design parameters without solving any perturbed eigenvalue problem. The proposed approaches utilize on-grid central parameter perturbations to approximate the derivatives of the system matrices using virtual perturbations. This central adjoint variable method (CAVM) has a second order accuracy

as will be shown later in this chapter.

7.2 SENSITIVITY ANALYSIS OF TIME INDEPENDENT SCHRÖDINGER EQUATION

We start by writing the time independent Schrödinger equation (TISE) [4]

$$\mathbf{H}\psi_k = E_k\psi_k \quad (7.1)$$

where \mathbf{H} is the Hamiltonian matrix. A simple form of this matrix can be given as

$$\mathbf{H} = -\frac{\hbar^2}{2m}\nabla^2 + V \quad (7.2)$$

where \hbar and m is the reduced Plank constant, and the electron mass, respectively. The potential distribution V is asymmetric in the general form. Once the Laplacian operator is formulated as a matrix, the Hamiltonian matrix \mathbf{H} is a system matrix. E_k in (7.1) is the energy of the k^{th} level (k^{th} eigenvalue) and ψ_k is the k^{th} wavefunction (k^{th} eigenvector).

By differentiating (7.1) with respect to the design parameter p_i , we get

$$\frac{\partial \mathbf{H}}{\partial p_i}\psi_k + \mathbf{H}\frac{\partial \psi_k}{\partial p_i} = \frac{\partial E_k}{\partial p_i}\psi_k + E_k\frac{\partial \psi_k}{\partial p_i} \quad (7.3)$$

where $i = 1, 2, \dots, N$ is the index of the design parameters.

The Hamiltonian operator can be Hermitian or non Hermitian according to the included effects. For example, in some cases, such as the electro-absorption modulators and quantum dot structures, the coupling with contacts or the applied electric field can be incorporated in a manner that results in a non Hermitian Hamiltonian [2], [5]-[9]. The non Hermitian Hamiltonian can be also utilized to characterize the quantum systems in

applications other than the quantum lasers. For example, it can be utilized in studying localization-delocalization transitions in superconductors[10]. It may also be used in the theoretical description of diffraction of atoms by standing light waves [11]. In this case, the complex energy states and the wavefunction can be obtained by solving an eigenvalue problem. The real part of the energy states represents the energy levels while the imaginary part represents the decay rate of the energy state. The imaginary part indicates the possibility of the electron to tunnel from the quantum structure.

For most of the applications in quantum well lasers, however, the Hermitian case can be utilized especially if the Dingle particle model is utilized [2], [12], [13]. In the following subsections the derivation of both cases is given.

7.2.1 Non Hermitian Hamiltonian

Multiplying both sides of (7.3) by the Hermitian transpose of the left eigenfunction Φ_k^H , we get

$$\Phi_k^H \frac{\partial H}{\partial p_i} \psi_k + \Phi_k^H H \frac{\partial \psi_k}{\partial p_i} = \frac{\partial E_k}{\partial p_i} \Phi_k^H \psi_k + E_k \Phi_k^H \frac{\partial \psi_k}{\partial p_i} \quad (7.4)$$

where Φ_k can be obtained by solving the following problem

$$\Phi_k^H H = E_k \Phi_k^H. \quad (7.5)$$

It follows that the sensitivity of the energy levels can be written as [14]

$$\frac{\partial E_k}{\partial p_i} = \frac{\Phi_k^H \frac{\partial H}{\partial p_i} \psi_k}{\Phi_k^H \psi_k} \quad (7.6)$$

The expression (7.6) supplies the sensitivities of the k^{th} eigenvalue (energy level) with respect to all parameters. It requires only the sensitivities of Hamiltonian matrix with respect to each parameter.

The sensitivities of the eigenvectors (wavefunctions) can be obtained as well with respect to all parameters. Rearranging (7.3), we obtain

$$(\mathbf{H} - E_k \mathbf{I}) \frac{\partial \boldsymbol{\psi}_k}{\partial p_i} = \left(\frac{\partial E_k}{\partial p_i} \mathbf{I} - \frac{\partial \mathbf{H}}{\partial p_i} \right) \boldsymbol{\psi}_k \quad (7.7)$$

This system of equations can be rewritten in the following form:

$$\begin{bmatrix} \mathbf{H}_r - E_k \mathbf{I} & -\mathbf{H}_i \\ \mathbf{H}_i & \mathbf{H}_r - E_k \mathbf{I} \end{bmatrix} \begin{bmatrix} \frac{\partial \boldsymbol{\psi}_{rk}}{\partial p_i} \\ \frac{\partial \boldsymbol{\psi}_{ik}}{\partial p_i} \end{bmatrix} = \begin{bmatrix} \text{Re} \left(\left(\frac{\partial E_k}{\partial p_i} \mathbf{I} - \frac{\partial \mathbf{H}}{\partial p_i} \right) \boldsymbol{\psi}_k \right) \\ \text{Im} \left(\left(\frac{\partial E_k}{\partial p_i} \mathbf{I} - \frac{\partial \mathbf{H}}{\partial p_i} \right) \boldsymbol{\psi}_k \right) \end{bmatrix} \quad (7.8)$$

where \mathbf{H}_r and \mathbf{H}_i are the real and the imaginary parts of the Hamiltonian matrix \mathbf{H} , respectively. Similarly, $\boldsymbol{\psi}_{rk}$ and $\boldsymbol{\psi}_{ik}$ are the real and the imaginary parts of the wavefunction $\boldsymbol{\psi}_k$, respectively. The system of equations (7.7) can be used to obtain the derivatives of the wavefunctions. This system of equations is, however, rank deficient. In order to obtain a unique solution, we make use of the normalization property. This property can be written as

$$\boldsymbol{\psi}_k^H \boldsymbol{\psi}_k = \begin{bmatrix} \boldsymbol{\psi}_{rk}^T & \boldsymbol{\psi}_{ik}^T \end{bmatrix} \begin{bmatrix} \boldsymbol{\psi}_{rk} \\ \boldsymbol{\psi}_{ik} \end{bmatrix} = 1 \quad (7.9)$$

By differentiating (7.9) with respect to the design parameter p_i , we obtain

$$\begin{bmatrix} \psi_{rk}^T & \psi_{imk}^T \end{bmatrix} \begin{bmatrix} \frac{\partial \psi_{rk}}{\partial p_i} \\ \frac{\partial \psi_{imk}}{\partial p_i} \end{bmatrix} = 0 \quad (7.10)$$

The equation (7.10) would make the system of equations (7.7) full rank only if it is independent of the matrix $(\mathbf{H} - E_k \mathbf{I})$. We assume the opposite situation. Assume that ψ_k^H is in the space of the matrix $(\mathbf{H} - E_k \mathbf{I})$, thus the following relation is satisfied

$$\psi_k^H = \mathbf{y}(\mathbf{H} - E_k \mathbf{I}) \quad (7.11)$$

where \mathbf{y} is any vector, multiplying both sides by ψ_k

$$\psi_k^H \psi_k = \mathbf{y}(\mathbf{H} - E_k \mathbf{I}) \psi_k \quad (7.12)$$

Using (7.1), the RHS is given by

$$\mathbf{y}(\mathbf{H} \psi_k - E_k \psi_k) = 0, \quad (7.13)$$

which contradicts the normalization property of the eigenfunctions given in (7.9). It follows that equation (7.10) is independent of the system equation (7.7) and the complete full rank system of equations is given by

$$\begin{bmatrix} \mathbf{H}_r - E_k \mathbf{I} & -\mathbf{H}_i \\ \mathbf{H}_i & \mathbf{H}_r - E_k \mathbf{I} \\ \psi_{rk}^T & \psi_{imk}^T \end{bmatrix} \begin{bmatrix} \frac{\partial \psi_{rk}}{\partial p_i} \\ \frac{\partial \psi_{imk}}{\partial p_i} \end{bmatrix} = \begin{bmatrix} \text{Re} \left(\left(\frac{\partial E_k}{\partial p_i} \mathbf{I} - \frac{\partial \mathbf{H}}{\partial p_i} \right) \psi_k \right) \\ \text{Im} \left(\left(\frac{\partial E_k}{\partial p_i} \mathbf{I} - \frac{\partial \mathbf{H}}{\partial p_i} \right) \psi_k \right) \\ 0 \end{bmatrix} \quad (7.14)$$

7.2.2 Hermitian Hamiltonian

In this case the left eigenfunctions and the right eigenfunctions are the same, i.e. $\Phi_k = \psi_k$. Thus, the sensitivity of the eigen energies can be written as

$$\frac{\partial E_k}{\partial p_i} = \psi_k^H \frac{\partial \mathbf{H}}{\partial p_i} \psi_k \quad (7.15)$$

On the other hand, the sensitivity of the eigenfunction (wavefunction) with respect to the design parameter p_i is obtained by solving the same system of equations given in (7.14). It should be noted that one LU decomposition can be used to solve these equation, regardless of the number of parameters, as the left hand side is independent of the design parameters. We denote the system in (7.14) as the adjoint system.

In order to calculate the sensitivities of the wavefunctions and energy levels with respect to the design parameter p_i , $i = 1, 2, \dots, N$, the derivative of the Hamiltonian matrix with respect to p_i is needed. Perturbation theory is utilized to calculate the system derivatives by assuming on-grid virtual perturbation of the system matrix due to the change in the design parameters. The central differences are utilized to calculate an approximate derivative of the system matrices

$$\frac{\partial \mathbf{H}}{\partial p_i} \approx \frac{\mathbf{H}(p_i + \Delta p_i) - \mathbf{H}(p_i - \Delta p_i)}{2\Delta p_i} \quad (7.16)$$

where Δp_i is the perturbation in the design parameter p_i . In (7.16), $\mathbf{H}(p_i + \Delta p_i)$, $\mathbf{H}(p_i - \Delta p_i)$ are the perturbed Hamiltonian matrices due to the forward and the backward perturbations in the design parameter p_i , respectively.

Our sensitivity analysis approach is also applicable for the degenerate state where some of the eigenvalues are repeated. In this case, the adjoint system of equations (7.14) can be modified by adding additional rows that contain the wavefunctions which correspond to the repeated eigenvalues. Moreover, without adding these wavefunctions the system of equations can also be solved using a least square method to obtain the pseudoinverse of the rank deficient matrix.

7.2.3 Numerical Examples

Here, we give different examples to illustrate the efficiency of our approach to extract the sensitivities of the eigen parameters with respect to all the design parameters without resolving the perturbed eigenvalue problem. Different objective functions are also utilized to illustrate the universality of our CAVM approach. In the proposed approach, central perturbation is utilized with the Hamiltonian matrices for solving the

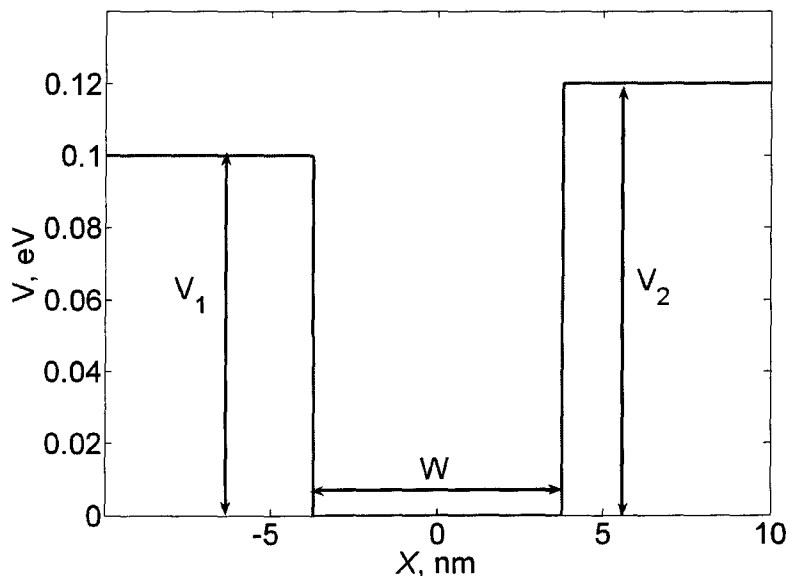


Fig. 7.1. Schematic diagram of the quantum well in the conduction band of single quantum well double hetrostructure laser.

adjoint system. Our results are compared with the accurate and time-intensive central finite difference (CFD) approximation applied at the response level. This approximation is given by

$$\frac{\partial f}{\partial p_i} \approx \frac{f(p_i + \Delta p_i) - f(p_i - \Delta p_i)}{2\Delta p_i} \quad (7.17)$$

where f is the objective function which can be the energy levels or the wavefunctions. For the CFD approach, the eigenvalue problem is resolved for the perturbed system due to the perturbation in the design parameter p_i as given in (7.17).

Table 7.1
The Sensitivity of the ground energy level with respect to the design parameters of asymmetric QW using AVM and CFD.

| | $\partial E_o / \partial V_1$ | $\partial E_o / \partial V_2$ | $\partial E_o / \partial W$, eV.nm ⁻¹ |
|-----|-------------------------------|-------------------------------|---|
| AVM | 7.553×10^{-4} | 6.971×10^{-4} | -0.0055601 |
| CFD | 7.5521×10^{-4} | 6.97×10^{-4} | -0.0055608 |

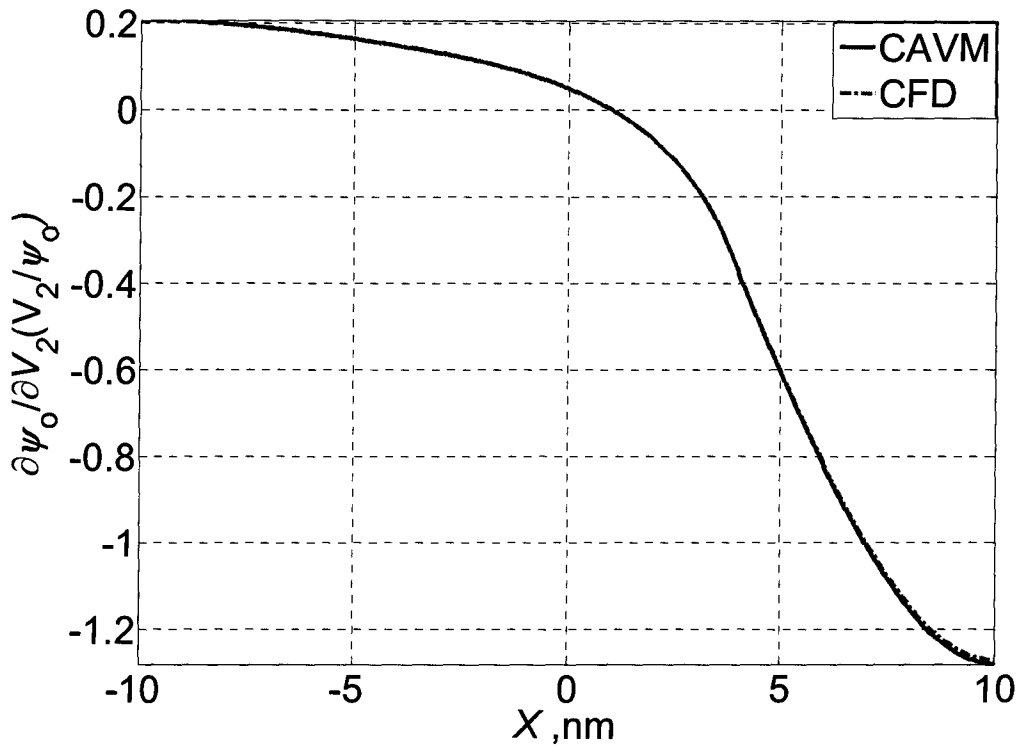


Fig. 7.2 Normalized sensitivity of the wavefunction of the ground state with respect to V_2 .

7.2.3.1 Single Quantum Well In Asymmetric Double Heterostructure

The sensitivities of the energy levels and the wavefunctions with respect to the design parameters $p=[V_1 \ V_2 \ W]^T$ are calculated for the asymmetric quantum well (QW) shown in Fig. 7.1. The width of the QW (W) is 7.5 nm and the effective mass m is $0.066 m_0$, where m_0 is the mass of the electron. The sensitivities obtained using our approach has a good agreement with those obtained using CFD as shown in Fig. 7.2. The sensitivities of the ground state energy level is shown in Table 7.1. We define a time saving factor as the ratio $S_T= T_{CFD}/ T_{CAVM}$, where T_{CFD} and T_{CAVM} are the computational

time of the CFD approach and our CAVM approach, respectively. The value of S_T is calculated to be 2.31 for the case ($N=3$), where N is the total number of design parameters. The value of S_T for sensitivities calculation of two parameters only ($N=2$), $p=[V_2 \ W]^T$, is calculated to be 2.1.

7.2.3.2 Asymmetric multiple quantum well tunable lasers

The asymmetric multiple quantum well (AMQW) shown in Fig. 7.3 is utilized to achieve a broadband tunable laser [15],[16]. AMQWs are usually created from the QWs by varying their widths or compositions or both. Each QW has different energy levels. Thus, it contributes to the gain profile differently. By proper design of the different wells, a broadband tunable laser can be obtained. The sensitivity of the energy levels with respect to the dimensions and composition of each well is essential to optimize the gain profile. For our structure, GaAs-Al_xGa_{1-x}As system is utilized to obtain a wideband response [15]. The variation of the Al molar content x of any region will result in a variation in both the barrier height and the effective mass of this region [16]. The sensitivity of the energy level E_1 with respect to the width of the well L_1 and the Al molar content of the first barrier x_1 and the second barrier x_2 ($p=[x_1 \ L_1 \ x_2]^T$) is calculated. The widths of the QWs L_1 , L_2 and L_3 are equal to 10.0 nm, 8.0 nm, and 6.0 nm, respectively. The sensitivities obtained using our approach has an excellent agreement with those obtained using CFD as shown in Fig. 7.4. We define a time saving factor as the ratio $S_T = T_{CFD} / T_{AVM}$, where T_{CFD} and T_{CAVM} are the computational times of the CFD approach and our AVM approach, respectively. The value of S_T is calculated to be 5.09 for the sensitivity analysis with three parameters ($N=3$). The value of S_T for sensitivities

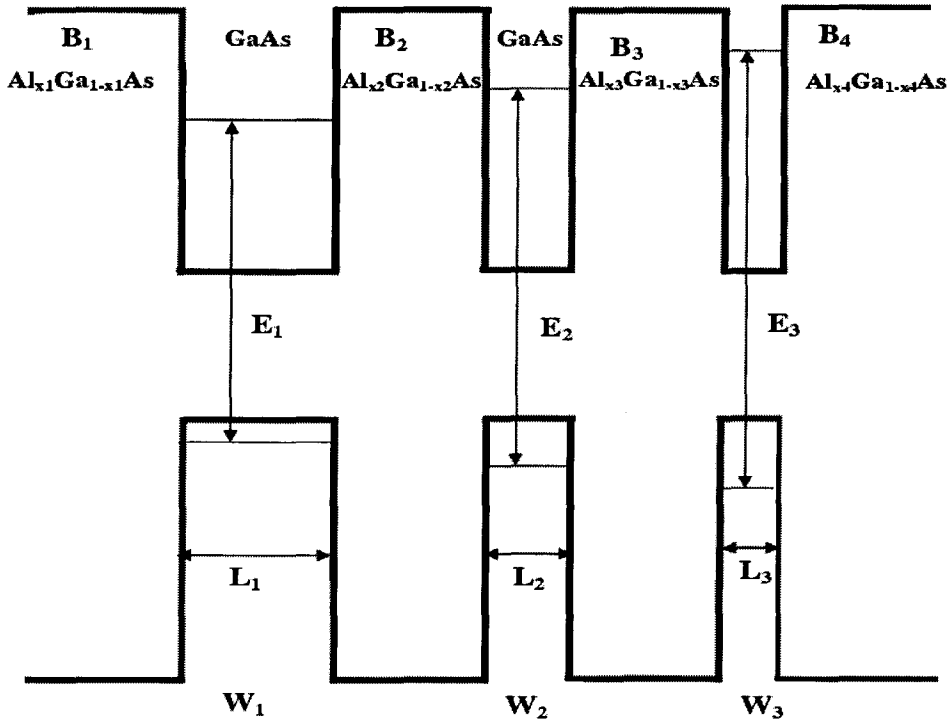


Fig. 7.3. Schematic diagram of asymmetric quantum well laser.

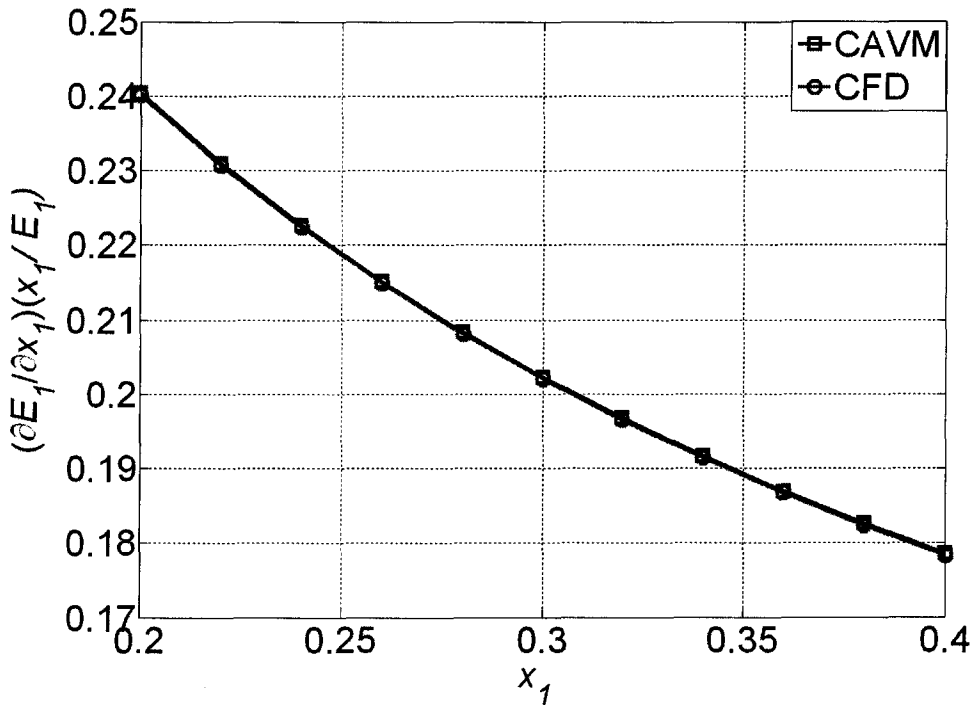


Fig. 7.4. Normalized sensitivity of the energy level of the ground state of the first QW with respect to x_1 for $L_1=10$ nm, $L_2=8$ nm, $L_3=6$ nm, $x_2=x_3=x_4=0.3$.

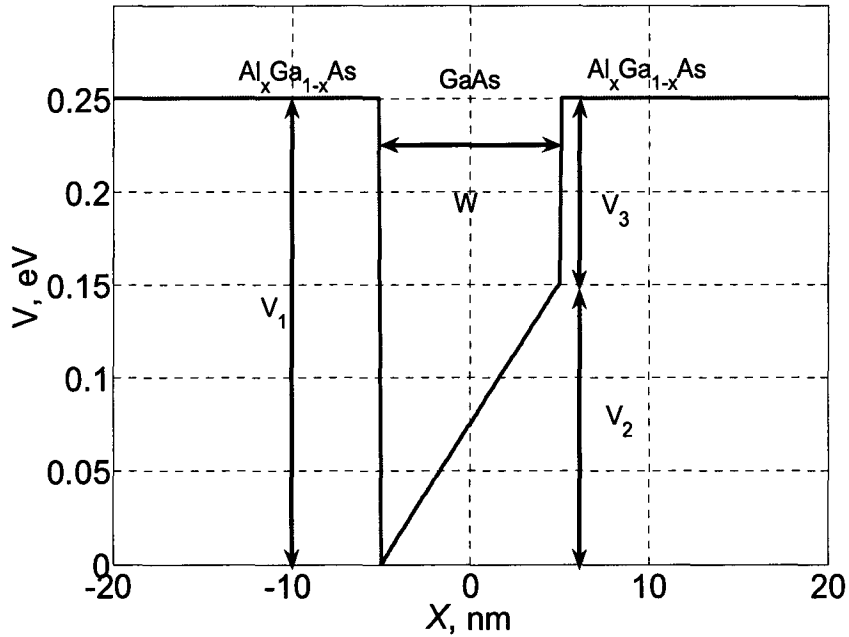


Fig. 7.5. Schematic diagram of the trapezoidal quantum well in the conduction band of a single quantum well double heterostructure laser.

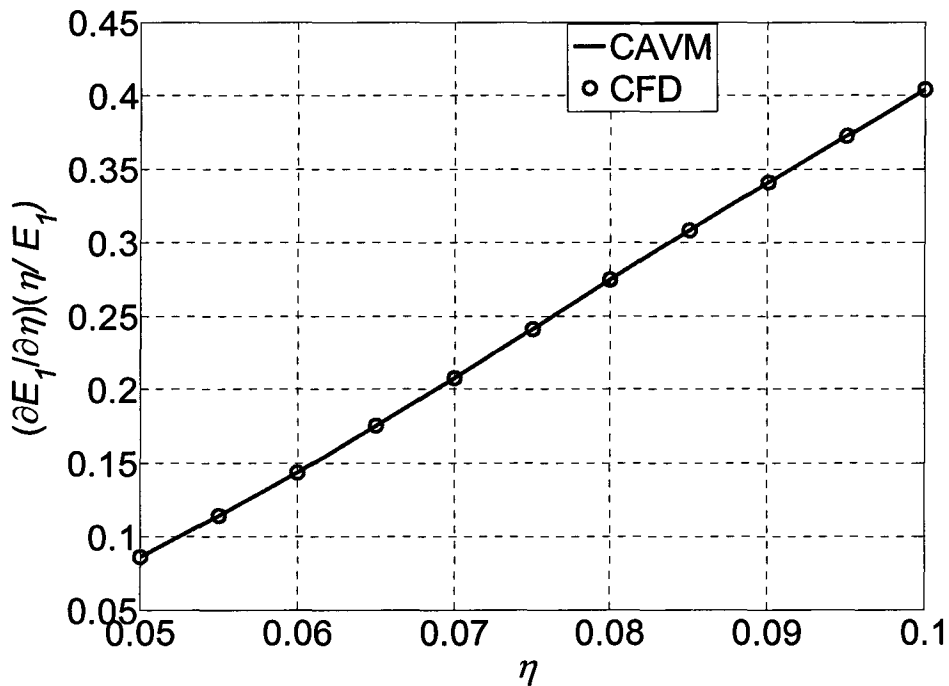


Fig. 7.6. Normalized sensitivity of the energy level of the ground state of the trapezoidal QW with respect to η for $V_1=0.2501$ eV, $V_2 =0.15$ eV, $V_3=0.101$ eV, $W=10$ nm, and $x=0.3$.

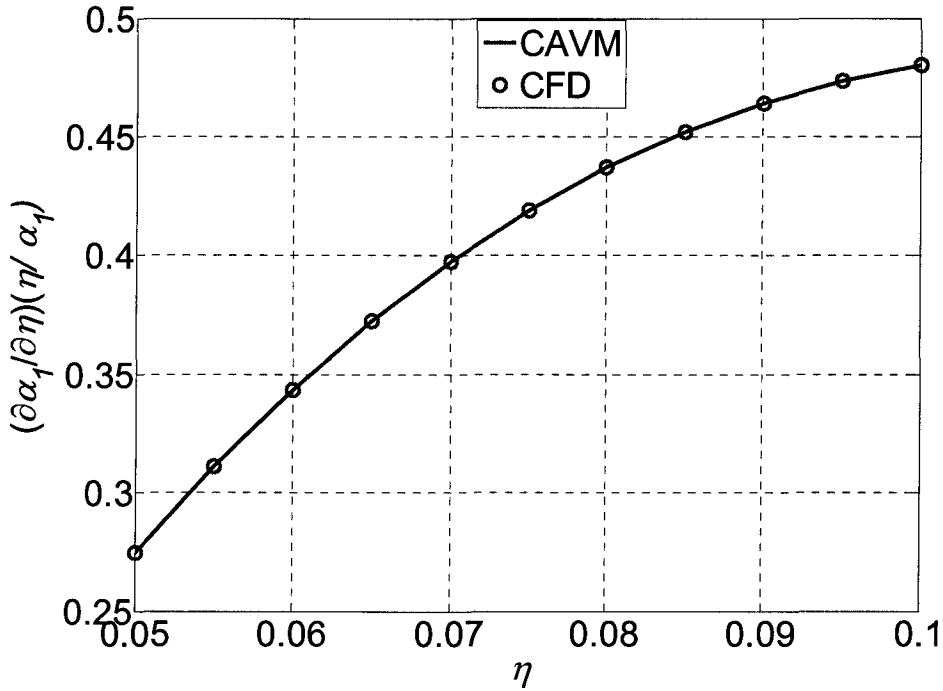


Fig. 7.7. Normalized sensitivity of α_1 of the ground state of the trapezoidal QW with respect to η for $V_1=0.2501$ eV, $V_2=0.15$ eV, $V_3=0.101$ eV, $W=10$ nm, and $x=0.3$.

calculation of two parameters only ($N=2$), $\mathbf{p}=[x_1 \ L_1]^T$, is 4.0. It is thus clear that our approach becomes more efficient with the increase of the number of design parameters N .

7.2.3.3 Non Hermitian Trapezoidal Quantum Well With Leads Included

Open quantum well systems may include semi infinite leads to transport electrons to and from the system. These leads can be replaced by a self energy term added to the Hamiltonian operator [7]. The time independent Schrödinger equation can thus be written as [7]:

$$(\mathbf{H} + i\eta\mathbf{I})\psi_k = \lambda_k\psi_k \tag{7.18}$$

where $\eta > 0$, is infinitesimal term that accounts for the leads effect and I is the identity matrix. λ_k in (7.18) is the complex eigenvalue whose real part represents the energy level E_k while the imaginary part α_k represent the decay rate due to the leads effect. The system matrix $H' = H + i\eta I$ is non Hermitian and the sensitivity of the eigenvalues and wavefunction can be obtained using (7.6), and (7.14), respectively.

To demonstrate the universality of our approach, the sensitivity of the eigenvalues of a single trapezoidal quantum well shown in Fig. 7.5 is calculated. For this structure, the sensitivity of E_k and α_k of the ground state is calculated with respect to the design parameters $p = [V_1 V_2 V_3 \eta W x]^T$. Excellent agreement is obtained between our approach and the expensive CFD. The sensitivity of the eigenvalues with respect to η is given as an example in Fig. 7.6 and Fig. 7.7. Using our approach two eigenvalue problems are solved to obtain the right and the left eigenvalues. Then the sensitivities with respect to all the design parameters using (7.6) are efficiently obtained. The CFD approach, however, solves 12 additional eigenvalue problems to obtain the sensitivities. The time saving factor in this example is calculated to be 4.56.

7.3 SENSITIVITY ANALYSIS OF TIME DEPENDENT SCHRÖDINGER EQUATION

Let us discuss a formal approach to the time-dependent problem

$$H\psi(x,t) = \left[-\frac{\hbar^2}{2m} \frac{\partial^2}{\partial x^2} + V(x) \right] \psi(x,t) = i\hbar \frac{\partial \psi}{\partial t} \quad (7.19)$$

The formal solution of (7.19) is expressed by the time evolution operator, which is represented by a matrix exponential function [17]

$$\psi(x,t) = e^{-\frac{iH}{\hbar}t} \psi(x,0) \quad (7.20)$$

We denote the wavefunctions $\psi(x,t)$ by ψ_j^n , where j represents a spatial mesh point and n represents a point in time using discrete spatial steps Δx and time steps Δt , respectively. To evaluate the time evolution of the wavefunction we can use the relationship

$$\psi(x,t + \Delta t) = e^{-\frac{iH}{\hbar}\Delta t} \psi(x,t) \quad (7.21)$$

The Crank-Nicholson scheme (CN) has been widely used in which the exponential function is approximated by Cayley transform [17]

$$\psi(x,t + \Delta t) = \left(\frac{1 - \frac{iH}{2\hbar}\Delta t}{1 + \frac{iH}{2\hbar}\Delta t} \right) \psi(x,t) \quad (7.22)$$

The solution results by using the implicit form of the time evolution equation

$$\left(1 + \frac{iH}{2\hbar}\Delta t \right) \psi(x,t + \Delta t) = \left(1 - \frac{iH}{2\hbar}\Delta t \right) \psi(x,t) \quad (7.23)$$

Thus, the difference form of our approximation is given as

$$\left(1 + \frac{iH}{2\hbar}\Delta t \right) \psi_j^{n+1} = \left(1 - \frac{iH}{2\hbar}\Delta t \right) \psi_j^n \quad (7.24)$$

By using finite difference approximation to the Laplacian operate of the Hamiltonian matrix, we can write the system of equation

$$\psi_{j+1}^{n+1} + a_j^{n+1} \psi_j^{n+1} + \psi_{j-1}^{n+1} = -\psi_{j+1}^n + b_j^n \psi_j^n - \psi_{j-1}^n \quad (7.25)$$

where

$$a_j^n = i \frac{4m(\Delta x)^2}{\hbar \Delta t} - \frac{2m(\Delta x)^2}{\hbar^2} V_j^n - 2 \quad (7.26)$$

$$b_j = i \frac{4m(\Delta x)^2}{\hbar \Delta t} + \frac{2m(\Delta x)^2}{\hbar^2} V_j^n + 2 \quad (7.27)$$

For the 2D case, (7.25) can be modified to the following form

$$\begin{aligned} & i \frac{4m}{\hbar \Delta t} \psi_{j,k}^{n+1} - \frac{2mV_{j,k}^n}{\hbar^2} \psi_{j,k}^{n+1} + \left[\frac{\psi_{j-1,k}^{n+1} - 2\psi_{j,k}^{n+1} + \psi_{j+1,k}^{n+1}}{\Delta x^2} + \frac{\psi_{j,k-1}^{n+1} - 2\psi_{j,k}^{n+1} + \psi_{j,k+1}^{n+1}}{\Delta y^2} \right] \\ & = i \frac{4m}{\hbar \Delta t} \psi_{j,k}^n + \frac{2mV_{j,k}^n}{\hbar^2} \psi_{j,k}^n - \left[\frac{\psi_{j-1,k}^n - 2\psi_{j,k}^n + \psi_{j+1,k}^n}{\Delta x^2} + \frac{\psi_{j,k-1}^n - 2\psi_{j,k}^n + \psi_{j,k+1}^n}{\Delta y^2} \right] \end{aligned} \quad (7.28)$$

From equation (7.25) and (7.28) it is obvious this method solves the following system of equation at each time step

$$A^{n+1} \psi^{n+1} = B^n \psi^n \quad (7.29)$$

where A and B are the system matrices. These matrices are tridiagonal matrices for the 1D case and pentadiagonal for the 2D case. For example, in the 1D case these matrices are given as

$$A^n = \begin{bmatrix} a_1^n & 1 & 0 & 0 \\ 1 & a_2^n & 1 & 0 \\ 0 & .. & .. & 0 \\ 0 & 0 & 1 & a_N^n \end{bmatrix}, \quad (7.30)$$

$$B^n = \begin{bmatrix} b_1^n & -1 & 0 & 0 \\ -1 & b_2^n & -1 & 0 \\ 0 & .. & .. & 0 \\ 0 & 0 & -1 & b_N^n \end{bmatrix} \quad (7.31)$$

ψ^n and ψ^{n+1} are the wave function at the time step n and $n+1$:

$$\psi^n = \begin{bmatrix} \psi_1^n \\ \psi_2^n \\ \vdots \\ \psi_N^n \end{bmatrix}, \text{ and } \psi^{n+1} = \begin{bmatrix} \psi_1^{n+1} \\ \psi_2^{n+1} \\ \vdots \\ \psi_N^{n+1} \end{bmatrix} \quad (7.32)$$

In general, the TDSE is utilized for tunneling problems in semiconductor and for problems with time dependent Hamiltonian such as quantum lasers under time varying bias. However, it is also widely utilized in stationary (static) application for efficient extraction of eigen parameters.

Due to the close analogy of the system of equation in (7.29) with the system of equation of the BPM shown in Chapter 2, the extraction of the eigen parameters and their sensitivities follows the same approach given in Sections 5.3.3.1 and 5.3.3.2.

7.3.1 Numerical Examples

In order to illustrate the applicability of our sensitivity approach presented in Chapter 5 to the TDSE, here we give examples for extracting the eigen parameters. The imaginary distance approach described in Section 5.3.3.1 is also applicable for TDSE. This approach called imaginary time propagation (ITP) approach. In this approach, the propagation time step Δt is replaced by $\Delta \tau = j\Delta t$ [18]. Following similar approach, the sensitivity of the energy levels can be obtained efficiently. For example, the sensitivity of the ground energy level E_o of a quantum wire with width $W_x=3.0$ nm, length W_y , and barrier height of 0.1 eV is calculated over a sweep of different values of W_y . The obtained sensitivity using our CAVM is also compared with those obtained using CFD approach applied directly on the level of response. The results are shown in Fig. 7.8. A good match

is obtained between the CAVM sensitivities and CFD sensitivities which proves the accuracy of our approach.

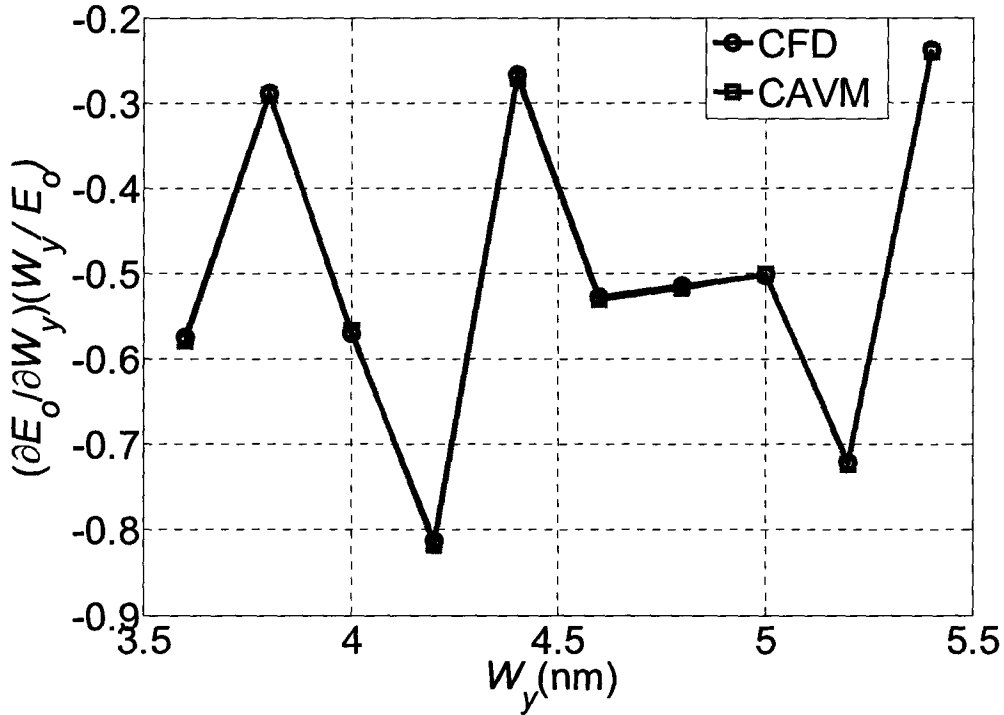


Fig. 7.8 Normalized sensitivity of E_0 of the ground state of the quantum wire with respect to W_y for $W_x=0.3$ nm, and barrier height of 0.1 eV.

7.4 CONCLUSION

A novel approach for the sensitivity analysis of semiconductor quantum structures for optical application is presented. We propose a simple and efficient approach for extracting the sensitivities of the energy levels and the wavefunctions with respect to all the design parameters of quantum structures using the time independent and time dependent Schrödinger equation. It requires no extra solution of eigenvalue problems.

The accuracy of the obtained sensitivities is second order and have a good match with time intensive CFD.

7.5 REFERENCES

- [1] N. Vukmirovic, Z. Ikonic, V. D. Jovanovic, D. Indjin, and P. Harrison, “Optically pumped intersublevel MidInfrared lasers based on InAs-GaAs quantum dots,” *IEEE J. Quantum Electron.*, vol. 41, pp. 1361-1368, Nov. 2005.
- [2] S. L. Chuang, *Physics of optoelectronic devices*, John Wiley, NY, 1995.
- [3] J. C. Ranuarez, M. J. Deen, and C. Chen, “A review of gate tunneling current in MOS devices,” *Microelectronics Reliability*, vol. 46, pp. 1939-1956, Dec. 2006.
- [4] L. Schiff, *Quantum Mechanics*, 3rd Ed., McGraw-Hill , 1968.
- [5] R. P. Leavitt, “Empirical two-band model for quantum wells and superlattices in an electric field,” *Phys. Rev. B.*, vol. 44, pp. 11270-11280, Nov.1991.
- [6] M. F H. Schuurmans, G. W.‘t Hoof, “Simple calculations of confinement states in a quantum well, ” *Physc. Rev. B.* vol. 31, pp. 8041-8048, June 1985.
- [7] F. Michael and D. Johnson, “Replacing leads by self-energies using non-equilibrium Green’s functions,” *Physica B*, vol. 339, pp. 31-38, 2003.
- [8] M. A. Naser, M. J. Deen and D.A. Thompson, “Spectral function and responsivity of resonant tunneling and superlattice quantum dot infrared photodetectors using Green’s function,” *J. Appl. Phys.*, vol. 102, pp. 083108-1-083108-12. Oct. 2007.

- [9] M. A. Naser, M. J. Deen and D. A. Thompson, “Spectral function of InAs/InGaAs quantum dots in a well detector using Green’s function,” *J. Appl. Phys.*, vol. 100, pp. 093102-1-093102-6, Nov. 2006.
- [10] J. Feinberg, and A. Zee, “Non-Hermitian localization and delocalization,” *Phys. Rev. E*, vol. 59, pp. 6433-6443, June 1999.
- [11] M. V. Berry and D. H. J O’Dell, “Diffraction by volume gratings with imaginary potentials,” *J. Phys. A*, vol. 31, pp. 2093- 2101, 1998.
- [12] W. W. Chow and S. W. Koch, *Semiconductor Laser Fundamentals, Physics of the Gain Materials*, Springer, NY, 1999.
- [13] R. Dingle, *Advances in solid state physics*, vol. 15 pp. 21-48, 1975.
- [14] R. A. Horn, and C. Johnson, *Matrix analysis*, Cambridge University Press, NY, 1995.
- [15] T. F. Krauss, G. Hondromitros, B. Vogel, and R. M. De La Rue, “Broad spectral bandwidth semiconductor lasers,” *Electron. Lett.*, vol. 33, pp. 1142-1143, Jun. 1997.
- [16] V. K. Kononenko, I. S. Manak, and S. V. Nalivko, “Design and characteristics of widely tunable quantum-well laser diodes,” *Spectrochim. Acta A* vol. 55, pp. 2091–2096, Sept. 1999.
- [17] A. Goldberg, H. M Schey, and J. L. Schwart, “Computer-generated motion pictures of one-dimensional quantum mechanical transmission and reflection phenomena,” *J Americ. Phys.* vol. 35, pp. 177-186, Mar. 1967.

- [18] L. Lehtovaara, J.Toivanen, and J. Eloranta, “Solution of time-independent Schrödinger equation by the imaginary time propagation method,” *J. Comput. Phys.* vol 221, pp. 148-157, Jan. 2007.

8 DESIGN OPTIMIZATION OF MULTILAYER OPTICAL COATING USING CONVEX OPTIMIZATION

8.1 INTRODUCTION

Multilayer thin film optical coatings have a wide range of applications in different fields. These fields include optical communication systems, optical storages and biomedical applications [1]. Thin film technology has been used in many optical components such as bandpass filters, antireflection (AR) coatings, high-reflection (HR) coatings, beam-splitters, and polarization splitters [2],[3]. Antireflection (AR) coating with ultra low reflectivity and broad bandwidth is a required feature for semiconductor lasers and optoelectronic devices. For semiconductor laser amplifiers (SLAs), the reflectivity should be minimized over the working band to suppress any oscillations. On the other hand, high reflectivity (HR) is a desirable feature in integrated distributed Bragg reflector lasers (DBR), dielectric mirrors and optical routers. Conceptually, the design procedure of antireflection coatings and high reflection coatings follow the same steps. We therefore focus on the design of antireflection coatings and selective filters.

To obtain antireflection response at a single wavelength, a single layer or two

layers are sufficient. However, when the antireflection function is broadened to cover a range of wavelengths, the number of layers must also be increased and the antireflection structure is a multilayer structure.

Many design procedures have been applied to solve this design problem. Most of these procedures address the problem of having a fixed number of refractive indices that are repeated periodically. The optimal length of each layer that satisfies the required specifications is then determined [4], [5]. Following these design procedures, however, involve solving a non-convex problem [6], [7]. The obtained results are thus only locally optimal.

Convex optimization is a specific class of optimization problems where both the objective function and the constraints set are convex. This optimization class is also called convex programming. Convex problems have the unique property that the obtained local minimum is also the global minimum [8]. Thus starting from any feasible point, the obtained optimal solution is the global solution and the optimal value is unique. Linear programming (LP) is a special class of convex programming where the objective function and all constraint functions are linear. Convex problems can be solved efficiently using interior point methods (IPM) [9]. These methods are efficient, powerful, and reliable. They allow for solving problems with hundreds of variables and thousands of constraints in fractions of a second [8]. The complexity and the convergence of such methods are studied and proved for the LP case [8],[10].

Recently, the refractive indices are also included in the optimization process of multilayer structures as optimization parameters. This gives more degrees of freedom to

the optimizer [11]. This approach may produce unrealizable refractive indices. Each layer with unrealizable refractive index is replaced with three layers having two fixed indices using equivalent layer theory [11], [12].

In this chapter, we propose a new approach for solving the design problem of multilayer optical coatings. In this approach, the optical length of each layer is fixed. The design parameters are thus the refractive indices of the layers only. Addressing the problem in this way allows us to approximate the original design problem with a convex optimization problem.

8.2 THEORY OF MULTILAYER STRUCTURES

The general shape of a multilayer dielectric structure is shown in Fig. 8.1. The design parameters are the number of layers M , the length of the i th layer d_i , and the impedance of the i th layer Z_i , or equivalently the refractive index n_i . The elementary reflection coefficient of the i th layer is defined in terms of the characteristic impedance and the refractive indices as follows

$$\rho_i = \frac{Z_i - Z_{i-1}}{Z_i + Z_{i-1}} = \frac{n_{i-1} - n_i}{n_{i-1} + n_i} \quad (8.1)$$

where Z_i and n_i are the characteristic impedance and the refractive index of the i th layer, respectively. The field components at two adjacent interfaces are related by [5]

$$\begin{bmatrix} E_{inc}^i \\ E_R^i \end{bmatrix} = \frac{1}{\rho_i + 1} \begin{bmatrix} e^{j\varphi_i} & \rho_i e^{-j\varphi_i} \\ \rho_i e^{j\varphi_i} & e^{-j\varphi_i} \end{bmatrix} \begin{bmatrix} E_{inc}^{i+1} \\ E_R^{i+1} \end{bmatrix} \quad (8.2)$$

where E_{inc}^i and E_R^i are the incident and reflected electric field at the i th interface, respectively. The angular phase shift φ_i of each layer is given by

$$\varphi_i = \frac{\omega}{c} n_i d_i \cdot \cos \theta_i \quad (8.3)$$

where θ_i and d_i are the incident angle and the length of the i th layer, respectively. In (8.3), ω is the angular frequency and c is the velocity of light in free space.

The incident and the reflected field of the multilayer system can be calculated using the expression:

$$\begin{bmatrix} E_{inc} \\ E_R \end{bmatrix} = U \begin{bmatrix} E_T \\ 0 \end{bmatrix}, \quad (8.4)$$

where E_{inc} and E_R are the incident field and the reflected field from the leftmost layer, respectively. E_T is the transmitted field from the rightmost layer as shown in Fig. 8.1.

The layer multiplication matrix U is given by

$$U = \prod_{i=1}^{M+1} \frac{1}{\rho_i + 1} \begin{bmatrix} e^{j\varphi_i} & \rho_i e^{-j\varphi_i} \\ \rho_i e^{j\varphi_i} & e^{-j\varphi_i} \end{bmatrix} \quad (8.5)$$

The total reflection is calculated as

$$\Gamma(\omega) = \frac{E_R}{E_{inc}}. \quad (8.6)$$

It is clear from (8.6) that the reflection expression can be simplified if the angular phase shift of all layers is assumed to be constant. Here, the angular phase shift is written as

$$\varphi = \frac{\omega}{c} n_i d_i \cdot \cos \theta_i = \frac{\pi}{2} \frac{\omega}{\omega_o}, \text{ and } \omega_o = \frac{\pi c}{2 n_i d_i \cdot \cos \theta_i} \quad (8.7)$$

The layer multiplication matrix U can be simplified to the form [13]

$$U = \prod_{i=1}^{M+1} \frac{z^{1/2}}{\rho_i + 1} \begin{bmatrix} 1 & \rho_i z^{-1} \\ \rho_i & z^{-1} \end{bmatrix} \quad (8.8)$$

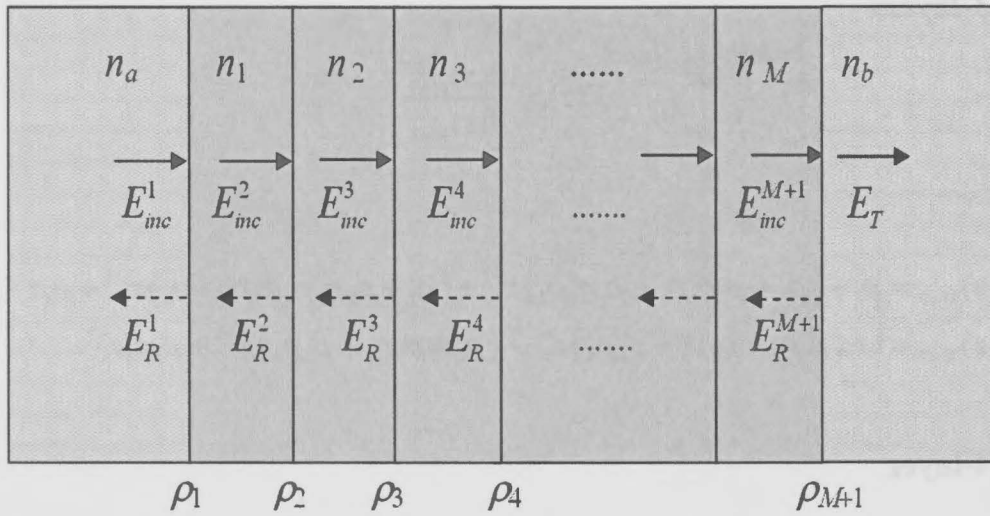


Fig. 8.1. Schematic diagram of a multilayer dielectric structure with M layer.

where

$$z = e^{2j\varphi} . \quad (8.9)$$

The reflection coefficient (8.6) can thus be written in the following rational form [13]:

$$\Gamma(z) = \frac{E_R}{E_{inc}} = \frac{B(z)}{A(z)} , \quad (8.10)$$

where $B(z)$, and $A(z)$ are polynomials in the variable z^{-1} . In order to investigate these polynomials, we evaluate the reflection coefficient for different number of layers using (8.4), (8.8), and (8.10)

8.2.1 2-layers

$$\Gamma(z) = \frac{\rho_1 + (\rho_2 + \rho_1\rho_2\rho_3)z^{-1} + \rho_3z^{-2}}{1 + (\rho_1\rho_2 + \rho_2\rho_3)z^{-1} + \rho_2\rho_3z^{-2}} \quad (8.11)$$

8.2.2 3-layers

$$\Gamma(z) = \frac{B(z)_{M=3}}{A(z)_{M=3}}$$

where

$$\begin{aligned} B(z)_{M=3} &= \rho_1 + (\rho_2 + \rho_1\rho_2\rho_3 + \rho_1\rho_3\rho_4)z^{-1} + (\rho_3 + \rho_2\rho_3\rho_4 + \rho_1\rho_2\rho_4)z^{-2} + \rho_4z^{-3}, \\ A(z)_{M=3} &= 1 + (\rho_1\rho_2 + \rho_2\rho_3 + \rho_3\rho_4)z^{-1} + (\rho_1\rho_2\rho_3\rho_4 + \rho_2\rho_4)z^{-2} + \rho_1\rho_4z^{-3}. \end{aligned} \quad (8.12)$$

8.2.3 4-layer

$$\begin{aligned} B(z)_{M=4} &= \rho_1 + (\rho_2 + \rho_1\rho_2\rho_3 + \rho_1\rho_3\rho_4 + \rho_1\rho_4\rho_5)z^{-1} \\ &\quad + \left(\begin{array}{l} \rho_3 + \rho_2\rho_3\rho_4 + \rho_1\rho_2\rho_4 + \rho_2\rho_4\rho_5 \\ + \rho_1\rho_2\rho_3\rho_4\rho_5 + \rho_1\rho_3\rho_5 \end{array} \right) z^{-2} \\ &\quad + (\rho_4 + \rho_3\rho_4\rho_5 + \rho_2\rho_3\rho_5 + \rho_2\rho_2\rho_5)z^{-3} + \rho_5z^{-4}, \\ A(z)_{M=4} &= 1 + (\rho_1\rho_2 + \rho_2\rho_3 + \rho_3\rho_4 + \rho_4\rho_5)z^{-1} \\ &\quad + \left(\begin{array}{l} \rho_1\rho_2\rho_3\rho_4 + \rho_1\rho_2\rho_4\rho_5 \\ + \rho_2\rho_3\rho_4\rho_5 + \rho_2\rho_4 + \rho_3\rho_5 \end{array} \right) z^{-2} \\ &\quad + (\rho_1\rho_4 + \rho_1\rho_2\rho_3\rho_5 + \rho_1\rho_3\rho_4\rho_5 + \rho_2\rho_5)z^{-3} + \rho_1\rho_5z^{-4}. \end{aligned} \quad (8.13)$$

As the values of the elementary reflection coefficients ($|\rho_i| \leq 1$) are usually small, a practical assumption is to ignore the higher order terms (terms containing two or more factors of ρ_i) [13]. This assumption can be physically interpreted as ignoring the multiple reflections within each coating layer. Using this assumption, the reflection response is approximated by

$$\Gamma(z) \approx \sum_{i=1}^{M+1} \rho_i z^{-(i-1)} = \rho_1 + \rho_2 z^{-1} + \rho_3 z^{-2} + \dots + \rho_{M+1} z^{-M}. \quad (8.14)$$

The reflection response given in (8.14) is a good approximation to the exact one given in (8.4)-(8.6) especially for a sufficient number of layers where the refractive index change

between any two adjacent layers is small. For example, if the relative refractive index changes between any two adjacent layers δn_i , and δn_{i+1} are less than 10%, the error induced by ignoring the term $\rho_i \rho_{i+1}$ is less than 1%.

8.3 PROBLEM FORMULATION

The approximate reflection coefficient given in (8.14) can be optimized to satisfy certain specifications on the pass and stop bands. These specifications may vary according to the desired application. These specifications can be imposed to reduce the reflection over a certain band of frequencies between two media with different refractive indices n_a and n_b as in the AR coatings designs. Additional constraints may be imposed to limit the ripples in the passband as in selective filters designs. Our general formulation for these problems is in the following form

$$\begin{aligned} \min_{\rho} \quad & \max_{f \in [f_s, 2f_o - f_s]} |\Gamma(f)| \\ \text{subject to} \quad & C - \alpha \leq |\Gamma(f)| \leq C + \alpha, \quad f \in [0, f_p], [2f_o - f_p, 2f_p] \\ & \Gamma(0) = C \\ & |\rho_i| \leq 1 \quad \forall i \end{aligned} \quad (8.15)$$

where

$$C = \frac{n_a - n_b}{n_a + n_b} \quad (8.16)$$

Here f_s is the stopping frequency and f_o is the center frequency. In (8.15), α is the passband ripples and f_p is the passband frequency. The bandwidth over which the reflection is minimized is $2(f_o - f_s)$ as shown in Fig. 8.2.

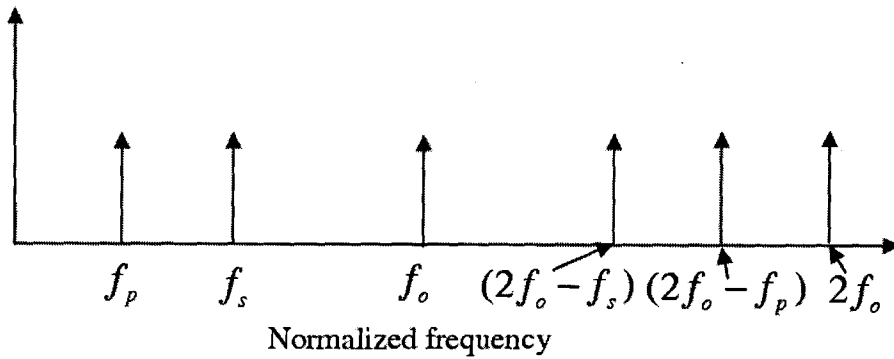


Fig. 8.2. Schematic diagram of the entire frequency band.

The design variables in the optimization problem (8.15) are the elementary reflection coefficients

$$\rho = [\rho_1 \rho_2 \dots \rho_{M+1}]^T, \quad (8.17)$$

The values of the refractive indices of all layers are extracted from the optimized elementary reflection coefficients given in (8.17) using (8.1) starting with $n_0 = n_a$.

The second constraint in (8.15) is added to ensure that the reflection coefficient is equal to its unmatched value when the angular phase shift φ vanishes at dc. The last constraint is added to ensure that the optimized elementary reflection coefficient is physically realizable.

The minimax problem described in (8.15) is not convex if the reflection response is complex. The function (8.14), however, has the same form of a digital filter with finite impulse response (FIR). Formulating the optimization problem as a linear program can thus be done in two different ways; by imposing linear phase polynomials [14] or by using the autocorrelation coefficients of the elementary reflection coefficients ρ as our design variables [8], [9], [10]. Hereafter, the two methods are described in detail.

8.3.1 Linear phase Formulation

For even number of dielectric layers M , we assume that the coefficients of the polynomials given in (8.14) are symmetric around the middle coefficient [14]

$$\rho_i = \rho_{M+2-i}, \quad i = 1, 2, \dots, M + 1. \quad (8.18)$$

Now, the total reflection coefficient can be represented as:

$$\Gamma(\omega') = \rho_1 + \rho_2 e^{-j\omega'} + \dots + \rho_{M+1} e^{-jM\omega'}, \quad (8.19)$$

where

$$\omega' = 2\varphi = \pi \frac{\omega}{\omega_o} \quad (8.20)$$

Simplifying, we get

$$\Gamma(\omega') = e^{-jN\omega'} (2\rho_1 \cos N\omega' + 2\rho_2 \cos((N-1)\omega') + \dots + \rho_{N+1}) = e^{-jN\omega'} \widehat{\Gamma}(\omega') \quad (8.21)$$

where $N = M / 2$ and $\widehat{\Gamma}(\omega')$ is real. It follows that we have

$$|\Gamma(\omega')| = |\widehat{\Gamma}(\omega')|. \quad (8.22)$$

Since $\widehat{\Gamma}(\omega')$ is even and periodic with period 2π , it is sufficient to consider $\omega' \in [0, \pi]$.

The representation of the reflection response in (8.21) is called *linear phase filter response*. This representation makes it possible to apply certain conditions on the elementary reflection coefficients ρ_i . Now, we can reformulate the optimization problem given in (8.15) combined with the expression of the reflection response given in (8.21) and (8.22) as a convex problem given by

$$\begin{aligned}
 & \min_{\rho, \sigma} \quad \sigma \\
 & \text{subject to} \quad -\sigma \leq \widehat{\Gamma}(\omega') \leq \sigma, \quad \omega' \in [\omega_s, \pi], \\
 & \quad \quad \quad C - \alpha \leq \widehat{\Gamma}(\omega') \leq C + \alpha, \quad \omega' \in [0, \omega_p], \\
 & \quad \quad \quad \widehat{\Gamma}(0) = C, \\
 & \quad \quad \quad |\rho_i| \leq 1 \quad \forall i
 \end{aligned} \tag{8.23}$$

where $\omega_s = \pi f_s / f_o$ and $\omega_p = \pi f_p / f_o$. In (8.23), σ is a slack variable used to convert the minimax problem to an equivalent linear program (LP) which can be solved efficiently using IPM.

8.3.2 Autocorrelation Formulation

In the linear phase formulation, the elementary reflection coefficients ρ are used as the design parameters. Here, the autocorrelation coefficients are used instead [8]-[10]. The autocorrelation coefficients of the polynomial in (8.14) are given by

$$r_t = \sum_{\tau} \rho_{\tau} \rho_{t+\tau}, \quad r_t = r_{-t} \tag{8.24}$$

The Fourier transform of the autocorrelation coefficients is the power reflectivity and is given by

$$R(\omega') = \sum_t r_t e^{-j\omega't} = r_o + \sum_{t=1}^M 2r_t \cos \omega't = |\Gamma(\omega')|^2 \tag{8.25}$$

where $R(\omega') \geq 0$ for all ω' . Any condition on the magnitude of the reflection coefficient given as

$$L(\omega) \leq |\Gamma(\omega)| \leq U(\omega) \quad \omega \in [0, \pi] \tag{8.26}$$

where $L(\omega)$ and $U(\omega)$ are the lower and the upper bounds of the magnitude, can be expressed in terms of the autocorrelation coefficients as [10]

$$L(\omega)^2 \leq R(\omega) \leq U(\omega)^2 \quad \omega \in [0, \pi]. \quad (8.27)$$

The optimization problem (8.15) is thus formulated as an LP using the autocorrelation coefficients:

$$\begin{aligned} \min_{r, \sigma'} \quad & \sigma' \\ \text{subject to} \quad & R(\omega') \leq \sigma', \quad \omega' \in [\omega_s, \pi], \\ & (C - \alpha)^2 \leq R(\omega') \leq (C + \alpha)^2, \quad \omega' \in [0, \omega_p], \\ & R(\omega') \geq 0, \quad \omega' \in [0, \pi], \\ & r_o \leq 1, \\ & R(0) = C^2, \end{aligned} \quad (8.28)$$

where σ' corresponds to σ^2 in the original problem. The design variables in the optimization problems given in (8.28) are the autocorrelation coefficients

$$r = [r_o r_1 \dots r_M]^T. \quad (8.29)$$

The third constraint in (8.28) is added to ensure that the optimized sequence r satisfies (8.25) [8], [10]. It can be shown that the fourth constraint in (8.28) satisfies the third one in (8.15).

The convex problem given in (8.28) is a linear program and can be solved efficiently using IPM. Minimum phase spectral factorization [8] is then applied to recover the elementary reflection coefficients ρ from the optimized autocorrelation sequences r . Recurrence in (8.1) is then used to obtain the values of the optimal refractive indices.

Obtaining the sequence $\Gamma(z)$ from its magnitude spectrum $R(z)$ is not unique. There are 2^M possibilities to recover the sequence [13], [14]. Using a spectral factorization approach, a minimum phase factor can be recovered.

8.4 EXAMPLES

Here, we give some numerical examples that illustrate the application of our formulations. The examples are solved using the optimization package SeDuMi [18]. This package automatically finds a feasible starting point. The user does not supply an initial design. The optical length of the layers is fixed at a quarter of a wavelength in all the antireflection examples. In these examples the second constraint in (8.23) and (8.28) is ignored as it does not affect our design problem. Normal incidence is also assumed. The number of frequency points is 1024 over the band of interest.

8.4.1 10-layer Antireflection Coatings

In this example, we utilize both the linear phase and the autocorrelation formulations. The number of dielectric layers in this example is 10 layers. The required bandwidth is $1.5 f_o$ centered around f_o . The values of the refractive indices of the two outside layers are 3.5 (semiconductor) and 1.0 (air).

To check the accuracy of our approximation, the obtained optimal refractive indices are used to get the actual reflection response using (8.1)-(8.6). Fig. 8.3 and Fig. 8.4 show the optimal response obtained using the linear phase and the autocorrelation formulations of the convex problem as compared with the exact response, respectively. These figures show that the difference between the exact response and the optimal response is small. This illustrates the accuracy of the utilized approximations. Table 8.1 shows the optimized values of the refractive indices obtained using the linear phase approach n_{lp} , and the autocorrelation approach n_{ac} .

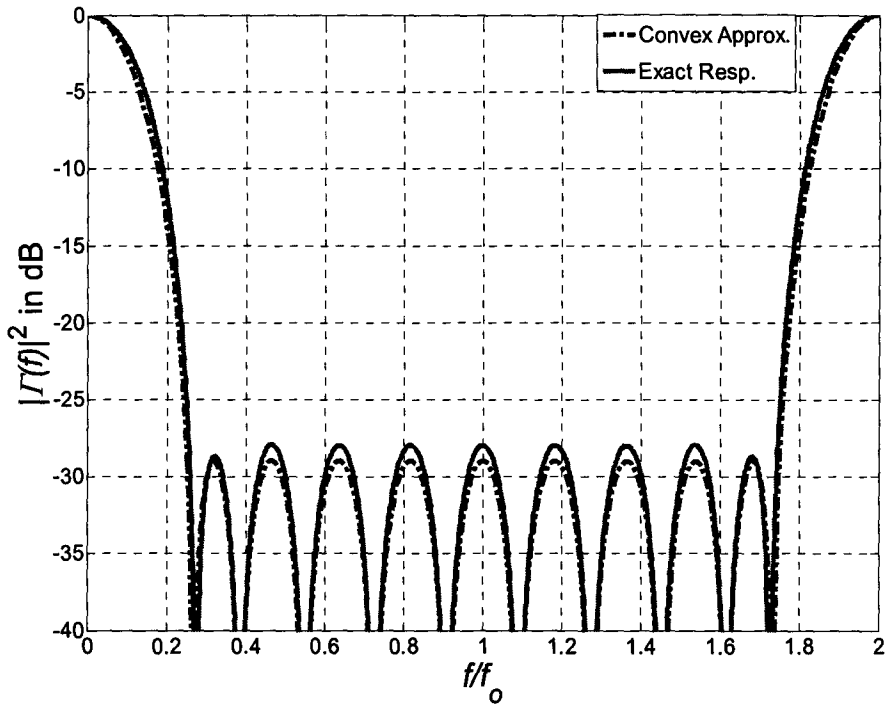


Fig. 8.3. The optimal normalized reflectivity response using the linear phase formulation of the 10-layer AR structure.

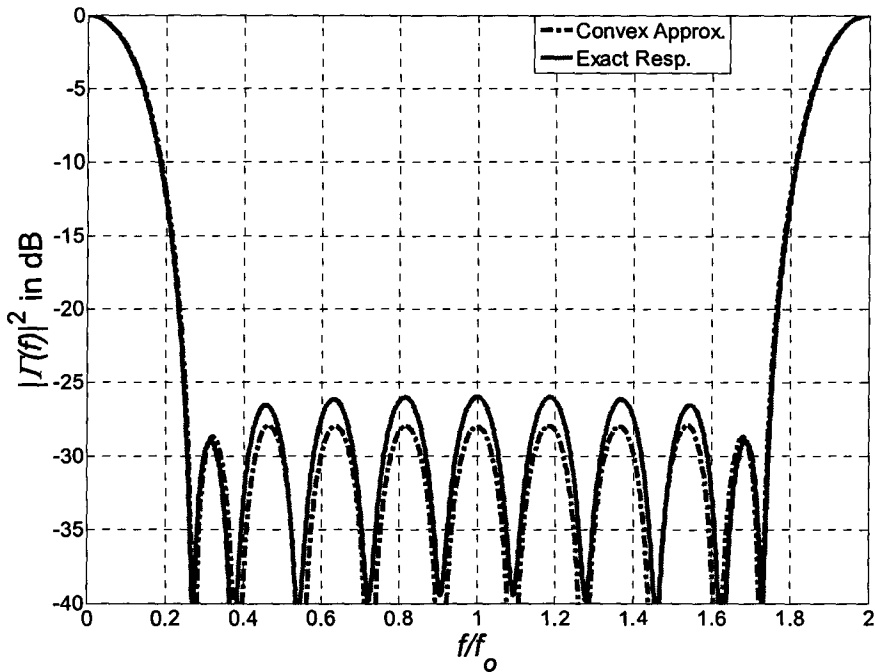


Fig. 8.4. The optimal normalized reflectivity response using the autocorrelation formulation of the 10-layer AR structure.

Table 8.1.

The optimal values of the refractive indices for the 10-layer AR structure.

| | | | | | | | | | | | | |
|----------|-----|-------|-------|-------|-------|------|-------|-------|-------|------|-------|---|
| n_{ac} | 3.5 | 3.333 | 3.10 | 2.78 | 2.412 | 2.04 | 1.712 | 1.449 | 1.256 | 1.13 | 1.05 | 1 |
| n_{lp} | 3.5 | 3.334 | 3.105 | 2.789 | 2.42 | 2.05 | 1.725 | 1.462 | 1.269 | 1.14 | 1.062 | 1 |

Table 8.2.

The optimal refractive indices for the 6-layer AR structure.

| | | | | | | | | |
|-----|-----|------|-----|-------|-------|-------|------|-----|
| n | 3.5 | 3.67 | 2.9 | 2.204 | 1.588 | 1.207 | 1.04 | 1.0 |
|-----|-----|------|-----|-------|-------|-------|------|-----|

Table 8.3.

The optimal refractive indices for the 4-layer AR structure.

| | | | | | | |
|----------|--------|--------|--------|--------|--------|-----|
| n_{sa} | 3.2860 | 2.2678 | 1.6886 | 1.9536 | 1.4546 | 1.0 |
| n_{sb} | 3.2860 | 2.2678 | 1.6938 | 1.9477 | 1.4548 | 1.0 |

8.4.2 6-layer Antireflection Coatings

In this example, a multilayer antireflection coating of 6 layers is designed such that the reflection is minimized over a bandwidth of f_o centered around f_o . The outer layers have refractive indices of 3.5 and 1.0. A reflectivity of less than -58 dB over a bandwidth of $0.4 f_o$ centered around f_o is also required. The autocorrelation formulation is used to design this structure. The optimized response is shown in Fig. 8.5. A minimum reflectivity of -35 dB is achieved over the f_o bandwidth. Also, a reflectivity of -59 dB is achieved over the $0.4 f_o$ band. The values of the optimal refractive indices are shown in Table 8.2.

8.4.3 4-layer Antireflection Coatings

In this example, the linear phase formulation is applied to an SLA antireflection coating design. The number of layers is 4 layers. In this design, it is required to minimize the reflection from GaInAs/AlGaInAs multiple quantum well laser facet which has

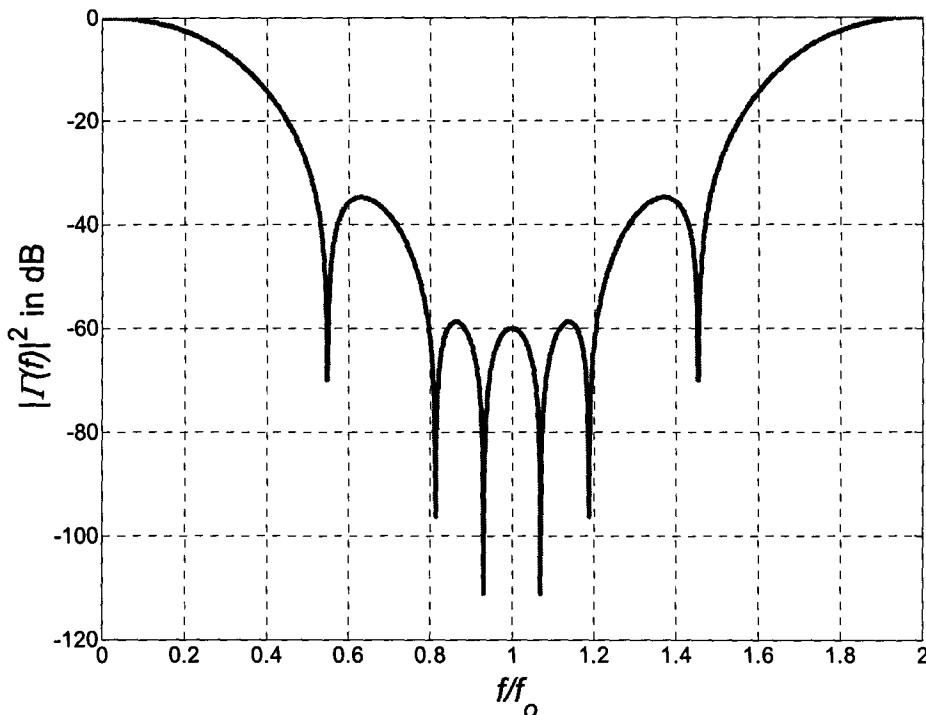


Fig. 8.5. The optimal normalized reflectivity response of the 6-layer AR structure.

an effective index of 3.286 [7]. The bandwidth over which the power reflectivity is minimized is chosen to be 170.0 nm around $\lambda_o = 1.55 \mu\text{m}$. The values of the refractive indices of the layers are chosen to satisfy the following condition

$$1.44 \leq n_i \leq 2.3 \quad i = 1, \dots, 4 \quad (8.30)$$

The optimized power reflectivity of the multilayer structure is shown in Fig. 8.6. It is clear that the reflected power is minimized to -41 dB over the entire bandwidth. The optimized values of the refractive indices of this multilayer structure are shown in the first row of Table 8.3.

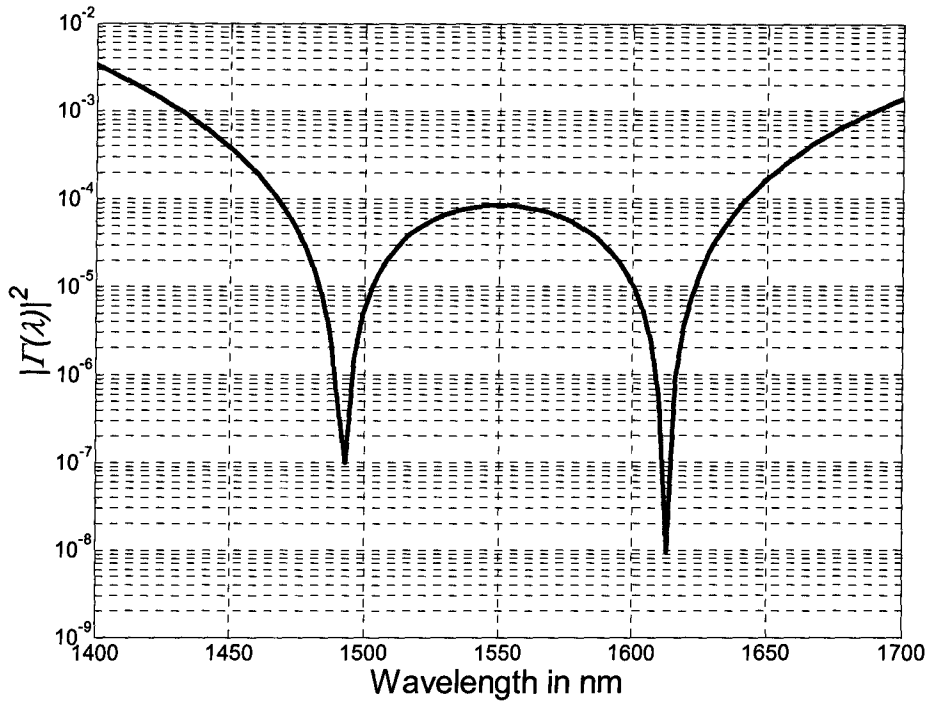


Fig. 8.6. The optimal reflectivity of 4-layer AR structure with 170 nm bandwidth.

We also consider another design for the same structure. Here, the bandwidth over which the reflectivity is minimized is 100.0 nm. The optimized response is shown in Fig. 8.7. As shown from the results, a reflectivity of less than -50 dB is achieved over the entire bandwidth. The results obtained in this example are comparable to those obtained in [7]. However, our optimization procedure is simpler than that represented in [7]. The values of the optimal refractive indices are shown in the second row of Table 8.3.

8.4.4 10-layer Selective Filter

In this example, we illustrate the flexibility of our approach by designing a selective filter. In this case, the optical length of each layer is a half wavelength. The

center frequency f_c is thus $f_c = 2f_o$. The second constraint in (8.23) and (8.28) is exploited to specify the maximum allowable ripples in the passband.

A 10-layer structure is utilized in this example. The passband over which the reflectivity is maximized is chosen to be $0.2 f_c$ around the center frequency f_c . The value of α is 0.1. The outer layers have refractive indices of 3.5 and 1.0. Here, the two proposed formulations are utilized. The optimized response using the autocorrelation formulation is shown in Fig. 8.8 as compared with the exact response. In Fig. 8.9, the optimized response using the linear phase formulation is shown along with the exact response. It is clear from these figures that the autocorrelation formulation has a minimum reflectivity of -7.8 dB in the stopband while the linear phase formulation has minimum reflectivity of -6.7 dB. This is mainly due to symmetry constraint of the reflection coefficients which is imposed in the linear phase approach. This constraint reduces the feasibility region, which in turn affects the results. On the other hand, the linear phase formulation allows for imposing constraints that directly limit the indices values.

In this example, we demonstrate the design procedure of band stop filter utilizing our simple approaches. On the other hand, the AR coatings designs can be considered as band pass filters. Thus, the universality of our approach for any filter design is clearly illustrated.

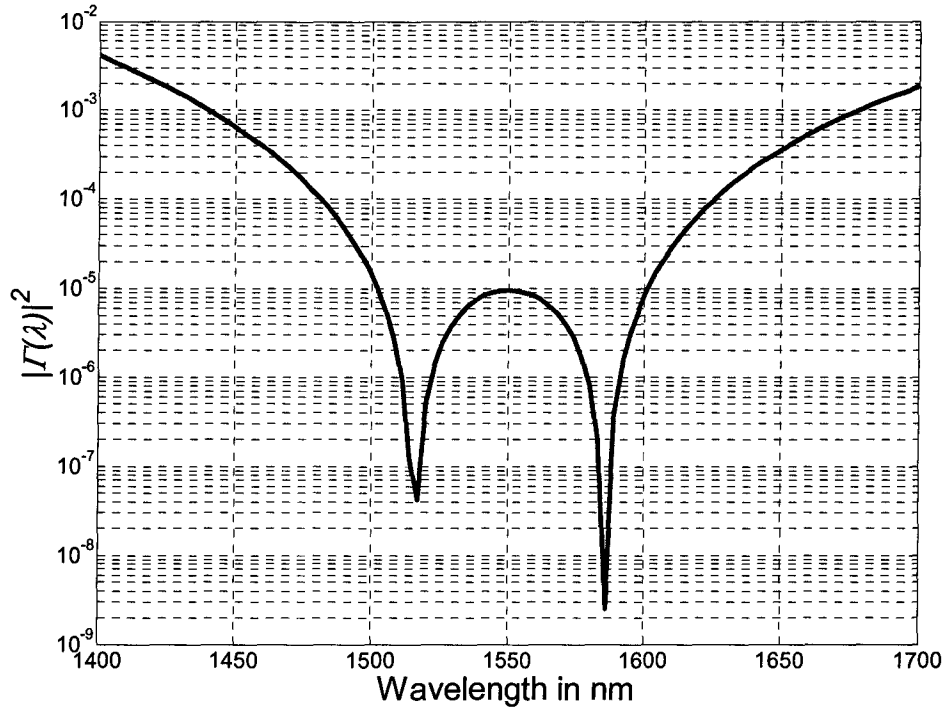


Fig. 8.7. The optimal reflectivity of 4-layer AR structure with 100 nm bandwidth.

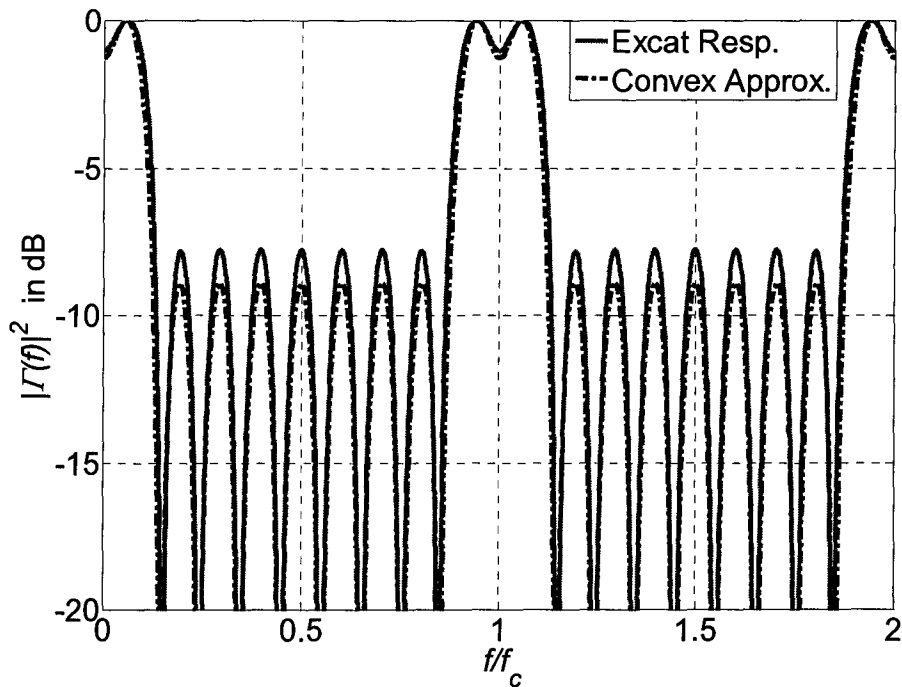


Fig. 8.8. The optimal normalized reflectivity of 10-layer selective filter structure using the autocorrelation formulation.

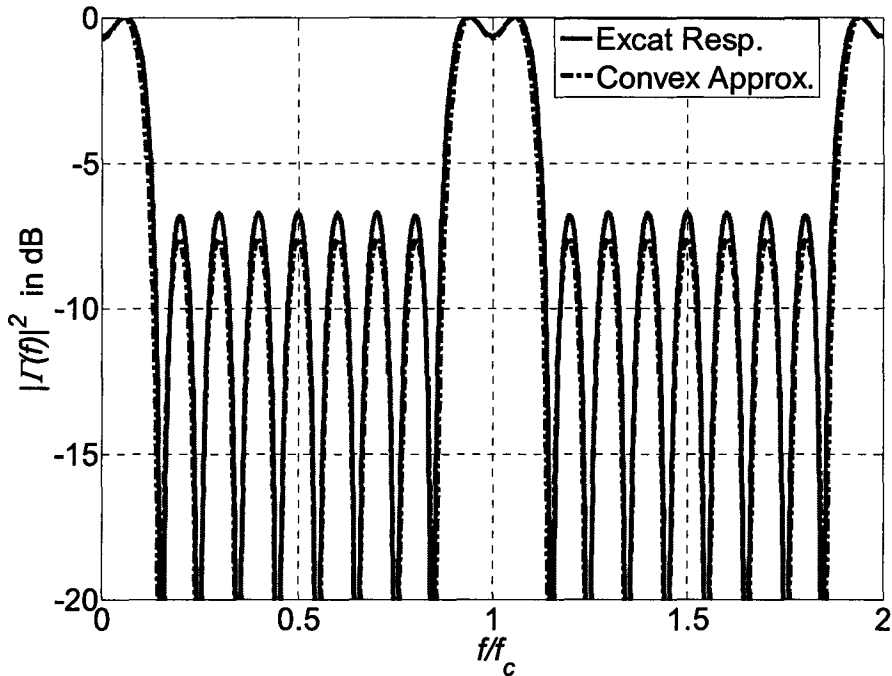


Fig. 8.9. The optimal normalized reflectivity of 10-layer selective filter structure using the linear phase formulation.

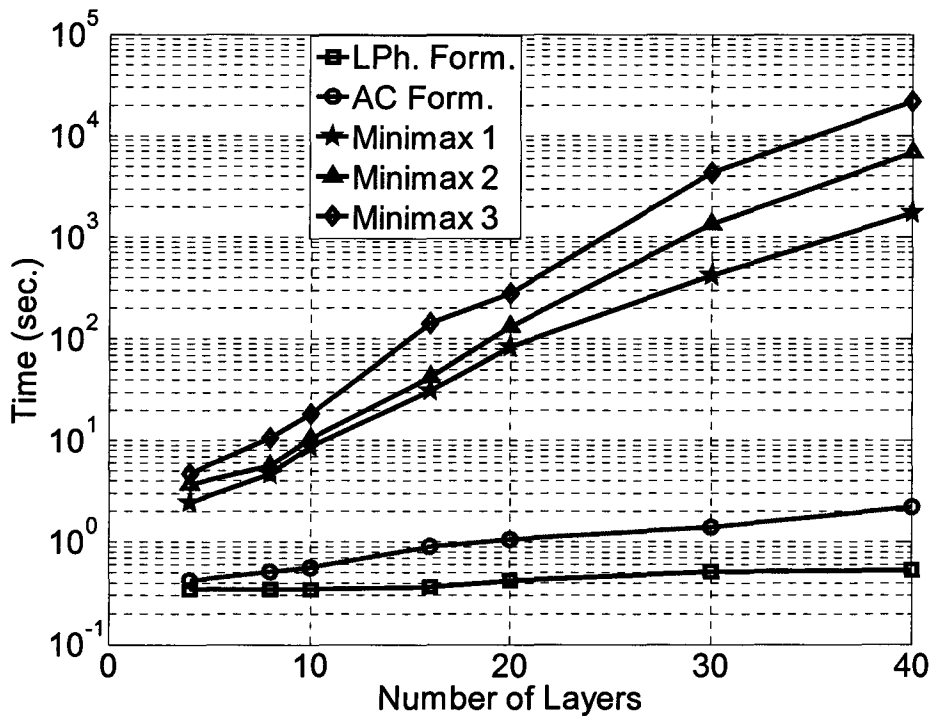


Fig. 8.10. The computational time of solving the benchmark problem for different number of layers.

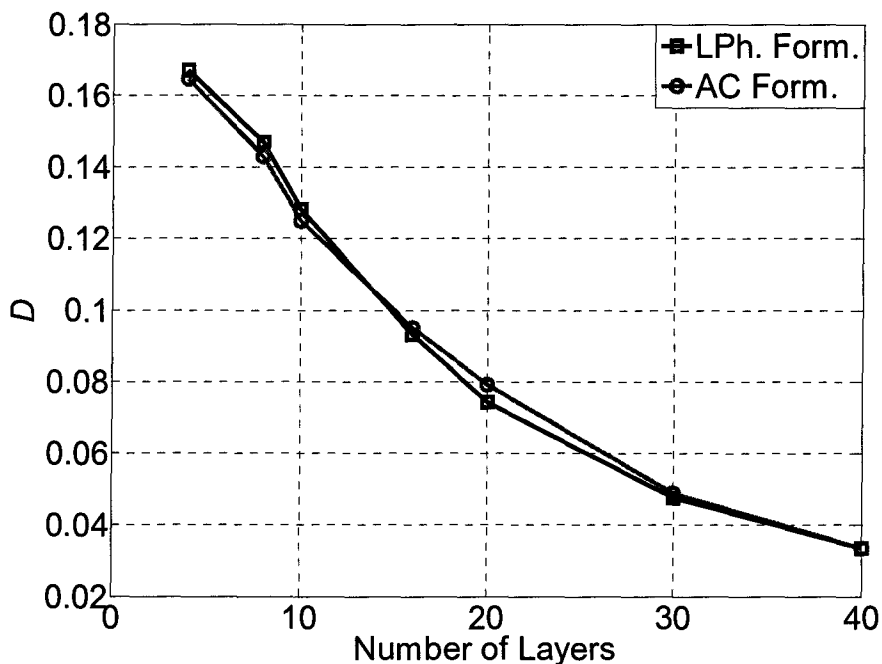


Fig. 8.11. The relative deviation of the minimum reflectivity obtained by solving the benchmark problem for different number of layers.

8.5 DISCUSSION

In this Section, we present a detailed evaluation of the performance of the proposed approaches. A benchmark problem is used for comparing our convex optimization approach and the solution of the exact formula given in (8.4)-(8.6) using Matlab's minimax optimization [23]. For our approach, the Matlab- implemented optimization package (SeDuMi) is used to solve our convex problem. The power reflectivity from a multilayer structure is minimized over a bandwidth of $1.5 f_o$ centered around f_o . This problem is solved using both approaches for a different number of layers. This comparison is performed on a 3.2 GHz Pentium 4 computer with 1.0 GB of RAM.

We study both the computational time and the obtained optimal values for the two proposed approaches.

8.5.1 Computational Time

We first calculate the computational time of both techniques for different number of layers. The results are shown in Fig. 8.10. As shown in this figure, the linear phase formulation (LPh. Form.) takes fractions of a second to obtain the optimal response. The autocorrelation formulation (AC Form.) takes more time due to the cost of the spectral factorization. Sequential quadratic programming (SQP) included in the minimax optimization toolbox in Matlab [23] is utilized to solve the exact problem (8.4)-(8.6) with different initial points. In Fig. 8.10, the first approach (Minimax1) represents the computational time of the minimax problem using the optimal parameters resulting from our approach as the starting point. In the second approach (Minimax2), the initial point is the optimal point obtained from our approach perturbed with a constant perturbation of 0.05 in all dimensions. In the third case (Minimax3), the initial point is the same initial point used in our approach. Our LP solver (SeDuMi) calculates this point automatically by solving an initial feasibility problem using a self-dual embedding technique [20]. It is clear from Fig. 10 that our approach is very efficient in terms of the computational time. The achieved time saving increases with the increase of the number of layers as the complexity of the optimization problem increases. This significant time saving is mainly due two reasons. First, the evaluation cost of the approximate expression (8.14) in our approach is much less than that of the exact expression (8.4)-(8.6). This is especially true for a sufficiently large number of layers. Second, solving a linear programming problem

using an IPM is much faster than solving a non-convex minimax problem using SQP and requires less number of iterations and less number of function evaluations.

8.5.2 Optimal Value

The obtained optimal value in our benchmark problem is the minimum reflectivity. The deviation of our optimal response from the optimal response obtained using the minimax-SQP is calculated using the following expression

$$D = \left| \frac{m_c - m_m}{m_m} \right|, \quad (8.31)$$

where m_c and m_m are the minimum power reflectivity obtained using our approach and using the minimax-SQP method in decibels, respectively. This relative deviation of the optimum is calculated for different number of layers as shown in Fig. 8.11. It is clear from this figure that the relative deviation of the optimal value is decreasing with the increase in the number of layers as the approximate reflection coefficient becomes more accurate as explained in Section 8.2.

In order to further investigate the effect of the starting point which is calculated automatically by the SeDuMi, we execute the benchmark problem 100 times for structures with 10, 20, 30, and 40 layers. At each run, the software calculates different initial point for each design. However, the results show that the obtained optimal values and optimal refractive indices do not change with the variation of the initial point. This is a consequence of the convexity of the problem. The variation in the computational time due to the variation of the initial point does not exceed 5% of the mean computational time for each case.

8.6 CONCLUSION

A novel approach for the design of multilayer structures is presented. The design problem is formulated as a convex optimization problem. Two different possible formulations are introduced. The solutions obtained using our approaches are globally optimal because of the convexity of the formulation. Our formulations are successfully illustrated through the design of a number of multilayer structures. They are shown to be computationally efficient and accurate compared to other optimization approaches.

8.7 REFERENCES

- [1] B. Kjomrattanawanich, D. L. Windt, J. F. Seely, and Y. A. Uspenskii, “SiC/Tb and Si/Tb multilayer coatings for extreme ultraviolet solar imaging,” *Appl. Opt.*, vol. 45 pp. 1765–1772. March 2006.
- [2] R. R. Willey, *Practical Design and Production of Optical Thin Films*, 2nd ed. Marcel Dekker Inc., New York, 2002.
- [3] P. Yeh, *Optical Waves in Layered Media*, Wiley, New York, 1988.
- [4] H. A. Macleod, *Thin-Film Optical Filters*, 3rd ed. New York: McGraw-Hill, 2001.
- [5] A. Thelen, *Design of Optical Interference Coatings*, in McGraw-Hill Optical and Electro-Optical Engineering Series. New York: McGraw- Hill, 1989.
- [6] N. Kaiser and H. K. Pulker, *Optical Interference Coatings*. Springer-Berlin; NY, 2003.
- [7] J. Lee, T. Tanaka, S. Sasaki, S. Uchiyama, M. Tsuchiya, and T. Kamiya, “Novel design procedure of broad-band multilayer antireflection coatings for optical and

optoelectronic devices,” *IEEE/OSA J. Lightwave Technol.*, vol. 16, pp. 884–891, May 1998.

- [8] S. Boyd and L. Vandenberghe, *Convex Optimization*. Cambridge University Press, 2004.
- [9] Y. Nesterov and A. Nemirovsky, *Interior-point Polynomial Methods in Convex Programming*, SIAM, Philadelphia, PA, 1994.
- [10] J. Nocedal and S. J. Wright, *Numerical Optimization*. Springer, New York, 1999.
- [11] V. Tikhonravov, M. K. Trubetskov, T. V. Amotchkina, and A. Thelen, “Optical coating design algorithm based on the equivalent layers theory,” *Appl. Opt.*, vol. 45, pp. 1530–1538, March. 2006.
- [12] J. A. Dobrowolski and S. H. C. Piotrowski, “Refractive index as a variable in the numerical design of optical thin film systems,” *Appl. Opt.*, vol. 21, pp. 1502–1511, April. 1982.
- [13] S. J. Orfanidis, *Optimum Signal Processing: An Introduction*, 2nd ed., McGraw-Hill, New York, 1988.
- [14] A. V. Oppenheim, R. W. Schaffer, *Discrete Time Signal Processing*. New Jersey: Prentice-Hall, 1999.
- [15] S.-P. Wu, S. Boyd, and L. Vandenberghe, “FIR filter design via semidefinite programming and spectral factorization,” *In Proc. IEEE Conf. on Decision and Control*, 1996, pp. 271–276.

- [16] B. Alkire and L. Vandenberghe, “Convex optimization problems involving finite autocorrelation sequences,” *Mathematical Programming*, vol. 93, pp. 331–359, July 2002.
- [17] S.-P. Wu, S. Boyd, and L. Vandenberghe, “FIR filter design via spectral factorization and convex optimization,” In B. Datta, editor, *Applied and Computational Control, Signals, and Circuits*, vol. 1, pp.215–245. Birkhauser, 1998.
- [18] J. F. Sturm, “Using SeDuMi 1.02, a MATLAB toolbox for optimization over symmetric cones,” *Optimization Methods and Software*, vol. 11–12, pp. 625– 653, 1999. Available from <http://sedumi.mcmaster.ca>.
- [19] Matlab™, 2005. Version 7.04.
- [20] J. F. Sturm, “Implementation of interior point methods for mixed semidefinite and second order cone optimization problems,” *Optimization Methods and Software*, vol. 17, pp.1105–1154, Dec. 2002.

9 CONCLUSIONS

This thesis is considered as a milestone for efficient optimization techniques based on numerical simulation for photonic devices. It presents the recent advances in the application of the adjoint variable method to photonic devices. It also presents a novel approaches for formulating the design of any photonic devices as an optimization problem. These optimization problems are then solved efficiently using gradient-based optimization algorithms. This optimization problem can be also formulated as convex program and solved efficiently using interior point method. These approaches will highly accelerate the design cycle of novel structures to meet the ever demanding requirements of the photonic devices.

Chapter 2 is dedicated for reviewing the fundamentals of some of the well known numerical techniques for modeling photonic devices. The governing equations of both FDTD and BPM have been discussed and presented. The implementation details for both techniques are also briefly discussed. We also explained the advantage and disadvantage of both techniques. We discussed the different versions of the BPM approach and the application of each of these versions.

Chapter 3 concerned itself with reviewing the existing AVM approaches for time domain and frequency domain numerical techniques. The basic concepts and mathematical details of both approaches are presented in detail. We also discussed the implementation of these techniques to the photonic design problem.

In Chapter 4 we proposed a second order accurate AVM-based approach for sensitivity analysis and design optimization of photonic devices using the FDTD method. This approach has been utilized for sensitivity analysis and design optimization of different structures such as power splitters. It is also utilized for sensitivity analysis of the power reflectivity of deeply etched waveguide terminators and SOA antireflection coatings. The sensitivities of the reflectivity with respect to all the design parameters are obtained over the desired bandwidth with minimum additional cost. No additional simulation is needed for obtaining this sensitivity information. The obtained sensitivities are also compared with those obtained using the time intense central finite difference (CFD) approach applied directly at the response level.

Chapter 5 presented a novel approach for efficient sensitivity analysis of photonic devices using the BPM. This approach has been applied to the 2D scalar version as well as the full vectorial and semi-vectorial 3D versions of the BPM. Two different approaches for both the iterative BPM and the alternative direction implicit BPM have been proposed and discussed. The sensitivity analysis of the guided modes and their modal properties has been also obtained using the imaginary distance BPM and the full vectorial BPM. Our approach has been utilized for efficient sensitivity analysis of different photonic devices such as power splitters, polarization converters, rib waveguides, and fiber couplers. This technique is also utilized for efficient sensitivity analysis of different surface plasmon waveguide structures. The obtained sensitivity has been also incorporated in a gradient-based optimization algorithm to maximize the power transfer through a fiber coupler.

In Chapter 6, we proposed an efficient approach for design optimization of a novel design of an optical switch with compact size operating over a wide working wavelength band. This device is based on utilizing a multimode waveguide with a stair case index profile as an approximation for the parabolic index. A two-step optimization technique has been utilized for this purpose. The optimization algorithm utilizes the sensitivity of the response obtained using the AVM approach with the BPM simulation. The optimized device has a wide bandwidth and compact size and low loss compared with the traditional approaches for realizing this application.

Chapter 7 highlighted the efficient approaches for sensitivity analysis of the eigenvalues and eigenvectors obtained using the Schrödinger equation. Different approaches have been proposed for both time-dependant and time-independent versions of the Schrödinger equation. Our approaches proved their efficiency compared to the sensitivity obtained using CFD approach.

In Chapter 8, a novel formulation of multilayer optical structures design problem as a convex programming is proposed and discussed. This approach is efficient and capable of obtaining the global solution of the problem by utilizing interior point methods. Fractions of a second are only needed, using our approach, to obtain the optimal design of up to 40 layers without providing initial design parameters. Our approach has been utilized for designing different types of filter response using multilayer structures. The types include, anti reflection coatings, high reflection coatings, and bandpass filters.

This thesis provides a useful guidance for opening new horizon in the photonic simulation- based optimization techniques. It provides key approaches that are suitable

for most of the existing photonic structures. From experience gained during the course of this thesis the author suggests the following research topics to be addressed in the future:

1-Applying the AVM approach for other BPM versions especially wide angle BPM and bi-directional BPM.

2-Exploiting the efficiently obtained sensitivity information in topology optimization algorithms to enhance the design process.

3-Exploiting the sensitivity obtained using the time-dependent Schrödinger equation for design optimization of electro-optic absorption modulators under bias effect.

4-Investigating the application of the transmission line modeling (TLM) approach and its associated AVM approach for designing different photonic devices.

BIBLIOGRAPHY

- N. K. Nikolova, R. Safian, E. A. Soliman, M. H. Bakr, and J. W. Bandler, "Accelerated gradient based optimization using adjoint sensitivities," *IEEE Trans. Antennas Propagat.*, vol. 52, pp. 2147–2157, Aug. 2004.
- M. H. Bakr and N. K. Georgieva, "An adjoint variable method for frequency domain TLM problems with conducting boundaries," *IEEE Microwave Wireless Comp. Lett.*, vol. 13, pp. 408–410, Nov. 2003.
- M. H. Bakr and N. K. Nikolova, "An adjoint variable method for time domain TLM with wideband Johns matrix boundaries," *IEEE Trans. Microwave Theory Tech.*, vol. 52, pp. 678–685, Feb. 2004.
- N. K. Nikolova, H. W. Tam, and M. H. Bakr, "Sensitivity analysis with the FDTD method on structured grids," *IEEE Trans. Microwave Theory Tech.*, vol. 52, pp. 1207–1216, Apr. 2004.
- H. Akel and J. P. Webb, "Design sensitivities for scattering-matrix calculation with tetrahedral edge elements," *IEEE Trans. Magn.*, vol. 36, pp. 1043–1046, July 2000.
- G. Veronis, R. W. Dutton, and S. Fan, "Method for sensitivity analysis of photonic crystal devices," *Optics Letters*, vol. 29, pp. 2288–2290, Oct. 2004.
- N. K. Georgieva, S. Glavic, M.H. Bakr, and J.W. Bandler, "Feasible adjoint sensitivity technique for EM design optimization," *IEEE Trans. Microwave Theory Tech.*, vol. 50, pp. 2751–2758, Dec. 2002.
- S.-P. Wu, S. Boyd, and L. Vandenberghe, "FIR filter design via semidefinite programming and spectral factorization," *Proc. IEEE Conf. on Decision and Control*, 1996, pp. 271–276.
- B. Alkire and L. Vandenberghe, "Convex optimization problems involving finite autocorrelation sequences," *Mathematical Programming*, vol. 93, pp. 331–359, July 2002.
- S.-P. Wu, S. Boyd, and L. Vandenberghe, "FIR filter design via spectral factorization and convex optimization," In B. Datta, editor, *Applied and Computational Control, Signals, and Circuits*, vol. 1, pp.215–245. Birkhauser, 1998.
- M. A. Swillam, M. H. Bakr, N. K. Nikolova, and X. Li, "Adjoint sensitivity analysis of dielectric discontinuities using FDTD," *J. Electromagnetics*, vol. 27 , pp. 123 – 140, Feb. 2007.
- M. A. Swillam, M. H. Bakr, and X. Li, "Accurate sensitivity analysis of photonic devices exploiting the finite- difference time-domain central adjoint variable method," *Appl. Opt.*, vol. 46 , pp. 1492 – 1499, Mar. 2007.
- M. A. Swillam, M. H. Bakr, and X. Li, "Accurate and efficient sensitivity extraction of complex structures using FDTD," *Photonics North, proceedings of SPIE 6796: 67963A-1– 67963A-8.I*, Ottawa 2007. Best student paper award.

- M. A. Swillam, M. H. Bakr, N. K. Nikolova, and X. Li, “Second order accurate sensitivities of dielectric discontinuities using FDTD,” *The 24th International Review of Progress in Applied Computational Electromagnetics (ACES)*: 1034–1039, Niagara falls 2008.
- M. A. Swillam, M. H. Bakr, and X. Li, “Full wave sensitivity analysis of guided wave structures using FDTD,” *J. Electromag. Waves Applicat. (JEMWA)*, vol. 22, no. 16, pp 2135-2145, 2008
- M. A. Swillam, M. H. Bakr, and X. Li, “Efficient Adjoint sensitivity analysis exploiting the FD-BPM,” *IEEE/OSA J. Lightwave Technol.*, vol. 25, no. 7, pp. 1861 – 1869, Jul. 2007.
- M. A. Swillam, M. H. Bakr, and X. Li, “BPM based efficient sensitivity analysis exploiting the adjoint variable method,” *Integrated Photonics and Nanophotonics Research and Applications (IPNRA)*, OSA Technical Digest (CD): IWB4. 1–3, Salt Lake City 2007.
- M. A. Swillam, M. H. Bakr, and X. Li, “Full vectorial 3D sensitivity analysis and design optimization using BPM,” *IEEE/OSA J. Lightwave Technol.*, vol. 26, pp 528 – 536, Mar. 2008.
- M. A. Swillam, M. H. Bakr, and X. Li, “Accurate and efficient sensitivity analysis using the beam propagation method,” *Photonics North, proceedings of SPIE 7099: 70991C-1–70991C-8*. Montreal 2008.
- M. A. Swillam, M. H. Bakr, and X. Li, “Efficient approach for 3D full vectorial sensitivity analysis using ADI-BPM,” *Integrated Photonics and Nanophotonics Research and Applications (IPNRA)*, OSA Technical Digest (CD): IWF8. 1–3, Boston 2008.
- M. A. Swillam, M. H. Bakr, and X. Li, “Design optimization of compact wideband optical switch exploiting stair case index MMI,” *IEEE/OSA J. Lightwave Technol.*, vol. 27. pp 80 – 87 Jan. 15th 2009.
- M. A. Swillam, M. H. Bakr, and X. Li, “Wide band optical switch using stair case MMI,” *LEOS Annual Meeting*, Newport Beach 2008.
- M. A. Swillam, M. H. Bakr, and X. Li, “Efficient 3D sensitivity analysis of surface plasmon waveguide structures,” *Opt. Express*, vol. 16, pp. 16371-16381 Oct. 2008.
- M. A. Swillam, M. H. Bakr, X. Li and J. Deen, “Efficient sensitivity analysis of time independent Schrödinger equation with application to quantum lasers,” *Optics Comm.* vol. 281, pp 4169-4554, Sep. 2008.
- M. A. Swillam, M. H. Bakr, and X. Li, “The design of multilayer optical coatings using convex optimization,” *IEEE/OSA J. Lightwave Technol.*, vol. 25 , pp. 1078 – 1085, Apr. 2007.
- M. A. Swillam, M. H. Bakr, and X. Li, “Design of multilayer optical filters using linear programming based on autocorrelation sequences,” *Integrated Photonics and Nanophotonics Research and Applications (IPNRA)*. OSA Technical Digest (CD): ITuA6.1–3, Salt Lake City 2007.

- M. A. Swillam, M. H. Bakr, and X. Li, “A novel design approach for multilayer dielectric filters exploiting linear programming,” *IEEE Antenna and propagation international symposium (APs)*: 3940 – 3943, Honolulu 2007.
- K. S. Yee, “Numerical solution of initial boundary value problems involving Maxwell's equations in isotropic media,” *IEEE Trans. Antenna Propagat.*, vol 14, pp 302-307, May 1966.
- A. Taflov, *Computational Electrodynamics: The Finite Difference Time Domain Method*. Norwood, MA: Artech House, 1995
- J. P. Berenger, “A Perfectly Matched Layer for the Absorption of Electromagnetic-Waves,” *J. of Comp. Phys.*, vol. 114, no. 2, pp. 185-200, Oct. 1994.
- W. C Chew, and W. H Weedon, “A 3-D perfectly matched medium from modified Maxwell’s equations with stretched coordinates,” *Microw. Opt. Technol. Lett.* , vol. 7, pp.599–603, Sept. 1994
- Z. S. Sacks, D. M. Kingsland, R. Lee, and J. F. Lee, “A perfectly matched anisotropic absorber for use as an absorbing boundary condition,” *IEEE Trans. Antennas Propagat.* vol. 43, pp. 1460-1463, Dec. 1995.
- M. D. Feit and J. A. Fleck, Jr., “ Light propagation in graded-index optical fibers,” *Appl. Opt.*, vol. 17, pp. 3990-3998, Dec. 1978.
- Y. Chung and N. Dagli, “An assessment of finite difference beam propagation method,” *IEEE J. Quantum Electron.*, vol. 26, pp.1335-1339, Aug. 1990.
- D. Yevick and B. Hermansson, “New formulations of the matrix beam propagation method: Application to rib waveguides,” *IEEE J. Quantum Electron.*, vol. 25, pp. 221-229, Feb. 1989.
- R. Scarmozzino, A. Gopinath, R. Pregla, and S. Helfert, “Numerical techniques for modeling guided-wave photonic devices,” *IEEE J. Select. Topics Quantum Electron.*, vol. 6, pp. 150–162, Jan./Feb. 2000.
- W. P. Huang, C. L. Xu, S. T. Chu, and S. K. Chaudhuri, “A vector beam propagation method for guided-wave optics,” *IEEE Photon. Tech. Lett.*, vol. 3, pp. 910-913, Oct. 1991.
- W. P. Huang and C. L. Xu, “Simulation of three-dimensional optical waveguides by a full-vector beam propagation method,” *IEEE J. Quantum Electron.*, vol. 29, pp. 2639–2649, Oct. 1993.
- C. L. Xu, W. P. Huang S. K. Chaudhuri, and J. Chrostowski, “An unconditionally stable vectorial beam propagation method for 3-D structures,” *IEEE Photon. Technol. Lett.*, vol .6, pp. 549 – 551, Apr. 1994.
- E. E. Kriezis and A. G. Papagiannakis, “A three-dimensional full vectorial beam propagation method for z-dependent structures,” *IEEE J. Quantum Electron.*, vol. 33, pp. 883–890, May 1997.
- Y. Hsueh, M. Yang, and H. Chang, “Three-dimensional noniterative full-vectorial beam propagation method based on the alternating direction implicit method,” *IEEE/OSA J. Lightwave Technol.*, vol. 19, pp. 2389–2397, Nov. 1999.

- I. Mansour, A. D. Capobianco, and C. Rosa, “Noniterative vectorial beam propagation method with a smoothing digital filter,” *IEEE/OSA J. Lightwave Technol.*, vol. 14, pp. 908–913, May 1996.
- J. Yamauchi, T. Ando, and H. Nakano, “Beam-propagation analysis of optical fibers by alternating direction implicit method,” *Electron. Lett.*, vol. 27, pp. 1663–1665, Aug. 1991.
- P. L. Liu and B. J. Li, “Semivectorial beam-propagation method for analyzing polarized modes of rib waveguides,” *IEEE J. Quantum Electron.*, vol. 28, pp. 778–782, Apr. 1992.
- G. R. Hadley, “Transparent boundary condition for the beam propagation method,” *IEEE J. Quantum Electron.*, vol. 28, pp. 363-370, Jan. 1992.
- W. P. Huang, C. Xu, W. W. Lui, and K. Yokoyama, “The perfectly matched layer (PML) boundary condition for the beam propagation method,” *IEEE Photon. Technol. Lett.*, vol. 8, pp. 649–651, May 1996.
- G. R. Hadley, “Wide-angle beam propagation using Padé approximant operators,” *Opt. Lett.*, vol. 17, pp. 1426-1428, Oct. 1992.
- I. Ilic, R. Scarmozzino, and R. M. Osgood Jr., “Investigation of the Pade approximant-based wide-angle beam propagation method for accurate modeling of waveguiding circuits,” *IEEE/OSA J. Lightwave Technol.*, vol. 14, pp. 2813–2822, 1996.
- H. El-Refaei, D. Yevick, and Ian Betty, “Stable and noniterative bidirectional beam propagation method,” *IEEE Photon. Technol. Lett.*, vol. 12, No. 4, pp. 389-391, April 2000.
- S. W. Director and R. A. Rohrer, “The generalized adjoint network and network sensitivities,” *IEEE Trans. Circuit Theory*, vol. CT-16, pp. 318–323, Aug. 1969.
- J. W. Bandler and R. E. Seviara, “Wave sensitivities of networks,” *IEEE Trans. Microwave Theory Tech.*, vol. MTT-20, pp. 138–147, Feb. 1972.
- K. C. Gupta, R. Garg, and R. Chadha, *Computer-Aided Design of Microwave Circuits*. Dedham, MA: Artech House, 1981.
- F. Alessandri, M. Mongiardo, and R. Sorrentino, “New efficient full wave optimization of microwave circuits by the adjoint network method,” *IEEE Microwave Guided Wave Lett.*, vol. 3, pp. 414–416, Nov. 1993.
- I. H. Park, I. G. Kwak, H. B. Lee, S. Y. Hahn, and K. S. Lee, “Design sensitivity analysis for transient eddy current problems using finite element discretization and adjoint variable method,” *IEEE Trans. Magn.* vol. 32, pp 1242-1245, May. 1996.
- H. Lee and T. Itoh, “A systematic optimum design of waveguide-to-microstrip transition,” *IEEE Trans. Microwave Theory Tech.*, vol. 45, pp. 803-809, May 1997.
- Y. Chung, J. Ryu, C. Cheon, I. Park, and S. Hahn, “Optimal design method for microwave device using time domain method and design sensitivity analysis— Part I : FETD case,” *IEEE Trans. Magn.*, vol. 37, pp. 3289-3293, Sept. 2001.
- E. J. Haug, K. K. Choi, and V. Komkov, *Design Sensitivity Analysis of Structural Systems*, Orlando, FL: Academic. 1986.

- N. K. Nikolova, J. W. Bandler, and M. H. Bakr, “Adjoint techniques for sensitivity analysis in high-frequency structure CAD,” *IEEE Trans. Microwave Theory Tech. (Special Issue)*, vol. 52, pp. 403–419, Jan. 2004.
- N. K. Nikolova, Ying Li, Yan Li, and M. H. Bakr, “Sensitivity analysis of scattering parameters with electromagnetic time-domain simulators,” *IEEE Trans. Microwave Theory Tech.* vol. 54, pp.1598-1610 Apr. 2006.
- M. H. Bakr, N.K. Nikolova, and P.A.W. Basl, “Self-adjoint *S*-parameter sensitivities for lossless homogeneous TLM problems,” *Int. J. of Numerical Modelling: Electronic Networks, Devices and Fields.* vol. 18, pp. 441-455 Nov. 2005.
- G. -R. Zhou, X. Li, and N.-N. Feng, “Design of deeply-etched antireflective waveguide terminators,” *IEEE J. Quantum Electron.* vol. 39, pp. 384–391, Feb. 2003.
- G. -R. Zhou, X. Li and N.-N.Feng, “Optimization of deeply-etched antireflective waveguide terminators by space mapping technique,” *Integrated Photonics Research (IPR)*, IThH2, San Francisco, 2004.
- T. Sitoh, T. Mukai, and O. Mikami, “Theoretical analysis and fabrication of antireflection coatings on laser-diode facets,” *IEEE/OSA J. Lightwave Technol.* vol. 3, pp. 288-293. Apr. 1985
- M. D. Feit and J. A. Fleck Jr., “Computation of mode properties in optical fiber waveguides by a propagation beam method,” *Appl. Opt.*, vol. 19, pp. 1154–1164, Apr. 1980.
- T. K. Sarkar and O. Pereira, “Using the matrix pencil method to estimate the parameters of a sum of complex exponentials,” *IEEE Antennas Propagat. Mag.*, vol. 37, pp. 48–55, Feb. 1995.
- K. Kawano and T. Kitoh, *Introduction of Optical Waveguide Analysis*, John Willy Canada 2001.
- W. -P. Huang, C. L. Xu, and S. K. Chaudhuri, “A finite-difference vector beam propagation method for three-dimensional structures,” *IEEE Photon. Technol. Lett.*, vol. 4, pp. 148–151, Feb. 1992.
- P. L. Ho and Y. Y. Lu, “A bidirectional beam propagation method for periodic waveguides,” *IEEE Photon. Technol. Lett.*, vol. 14, pp. 325–327, Mar. 2002.
- B. Saadany, D. A. Khalil, “Modeling of MOEMS components using HDL-A,” *IEEE J. Select. Topics Quantum Electron.*, vol. 33, pp. 132–138, Jan./Feb. 2002.
- K. Zinoviev, C. Dominguez, J. A Plaza, V. J. C Busto, and L. M Lechuga, “A novel optical waveguide microcantilever sensor for the detection of nanomechanical forces,” *IEEE/OSA J. Lightwave Technol.*, vol. 24 pp 2132 – 2138, May 2006.
- L. D. S. Alcantara, F. L. Teixeira, A. C. Cesar, and B. V. Borges, “A new full-vectorial FD-BPM scheme: application to the analysis of magneto optic and nonlinear saturable media,” *IEEE/OSA J. Lightwave Technol.*, vol. 23, pp 2579–2585, Aug. 2005.
- H. A. Haus, *Waves and Fields in Optoelectronics*, Englewood Cliffs, NJ: Prentice Hall, 1984.

- K. Okamoto, *Fundamentals of Optical Waveguides*, Academic Press, 2000.
- D. Marcuse, *Light Transmission Optics*, Van Nostrand Reinhold Company, 1972.
- L. B. Soldano, and E. C. Pennings, “Optical multi-mode interference devices based on self-imaging: principles and applications,” *IEEE/OSA J. Lightwave Technol.*, vol. 13, pp 615–627, Apr. 1995.
- C. L. Xu, W. P. Huang, and S. K. Chaudhuri, “Efficient and accurate vector mode calculations by beam propagation method,” *IEEE/OSA J. Lightwave Technol.*, vol. 11, pp. 1209–1215, July 1993.
- N. N. Feng, G. R. Zhou, and W. P. Huang, “Mode calculation by beam propagation method combined with digital signal processing technique,” *IEEE J. Quantum Electron.*, vol. 39, pp. 1111–1117, Sept. 2003.
- P. Chamorro-Posada, R. Gómez-Alcalá, and F. J. Fraile-Peláez “Modal analysis of optical waveguides using prony's method and BPM,” *Microw. Opt. Tech. Letters*, vol. 7, pp. 529-532, Aug. 1994.
- *Matlab*TM, 2005. Version 7.04.
- T. F. Coleman, and Y. Li, “An interior, trust region approach for nonlinear minimization subject to bounds,” *SIAM Journal on Optimization*, vol. 6, pp. 418-445, May 1996.
- T. F. Coleman, and Y. Li, “On the convergence of interior-reflective Newton methods for large-scale nonlinear minimization subject to bounds,” *Math. Programm.*, vol. 67, pp. 189-224, Oct. 1994.
- P. A. W. Basl, M. H. Bakr and N. K. Nikolova, “Efficient estimation of sensitivities in TLM with dielectric discontinuities,” *Microwave and Wireless Compon. Lett.* vol. 15, pp 89-91 Feb. 2005.
- G. Veronis, and S. Fan, “Modes of subwavelength plasmonic slot waveguides,” *IEEE/OSA J. Lightwave. Technol.*, vol. 25, pp 2511-2521, Sep. 2007.
- W. L. Barnes, A. Dereux and T. W. Ebbesen “Surface plasmon subwavelength optics,” *Nature*. vol. 424, pp. 824-830, Aug. 2003.
- P. Berini, “Plasmon-polariton waves guided by thin lossy metal films of finite width: Bound modes of symmetric structures,” *Phys. Rev. B, Condens. Matter.* vol 61, pp 10484–10503, Apr. 2000.
- I. Breukelaar, R. Charbonneau, and P. Berini, “Long-range surface plasmon-polariton mode cutoff and radiation in embedded strip waveguides,” *J. Appl. Phys.* vol 100, pp. 043104-1–043104-9, Aug. 2006.
- N. N. Feng; M. L Brongersma, and L. D Negro, “Metal–Dielectric slot-waveguide structures for the propagation of surface plasmon polaritons at 1.55 μm ,” *IEEE J. Quantum Electron.* vol. 43, pp. 479 - 485 Jun. 2007.
- J. Homola, S. S. Yee, G. Gauglitz, “Surface plasmon resonance sensors: review,” *Sensors and Actuators B*, vol. 54, pp. 3-15, Jan. 1999.
- R. D. Harris, J.S. Wilkinson, “Waveguide surface plasmon resonance sensors,” *Sensors and Actuators B* vol. 29, pp.261-267, Oct. 1995.
- J. Homola, “Present and future of surface plasmon resonance biosensors,” *Analytical and Bioanalytical Chemistry*, vol. 377, pp. 528-539, Oct. 2003.

- J. Shibayama, S. Takagi, T. Yamazaki, J. Yamauchi, and H. Nakano, “Numerical analysis of waveguide-based surface plasmon resonance sensor with adsorbed layer using two- and three-dimensional beam-propagation methods,” *IEICE TRANS. Electron.*, vol. E90–C, pp. 95-100, Jan. 2007.
- J. Shibayama, S. Takagi, T. Yamazaki, J. Yamauchi, and H. Nakano, “Eigenmode analysis of a light-guiding metal line loaded on a dielectric substrate using the imaginary-distance beam-propagation method,” *IEEE/OSA J. Lightwave Technol.* vol. 23, pp.1533- 1539, Mar. 2005.
- K. C. Lin and W. Y. Lee, “Guided-wave 1.30/1.55 μm wavelength division multiplexer based on multimode interference,” *Electron. Lett.* vol. 32, pp. 1259-1261, Jul. 1996.
- B. Li, G. Li, E. Liu, Z. Jiang, J. Qin, and X. Wang, “Low-loss 1x2 multimode interference wavelength demultiplexer in silicon-germanium alloy,” *IEEE Photon. Technol. Lett.* vol. 11, pp. 575-577, May. 1999.
- S. L. Tsao, H. C. Guo, and C. W. Tsai, “A novel 1x2 single-mode 1300/1550nm wavelength division multiplexer with output facet-tilted MMI waveguide,” *Optics Comm.* vol. 232, 371-379 Mar. 2004.
- J. Xiao, X. Liu, and X. Sun, “Design of an ultracompact MMI wavelength demultiplexer in slot waveguide structures,” *Opt. express*, vol. 15, pp. 8300-8308, Jun. 2007.
- M. H. Ibrahim, S. Lee, M. Chin, N. M. Kassim, A. B. Mohammad, “Multimode interference wavelength multi /demultiplexer for 1310 and 1550 nm operation based on BCB 4024-40 photo definable polymer,” *Opt. Comm.*, vol. 273, pp. 383–388, May 2007.
- A. Ferreras, F. Rodriguez, E. Gomez-Salas, J. L. de Miguel and F. Hernandez-Gil, “Useful formulas for multimode interference power splitter/combiner design,” *IEEE Photon. Technol. Lett.*, vol. 5, no. 10, pp. 1224-1227, Oct. 1993.
- M. Bouda, J. W. M. van Uffelen, C. van Dam and B. H. Verbeek, “Compact 1x16 power splitter based on 1x2 MMI splitters,” *Electron. Lett.*, vol. 30, pp. 1756-1758, Oct.1994.
- R. M. Jenkins, R. W. J. Devereux, and J.M. Heaton, " Waveguide beam splitters and combiners based on multimode propagation phenomen," *Opt. Lett.*, vol. 17, pp. 991-993, Jul. 1992.
- S. El-sabban, I. Schanen, D. Khalil and P. Benech, “Fabrication and test of an integrated optical magic T on a glass substrate,” *IEEE Photon. Technol. Lett.*, vol. 13, pp. 684-686, Jul. 2001.
- H. El-Refaei and Di. Khalil,“ Design of strip loaded weak guiding multimode interference structure for an optical route,” *IEEE J. of Quantum Electron.*, vol. 34, pp. 2286-2290, Dec. 1998.
- S. Nagai, G. Morishima, H. Inayoshi, and K. Utaka, “Multimode interference photonic switches (MIPS),” *IEEE/OSA J. Lightwave Technol.*, vol. 20, pp. 675-680, April 2002.
- J. S. Rodgers, S. E. Ralph, and R. P. Kenan, “Self-guiding multimode interference threshold switch,” *Opt. Lett.*, vol. 25, pp 1717-1719. Dec. 2000,

- F. Wang, J. Yang, L. Chen, X. Jiang, and M. Wang, “Optical Switch Based on Multimode Interference Coupler,” *IEEE Photon Technol. Lett.*, vol. 18 , Jan. 2006, pp. 421-423.
- M. A. Swillam, A. Yehia, A. H. Morshed, and D. Khalil, “Self-imaging in graded index multimode interference devices,” *Mediterranean Microwave Symposium (MMS’2003)*, Cairo, pp. 61-64, May 2003.
- R. L. White, *Basic Quantum Mechanics*, McGraw Hill, 1966, Ch.5.
- Donald L. Lee, *Electromagnetic Principles of Integrated Optics*, John Wiley, 1986, Ch.5.R
- Y. B. lin, J. Liu, and W. Wang, “Analysis of multimode interference couplers with lateral graded-index profiles,” *CLEO/Pacific Rim*, vol. 2, pp. 244 –245, 2001.
- M. A. Swillam, A. H. Morshed, and D. Khalil, “Optimization of optical wide Band 3-dB MMI splitter with graded-index side diffusions,” *IEEE International Conf. on Electrical, Electronic and Computer Engineering ICEEC’04*, no. 173, pp. 633 – 636, Sept. 2004.
- R. Yin, X. Jiang, J. Yang, and M. Wang, “Structure with improved self-imaging in its graded-index multimode interference region,” *J. Opt. Soc. Am. B*, vol. 19, pp. 1301-1303 , Jun. 2002.
- S. Gehrsitz, F. K. Reinhart and C. Gourgon, N. Herres, A. Vonlanthen and H. Sigg, “The refractive index of $\text{Al}_x\text{Ga}_{1-x}\text{As}$ below the band gap: accurate determination and empirical modeling,” *J. of Appl. Phys.* vol. 87, pp. 7825-7837, Jun. 2000.
- D. Dragoman and M. Dragoman, “Reconfigurable electro optical waveguide for optical processing,” *Appl. Opt.*, vol. 42, pp. 6439-6444, Nov. 2003.
- B. Bennett, R. Soref, and J. Alamo, “Carrier-induced change in refractive index of InP, GaAs, and InGaAsP,” *IEEE J. Quantum Electron.*, vol. QE-26, pp. 113–122, Jan. 1987.
- B. Kjornrattanawanich, D. L. Windt, J. F. Seely, and Y. A. Uspenskii, “SiC/Tb and Si/Tb multilayer coatings for extreme ultraviolet solar imaging,” *Appl. Opt.*, vol. 45 pp. 1765–1772. March 2006.
- R. R. Willey, *Practical Design and Production of Optical Thin Films*, 2nd ed. Marcel Dekker Inc., New York, 2002.
- P. Yeh, *Optical Waves in Layered Media*, Wiley, New York, 1988.
- H. A. Macleod, *Thin-Film Optical Filters*, 3rd ed. New York: McGraw-Hill, 2001.
- A. Thelen, *Design of Optical Interference Coatings*, in McGraw-Hill Optical and Electro-Optical Engineering Series. New York: McGraw- Hill, 1989.
- N. Kaiser and H. K. Pulker, *Optical Interference Coatings*. Springer-Berlin; NY, 2003.
- J. Lee, T. Tanaka, S. Sasaki, S. Uchiyama, M. Tsuchiya, and T. Kamiya, “Novel design procedure of broad-band multilayer antireflection coatings for optical and optoelectronic devices,” *IEEE/OSA J. Lightwave Technol.*, vol. 16, pp. 884–891, May 1998.
- S. Boyd and L. Vandenberghe, *Convex Optimization*. Cambridge University Press, 2004.

- Y. Nesterov and A. Nemirovsky, *Interior-point Polynomial Methods in Convex Programming*, SIAM, Philadelphia, PA, 1994.
- J. Nocedal and S. J. Wright, *Numerical Optimization*. Springer, New York, 1999.
- V. Tikhonravov, M. K. Trubetskov, T. V. Amotchkina, and A. Thelen, “Optical coating design algorithm based on the equivalent layers theory,” *Appl. Opt.*, vol. 45, pp. 1530–1538, March. 2006.
- J. A. Dobrowolski and S. H. C. Piotrowski, “Refractive index as a variable in the numerical design of optical thin film systems,” *Appl. Opt.*, vol. 21, pp. 1502–1511, April. 1982.
- S. J. Orfanidis, *Optimum Signal Processing: An Introduction*, 2nd ed., McGraw-Hill, New York, 1988.
- A. V. Oppenheim, R. W. Schaffer, *Discrete Time Signal Processing*. New Jersey: Prentice-Hall, 1999.
- J. F. Sturm, “Using SeDuMi 1.02, a MATLAB toolbox for optimization over symmetric cones,” *Optimization Methods and Software*, vol. 11–12, pp. 625– 653, 1999. Available from <http://sedumi.mcmaster.ca>.
- J. F. Sturm, “Implementation of interior point methods for mixed semidefinite and second order cone optimization problems,” *Optimization Methods and Software*, vol. 17, pp.1105–1154, Dec. 2002.